

CR-184239

Report R91-900065-F

VELOCITY AND PRESSURE CHARACTERISTICS OF A MODEL SSME  
HIGH PRESSURE FUEL TURBOPUMP

(NASA-CR-184239) VELOCITY AND PRESSURE  
CHARACTERISTICS OF A MODEL SSME HIGH  
PRESSURE FUEL TURBOPUMP Final Report  
(Scientific Research Associates) 214 P

N92-12273

CSCL 13K G3/37

Unclassified  
0046419

D. G-N. Tse, J.S. Sabnis, and H. McDonald

Scientific Research Associates, Inc.  
50 Nye Road, P.O. Box 1058  
Glastonbury, CT 06033

Final Report  
Contract NAS-~~36186~~  
8-36186

Prepared for:

NASA  
George C. Marshall Space Flight Center  
Marshall Space Flight Center, AL 35812

March 1991

## **LIST OF TABLES**

- 1. HPFTP Baseline Operating Condition.**
- 2. Flight and Model Operating Conditions.**
- 3. Optical Characteristics of the Laser Velocimeter.**
- 4. Flow and Head Coefficients of the HPFTP and the Air Model.**

## LIST OF FIGURES

1. The SSME High Pressure Fuel Turbopump.
2. Schematic of the SSME HPFTP research rig; a) Basic Geometry, b-d) Possible Modifications to the Basic Geometry.
3. Variation of Sample Size per 1° Window as a Function of Impeller Angle.
4. Discharge Flow Rate of the Turbopump.
5. Pump Curves for the Water and Air Tests.
6. Static Pressure Distribution in the Diffuser/Volute Assembly.
7. Variation of Mean Static Pressure with Impeller Angle.
8. Cyclic Variation of Mean Static Pressure.
9. Measuring Locations and Coordinate System.
10. Revolution-Averaged Velocities at the Bell-Mouth Inlet.
11. Ensemble-Averaged Velocities at the Bell-Mouth Inlet.
12. Revolution-Averaged Radial Velocities Across the Diffuser Width at 2.5 mm Downstream of the Impeller Outlet.
13. Ensemble-Averaged Radial Velocities Across the Diffuser Width at 2.5 mm downstream of the Impeller Outlet.
14. Ensemble-Averaged Tangential Velocities Across the Diffuser Width at 2.5 mm Downstream of the Impeller Outlet.
15. Ensemble-Averaged Radial Velocities in the Diffuser.
16. Ensemble-Averaged Tangential Velocities in the Diffuser.
17. A Plot of  $r$  Times the Revolution-Averaged Tangential Velocity Versus  $r$ .
18. Ensemble-Averaged Radial Velocities in the Turnaround Region.
19. Ensemble-Averaged Tangential Velocities in the Turnaround Region.
20. Ensemble-Averaged Tangential Velocities in the Volute.

## ABSTRACT

Under the present effort an experimental rig has been constructed, an instrumentation package developed and a series of mean and rms velocity and pressure measurements made in a turbopump which modelled the first stage of the Space Shuttle Main Engine High Pressure Fuel Turbopump. The rig was designed so as to allow initial experiments with a single configuration consisting of a bell-mouth inlet, a flight impeller, a vaneless diffuser and a volute. Allowance was made for components such as inlet guide vanes, exit guide vanes, downstream pumps, etc. to be added in future experiments. This flexibility will provide a clear baseline set of experiments and allow evaluation in later experiments of the effect of adding specific components upon the pump performance properties. The rotational speed of the impeller was varied between 4260 and 7680 rpm which covered the range of scaled SSME rotation speeds when due allowance is made for the differing stagnation temperature, model to full scale. The corresponding Reynolds numbers based on the hydraulic diameter and bulk velocity at the exit of the model turbopump varied between  $1.3 \times 10^4$  to  $2.5 \times 10^4$ . While these model Reynolds numbers are lower than flight conditions by several orders of magnitude they are sufficiently high to ensure turbulent flow throughout the model. The bell-mouth inlet allowed intake from atmosphere and was favored in initial testing reported here in order to have a base line flow with the minimum complexity inlet conditions. The flight impeller provided cyclical variability which resembled flight operation. A vaneless diffuser and volute assembly was chosen for a baseline because of its having best efficiency over the widest range and because of its ease of optical access. The results were obtained to aid the design of the inlet and diffuser and to improve the understanding of velocity and pressure characteristics of centrifugal pumps and of the cyclic load associated with the pulsation generated by the rotating impeller.

The results at the inlet obtained with rotational speeds of 4260, 6084 and 7680 rpm showed that the axial velocity at the bell-mouth inlet remained roughly constant at 2.2 of the bulk velocity at the exit of the turbopump near the center of the inlet, but it decreased rapidly with increasing radius at all three speeds. Reverse flow occurred at a radius greater than 0.9 R for all three speeds and the maximum negative velocity reduced from 1.3 of the bulk velocity at the exit of the turbopump at 4260 rpm to 0.35 at 7680 rpm, suggesting that operating at a speed closer to the design condition of 8700 rpm improved the inlet characteristics. The reverse flow caused positive prerotation at the impeller inlet which was negligibly small near the center but reached 0.7 of the impeller speed at the outer annulus.

The results in the diffuser and the volute obtained at 7680 rpm show that the hub and shroud walls of the diffuser were characterized by regions of transient reverse flow with negative revolution-averaged velocity of 8% of the maximum forward revolution-averaged velocity at the

center of the diffuser passage near the shroud wall. The transient recirculation region in the hub side occupied 17% of the diffuser width and that in the shroud side, 9%. The splitter blades reduced the preferential entrainment of flow to the pressure surfaces of the impeller blades but failed to prevent flow separation at conditions investigated. A large sector of negative velocity was observed behind the suction side of the main blade at the hub and shroud walls. The fluctuation attributed to the passing of the main blade persisted until the exit of the turn-around section of the volute. A 128 Hz cyclical fluctuation, which stemmed from blade-to-blade variation, persisted until the region just before the exit of the turbopump.

It is anticipated that the addition of inlet guide vanes (IGV) would eliminate this inlet flow separation, with the unfortunate but apparently inescapable addition of a certain amount of inlet flow distortion from the IGV wakes. Clearly, however, the IGV wakes are to be preferred over the region of inlet flow separation.

## 1. INTRODUCTION

The high pressure fuel turbopump (HPFTP) of the Space Shuttle Main Engine (SSME) is a three-stage radial turbopump powered by an axial turbine at 37,000 rpm. The critical operation of the fuel pump together with the extreme operating conditions makes its performance and reliability essential for flight safety and engine downtime. Problems of pump components cracking have been identified and attributed to excessive unsteady aerodynamic loads. Further to that, off-design operation performance of the turbopump is not well known and its improvement, together with that at design conditions, is desirable.

Despite the advances in turbocompressor technology there are still many areas where knowledge or understanding are incomplete. The review of Ref. 1 identifies some of these areas as, for example, the effect of inlet flow recirculation on compressor performance Refs. 2, 3 and 4, the low momentum secondary flows, diffusion characteristics and blade loading within the impeller Refs. 5, 6 and 7, and the effects of aerodynamic blockage, inlet flow conditions and incidence performance Refs. 8, 9 and 10. The matching of diffuser type with a specific impeller/volute combination is still an open issue while off-design volute performance in terms of pressure recovery can only be roughly approximated. The onset of rotating stall and surge is also an unresolved issue, Refs. 11 and 12.

Improvement of the turbopump loading and performance characteristics requires understanding of the unsteady aerodynamics of the interaction between impeller and diffuser, and this can be accomplished by coordinated experimental and numerical flow analysis investigations in relevant flow configurations. The experimental studies provide the necessary

insight into the physics of the flow and, at the same time, the validation data for the assessment of numerical simulation efforts. The results of numerical studies can in turn be used to guide further experiments with modified diffuser geometries with the further goal of improving the operational characteristics of the turbopump.

The experimental approach followed here focuses on the flow characterization of the first stage of the turbopump as a function of inlet and outlet conditions and diffuser geometry. The main experimental simplification concerns the working fluid which, in this simulation, is air instead of liquid hydrogen. The first task of this work was to design and build an experimental facility to accommodate the actual flight impeller of the first stage of the HPFTP in a flexible test rig in order to allow detailed flow measurements to be obtained nonintrusive by laser Doppler velocimetry at the inlet to the impeller and inside the diffuser. The second task was to develop and test a suitable anemometer system to study the flow field at the exit of the impeller.

Under this contract effort the design and fabrication of the rig was performed by Imperial College, London, under a subcontract. Preliminary measurements were also obtained at Imperial College which were followed by more detailed measurements at higher speeds at SRA. The present report discusses the SRA results. The Imperial College report detailing the work performed under subcontract (Ref. 13) is included as Appendix A of this report. Some of these results have also been presented by Cannon, Vafidis and Whitelaw (Ref. 14).

The following section describes the turbopump, the flow conditions, the instrumentation and the possible sources of uncertainties. Results are presented and discussed in Section 3. Summary conclusions and recommendations are stated in the final section.

## 2. FLOW CONFIGURATION AND INSTRUMENTATION

A line drawing of the SSME High Pressure Fuel Turbopump assembly is shown in Figure 1. It consists of a scroll-shaped entry stage equipped with guide vanes at its exit and is followed by three radial compressor stages, with the last one discharging into a collector volute. The geometry of the turbopump suggests that each of the three stages has different inlet or exit conditions. The design objective for the test rig described here was to simulate the inlet and outlet conditions of the first stage only.

The geometry of the first two stages is identical and consists of a 12" diameter enclosed (shrouded) impeller with six main (full) and three splitter (partial) blades in each passage, and an axisymmetric vaned diffuser volute. The use of the flight impeller defined the geometric scale of the test facility to actual size. The flow similarity between the research turbopump and the flight hardware requires matching the Mach number, flow coefficient, head coefficient, power

coefficient and Reynolds number. The turbopump research rig does not match the Reynolds number since the attempt to match this would result in the power requirement of the rig being impractically high. However, the rig was designed to operate a Reynolds number which would ensure turbulent flow throughout the model.

The HPFTP performance baseline data are summarized in Table 1. Similarity of tip Mach number between model and flight hardware implies a model rotational speed of 8,690 rpm. The expected flow coefficient similarity yields for the model an air mass flow rate of 0.286 kg/s, provided that the inlet and outlet flow conditions of the impeller are similar between flight and model hardware.

---

TABLE 1  
HPFTP Baseline Operating Conditions

---

|                                      | <u>Flight</u> | <u>Model</u> |
|--------------------------------------|---------------|--------------|
| Inlet pressure (abs), bar            | 15.2          | 1.013        |
| Discharge pressure (abs), bar        | 169.5         | 1.141        |
| Inlet temperature, K                 | 23.56         | 292.2        |
| Discharge temperature, K             | 34.4          |              |
| Inlet density, kg/m <sup>3</sup>     | 68.454        | 1.208        |
| Discharge density, kg/m <sup>3</sup> | 74.544        |              |
| Inlet flow rate, kg/s                | 73.75         | 0.286        |
| Pump speed, rpm                      | 36742         | 8690         |
| Pump tip speed, m/s                  | 586.4         | 138.7        |
| Speed of sound, m/s                  | 1456.3        | 344.4        |
| Tip Mach number                      | 0.4           | 0.4          |

---

Similar analysis for off-design speeds of 4000 and 12000 rpm gives the operating parameter estimates summarized in Table 2, below:

---

TABLE 2  
Flight and Model Operating Conditions

---

|                      | <u>Flight</u>     |                      | <u>Model</u>      |                       |
|----------------------|-------------------|----------------------|-------------------|-----------------------|
|                      | min               | Estimated<br>matched | max               | Measured<br>operating |
| Tip Mach number      | 0.4               | 0.18                 | 0.4               | 0.56                  |
| Mass flow rate, kg/s | 73.75             | 0.13                 | 0.29              | 0.39                  |
| Speed, rpm           | 36742             | 4000                 | 8690              | 12000                 |
| $Re_{annulus\ duct}$ | $3.5 \times 10^7$ | $3.5 \times 10^4$    | $8.1 \times 10^4$ | $1.1 \times 10^5$     |
| Pressure rise, bar   | 153.6             | 0.028                | 0.138             | 0.262                 |
| Pump power, kW       | 47170             | 1.07                 | 10.9              | 28.8                  |

---

This preliminary analysis demonstrated that the simulation of the HPFTP operation with air instead of liquid hydrogen as a working fluid is feasible, with relatively high speed and moderate power requirements from the driving device. The driving device selected was a thyristor-controlled DC motor to allow continuously variable and regulated speed. Cost consideration led to the decision to initially use a commercially available DC motor rated at 7.8 kW. Similarity of the power coefficient led to a maximum operational speed of 7680 rpm, 12% below the design speed. However, the test rig itself is designed for future service speed of 14,600 rpm.

Understanding of the impeller/diffuser aerodynamics is expected to benefit from simple inlet and outlet conditions, even if they are not representative of the flow situation in the actual flight turbopump. The simplest possible inlet and outlet conditions correspond to inlet from atmosphere via a vaneless bell-mouth shaped entry section and discharge into a long annular duct. The presence of the annular duct necessitates the introduction of a collector volute at its end in order to direct the discharge flow into a pipe and metering device. The annular duct downstream of the first stage volute was made 10 hydraulic diameters long in order to minimize the upstream effect of the collector scroll.

The geometry of the diffuser volute was also simplified by eliminating the vanes and slightly altering the geometry of the walls to enable better access for LDV velocity measurements. These simplifications are expected to affect the performance of this stage of the turbopump but they

provide a well-defined baseline reference geometry for the study of impeller/diffuser interaction and for the assessment of numerical simulations. The simplified test rig is shown schematically in Figure 2a and represents the basic flow configuration. The primary concern for the design of the basic test rig was the provision of ample optical access for LDV studies at the inlet to the impeller and inside the diffuser and volute. These sections were manufactured in clear cast acrylic (Transpalite SS), selected for its good optical properties and low cost. The turbopump volute was cast, machined, polished and thermally treated in two sections, joined together between two spider-shaped aluminum flanges. The splitting line of the volute is such that future insertion of simple geometry vanes in the radial diffuser would be permitted. Similarity of the leakage flow between model and flight hardware was also considered by arranging for identical clearance gaps between impeller and volute. The labyrinth seal gap width, however, had to be doubled because of the relative radial flexibility of the acrylic volute, and a brush seal was added to the first step of the labyrinth seal to reduce the leakage.

The basic test rig allows further additions of flight hardware to be incorporated in order to simulate more closely the HPFTP geometry. Figures 2b-d show examples of future modifications which have been considered in the design of the test rig. They include variations of inlet and outlet conditions. Incorporation of the upstream scroll and downstream (second) stage volute as well as the possibility of driving air through the rig with stationary or freely rotating impeller. The arrangements of Figures 2b-d clearly indicate that the closer to the flight configuration the rig geometry is, the more restricted the access for LDV flow studies becomes. This complexity and lack of access provided motivation for the decision of initially simplifying the flow configuration as much as possible.

The simultaneous determination of the angular position of the impeller with the LDV measurements called for a high resolution and high frequency response shaft encoder device. Given the 12" diameter of the impeller any uncertainty in terms of angular position would be magnified at the impeller tip. For this reason a hollow-shaft Teledyne 8709 encoder with two tracks of 2048 lines per revolution was used, mounted directly on the impeller shaft and giving angular resolution of 0.176°. Considering the 500 kHz frequency response of the reading head, the selected encoder is suitable for speeds up to 14,600 rpm.

Velocity information was obtained by a laser-Doppler velocimeter similar to that described in Refs. 13 and 14. It made use of rotating diffraction optics together with an Argon ion laser operated at 2 W and 514.5 nm. The optical characteristics of the velocimeter are given in Table 3, below.

Table 3  
Optical Characteristics of the Laser Velocimeter

|   |           |
|---|-----------|
| Half angle of the beam intersection (degrees)                         | 4.85      |
| Fringe spacing ( $\mu\text{m}$ )                                      | 3.04      |
| Number of fringes without frequency shift                             | 17        |
| Diameter of the control volume at $1/e^2$ intensity ( $\mu\text{m}$ ) | 53        |
| Length of the control volume at $1/e^2$ intensity ( $\mu\text{m}$ )   | 620       |
| Maximum frequency shift (MHz)   | $\pm 8.2$ |
| Frequency to velocity conversion ( $\text{ms}^{-1}/\text{MHz}$ )      | 3.04      |

An elliptical mirror at  $45^\circ$  to the laser axis was used to project the control volume into the transparent volute. The velocimeter was operated at off-axis back scattering or  $90^\circ$  scattering modes and the flow was seeded with corn oil of droplets less than  $2 \mu\text{m}$  diameter generated by a TSI atomizer. The signals from the photomultiplier were processed by a TSI 1990C counter. The angular position of the impeller was determined by a Teledyne 8709 shaft encoder with 2048 lines per revolution. A purpose-built DMA card interfaced the output of the TSI counter and the pulse train of the encoder to an IBM/PC compatible. The data acquisition and processing software, specially developed for high speed rotating turbomachinery studies, obtained flow velocity and impeller angular position for every validated Doppler burst and the results were ensemble-averaged to provide mean and rms velocities as a function of impeller angle. This software displayed continuously the number of valid measurements as a function of shaft angle and allowed the sampling procedure to be terminated after a statistically adequate number of data has been acquired in all predetermined angle window of  $1.05^\circ$  (6 encoder pulses) to estimate the mean and rms velocities.

Uncertainties in the laser velocimeter measurements in the present study arose mainly from finite sampling statistics, spatial velocity gradient broadening and seed biasing. Seed biasing was evident in the sample size per  $1.05^\circ$  averaging window for four measurement locations presented in Figure 3. The sample size curves were peaky with minima and maxima occurring over repeated angles. This indicated that a smaller number of seeding particles was being counted at some impeller angle than others over the averaging time and conventional averaging led to error in the revolution averaged result. The angle resolved averaging performed in this investigation

eliminated this effect.

Statistical uncertainty in the mean velocity associated with a finite sample size can be estimated using the expression:

$$\bar{U}_C = \frac{S}{\sqrt{N}} \times \frac{\sqrt{\bar{u}^2}}{\bar{U}}$$

where  $S$  is equal to 4 for a 99% confidence limit. The excellent blade-to-blade repeatability presented in Section 3.2 shows that averaging of velocity over six main blade passages would not introduce a significant uncertainty. The sample sizes over the six main blade passages were in general above 9000 and, in most cases the turbulence intensities were below 0.7. These resulted in a statistical uncertainty of less than 3% in each ensemble-averaged mean velocity. The corresponding uncertainty in the rms value can be estimated from the expression:

$$\sqrt{\bar{u}_C^2} = \frac{S}{\sqrt{2N}}$$

which indicates, with 99% confidence, an uncertainty of better than 3% for the sample size used in the measurements.

Since a linear velocity variation across a finite volume does not affect the mean value, the uncertainty associated with spatial gradient broadening need only be applied to the measured rms value which contained contributions from both the turbulence and spatial variation of the mean velocity across the control volume and a finite arc length. The contribution associated with mean velocity gradient is given by:

$$\sqrt{\bar{u}_g^2} = \frac{\Delta L}{4} \times \frac{d\bar{U}}{d\ell}$$

and the associated uncertainty can be deduced from:

$$\sqrt{\bar{u}_C^2} = \left[ 1 - \frac{\sqrt{\bar{u}_g^2}/\bar{u}^2}{1} \right]^{0.5} - 1$$

According to these equations, angle-broadening effect led to overestimation by 1% in the vicinity of the pressure and suction surfaces of each impeller blade, where the gradient was steepest, with velocity gradient of 4m/s per degree and local turbulence intensity of 7m/s. The use of a 200 $\mu$ m pinhole and off-axis and 90° scattering reduced the effect size of the control volume gradient

broadening across the control volume was reduced to less than 0.5% under the same condition. The above analysis indicates that the overall uncertainty in the mean and rms values in the present study are less than 3% and 4%, respectively.

A Kulite miniature transducer was used to analyze the pressure characteristics inside the volute. It was flush mounted on the shroud wall at  $\theta \approx 180^\circ$  to measure pressure pulsation associated with the passing blades. The pressure taps were installed at  $r = 161$  mm to 193 mm at 6 equally spaced positions in the diffuser, at  $z = 11.4$  mm to 30.5 mm in the turn-around section at 4 equally spaced positions and at  $r = 130$  mm to 178 mm at 6 equally spaced positions in the volute. The measuring position was selected by installing the transducer at the appropriate pressure tap. The instantaneous pressure was obtained as a function of impeller angle by an IBM/PC compatible based data acquisition system by means of external triggering. The results presented in Section 3.1 show that there is no steep pressure gradient and spatial gradient broadening was unimportant. Statistical uncertainties were maintained unimportant at 2 and 15% of the mean and rms value by ensuring a sufficient number of data in each ensemble average.

### 3. RESULTS AND DISCUSSION

The mass and volume flow rates were measured by a venturi meter downstream of the collector scroll. The results presented in Figure 4 indicate a linear increase of mass flow rate with rotational speed but a less than linear increase of volume flow rate with speed due to variable density effects. The mass flow rate was 60% less than that predicted by similarity analysis for the same impeller operating at design conditions with hydrogen working fluid. The velocity measurements presented in Subsection 3.2 show the presence of reverse flow at the inlet. This suggests that the impeller may require specific inlet conditions which cannot be provided by the existing bell-mouth configuration. Replacing the bell-mouth inlet by a long duct did not alter the flow and pressure characteristics of the turbopump. Adding splitter cones with small intake area to restrict the flow to the center removes the reverse flow at the outer annulus but the mass flow rate and the pressure head remained unchanged. Adding a large round baffle at an axial distance in the range of 12.7 to 76.2 mm from the edge of the bell-mouth entry to guide the flow into the turbopump radially has no effect on the performance. Further measurements conducted with an annular inlet that matched the wall inlet angle in the  $r$ - $z$  plane showed no improvement on the performance of the turbopump. Based upon these studies the mass flow rate and the pressure head of the turbopump appear to be insensitive to modifications of the inlet flow in the  $r$ - $z$  plane and pressure and velocity measurements in the remainder of this section were obtained

with the bell-mouth entry. Future work should investigate the result of varying the flow in the  $r-\theta$  plane and adding a downstream pump. Flow in the  $r-\theta$  plane is probably best controlled by the addition of inlet swirl guide vanes.

The performance of the turbopump was evaluated by the head coefficient,  $\psi$ , and flow coefficient,  $\phi$ . The head coefficient is calculated using the difference between static head at the outlet of the diffuser and the inlet of the impeller and a plot of  $\psi$  versus  $\phi$  for the air test conducted at SRA is shown in Figure 5(a). Figure 5(b) and Table 4 show the head and flow coefficients for the water and the actual SSME turbopump tests conducted at NASA MSFC. As expected, water tests are better able to match flow coefficients whereas air tests are better able to match head coefficients.

Table 4

Flow and Head Coefficients of the HPFTP and the Air Model

|                       | HPFTP | Air Model |
|-----------------------|-------|-----------|
| Impeller exit, $\psi$ | 3.47  | 4.64      |
| Stage exit, $\psi$    | 2.72  | 1.23      |
| $\phi$                | 0.058 | 0.023     |

In the air test the head coefficient at the impeller outlet of the model was 33% higher than that of the SSME turbopump but that at the stage discharge, 60% lower. Frictional losses in the model turbopump were relatively large, because of relatively large wetted areas associated with radial-flow machines and relatively low Reynolds number. These frictional losses can be reduced by increasing the rotational speed of the impeller to bring the operating condition closer to the design point and by adding a second impeller downstream of the collecting scroll to increase the flow rate through the turbopump. The streamline patterns in vaneless diffusers of centrifugal machineries resemble logarithmic spirals. Thus, the existing diffuser incurs high frictional losses because of the long length of the spiral flow. Diffuser vanes can be added in future works to remove swirl thus guiding the flow in the radial direction to increase the rate of diffusion and to decrease loss. Of critical importance, however, is the fact that diffuser vanes are present in the full scale turbopump, are thought to be a source of unsteady pressure, and thus must eventually

be represented. Their absence from the present model was simply to establish a representative base line from which to quantify the effect of the diffuser vanes.

Pressure measurements obtained before and after the exit bend show a large loss of 50% of the maximum static pressure rise attained at the diffuser. A bend can have a loss coefficient of up to 2.0 and can induce potentially large losses, due to flow separation at the walls and a secondary flow arising from centripetal acceleration. Turbulence and separation losses at a bend are generally proportional to the square of the absolute velocity. Tangential velocity is inversely proportional to the radius in a vaneless diffuser of a centrifugal pump and this is evident in the measurements of Subsection 3.2 which show revolution-averages of 65 and 76 m/s in the tangential components at the turn-around region ( $r = 157.5$  mm) and at the volute ( $r = 188.0$  mm), respectively. The absolute velocity at the exit bend of the turbopump is high because the flow has a swirl component of up to 10 times the magnitude of the bulk velocity of 7.7 m/s. The losses at the exit bend can be reduced by diffuser guide vanes which reduce the magnitude of the tangential component at the turn-around section and the volute. The high tangential velocity at the exit of the turbopump, which indicates that a considerable fraction of the impeller work is stored in the form of kinetic energy associated with swirl, is dissipated partly at the annular duct but mainly in the collecting scroll. The 33% higher-than-expected head coefficient at the impeller outlet of the model stems from back pressure induced by the losses at the exit bend and the dissipation of swirl by collection scroll.

The flow coefficient of the model is 60% lower than that of the SSME turbopump and this cannot be explained by the losses in the diffuser. Other experiments at SRA involving centrifugal pumps show that adding a second pump to a flow system increases the flow rate considerably, up to approximately 50%. The absence in the model of the second and third stages of the turbopump may alone account for the lower-than-expected flow coefficient of the model.

The efficiency of the air turbopump, evaluated by  $Q \times \Delta P$  divided by the input power, is approximately 12%. The efficiencies of the two turbopumps should be equal for perfect similarity but the HPFTP has a higher efficiency of 76%. The flow coefficient, head coefficient and efficiency observed in the present study are consistent with those described in Ref. 15 which show that reducing the Reynolds number by 3 orders of magnitude led to similar changes in these quantities. It is unlikely that reasonable Reynolds number similarity could be achieved with acceptable power levels in a continuously operated air facility.

### 3.1 Pressure Measurements

#### 3.1.1 Steady Pressure Measurements

The static pressure distribution in the diffuser/volute assembly, Figure 6, shows that the air pressure increases from near atmospheric at the impeller inlet to 8.5 kPaG (95% of the dynamic head of the impeller) at the impeller outlet. The pressure continues to increase in the diffuser and it reaches a maximum of 10.7 kPaG at the turn-around section. A pressure rise of 2.2 kPa between the impeller outlet and the turn-around section cannot be accounted for by the deceleration of the radial flow. It stems mainly from the reduction of tangential velocity from 90 m/s to 65 m/s associated with the conservation of angular momentum and this is evident from the result presented in the following velocity section. As expected, the static pressure in the turn-around section remains constant because there is no sharp change in the tangential velocity. The static pressure decreases from its maximum to 7.4 kPaG just upstream of the exit bend. A pressure drop of 3.3 kPa would correspond to an increase in the tangential velocity from 65 m/s in the turn-around section to 98 m/s just upstream of the final bend. Comparison of velocity deduced from pressure tap 13 and the tangential measurement at the same radial position confirms the velocity increase with difference due to frictional loss. The result indicates the importance of minimizing the residual swirl in the turn-around section by diffuser guide vanes. Otherwise the energy extracted from the impeller will be transferred back to swirl in the volute rather than to pressure rise and through flow in the stage resulting in a drastic reduction in the efficiency of the turbopump.

#### 3.1.2 Unsteady Pressure Measurements

The pressure maxima and minima associated with the pulsation of the passing main blade is clearly evident in the ensemble-averaged distributions in the diffuser over one revolution, presented in Figure 7 as a function of impeller angle. The maxima in the first pressure tap in the diffuser, turn-around section and the volute are 9.1 kPaG, 10.9 KPaG and 9.8 kPaG and the minima, 8.4 kPaG, 10.4 kPaG and 9.4 KPaG. These correspond to peak-to-peak fluctuations of 0.7 kPa, 0.5 kPa and 0.4 kPa (7.8%, 5.6% and 4.5% of the dynamic head of the impeller of 8.9 kPa) in the diffuser, turn-around section and the volute. In the actual turbopump, the dynamic head of the impeller is as high as 11.7 MPa and the guide vanes in the diffuser, turn-around section and the volute could potentially be subjected to fluctuating pressure of 920 kPa, 660 kPa and 530 kPa if perfect similarity apply. The influence of the splitter blades is small and their signatures are not detected by the miniature transducer. A 128 Hz cyclical

fluctuation stemming from blade-to-blade variation is also evident in the pressure distribution of Figure 8 obtained by ensemble-averaging over six revolutions. The signature of the main blade has disappeared after the turn-around section of the volute but the 128 Hz cyclical fluctuation persisted at the location just upstream of the exit bend because the amplitude of the highest maxima and the lowest minima within one revolution is higher than the amplitude of any single blade passage.

### 3.2 Velocity Measurements

Figure 9 shows the coordinate system for presenting the results. Measurements were obtained in the bell-mouth inlet, diffuser, turn-around rectify and the volute throughout 360° rotation but some results are presented as revolution-averaged or as six superimposed traces in a 60° window to illustrate the mean flow quantity or blade-to-blade variation. A marker pulse per rotation from the encoder identified the same angle on each rotation and it was synchronized with the first velocity minimum of the radial component at  $r = 2.5$  mm and  $z = 1.3$  mm, which corresponds to the wake of one of the main blade.

Velocity measurements obtained at a rotational speed of 4260, 6084 and 7680 rpm in the inlet section at 37.5 mm upstream of the impeller and the revolution-averaged velocities are shown in Figure 10(a). The axial velocity remains roughly constant at 2.2 times the bulk velocity near the center but it decreases rapidly with increasing radius at all three speeds. The bulk velocity,  $U_b$  is defined as the average velocity at the annular duct of the discharge. The results indicate the presence of flow reversal near the outer annulus of the bell-mouth entry section similar to that described in Refs. 2, 3 and 4. In all three cases, the change from forward to backward velocity occurs at 0.9 R and the reverse flow region occupies 27% of the intake area. The maximum negative velocity reduces from  $1.3 U_b$  at 4260 rpm to  $0.35 U_b$  at 7680 rpm, suggesting that operating closer to the design point improves the velocity characteristics at the inlet. The reverse flow causes positive prerotation at the impeller inlet, which is negligibly small near the center but reaching  $0.7 V_b$  near the outer annulus as indicated in the tangential velocity profiles of Figure 10(b), where  $V_b$  is the blade velocity. Prerotation is a common occurrence when pumps are operated at flow rates less than designed. The investigations described in Ref. 16 showed that prerotation occurred at near shut-off in pumps with vaneless diffuser. The signature of the impeller blades is clearly evident in the velocity profiles of Figure 11 - suggesting that the prerotation in the present investigation may be caused by viscous drag of the impeller or by reverse flows in the impeller.

The revolution-averaged radial velocity profiles across the diffuser width at 2.5 mm downstream of the impeller outlet are presented in Figure 12. The results indicated that the

shroud wall of the diffuser is characterized by large sectors of transient reverse flow which give rise to negative revolution-averaged velocity of the maximum revolution-averaged forward velocity at the center of the diffuser. The recirculation region occupies 10% of the diffuser width. The revolution averaged velocity near the hub wall remains positive but there are large sectors of transient reverse flow reaching 50% of the maximum positive value occupying 60% of the blade passage at  $z = 14$  mm, 1.24 mm (8% of the diffuser width) from the hub wall. The transient reverse flow is still noticeable at  $z = 12.7$  mm, 17% of the diffuser width from the hub wall, with magnitude and area diminished to 7% of the maximum positive velocity and roughly 8% of the blade passage. The transient recirculation regions near the hub and shroud are attributed to the secondary flow arising from the centripetal acceleration associated with turning the inlet flow from axial to radial direction and Coriolis acceleration associated with rotation.

The ensemble-averaged radial and tangential velocities at various diffuser widths at 2.5 mm downstream of the impeller outlet are presented in Figures 13 and 14, respectively. An excellent periodic repeatability over the 360° revolution on the centerline and a good periodic repeatability across the entire width of the impeller exit are evident in the figures but there are substantial variations in the velocity profiles in the cross-section direction. The wakes of the main blades are indicated by minima with steep gradients on both the mean and rms quantities of the tangential and radial profiles at every 60°. The wakes corresponding to the half and quarter splitter blades are also marked by secondary minima at every 15, 30 and 45° within the passage of the main blade. The wake of the quarter blade preceding the suction side of the leading main blade is less pronounced and the secondary peaks and troughs associated with the splitter blade have reduced amplitude.

Figure 13 shows that velocity peaks of different magnitude occur on the radial flow exiting in front of the pressure surface of the main and splitter blade. At the centerline of the diffuser, these peaks increase from a minimum of 16 m/s behind the suction side of the leading main blade to a maximum of 22 m/s in front of the pressure side of the trailing main blade. Preferential entrainment of flow to the pressure side in centrifugal machinery is associated with the influence of Coriolis forces [Ref. 17]. The Coriolis force stabilizes the boundary layers on the suction side of the impeller blade and suppresses turbulence. Consequently the momentum exchanges with the through-flow is retarded and the ability of the boundary layer to overcome the increasing pressure is reduced so that separation occurs. On the pressure side of the blade, the effect is reversed and the boundary layer is destabilized by Coriolis forces and this enhances mixing with the through-flow. Consequently, the pressure side boundary layers are energized and this side of the passage will always have a higher flow. The splitter blades reduce the preferential entrainment of flow to the pressure side but fail to prevent flow separation at a condition below the design point. Large sectors of negative velocity are observed behind the suction side of the

main blade near the hub and shroud walls, Figures 13(a), 13(g) and 13(h), suggesting that air is drawn in from the diffuser to fill the velocity defects.

Figure 14 shows that, contrary to the radial component, tangential velocity peaks of different magnitude occur behind the suction side of each main and splitter blades. At the centerline of the diffuser, for example, these peaks reduce from a maximum of  $0.86 V_b$  behind the suction side of the leading main blade to a minimum of  $0.74 V_b$  in front of the pressure side of the trailing main blade. Comparison of the tangential and radial velocities show that the maximum radial velocity occurs when the swirl velocity is minimum and vice-versa. The angle of the velocity vector in the  $r\theta$  plane varied between  $75^\circ$  to  $85^\circ$ .

The radial and tangential velocities obtained in the diffuser are presented in Figures 15 and 16. The tangential component has magnitude of up to four times higher than that of the radial component. The measurements in Section 3.1 show that there is an adverse pressure gradient acting on the radial component. Radial separation is evident in the velocity obtained close to the hub and shroud wall, Figures 13(a), 13(g) and 13(h). According to Ref. 18, when reverse flow occurs in the radial boundary layer, it is not possible for the tangential component to diffuse axisymmetrically because this would lead to a pressure increase in one component but not in the other. As a result, asymmetrical flow breakdown occurs producing flow spirals. These flow spirals were visible during the experiment when the seeding oil deposited on the shroud wall streaked and produce a trace of the flow pattern. Contrary to the results of Refs. 13 and 14, which showed that the radial velocity increase from  $r = 2$  mm to  $r = 5$  mm, the present results obtained at  $180^\circ$  apart, Figures 14(a) and 14(b), show that there is a reduction in the revolution averaged velocity from 21 m/s to 13 m/s at the same radial position. This is due to jets and wakes associated with the flow spirals. No sharp increase or decrease is observed in the revolution averaged velocity beyond  $r = 10$  mm because of the jets and wakes of the spiral is considerably damped by the longer mixing length at large radii. The wakes of the partial blades on the mean velocities are evident up to  $r = 15$  mm, one blade tip height. The influence of the partial blades is stronger on the rms profile and the wakes persist until  $r = 20$  mm. Beyond  $r = 20$  mm, the signature of the partial blade disappears from the velocity profiles and the periodical fluctuation within each main blade passage is smoothed out by turbulence mixing and has no further influence on the velocity field. In the absence of guide vanes, the tangential velocity is unaffected by area change and is inversely proportional to the radius, Ref. 18. This is evident in the plot of  $rW_{rev}$  versus  $r$  provided in Figure 17. The  $rW_{rev}$  value remains roughly constant at  $\pm 4\%$  above the mean value in the diffuser and the turn-around section and that in the volute, 8% below the mean due to frictional loss.

Comparison of the present results obtained at 7680 rpm with those obtained by Refs. 13 and 14 at 4260 rpm show that the velocity profiles obtained at the same location are similar. The

maximum and minimum velocity at the impeller exit and in the turn-around section scale with the impeller speed. The revolution averaged velocity, however, scales better with the measured flow rate. The flow characteristics in the radial diffuser are not significantly affected by the impeller speed.

The measurements in the turn-around section are presented in Figures 18 and 19, which show that the radial and tangential mean velocities over one revolution are all close to zero and 65 m/s, respectively. The signature of the main impeller blades is still noticeable in the profiles of both components but is considerably damped with maxima and minima of  $\pm 1$  m/s above the mean value. The flow enters the volute with swirl as the predominant component. This is due to the lack of guide vanes in the diffuser/volute assembly and is expected to be one of the reasons for the low flow coefficient. However, the results obtained with the vaneless diffuser geometry can be used in the design of guide vanes, Ref. 9, which should be incorporated in future work.

The tangential velocities in the volute at  $r = 157.5$  mm are presented in Figure 20. The signature of the blade has disappeared from both the mean and rms profiles and the velocities are independent from the impeller position. The revolution-averaged velocity has increased from 65 m/s at the exit of the turn-around section ( $r = 188.0$  mm) to 76 m/s.

## CONCLUSION AND RECOMMENDATIONS

A rig has been constructed and velocity and pressure measurements made for geometry and flow conditions relevant to the first stage SSME turbopump. These initial experiments have considered a simple geometry with a bell-mouth inlet, an actual SSME impeller and a vaneless diffuser. The initial results provide a baseline set of data which can be expanded at a later date through more complex and realistic inlet, exit and diffuser geometries. The following conclusions can be extracted from these initial results:

1. With the existing baseline hardware the flow coefficient was 60% less and the head coefficient was 33% higher than the SSME HPFTP first stage. This is likely due to the absence of the second and third stages of the turbopump and to operating speeds below the design condition. Another possible reason may be the lack of inlet guide vanes. The tangential velocity in a vaneless diffuser of a centrifugal pump is inversely proportional to the radius and this led to high velocity in the turn-around and the volute and consequently resulted in losses at the exit bend of the model turbopump of up to 50% of the maximum static pressure rise attained in the diffuser. The vaneless diffuser configurations also led to frictional losses associated with the long length of the spiral flow. The efficiency of the model turbopump at 7680 rpm was 12% as a result

of the losses described above. The addition of diffuser guide vanes should result in a significant reduction in the diffuser based losses.

2. The axial velocity at the bell-mouth inlet remained roughly constant at 2.2 of the bulk velocity at the exit of the turbopump near the center but it decreased rapidly with increasing radius at all three speeds. With the current configuration reverse flow occurs at a radius greater than 0.9 R for all three speeds and the maximum negative velocity reduced from 1.3 of the bulk velocity at the exit of the turbopump at 4260 rpm to 0.35 at 7680 rpm, suggesting that operating closer to the design condition improved the velocity characteristics at the inlet. The reverse flow caused positive prerotation at the impeller inlet which was negligibly small near the center but reaching 0.7 of the impeller speed at the outer annulus at all three speeds.

3. The hub and shroud walls of the diffuser were characterized by regions of transient reverse flow with negative revolution-averaged velocity of 8% of the maximum revolution-averaged forward velocity at the center of the diffuser passage near the shroud wall. The transient recirculation region in the hub side occupied 17% of the diffuser width and that in the shroud side, 9%. The transient recirculation regions stemmed from the secondary flow arising from the centripetal acceleration associated with turning the inlet flow from axial to radial direction and Coriolis acceleration associated with rotation.

4. The splitter blades reduced the preferential entrainment of flow to the pressure surfaces of the impeller blades but failed to prevent a flow separation condition at the current operating conditions. Large sectors of negative velocity were observed behind the suction side of the main blade close to the hub and shroud walls.

5. The pulsation generated by the passing of the main blade led to peak-to-peak fluctuation of 7.8%, 5.6% and 4.5% of the dynamic head of the impeller of 8.9 kPa in the diffuser, turn-around section and the volute. In the actual turbopump, the dynamic head of the impeller is as high as 11.7 MPa and the guide vanes in the diffuser, turn-around section and the volute could potentially be subjected to fluctuating pressures of 920 kPa, 660 kPa and 530 kPa if perfect similarity applies. The signature associated with the splitter blades disappeared from the pressure and velocity distributions at one impeller width downstream of the impeller. A 128 Hz cyclical fluctuation stemmed from blade-to-blade variation induced pressure fluctuations which persisted until the region just upstream of the exit of the turbopump. Fluctuations due to blade-to-blade variation were marginally higher than those associated with the main blade

because the amplitude of the highest maxima and the lowest minima within one cycle was higher than the amplitude of any single blade passage.

6. Future work should consider an addition of a second pump and diffuser vanes, inlet guide vanes and operating at higher impeller speed. With a second pump or at high rotational speed the flow will have a higher momentum to overcome the adverse pressure gradients in the impeller and diffuser and reduce losses due to friction and separation. Diffuser vanes will reduce frictional losses by removing swirl to increase the rate of diffusion and losses at the exit bend by reducing the tangential velocity at the turn-around region and the volute.

#### ACKNOWLEDGEMENT

This work was carried out under NASA MSFC contract NAS8-36186 in collaboration with Imperial College, whose help at all stages of the program is acknowledged. The authors are grateful to Mr. J.L. Cannon of NASA MSFC for providing the data for comparison. Thanks are also due to Mr. Gary Winch and Mr. Eugene Chen of SRA for maintenance of the experimental facilities and for development of instrumentation.

#### REFERENCES

1. Japikse, D.: "Future performance, design possibilities and goals for radial compressors," IMechE Paper C101/86, 1986.
2. Breugelmans, F.A.E. and Sen, M.: "Prerotation and fluid recirculation in the suction pipe of centrifugal pumps," Proc. 11th Annual Turbomachinery Symposium, Texas A&M University, pp. 165-180, Dec. 1982.
3. Japikse, D.: "A critical evaluation of stall concepts for centrifugal compressors and pumps - Studies in component performance, Part 7," in *Stability, Stall and Surge in Compressors and Pumps*, ASME, Dec. 1984.
4. Kammer, N. and Rautenberg, M.: "A distinction between different types of stall in centrifugal compressor stage," ASME Paper No. 85-GT-123, 1985.
5. Eckardt, D.: "Flow field analysis of radial and backswept centrifugal compressor impellers, Part 1: Measurements using a laser velocimeter," in *Performance Prediction of Centrifugal Pumps and Compressors*, ASME, 1980.

6. Eckhardt, D.: "Instantaneous measurements in the jet-wake discharge flow of a centrifugal compressor impeller," *J. Engng. for Power*, pp. 337-345, July 1975.
7. Krain, H.: "Interdependence of centrifugal compressor blade geometry and relative flow field," *ASME Paper No. 85-GT-85*, 1985.
8. Japikse, D.: "Turbomachinery diffuser design technology," in *The Design Technology Series*, (DTS-1), 1984.
9. Kano, F., Tasawa, N. and Fukao, Y.: "Study of flow distribution and aerodynamic performance of centrifugal compressors," *SAE Paper 820328*, 1982.
10. Rodgers, C.: "The performance of centrifugal compressor channel diffusers," *ASME Paper No. 82-GT-10*, 1982.
11. Elder, R.L. and Gill, M.E.: "A discussion on the factors affecting surge in centrifugal compressors," *ASME Paper No. 84-GT-194*, 1984.
12. Otugen, M.V., So, R.M.C. and Hwang, B.C.: "Diffuser stall and rotating zones of separated boundary layer," *Exp. in Fluids*, Vol. 6, 1988.
13. Vafidis, C. and Whitelaw, J.H.: Design and preliminary flow field evaluations of the SSME high pressure fuel turbopump research rig, *Imperial College Report FS/90/02*, 1990.
14. Cannon, J.L., Vafidis, C. and Whitelaw, J.H.: Design and flow field evaluation of a SSME high pressure fuel turbopump. Submitted for presentation at the 1990 Conference on Advanced Earth-to-Orbit Propulsion Technology, 15-17 May, NASA-MSFC, Huntsville, Alabama, U.S.A.
15. White, F.M.: *Fluid Mechanics*, McGraw-Hill, 1979.
16. Sheperd, D.G.: *Principles of Turbomachinery*, MacMillan, 1956.
17. Dean, R.C., Jr.: The fluid dynamic design of advanced centrifugal compressors, Lecture notes presented at Von Karman Institute, Brussels, Belgium, 1974.
18. Wilson, D.G.: *The Design of High Efficiency Turbomachinery and Gas Turbine*, MIT Press, 1984.

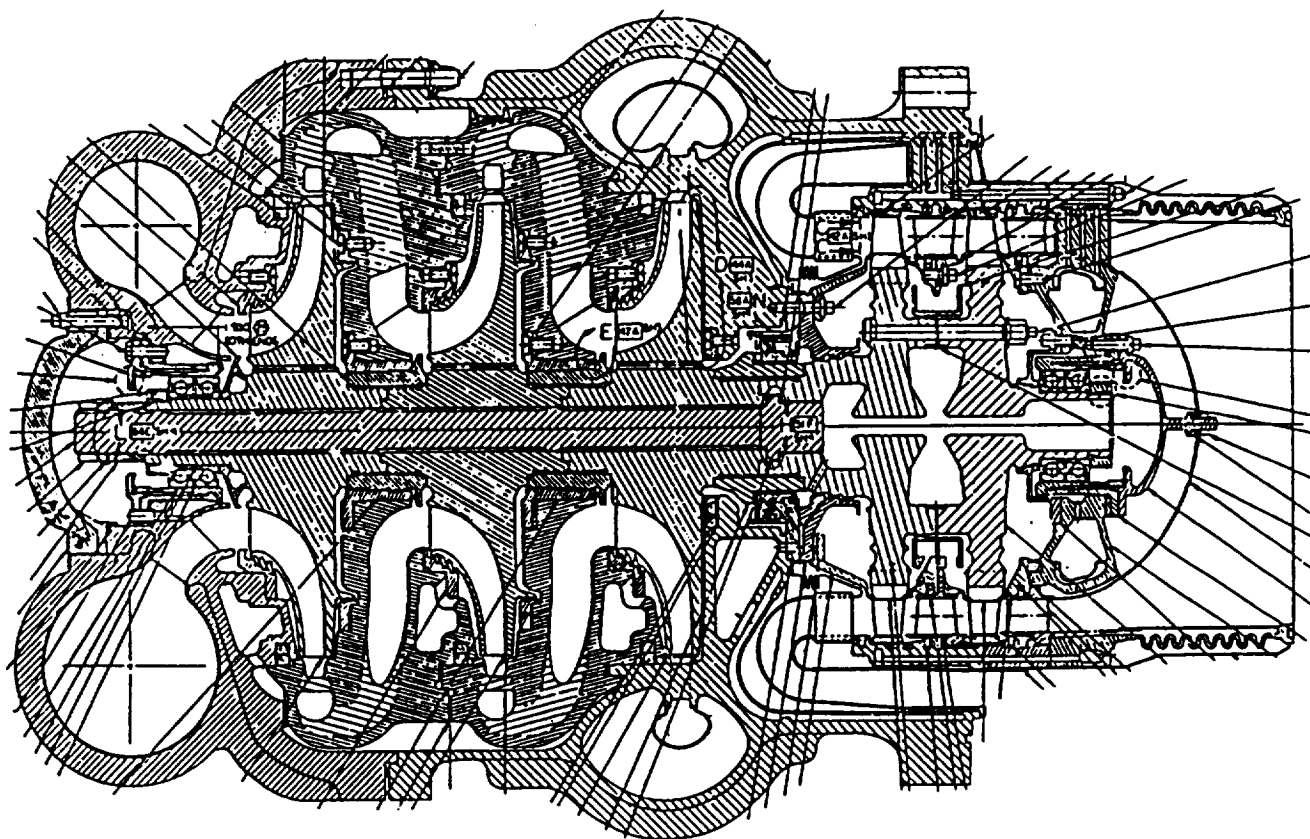


Fig.1. The SSME High Pressure Fuel Turbopump.

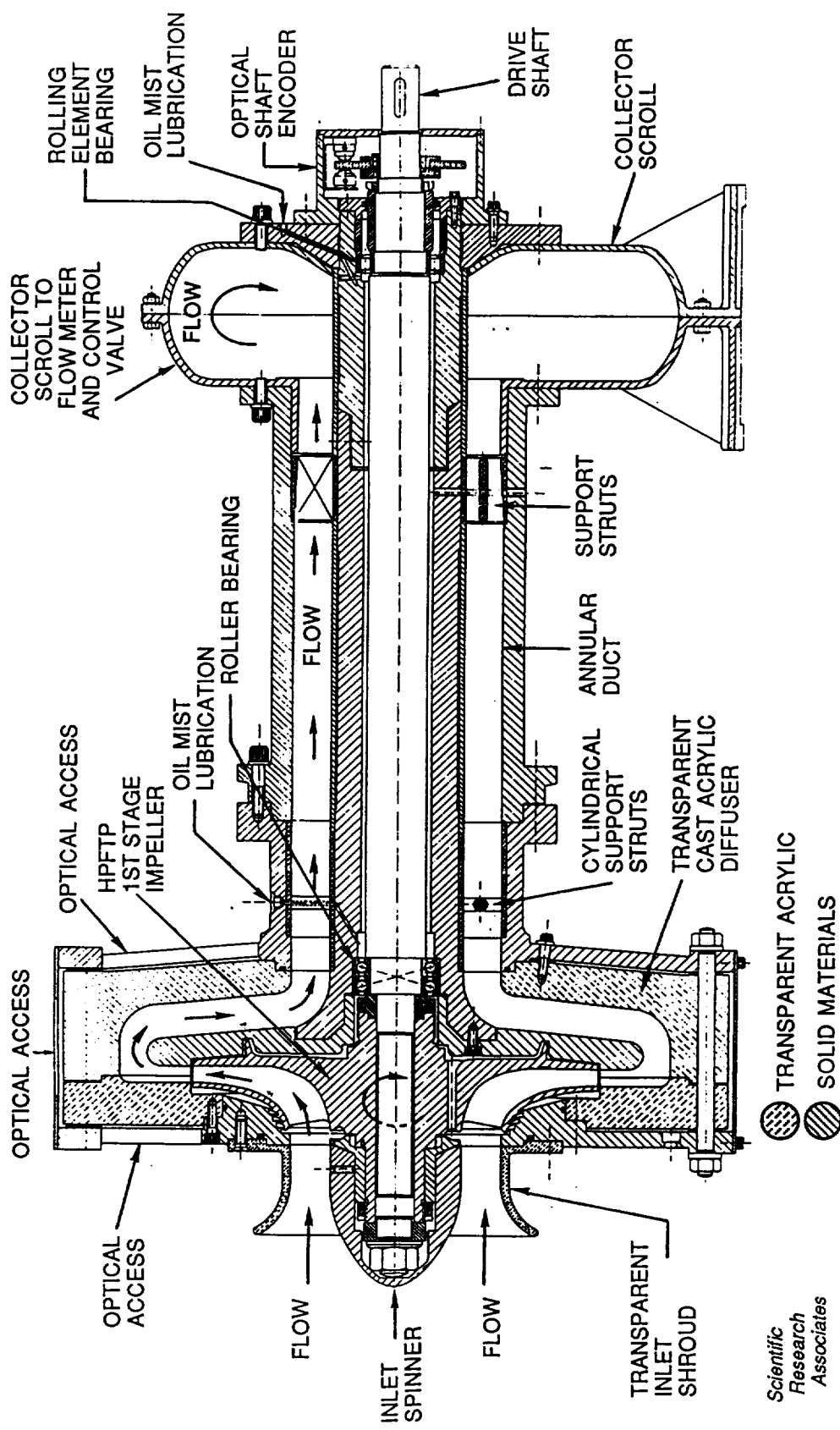


Fig. 2a. Schematic of the SSME HPFTP Research Rig. Basic Geometry.

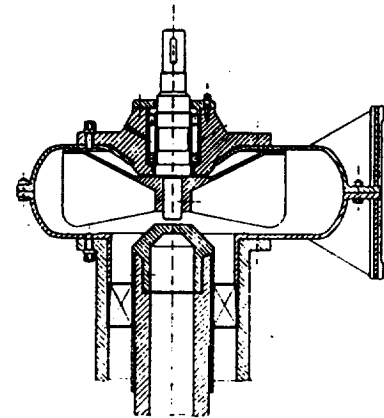
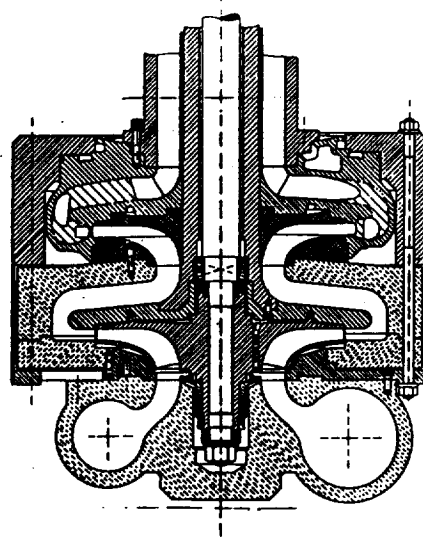
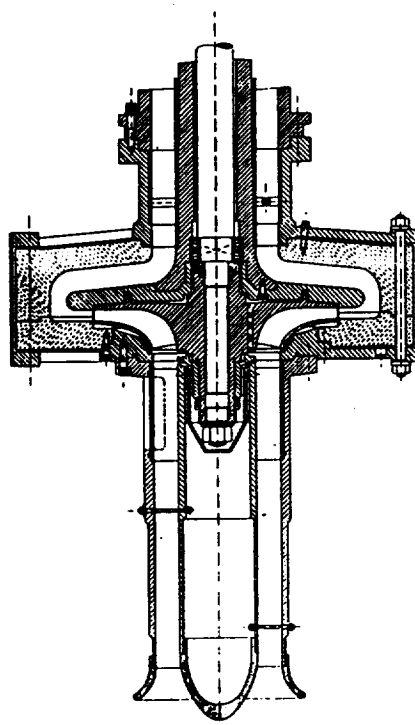


Fig. 2b-d. Schematic of the SSME HFTP Research Rig.  
Possible Modifications to the basic Geometry.

ORIGINAL PAGE IS  
OF POOR QUALITY

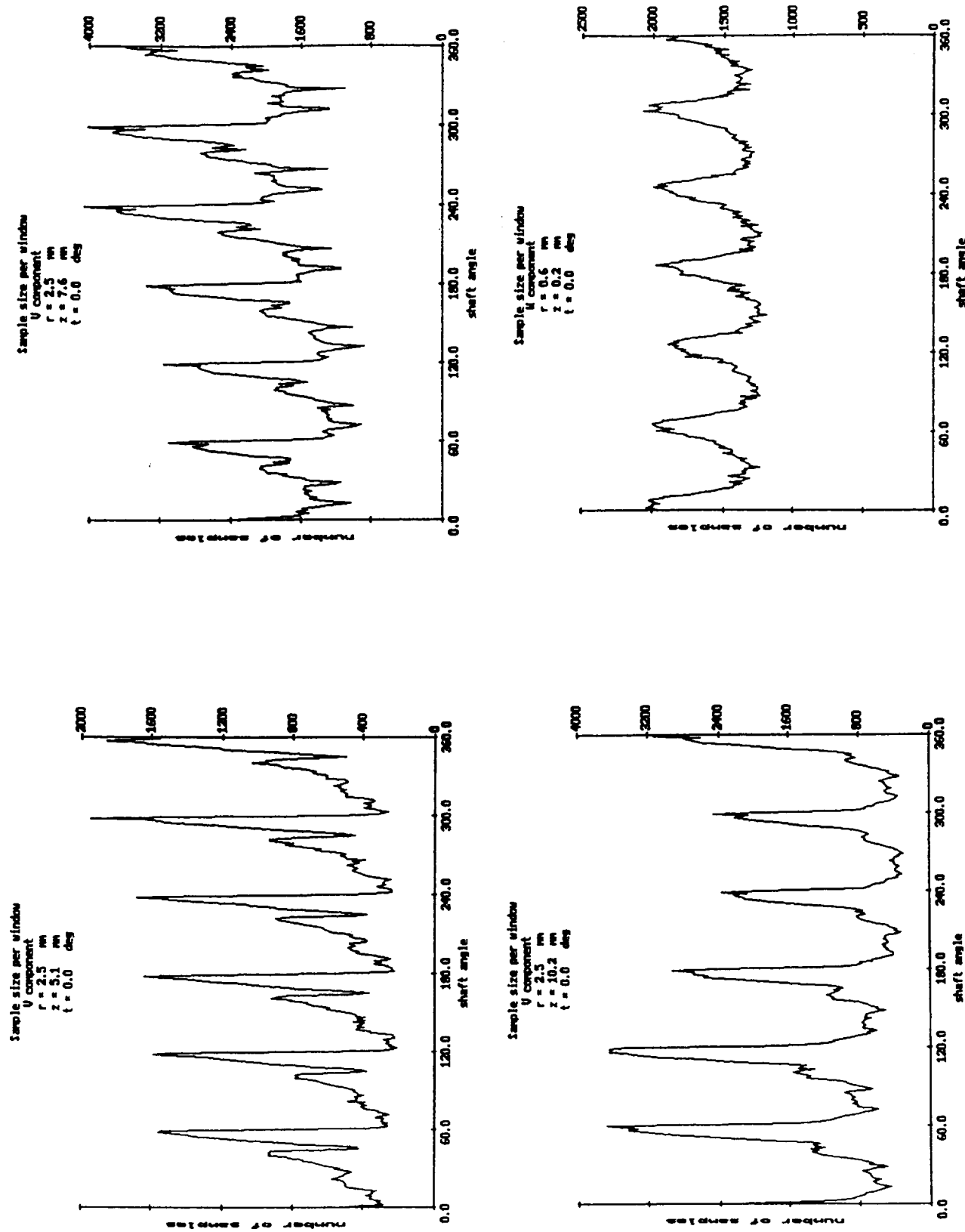


Fig. 3. Variation of Sample Size per  $1^\circ$  Window as a function of Impeller Angle.

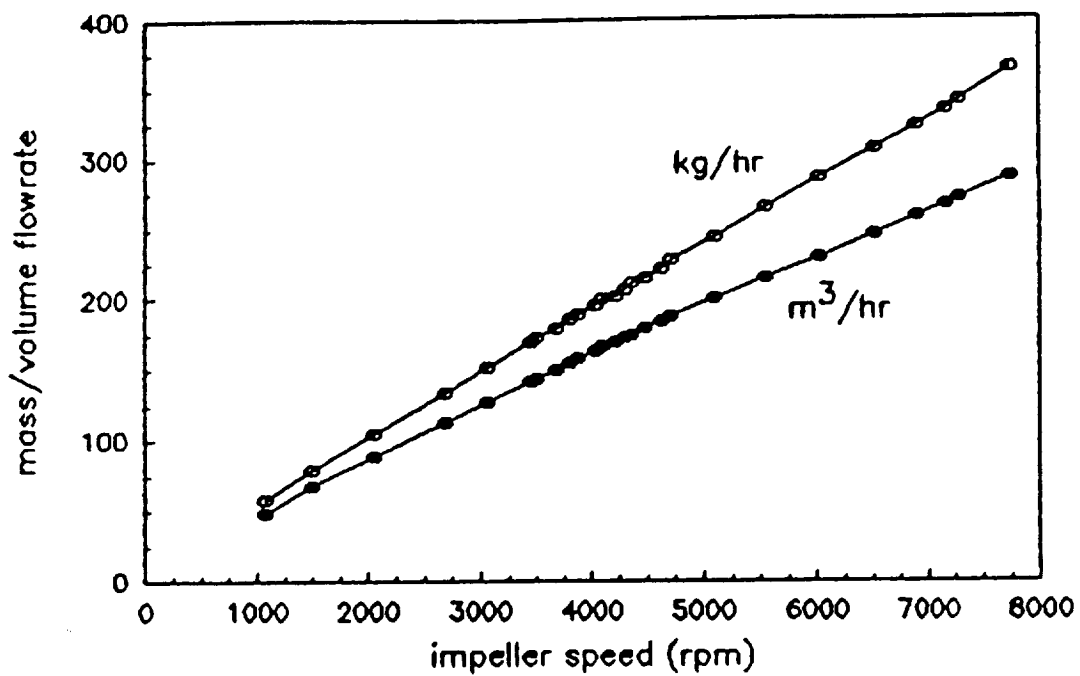
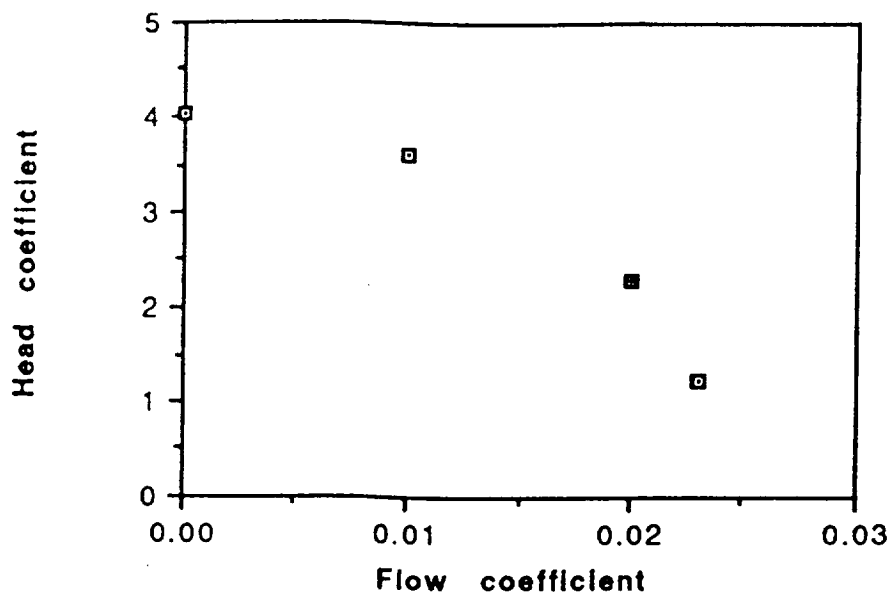
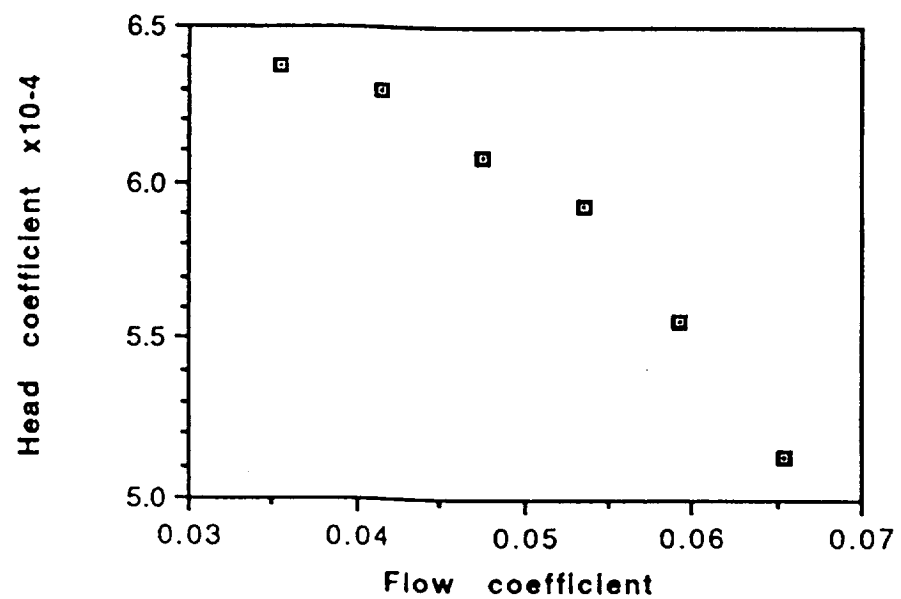


Fig. 4. Discharge Flow rate of the Turbopump.



(a)



(b)

Fig. 5. Pump Curves for the Water and Air Tests.

(a) Air Test  
(b) Water Test

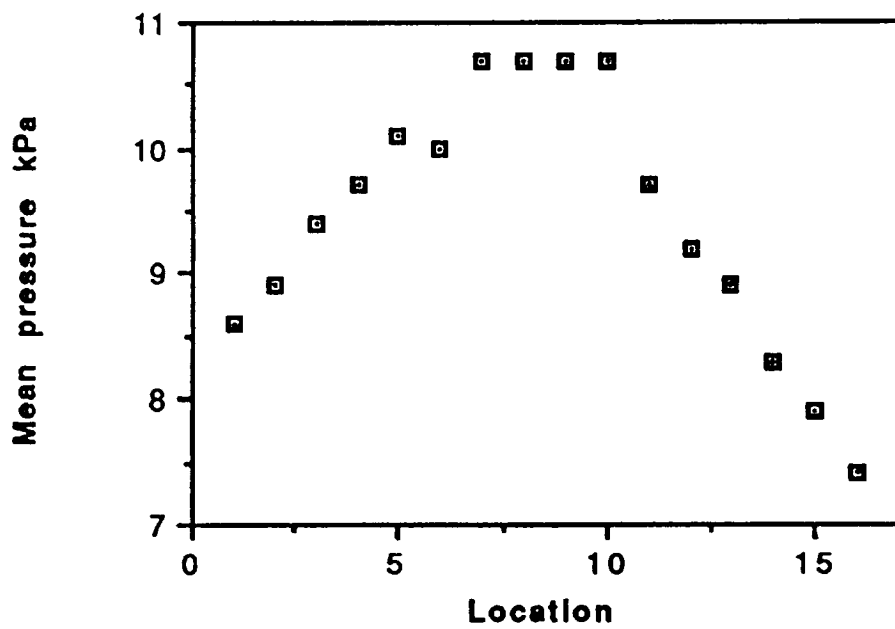


Fig. 6. Static Pressure Distribution in the Diffuser/Volute Assembly.

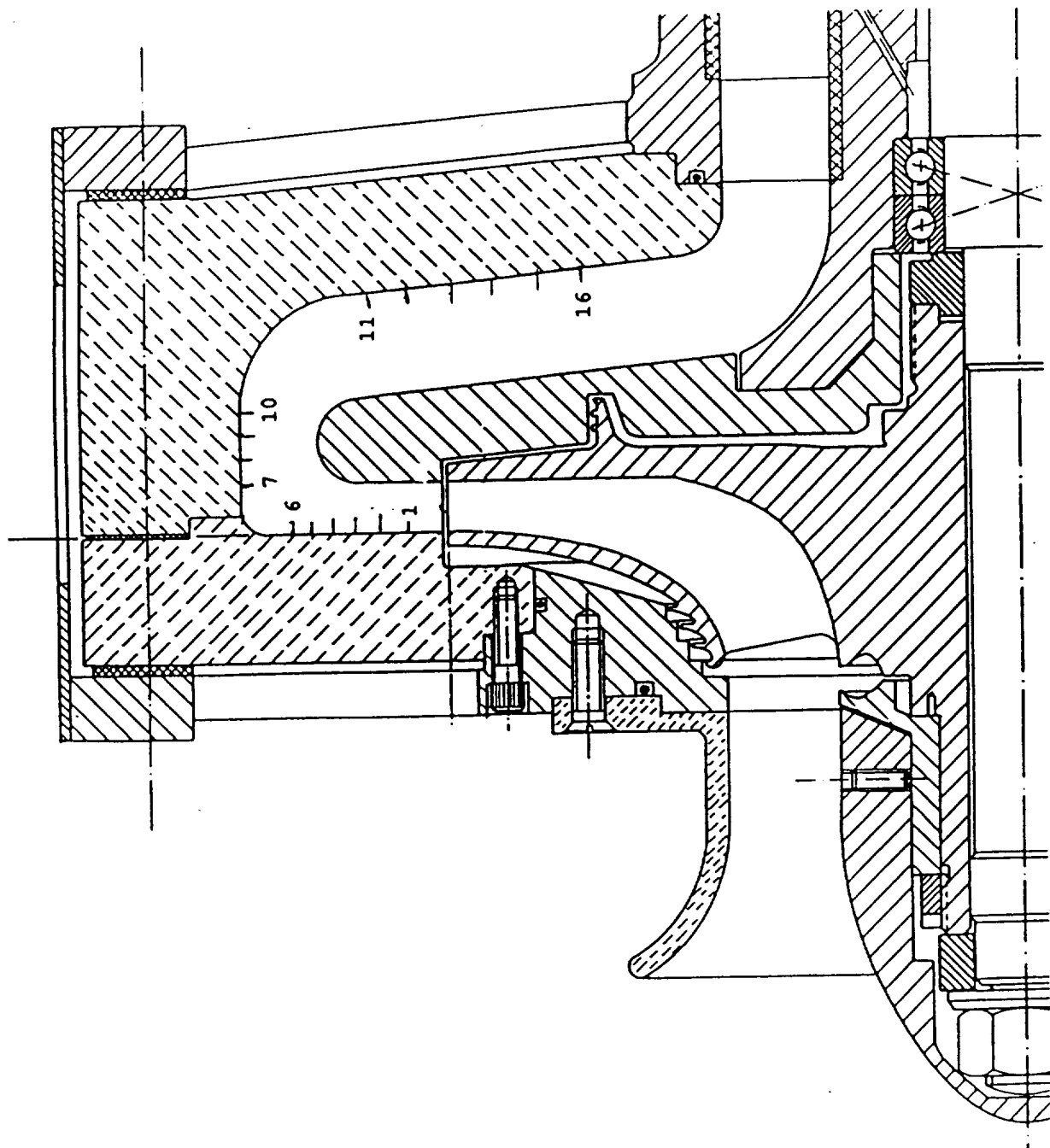


Fig. 7. Variation of Mean Static Pressure with Impeller Angle.

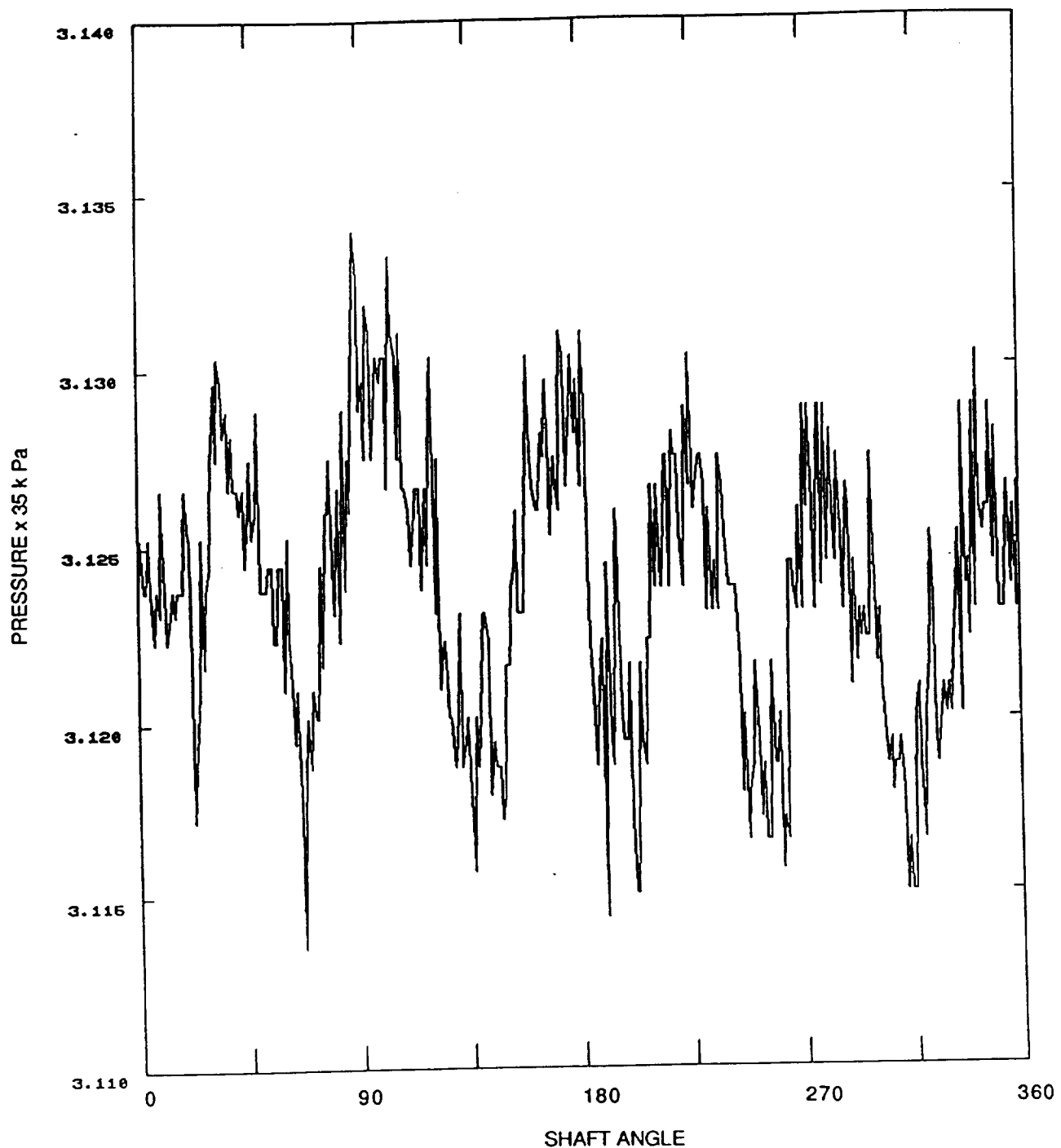


Fig. 7. Continued - Location 1.

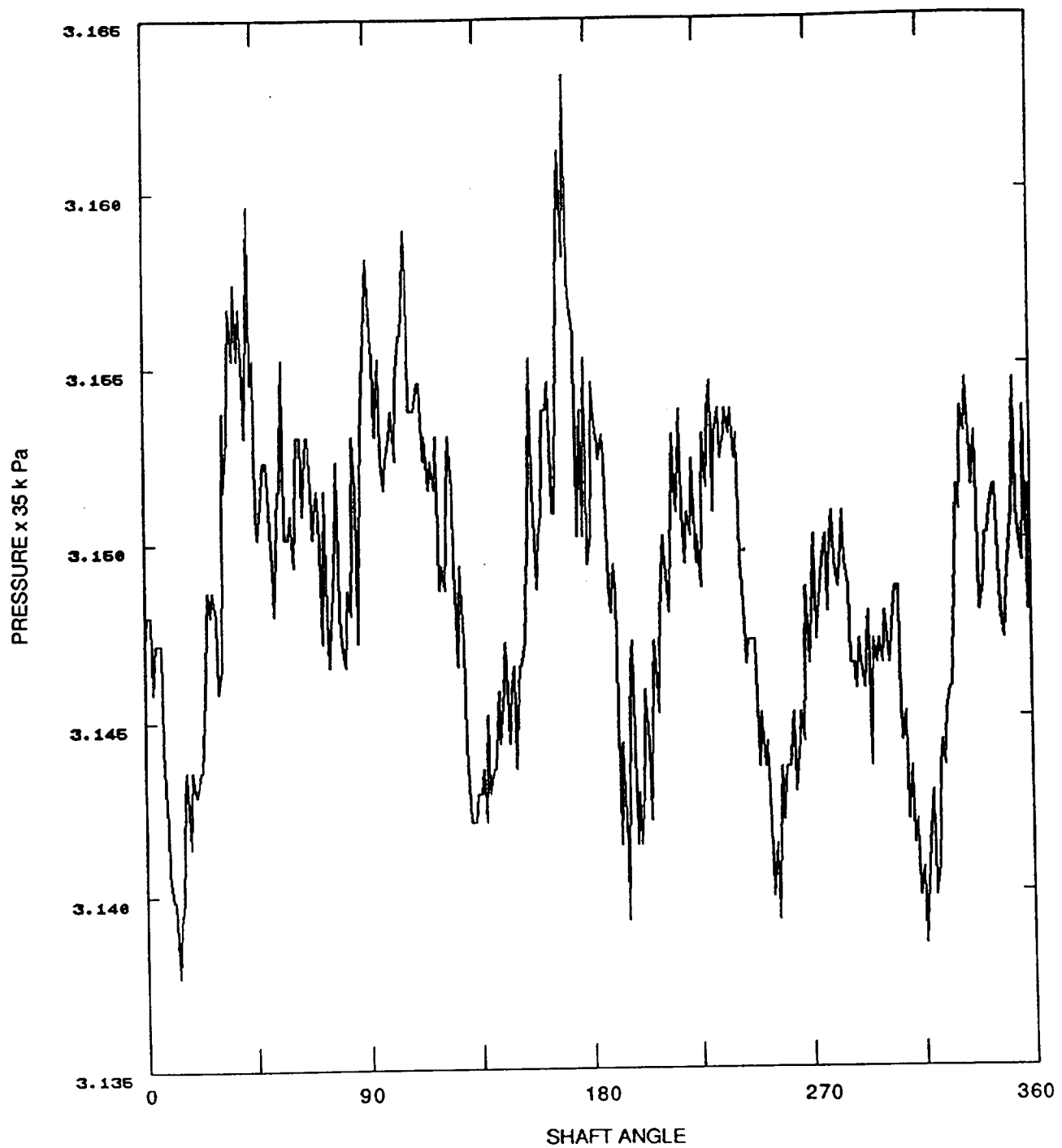


Fig. 7. Continued - Location 2.

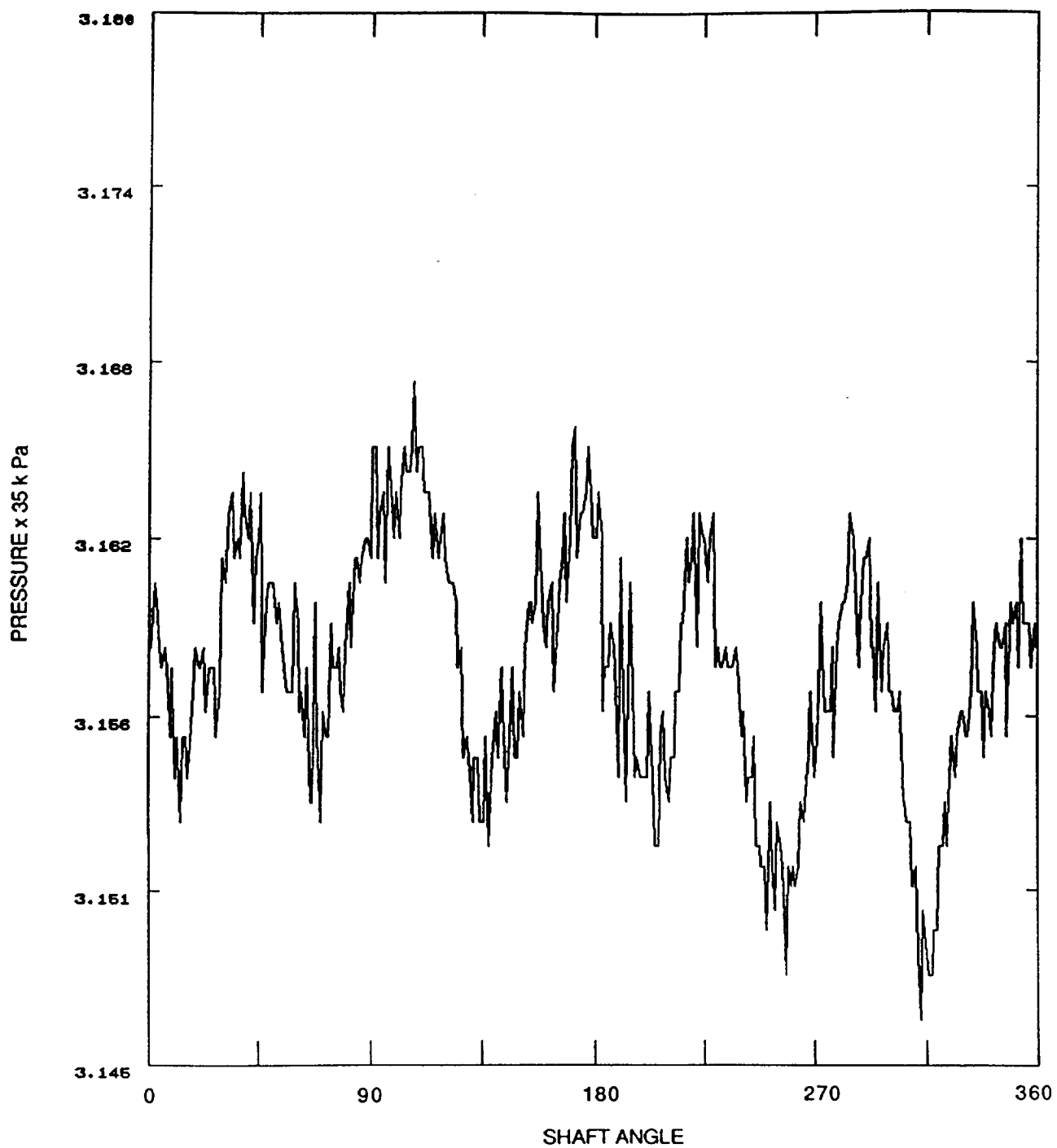


Fig. 7. Continued - Location 3.

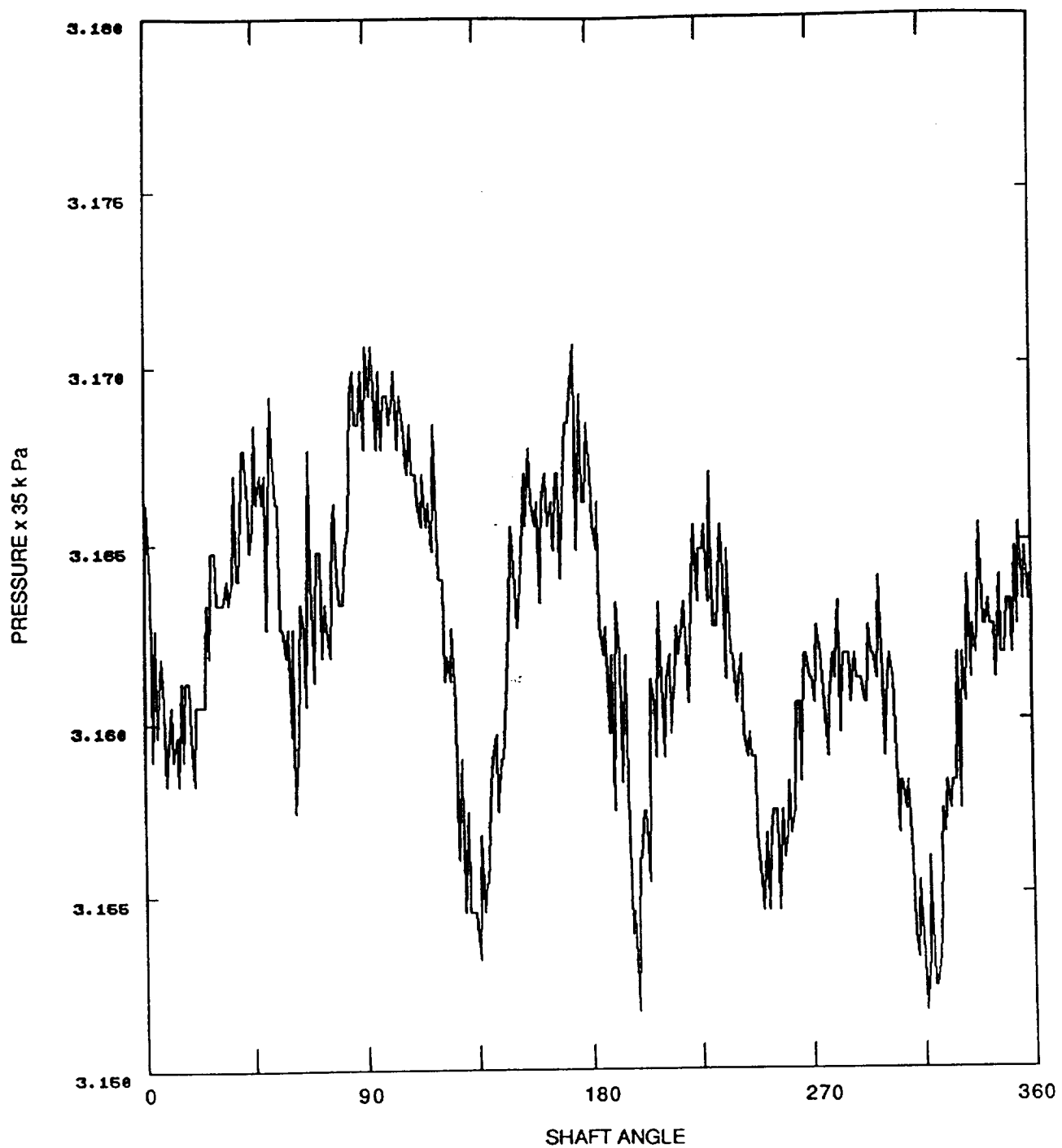


Fig. 7. Continued - Location 4.

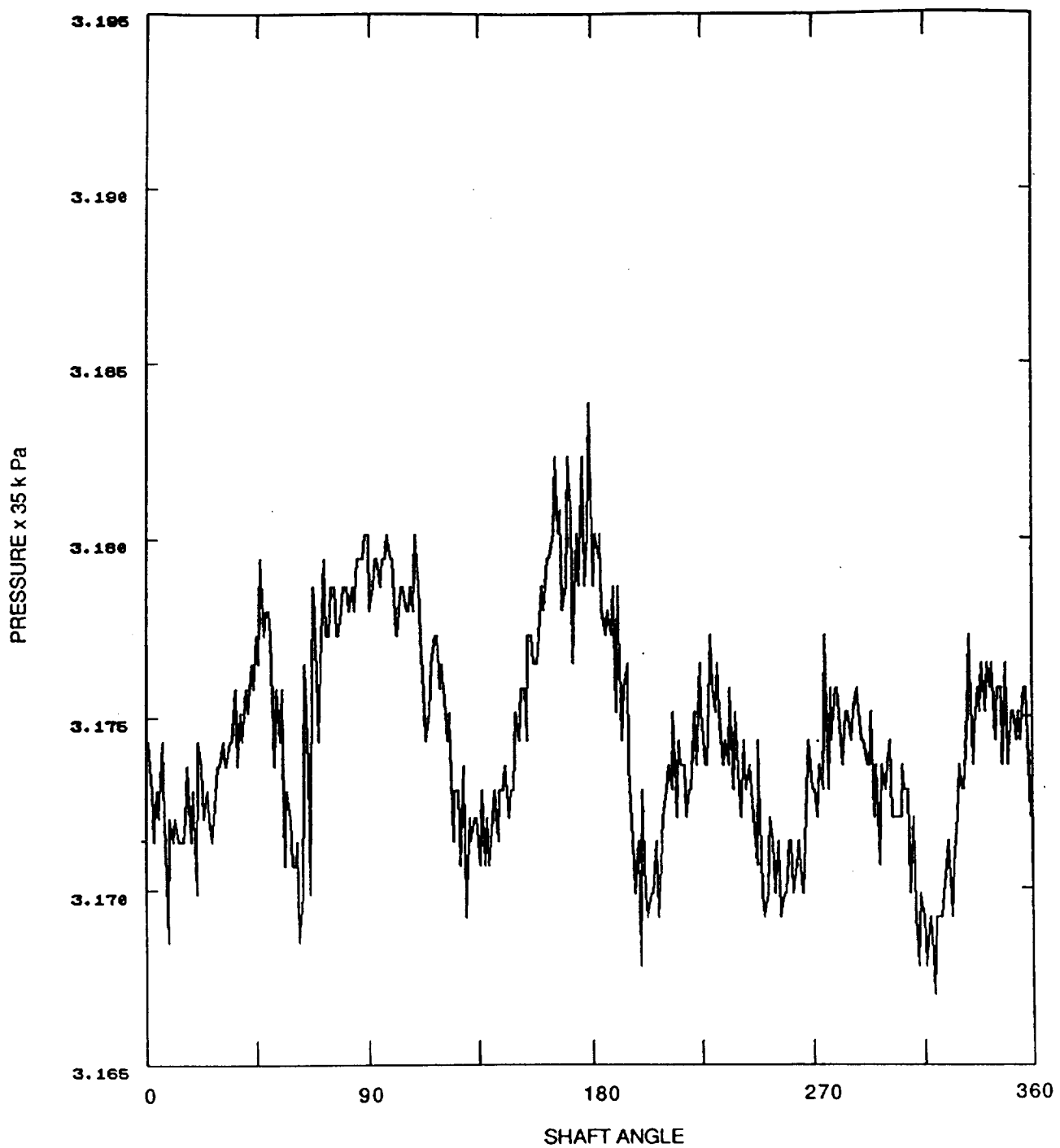


Fig. 7. Continued - Location 5.

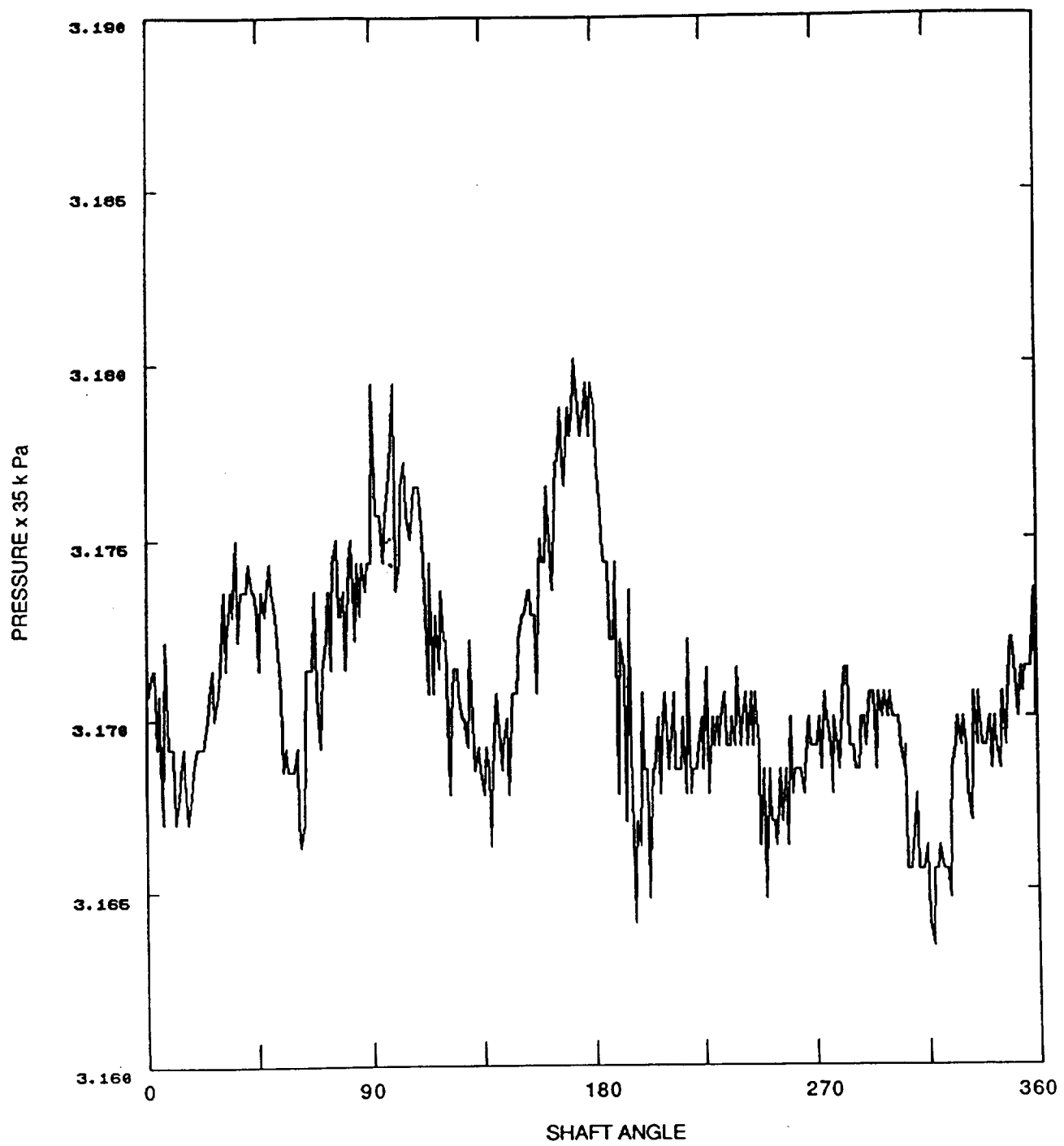


Fig. 7. Continued - Location 6.

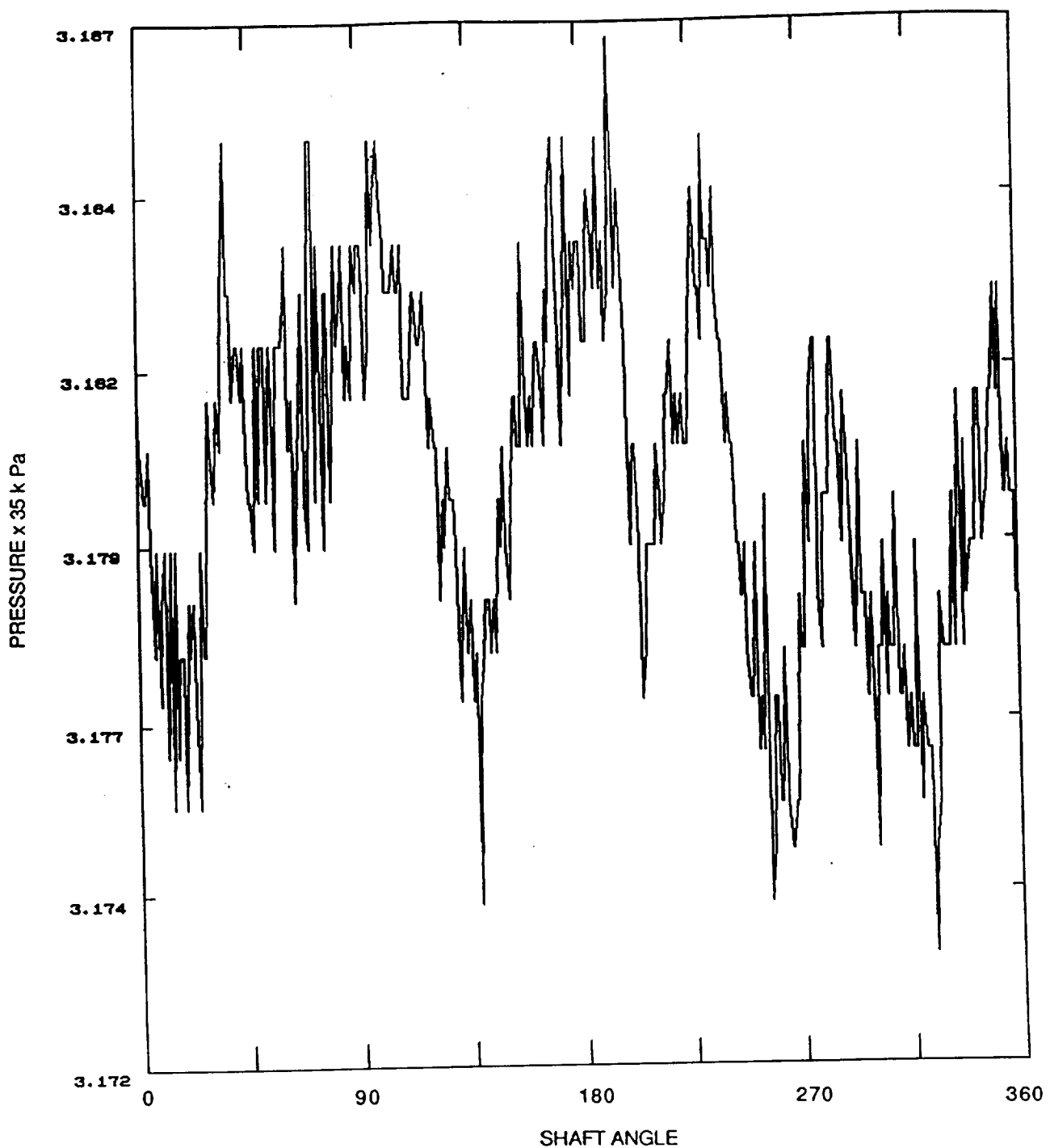


Fig. 7. Continued - Location 7.

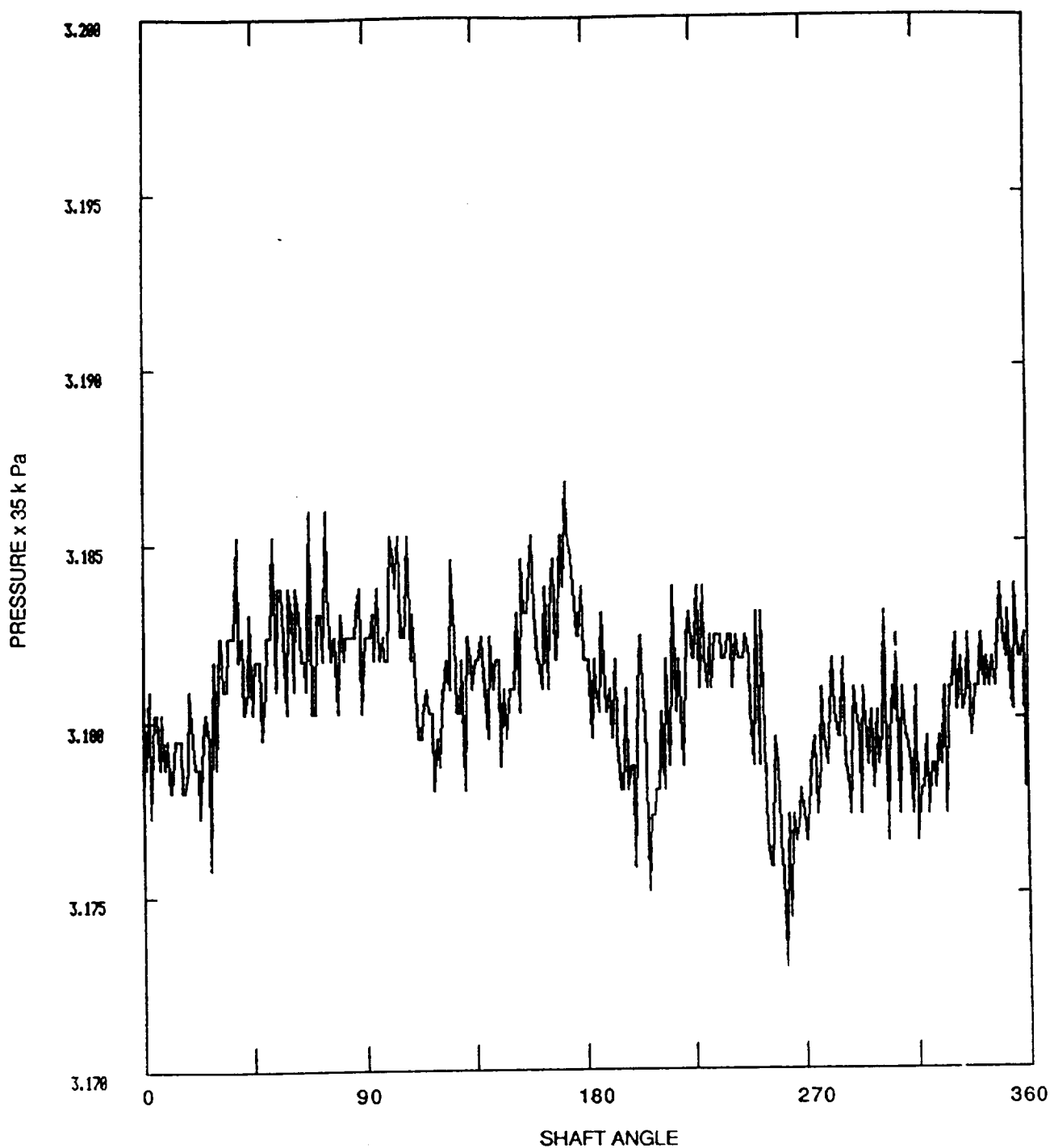


Fig. 7. Continued - Location 8.

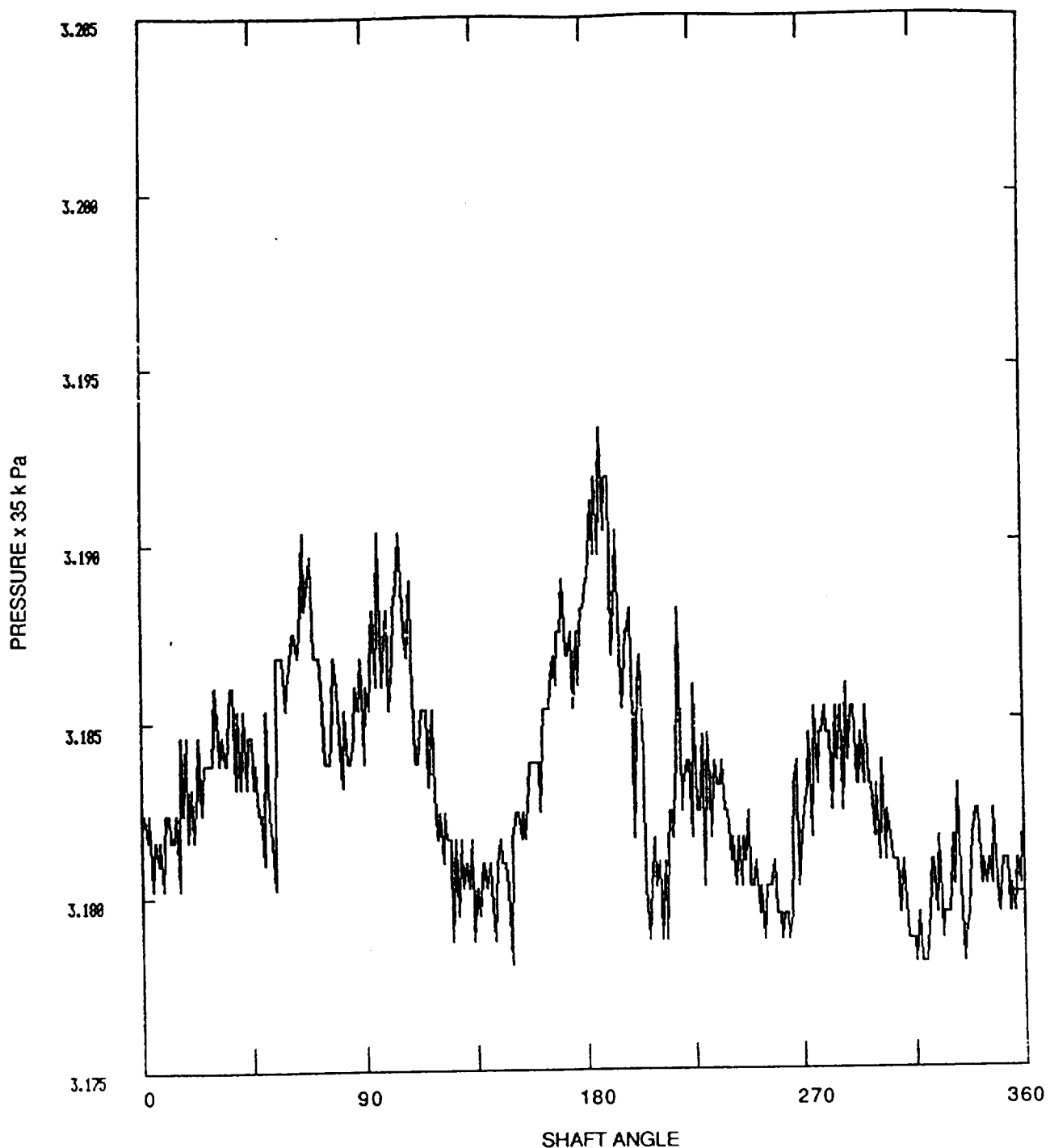


Fig. 7. Continued - Location 9.

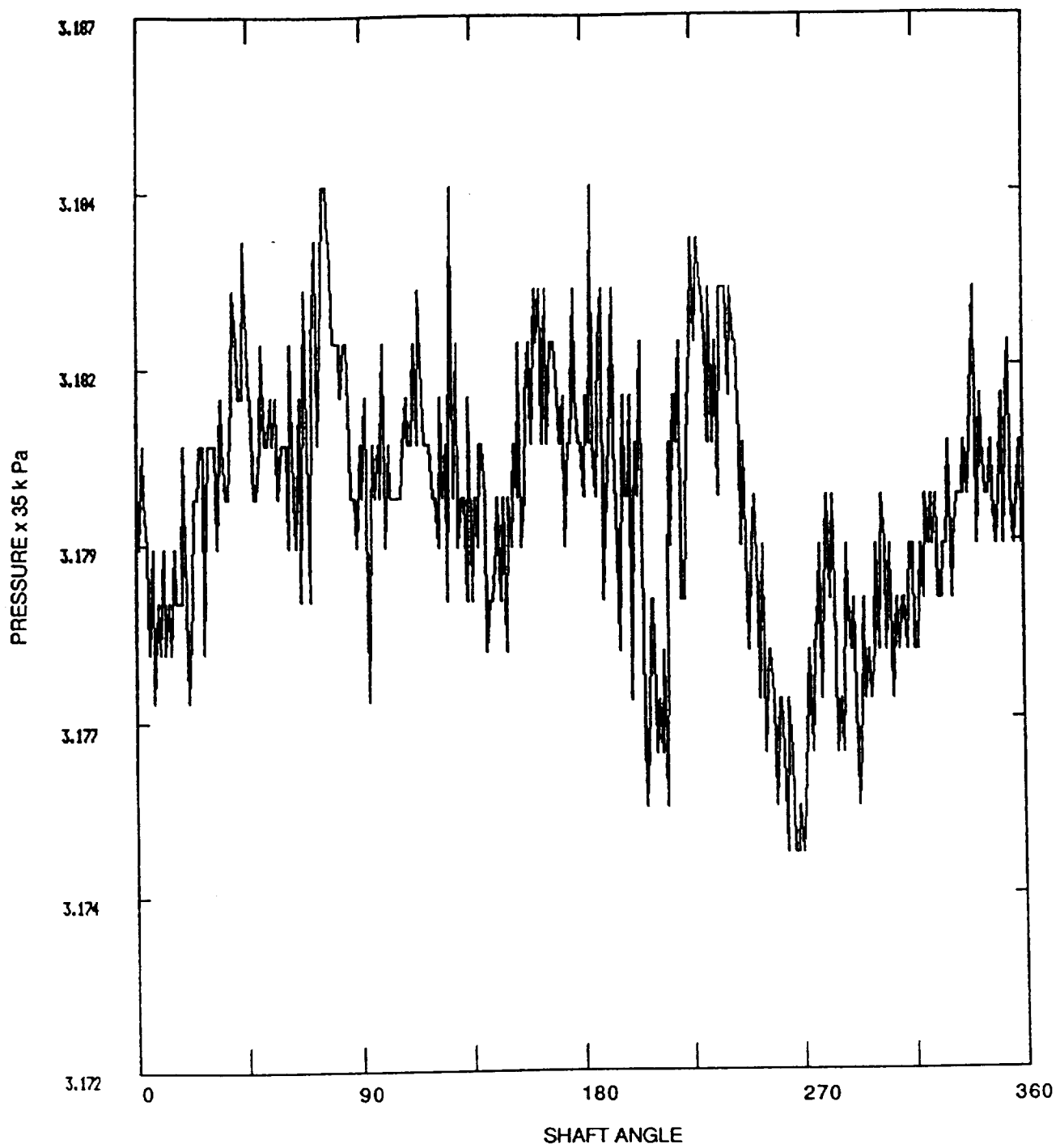


Fig. 7. Continued - Location 10.

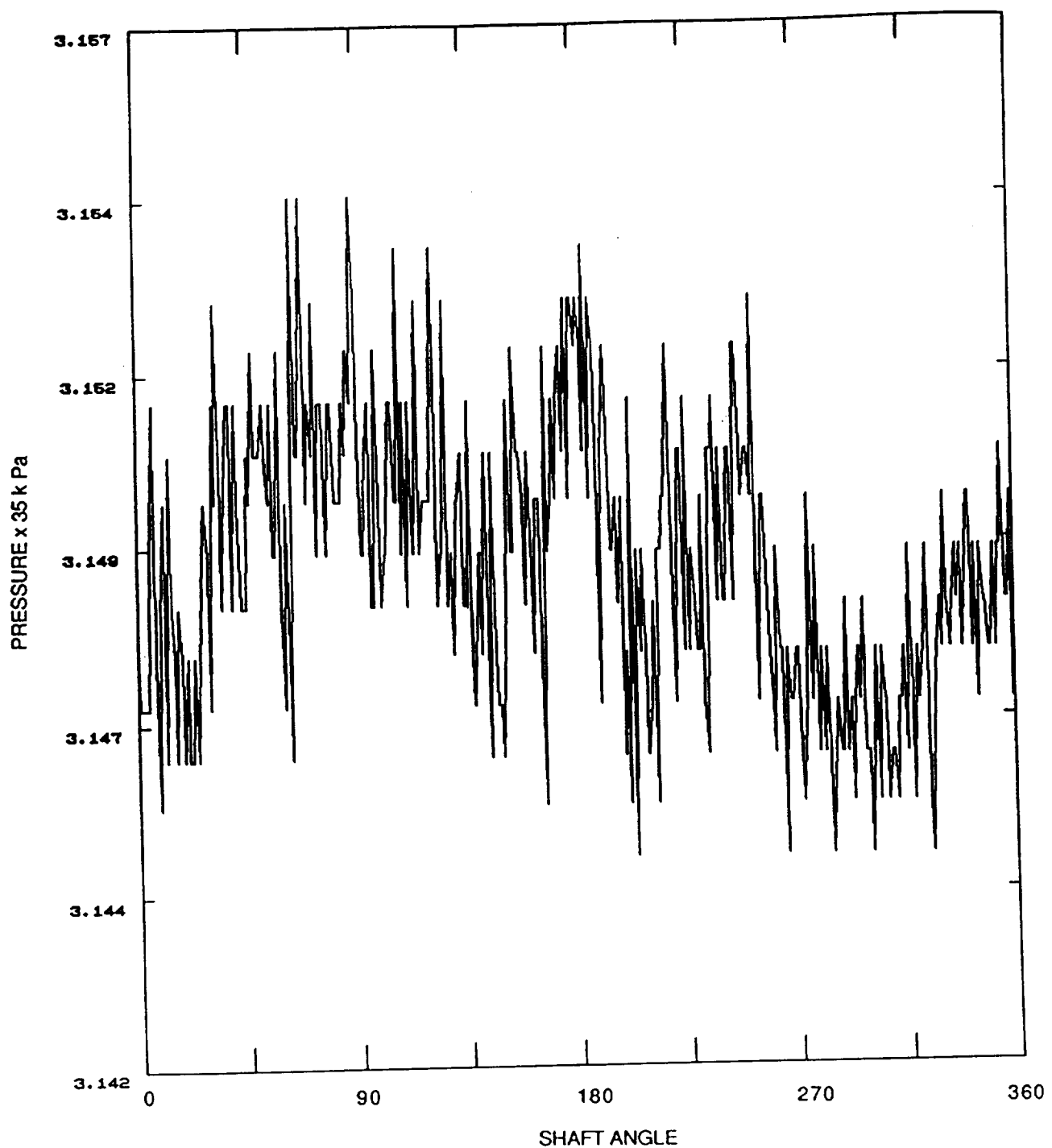


Fig. 7. Continued - Location 11.

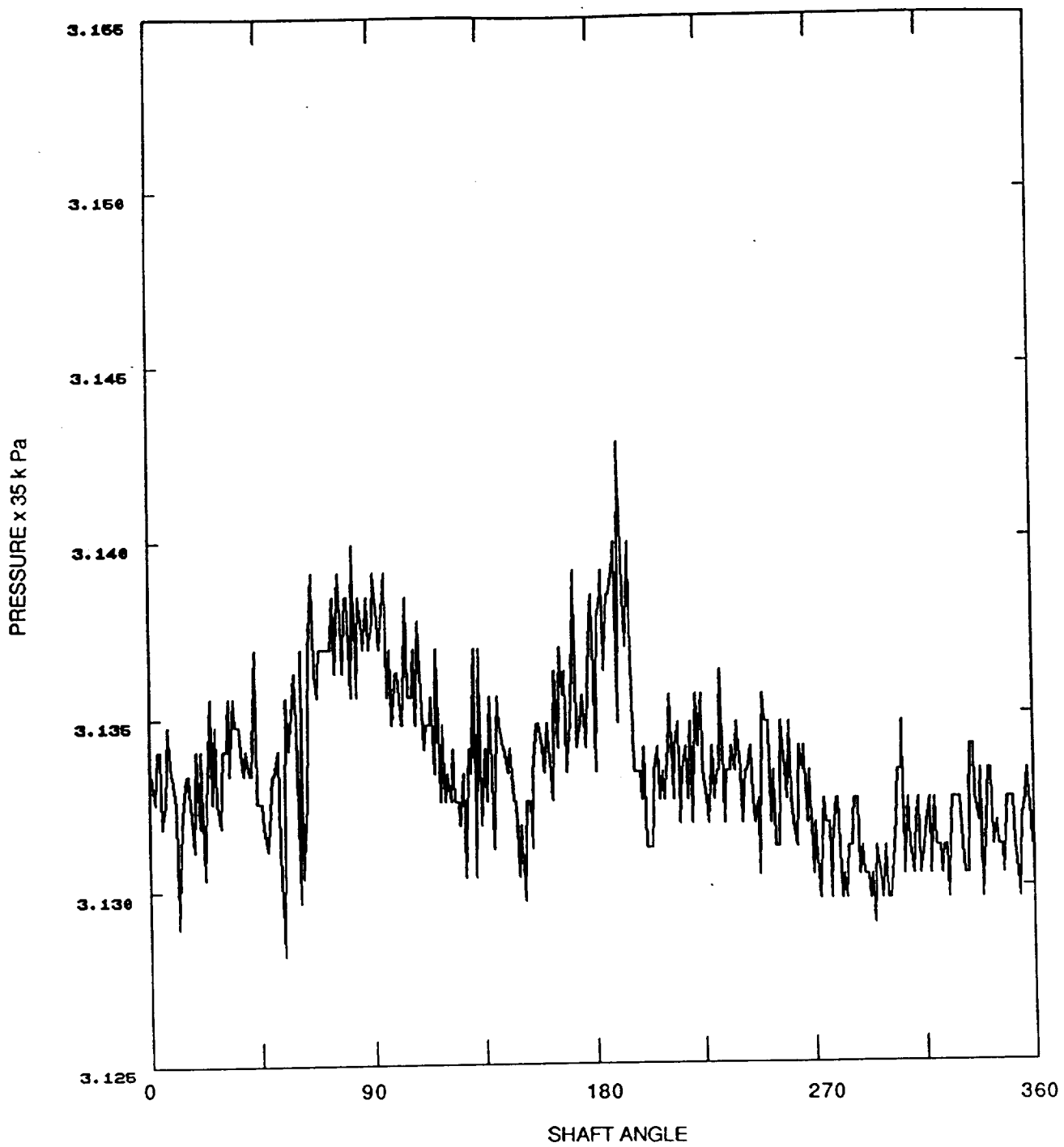


Fig. 7. Continued - Location 12.

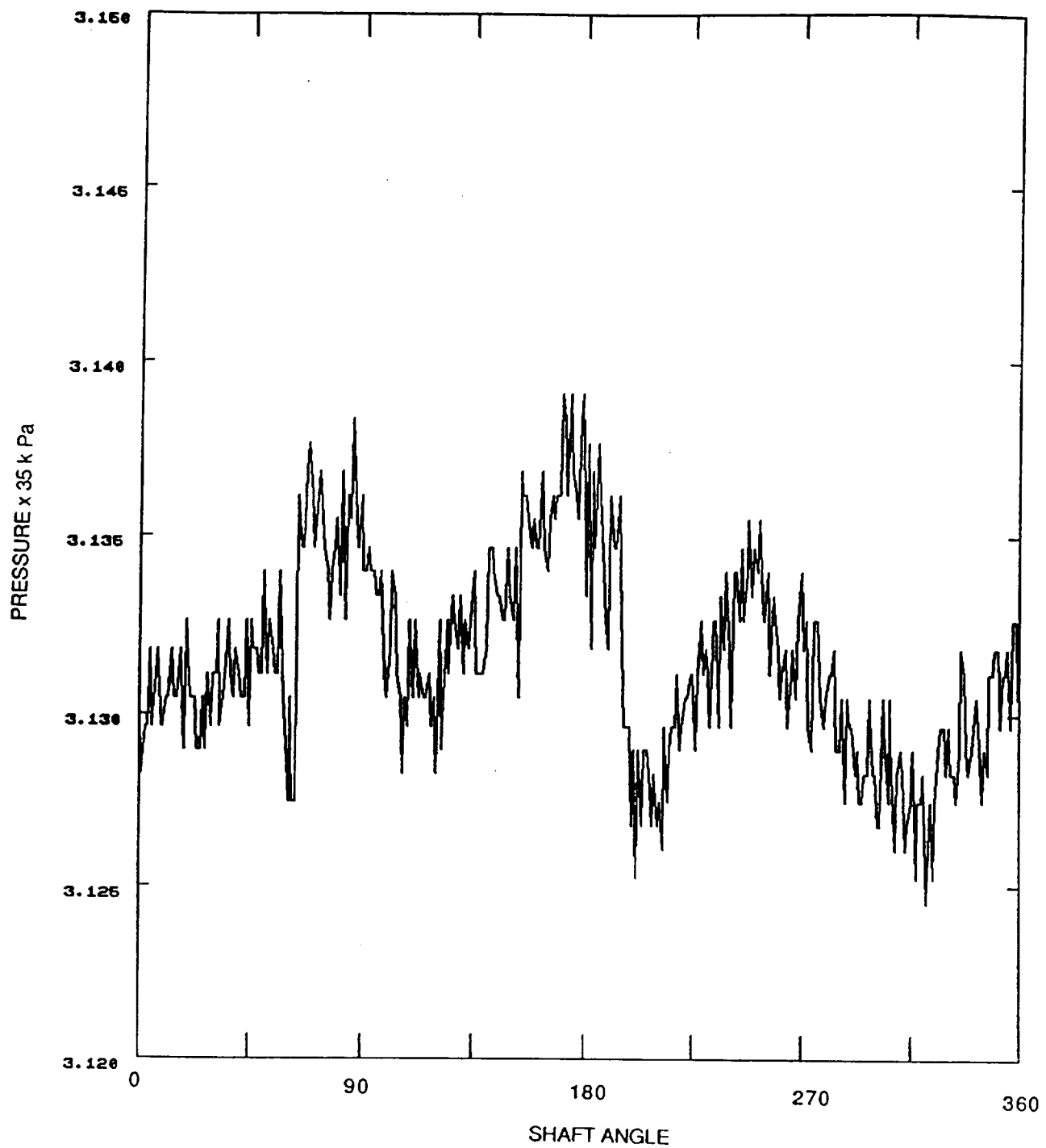


Fig. 7. Continued - Location 13.

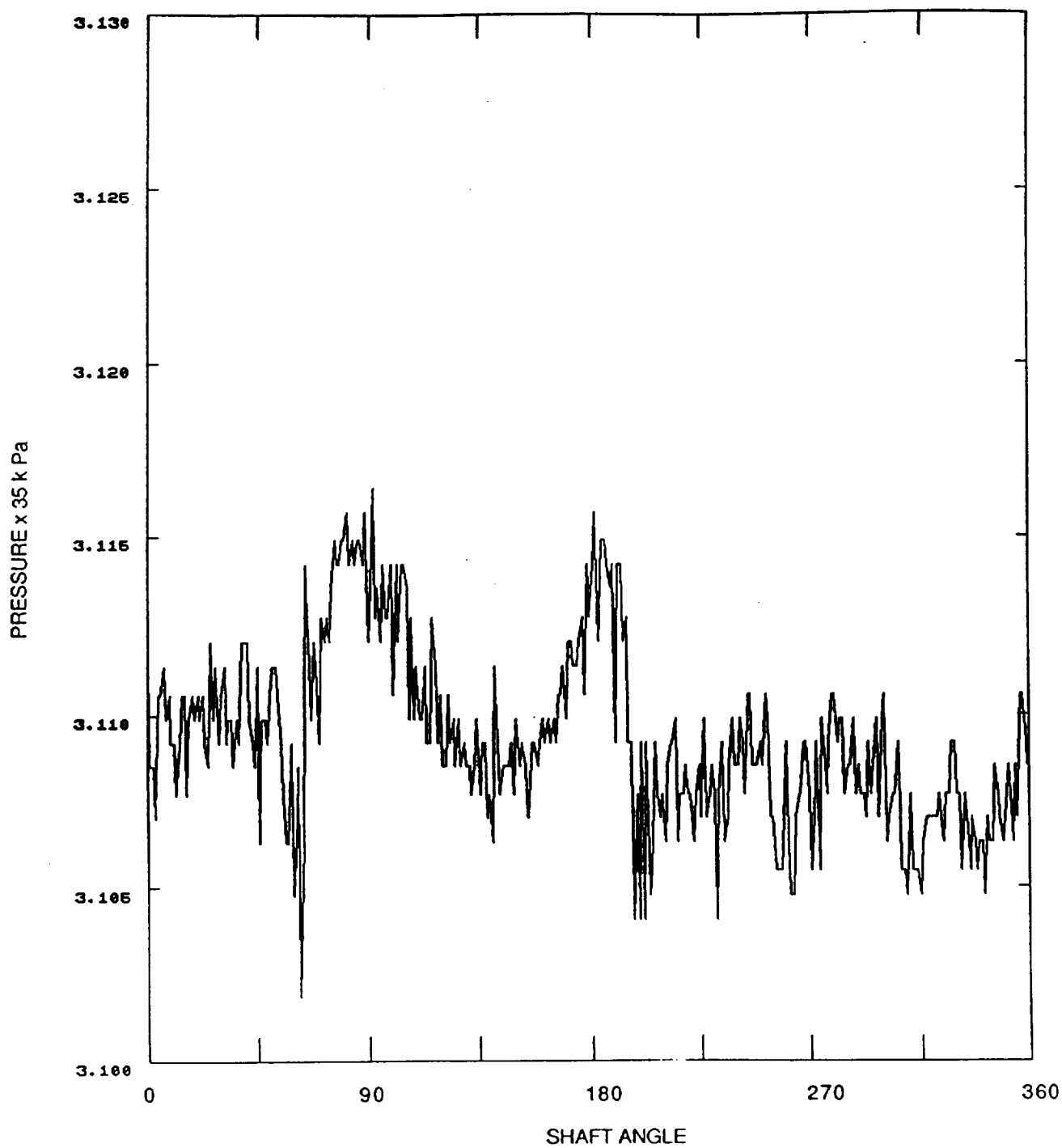


Fig. 7. Continued - Location 14.

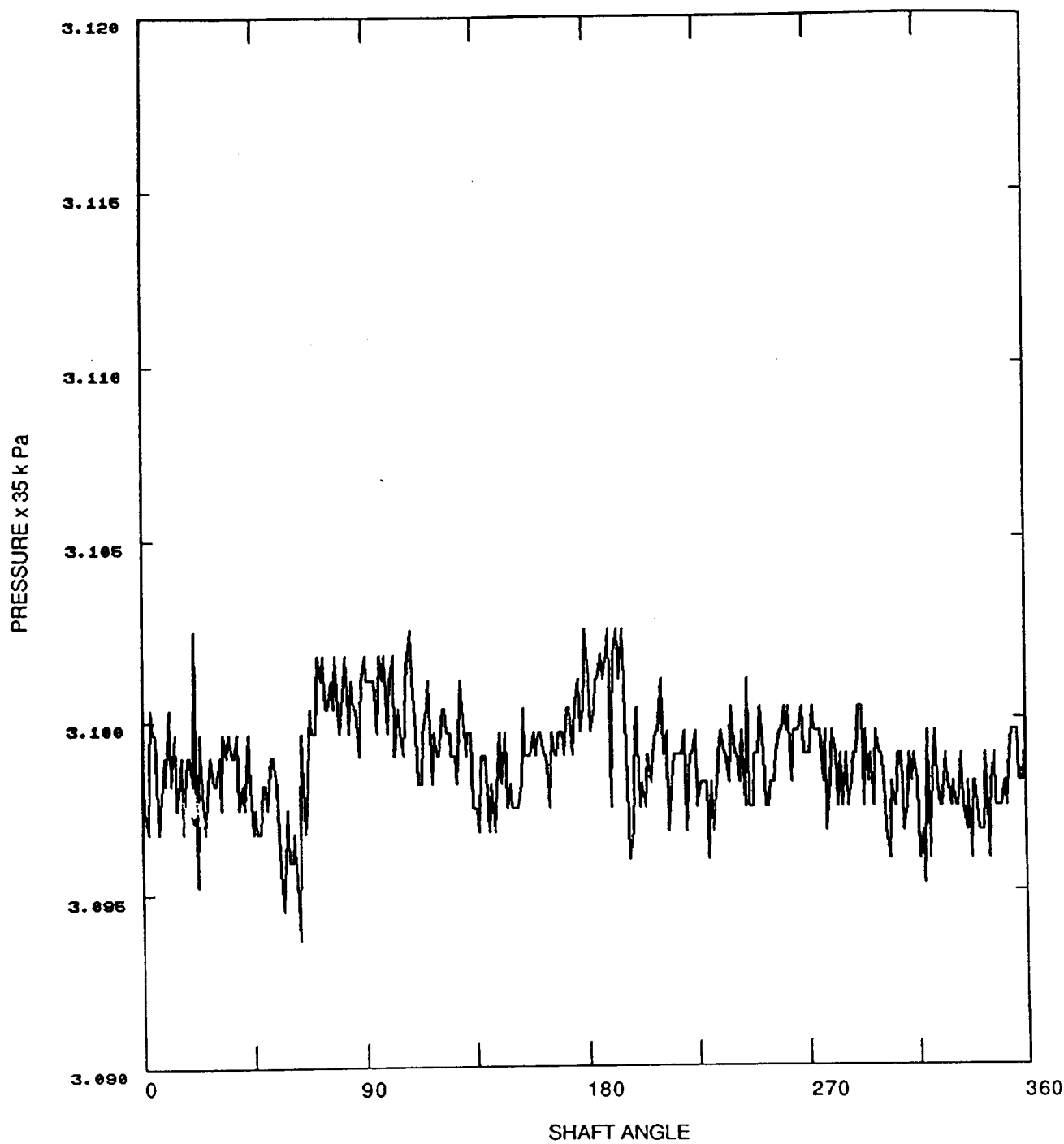


Fig. 7. Continued - Location 15.

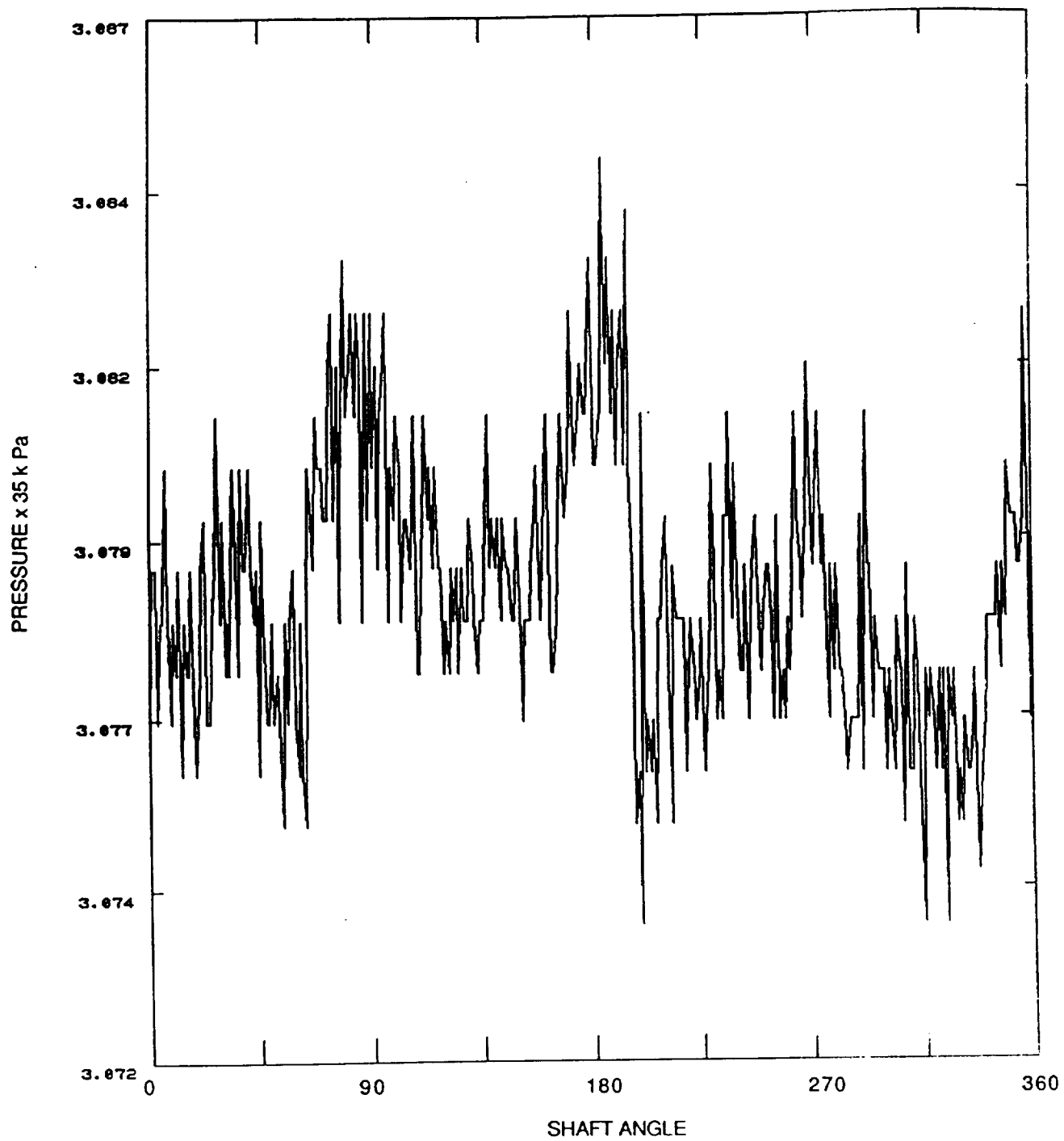


Fig. 7. Continued - Location 16.

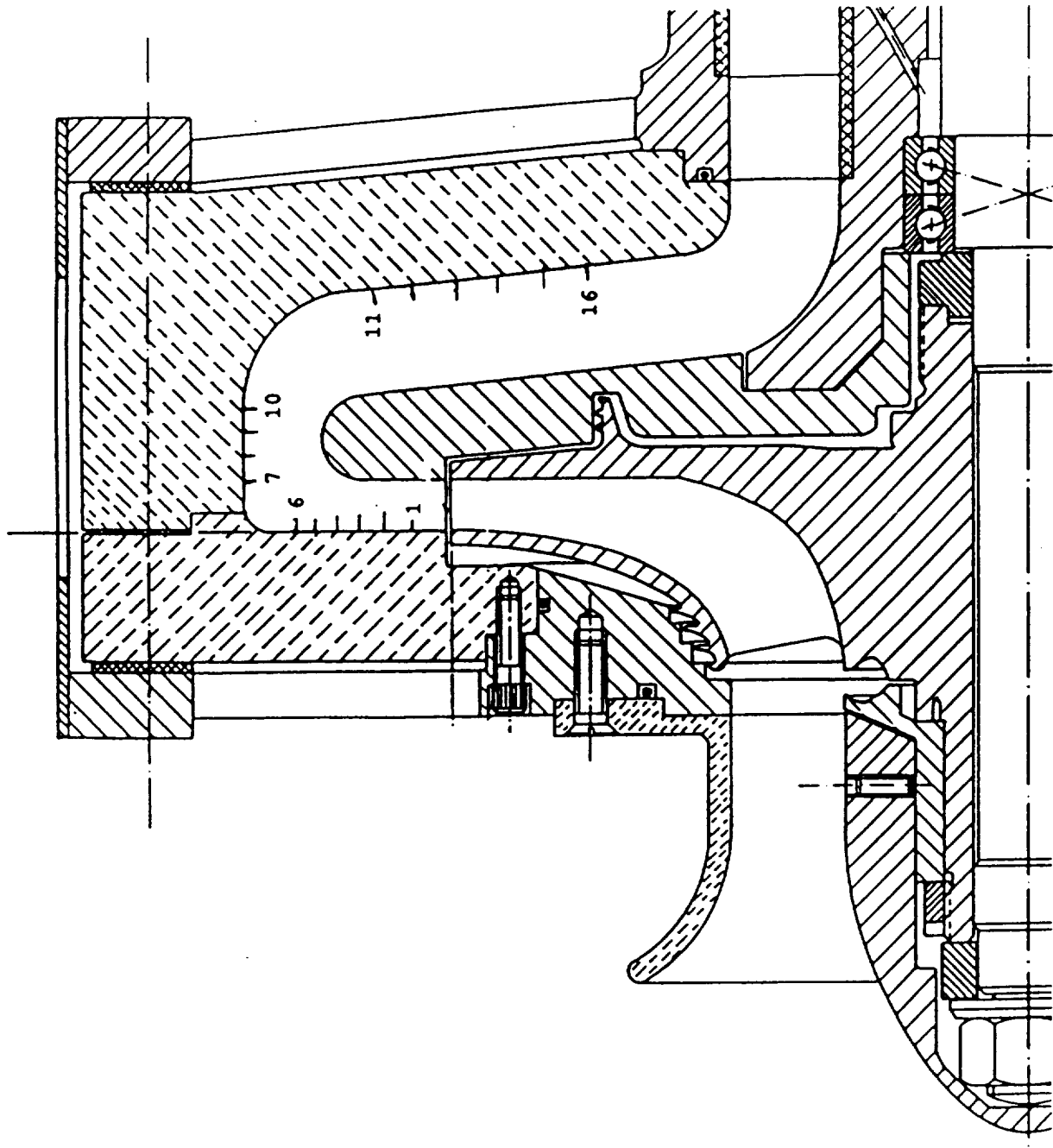


Fig. 8. Cyclic Variation of Mean Static Pressure

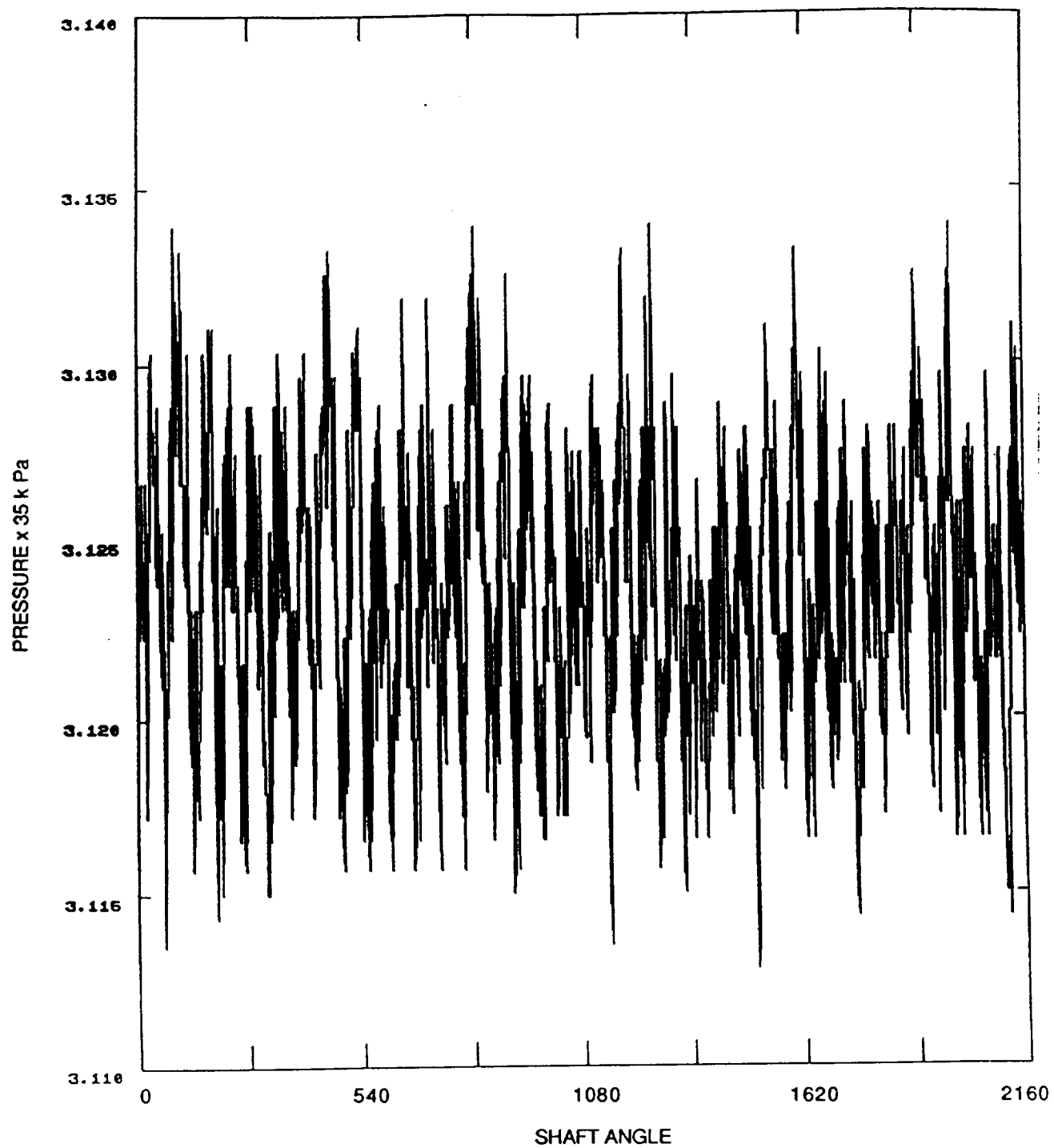


Fig. 8. Continued - Location 1.

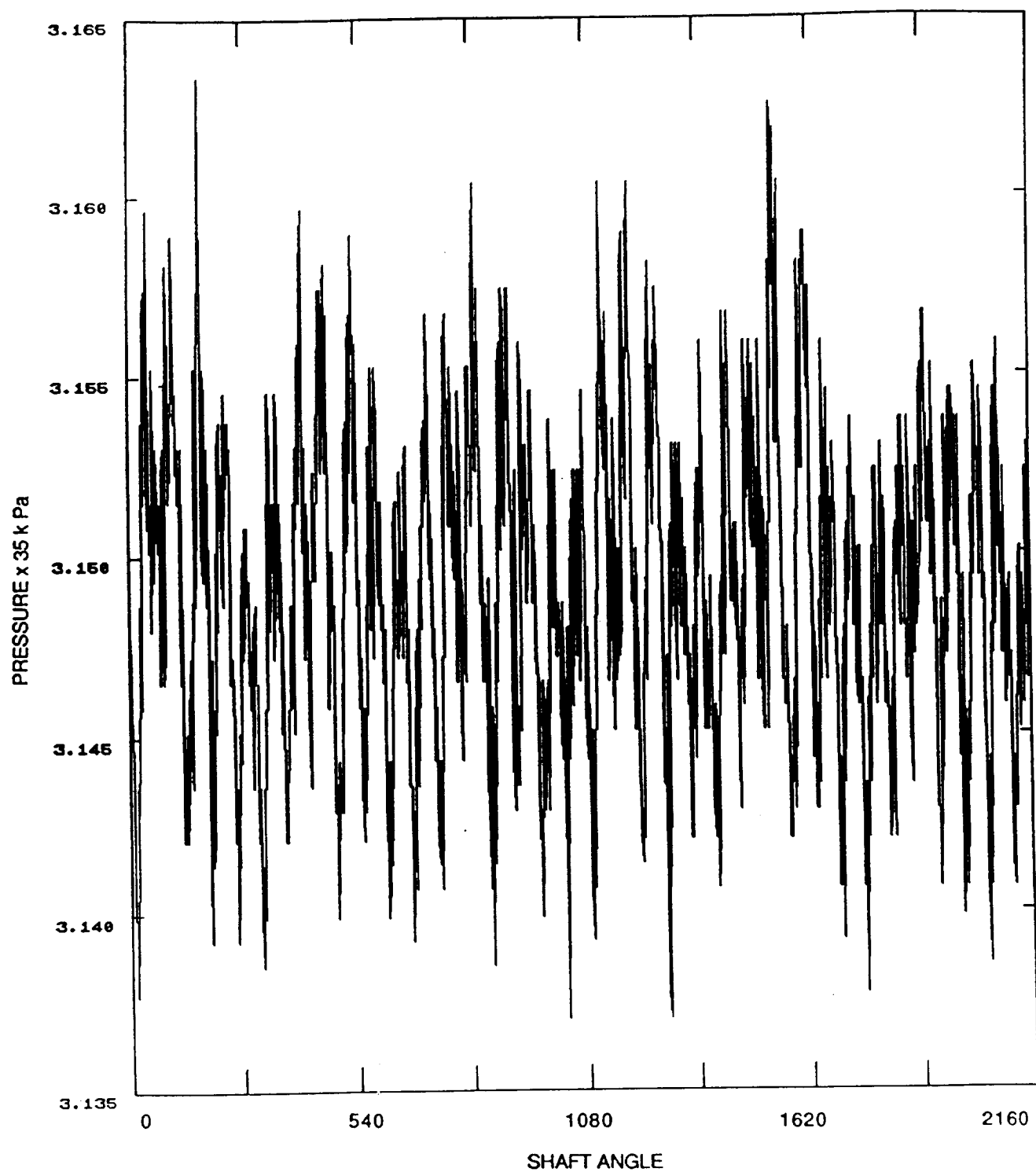


Fig. 8. Continued - Location 2.

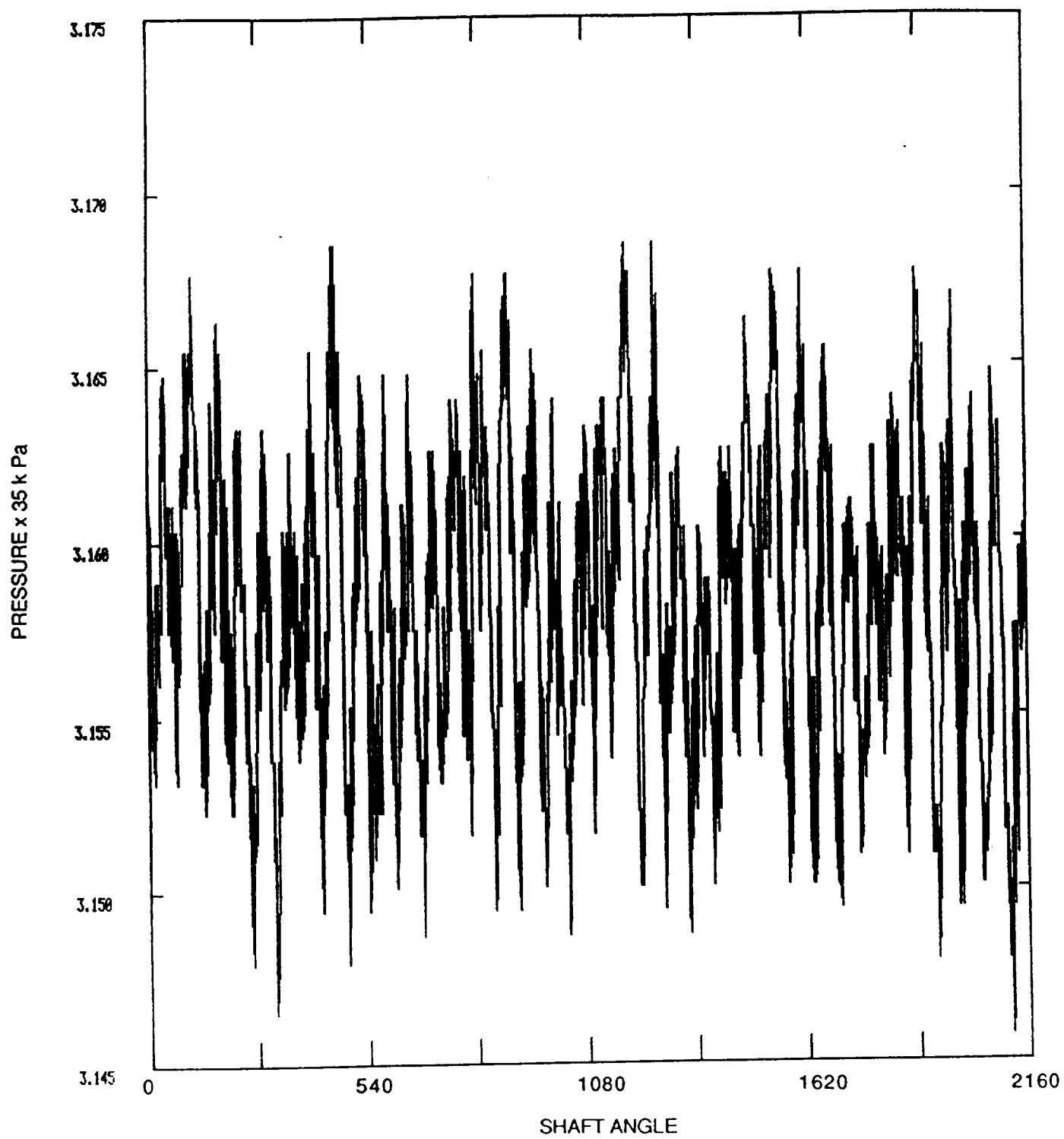


Fig. 8. Continued - Location 3.

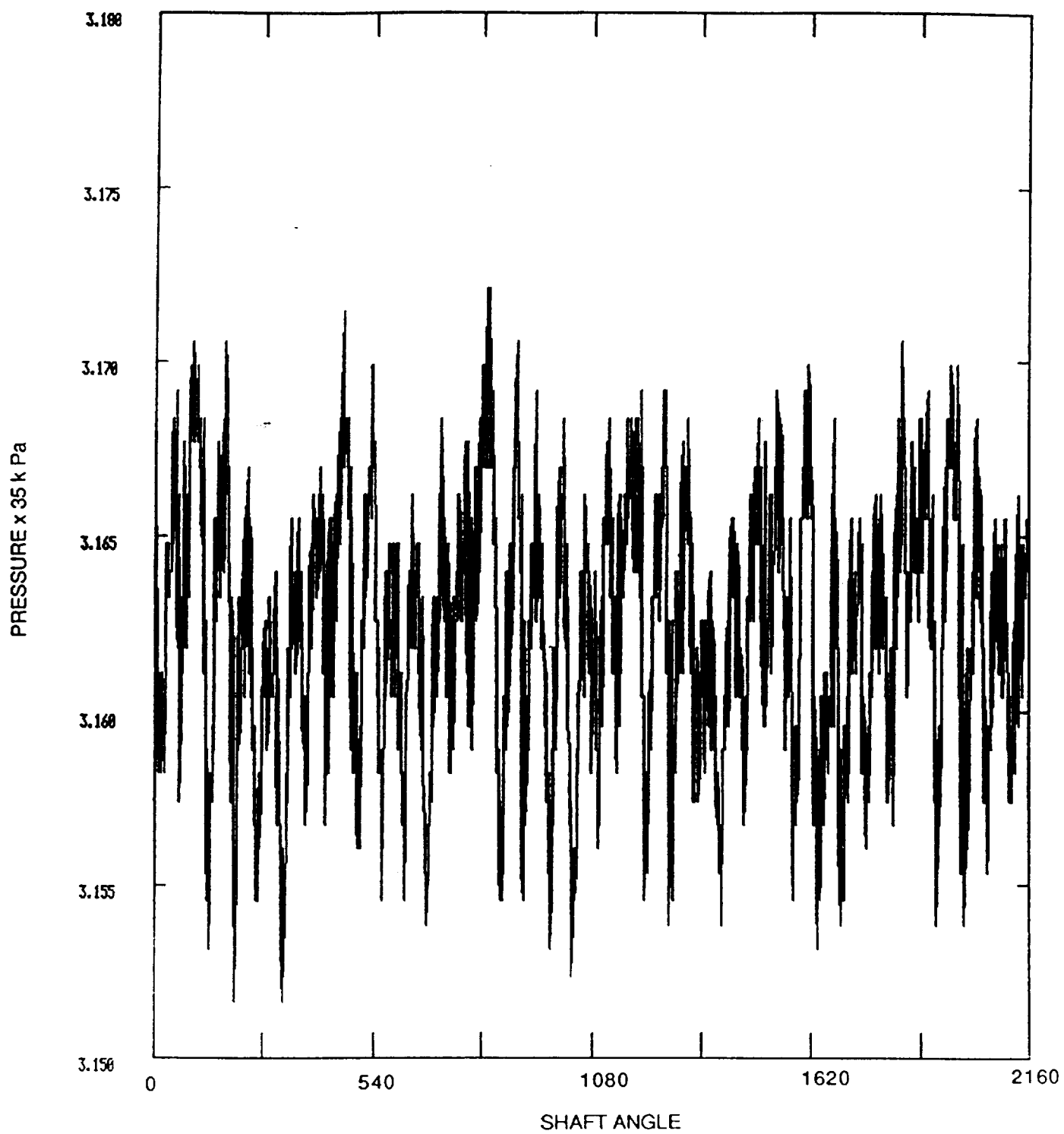


Fig. 8. Continued - Location 4.

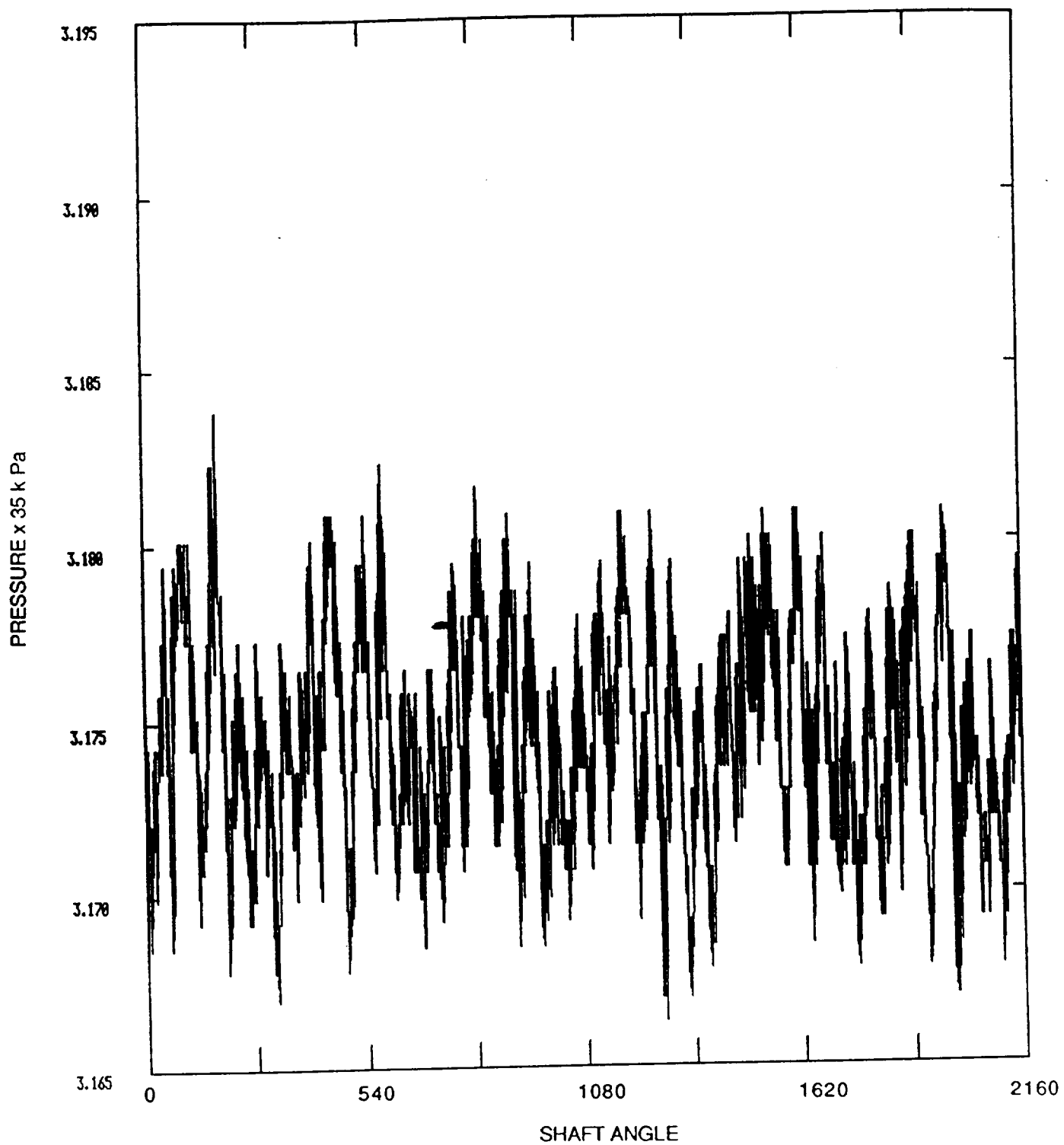


Fig. 8. Continued - Location 5.

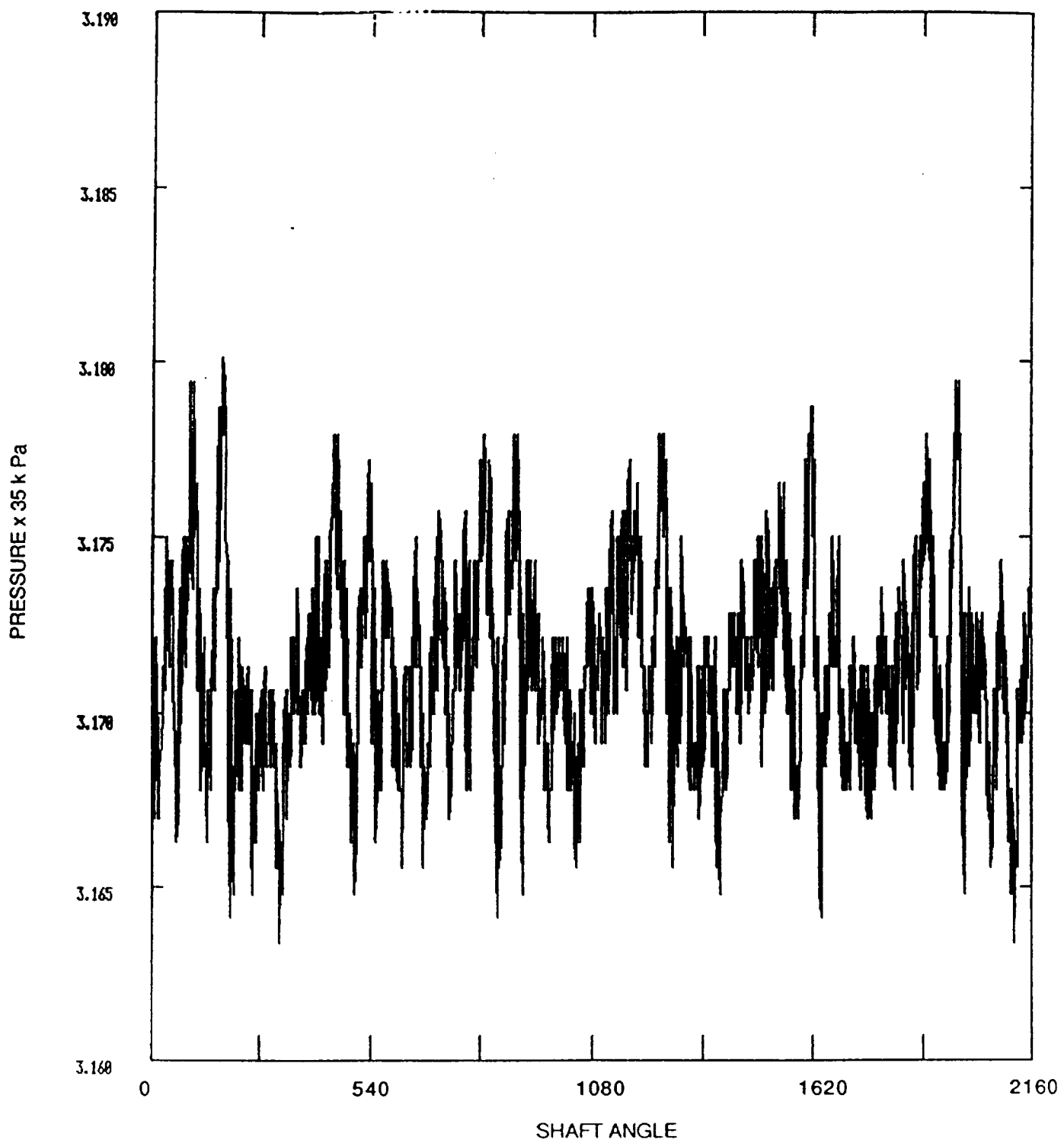


Fig. 8. Continued - Location 6.

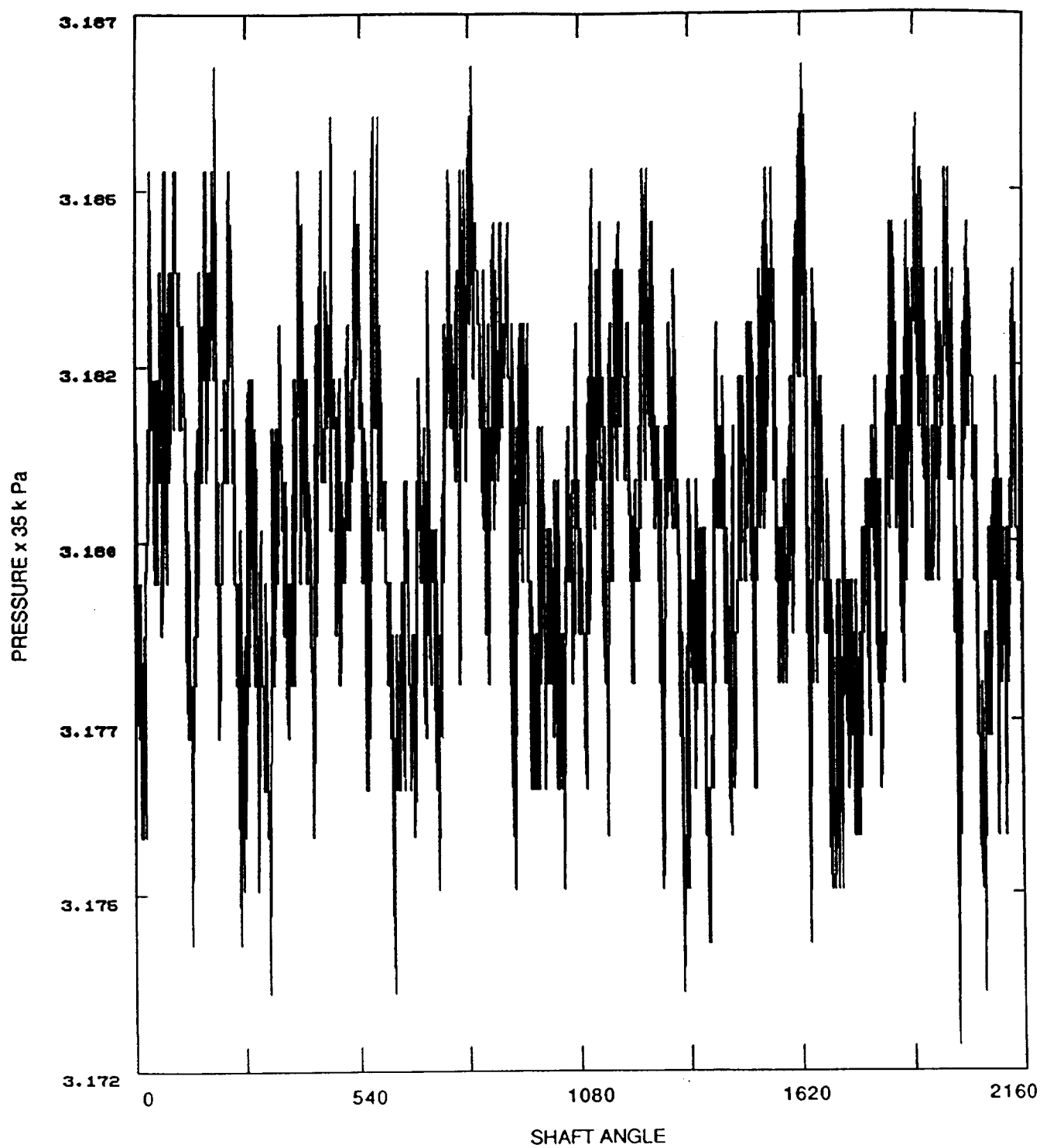


Fig. 8. Continued - Location 7.

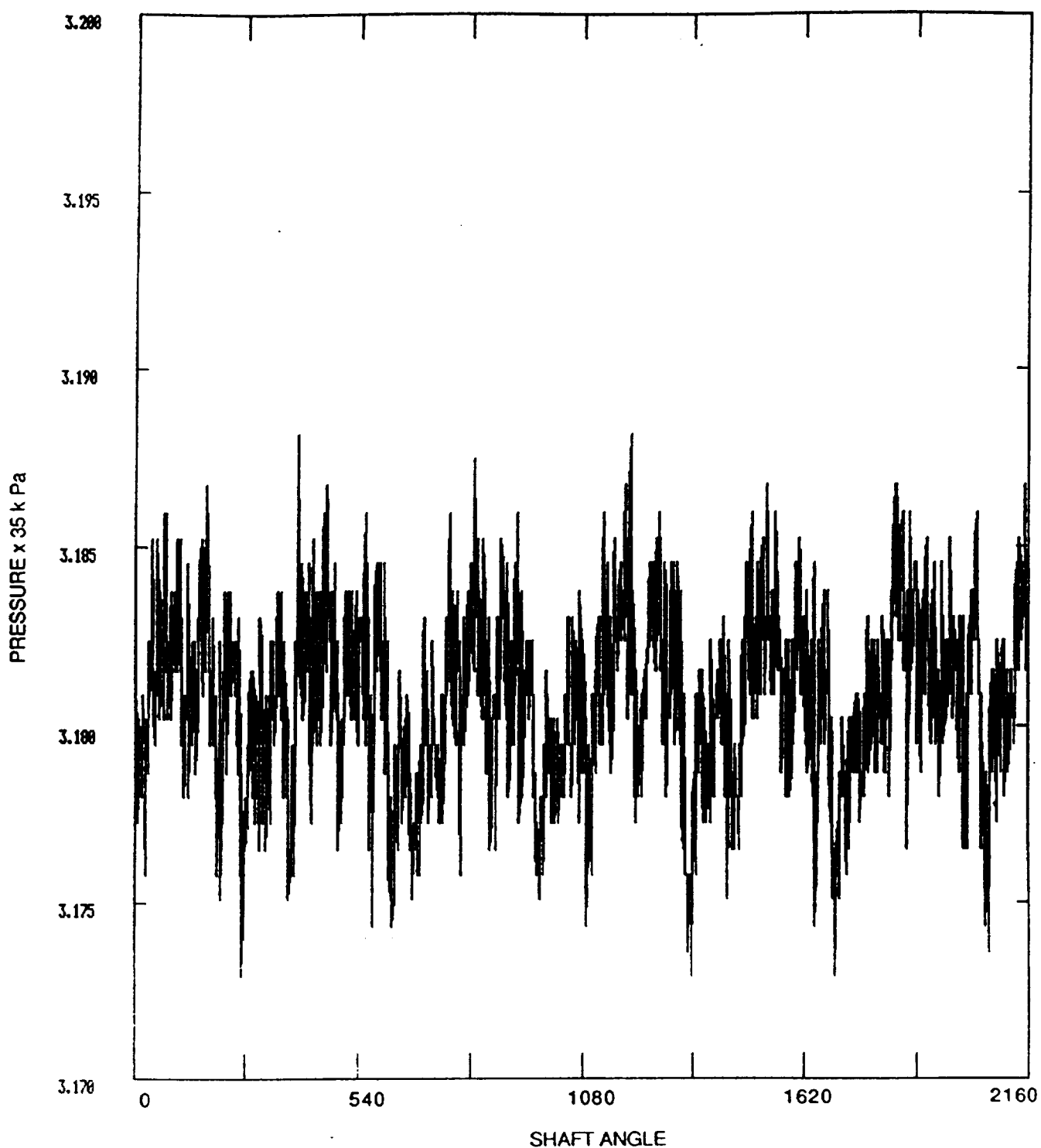


Fig. 8. Continued - Location 8.

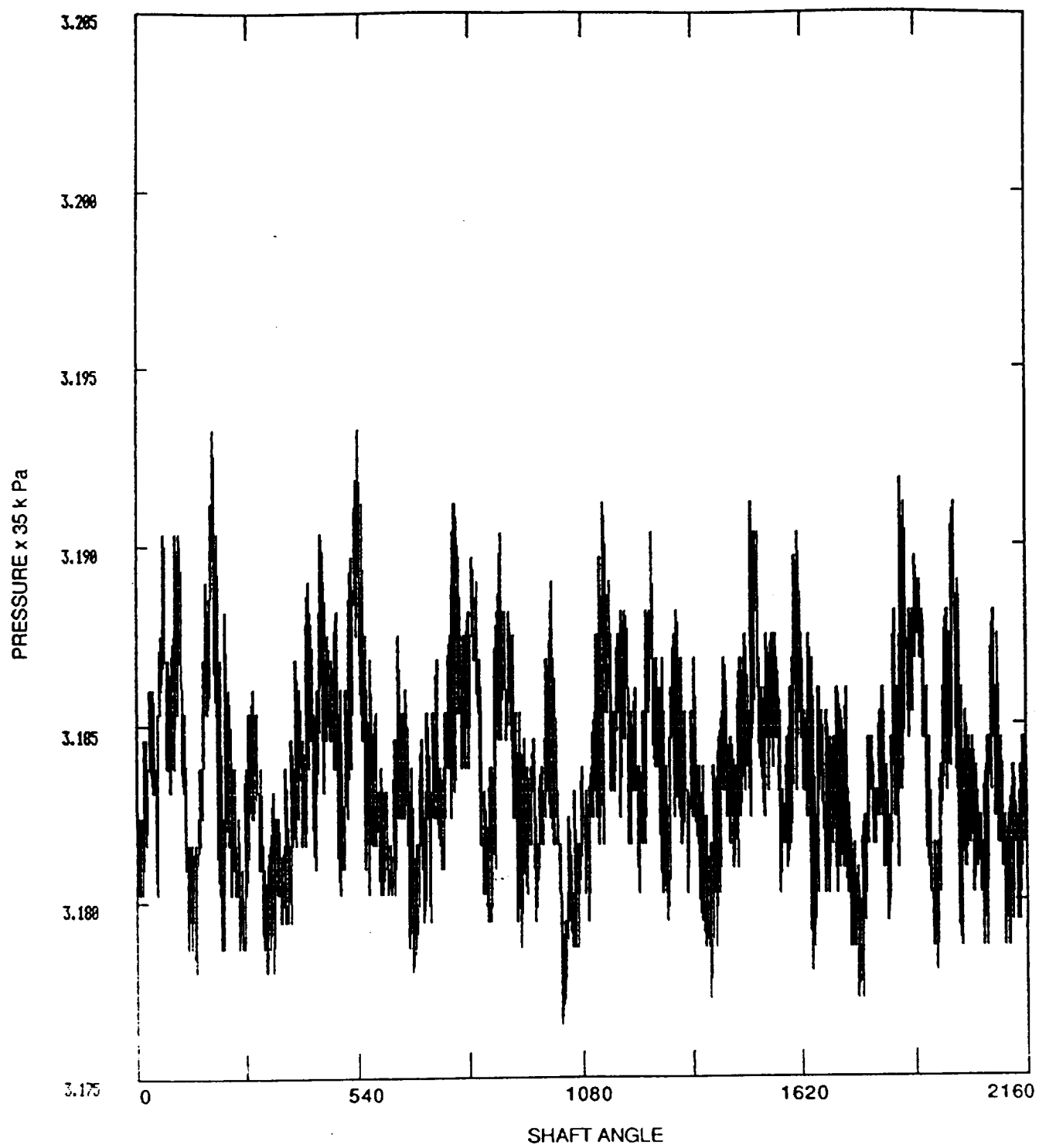


Fig. 8. Continued - Location 9.

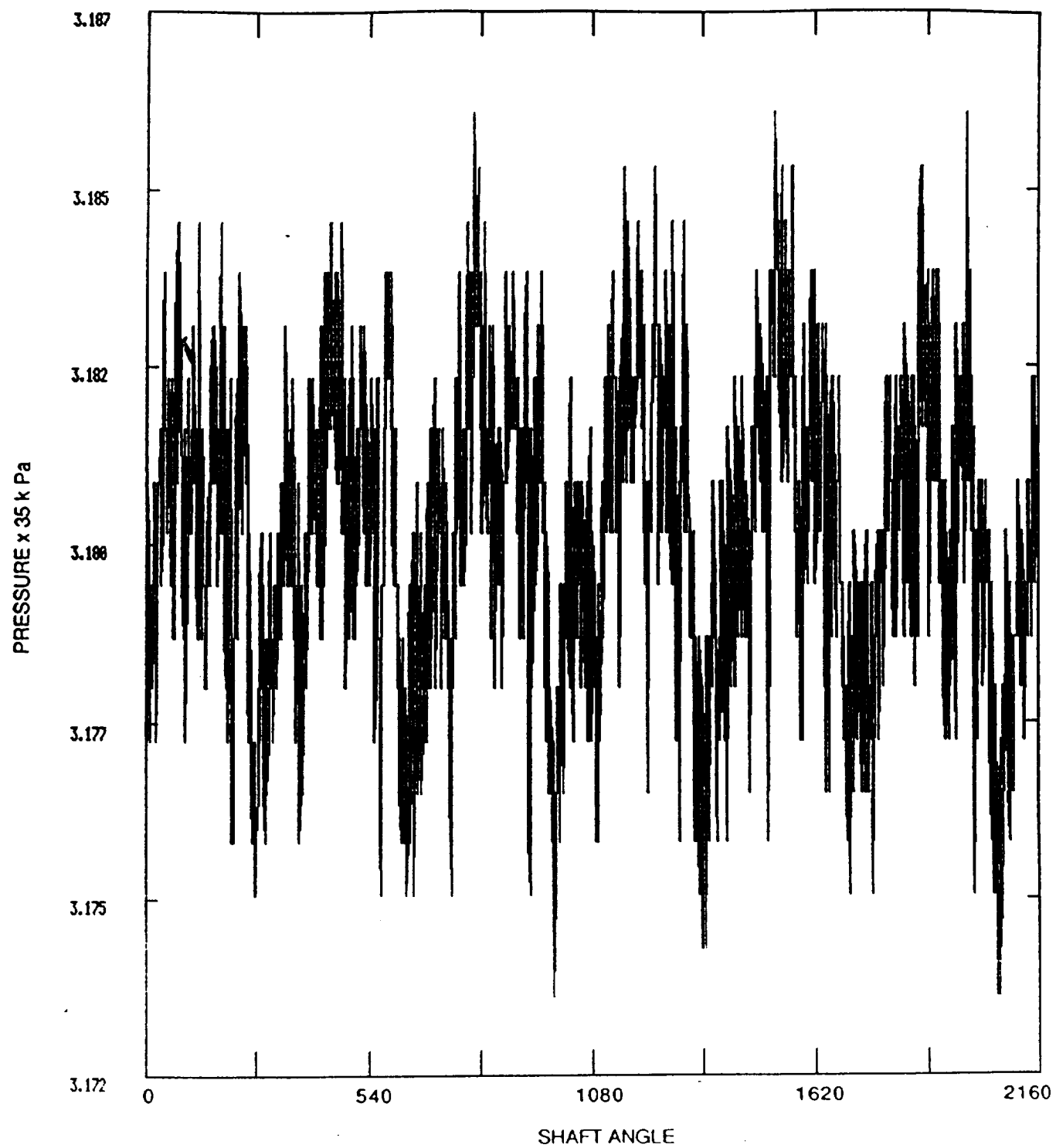


Fig. 8. Continued - Location 10.

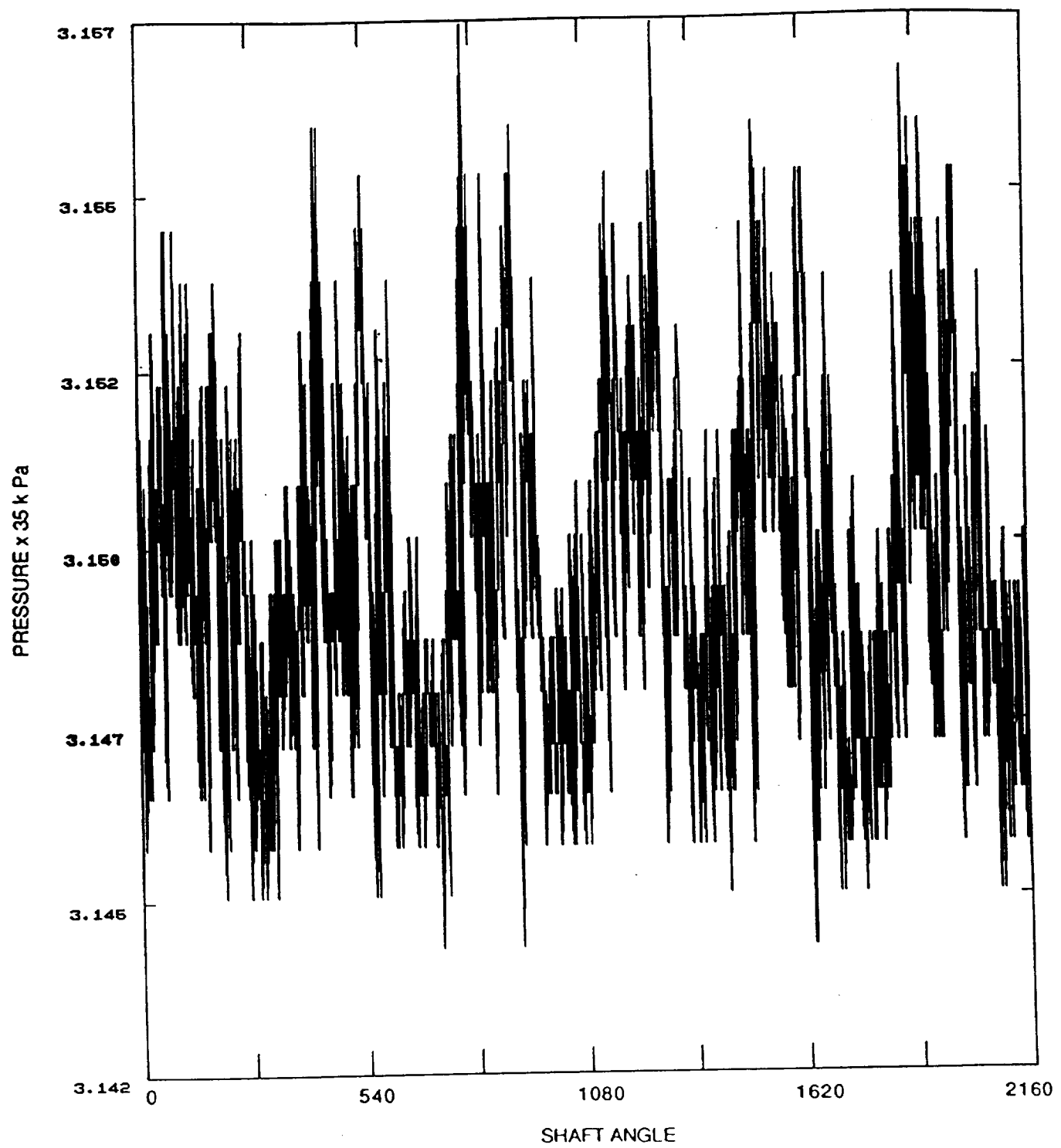


Fig. 8. Continued - Location 11.

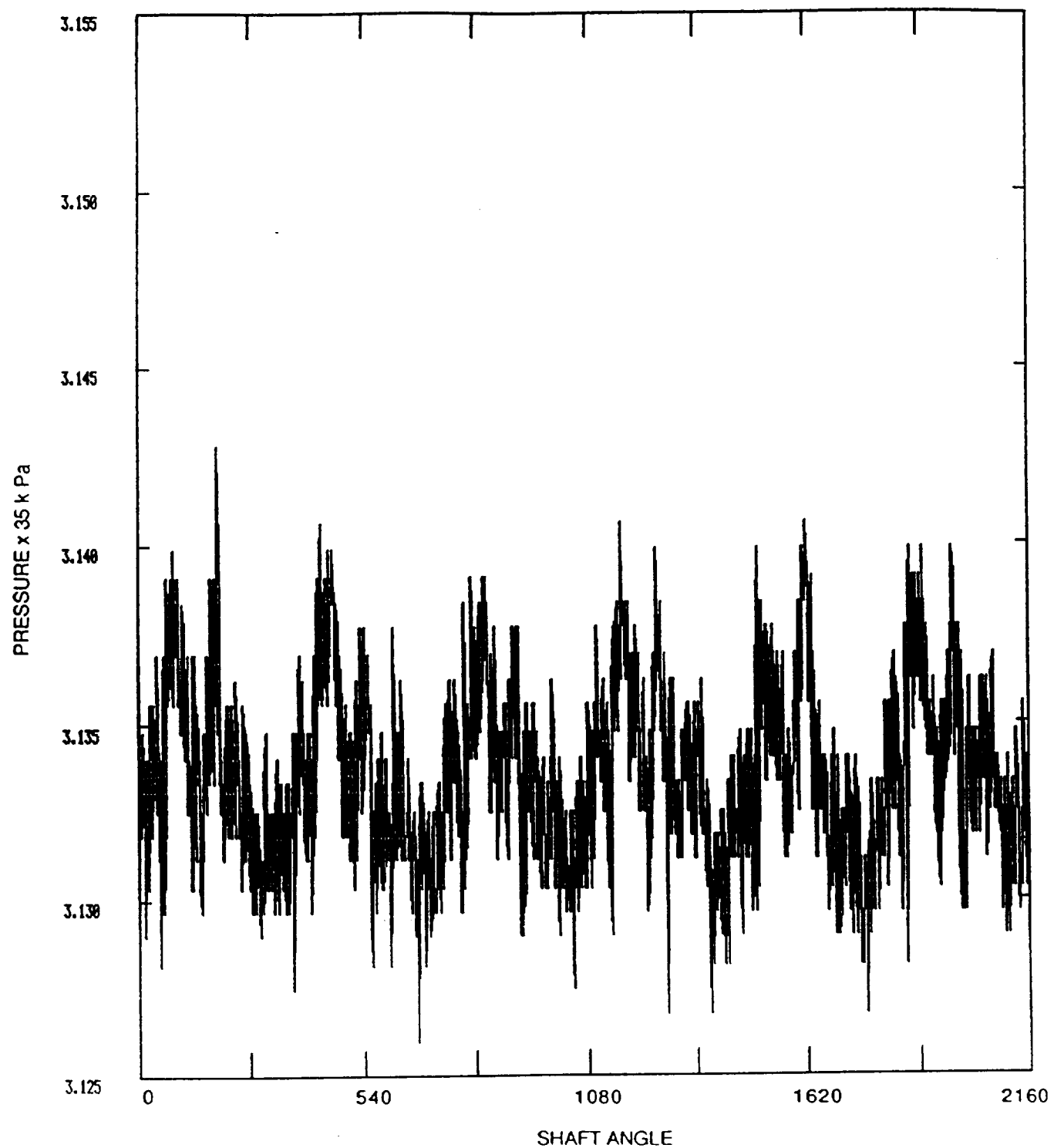


Fig. 8. Continued - Location 12.

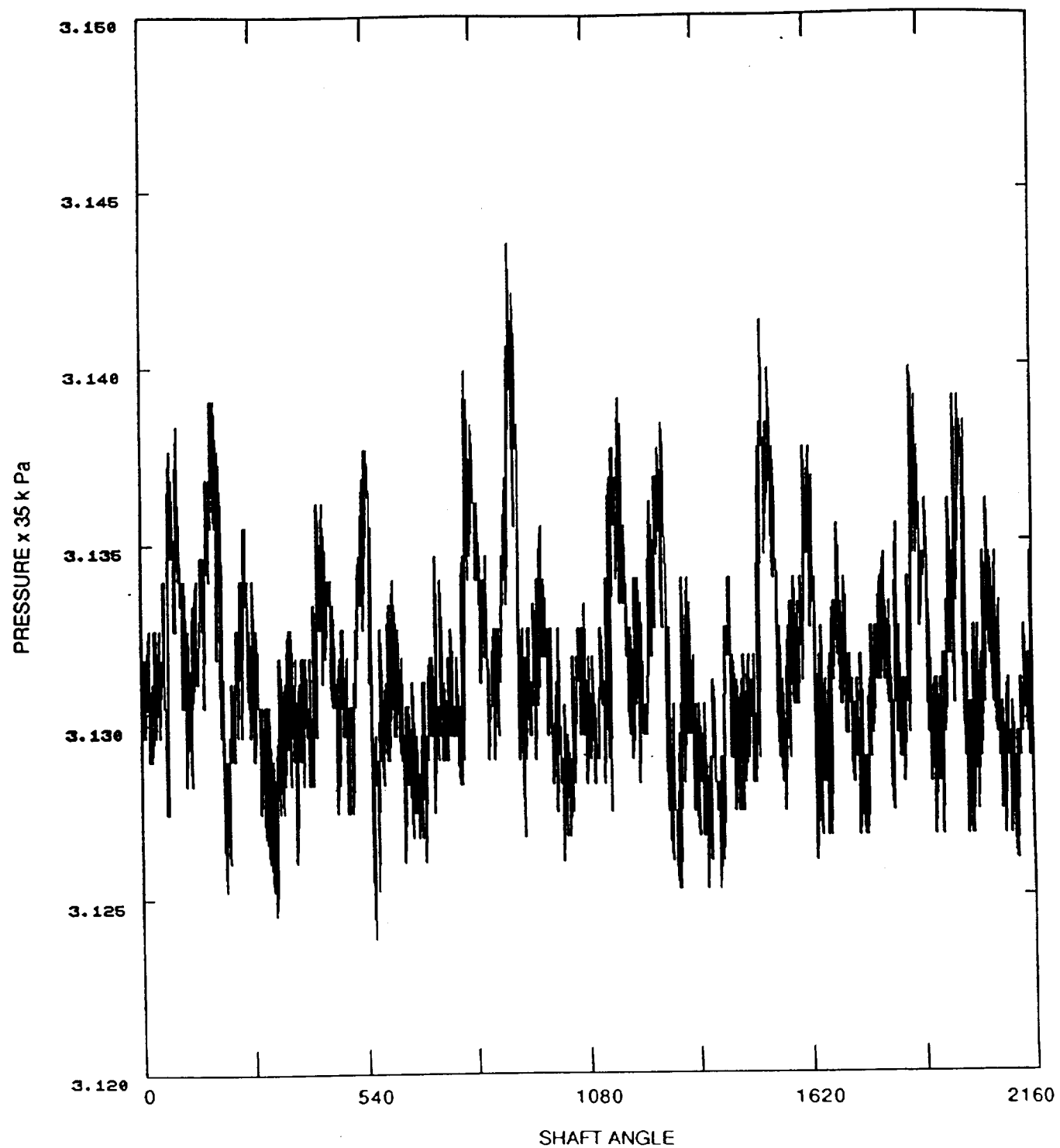


Fig. 8. Continued - Location 13.

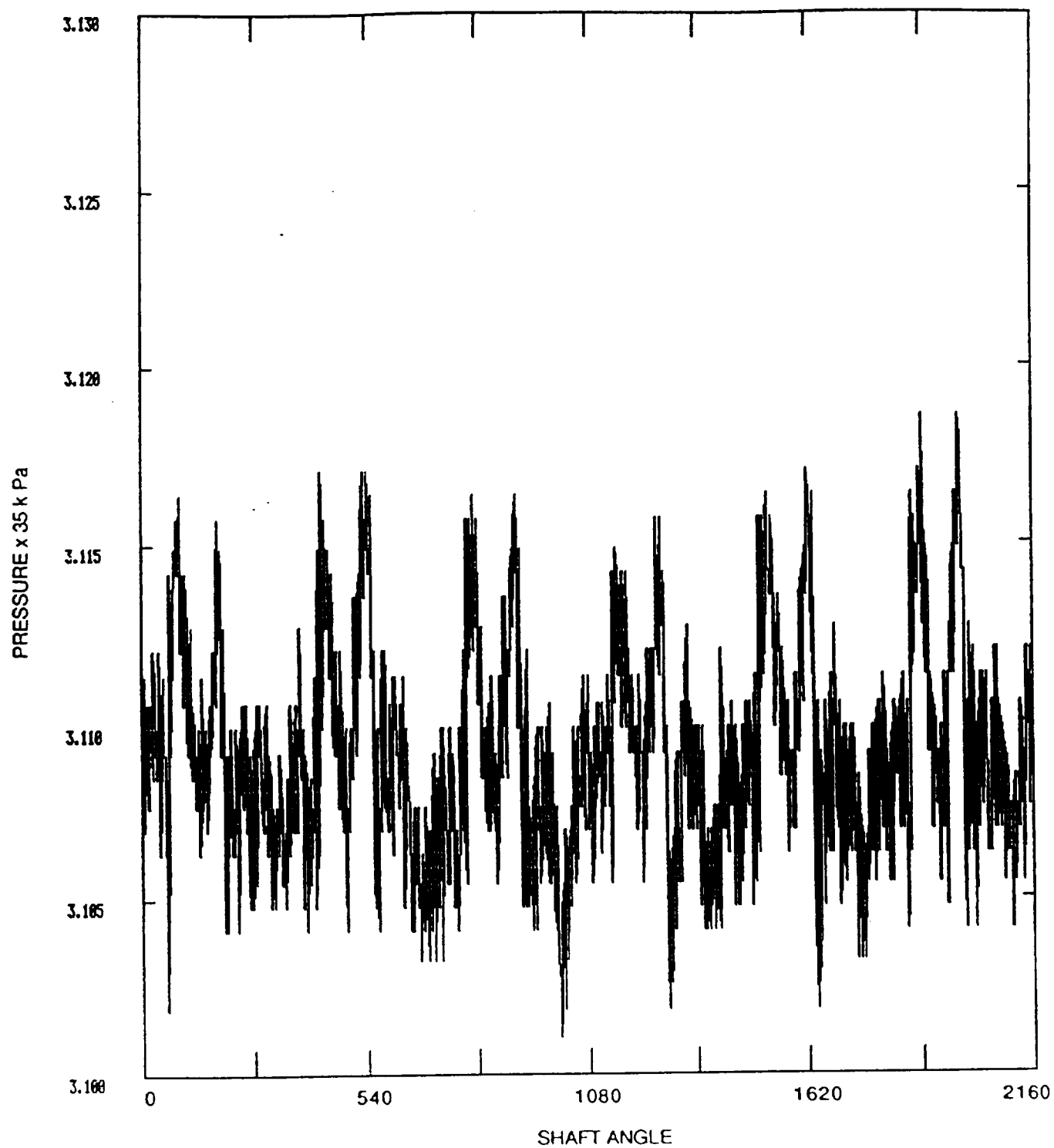


Fig. 8. Continued - Location 14.

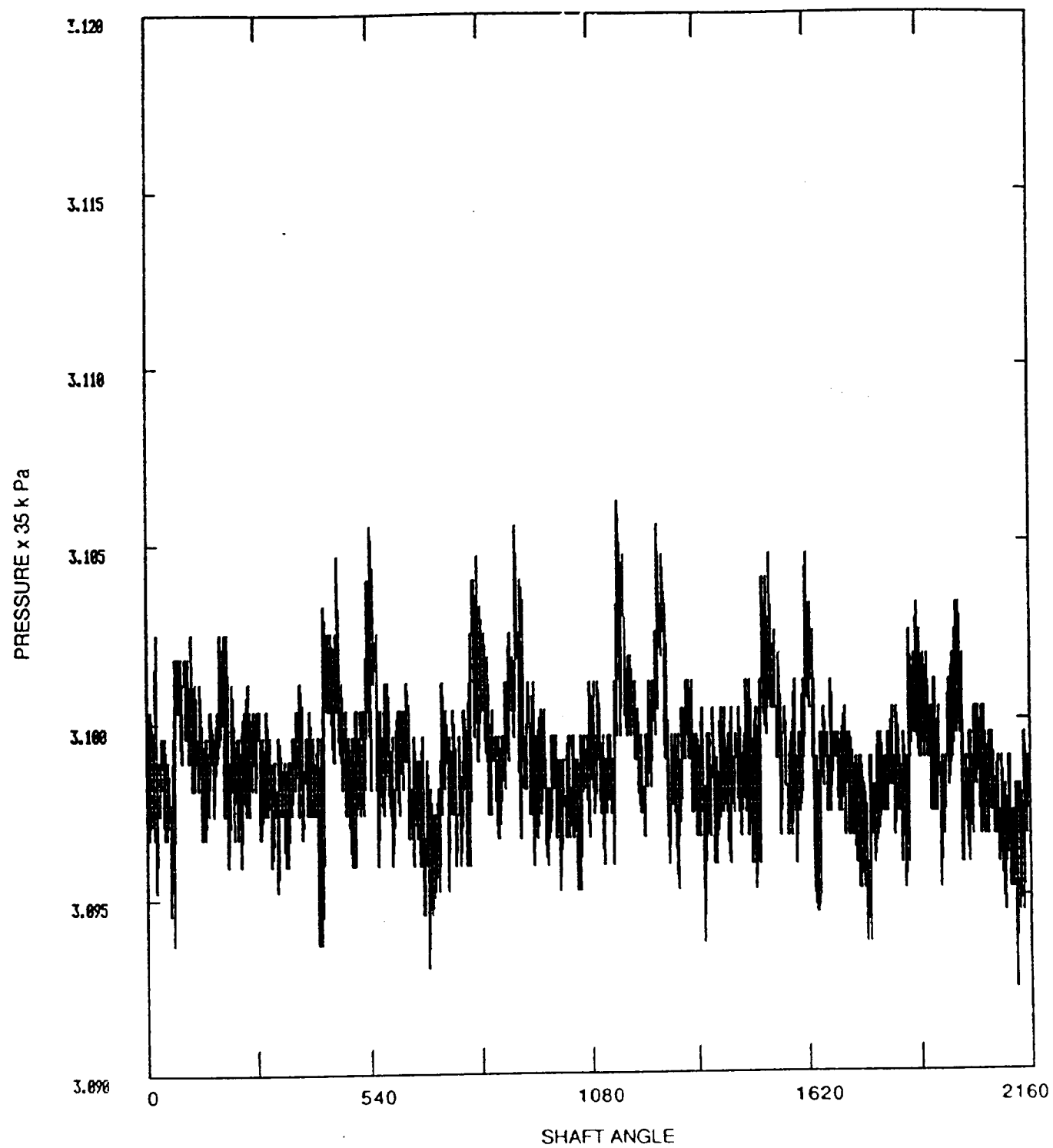


Fig. 8. Continued - Location 15.

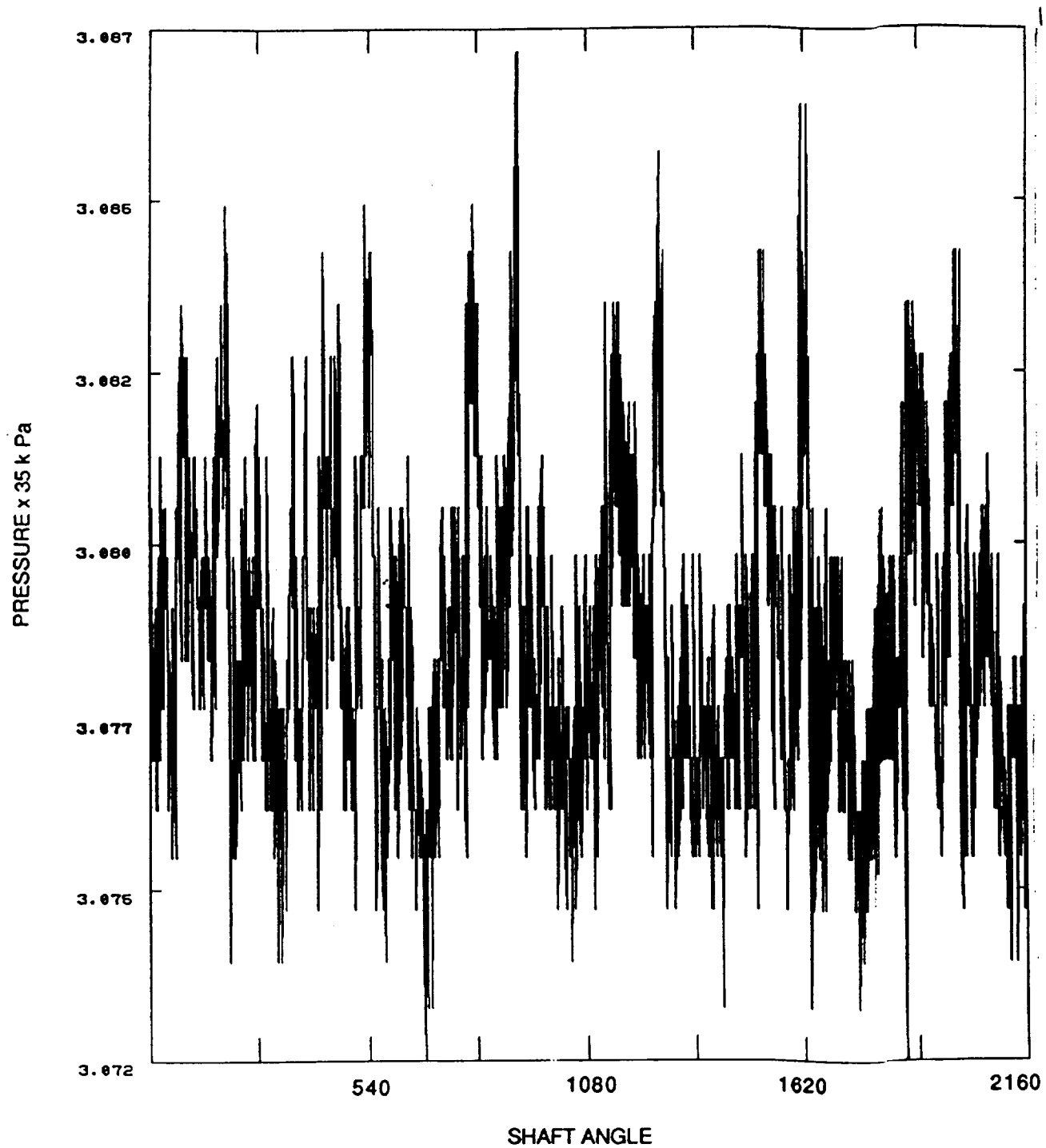


Fig. 8. Continued - Location 16.

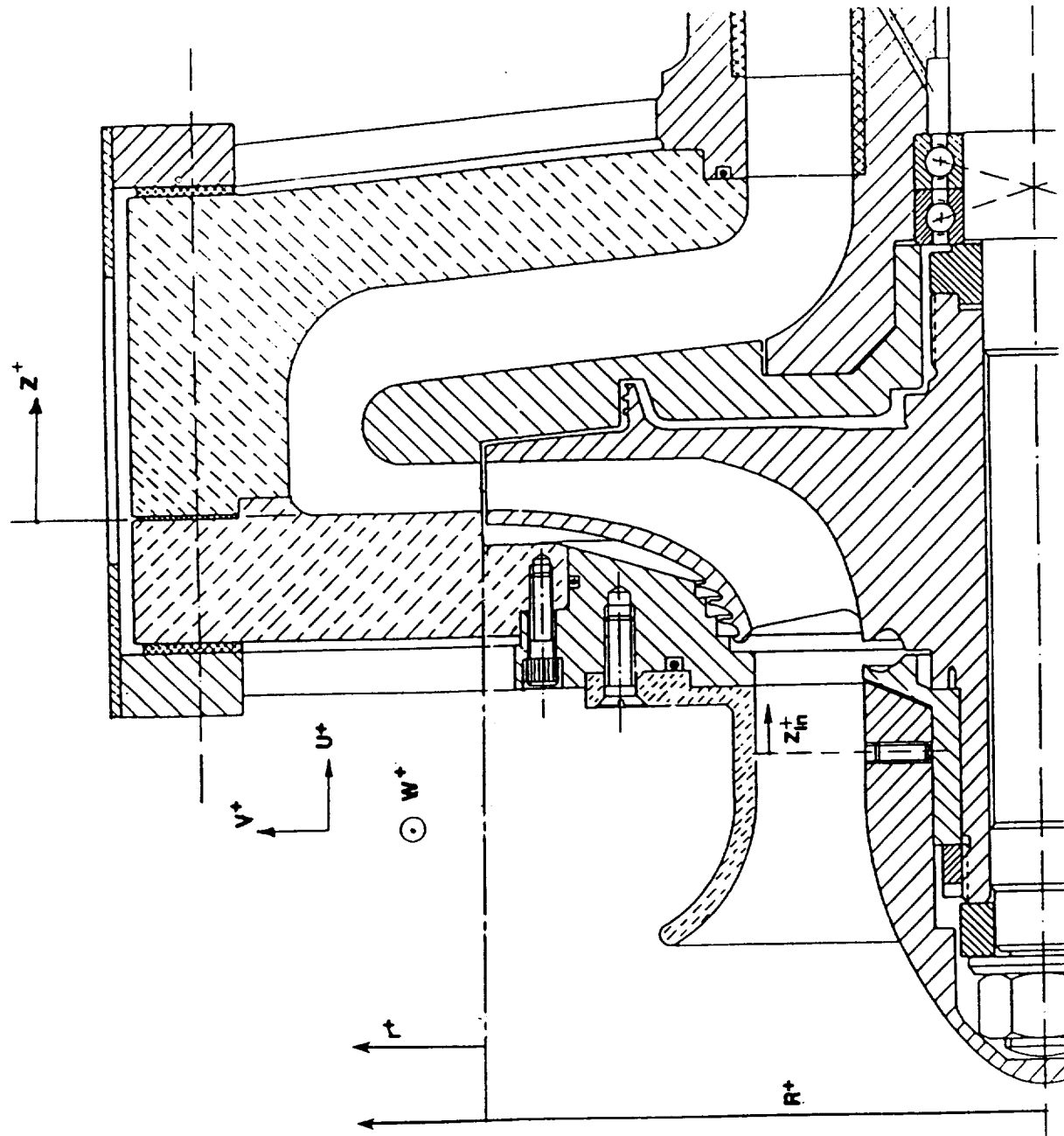


Fig. 9. Measuring Locations and Coordinate System.

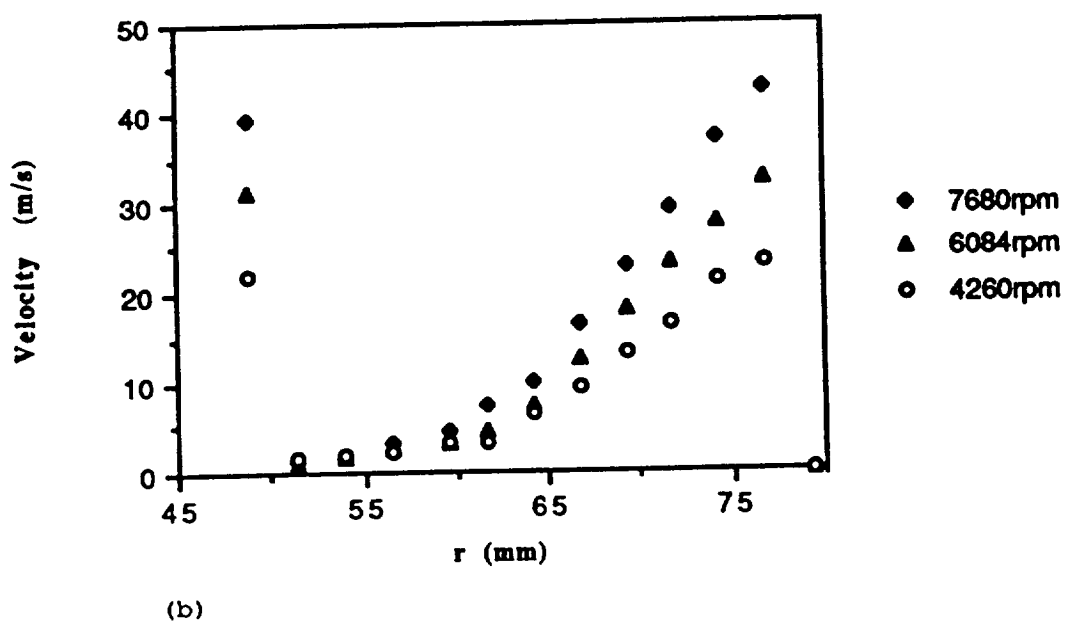
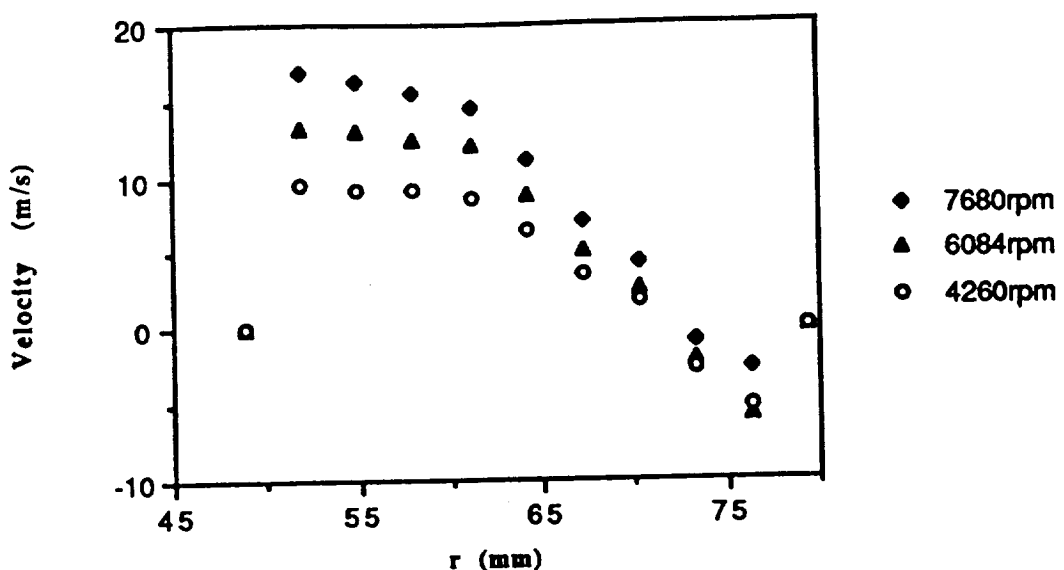


Fig. 10. Revolution-averaged Velocities at the Bellmouth Inlet.  
 (a) Axial Velocity.  
 (b) Tangential Velocity.

ORIGINAL PAGE IS  
OF POOR QUALITY

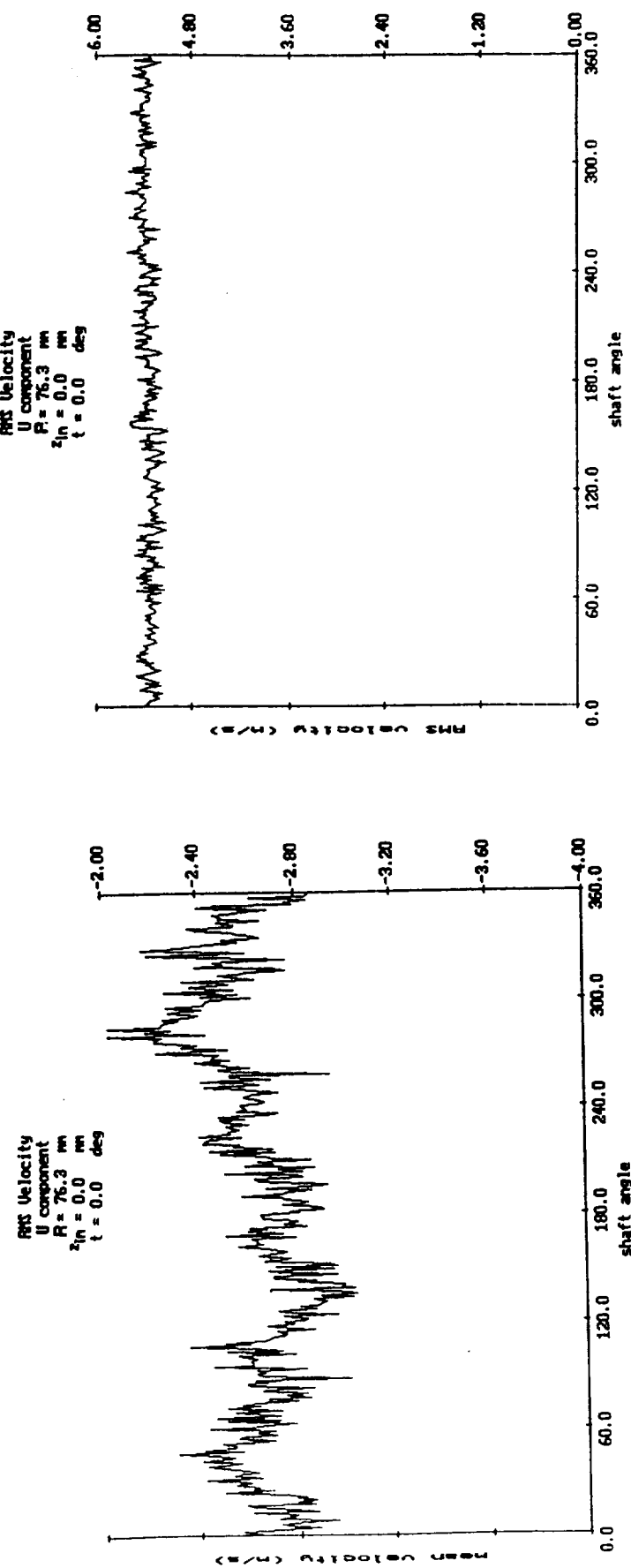


Fig. 11a. Ensemble-averaged Velocities at the Bellmouth Inlet.

OPTIONAL PAGE IS  
OF POOR QUALITY

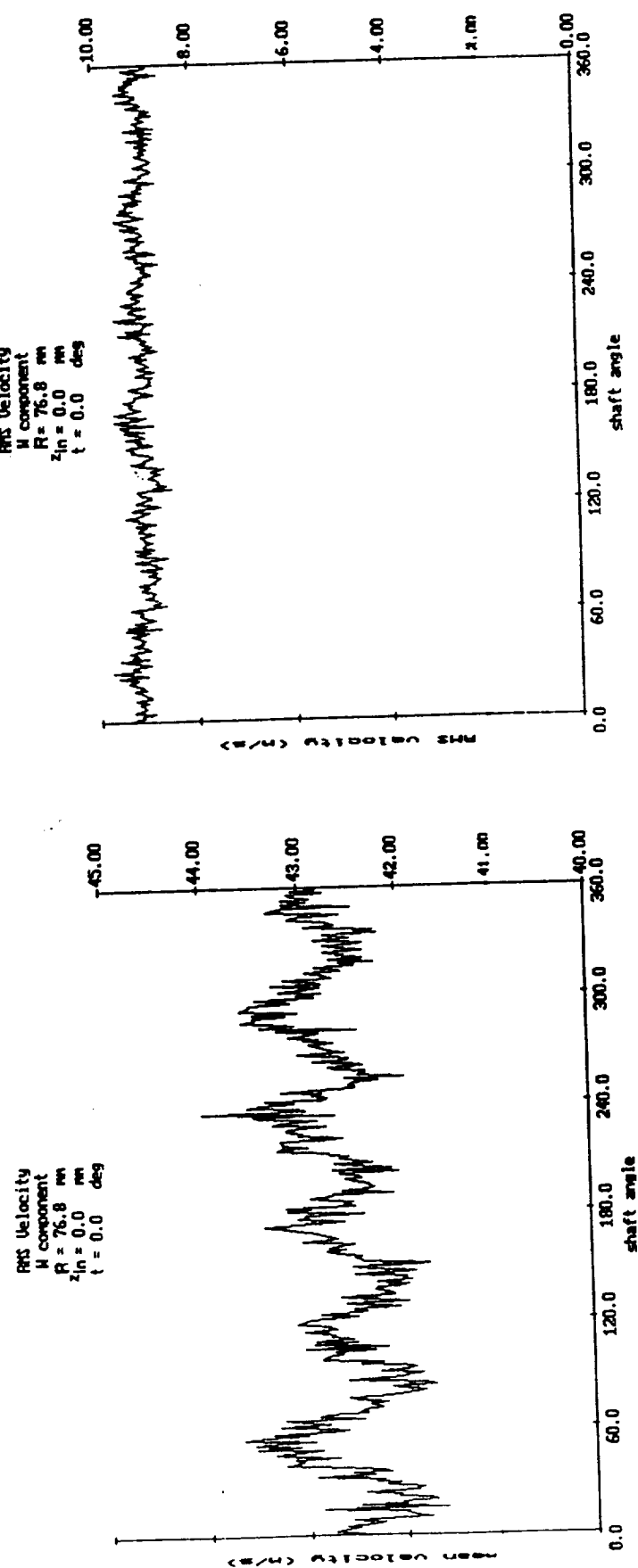


Fig. 11a. Continued.

ORIGINAL PAGE IS  
OF POOR QUALITY

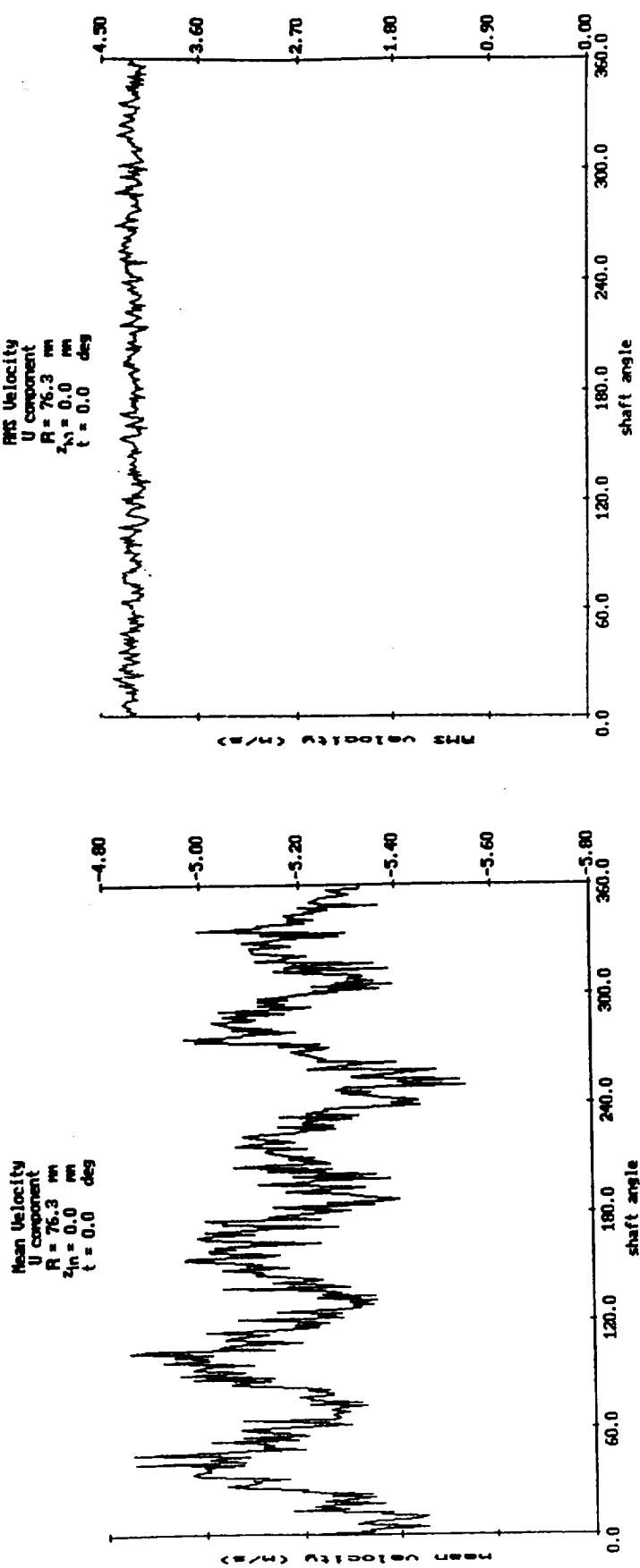


Fig. 11b. Ensemble-averaged velocities at the Bellmouth Inlet.

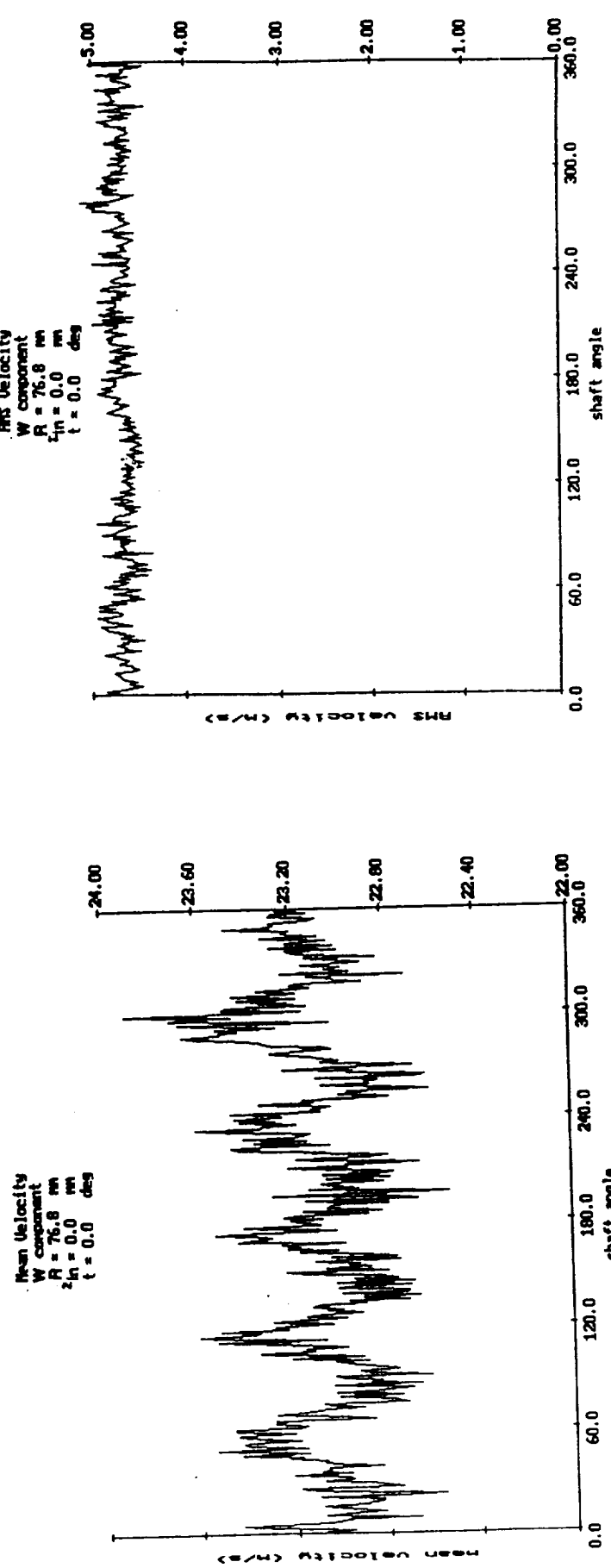


Fig. 11b. Continued.

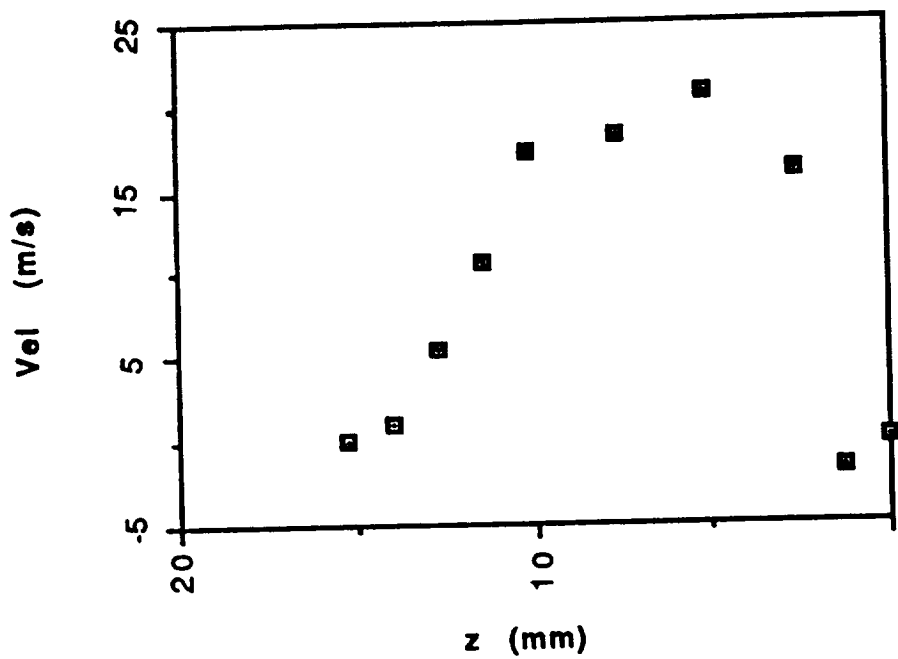


Fig. 12. Revolution-averaged Radial Velocities across the Diffuser Width at 2.5 mm Downstream of the Impeller Outlet.

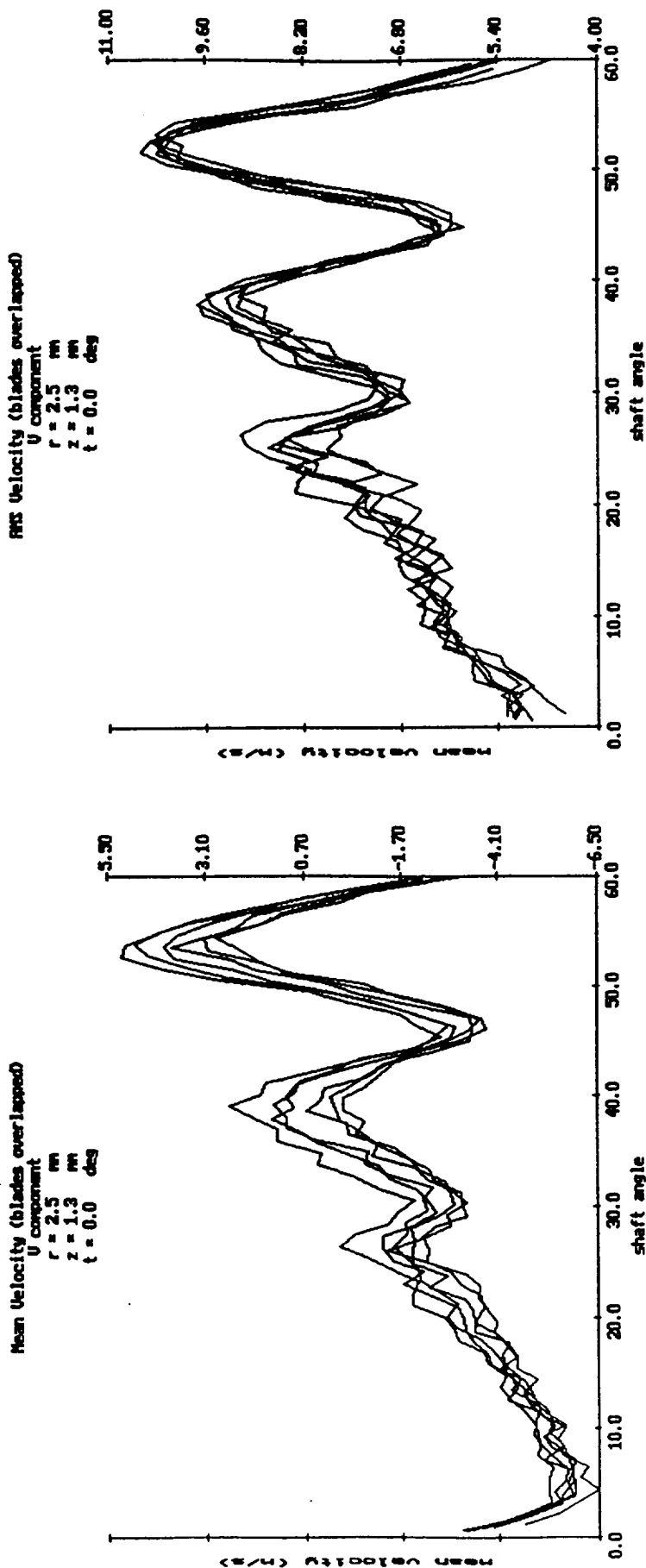


Fig. 13. Ensemble-averaged Radial Velocities across the Diffuser Width at 2.5 mm Downstream of the Impeller Outlet.

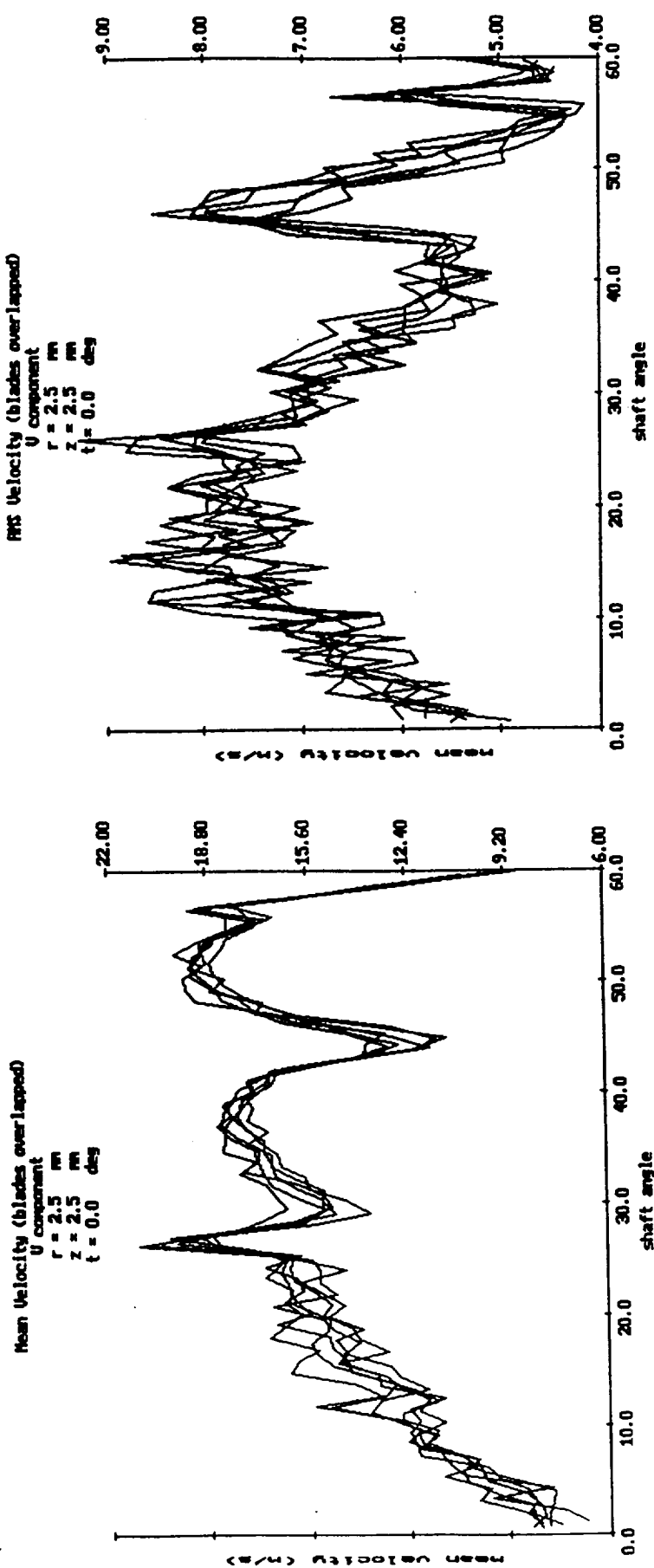


Fig. 13. Continued.

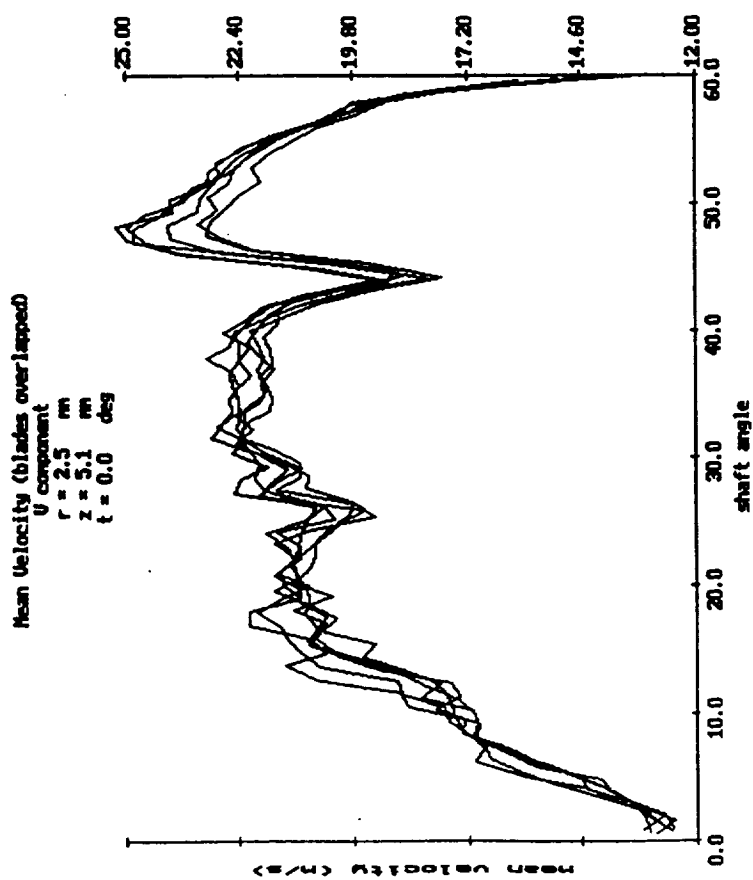
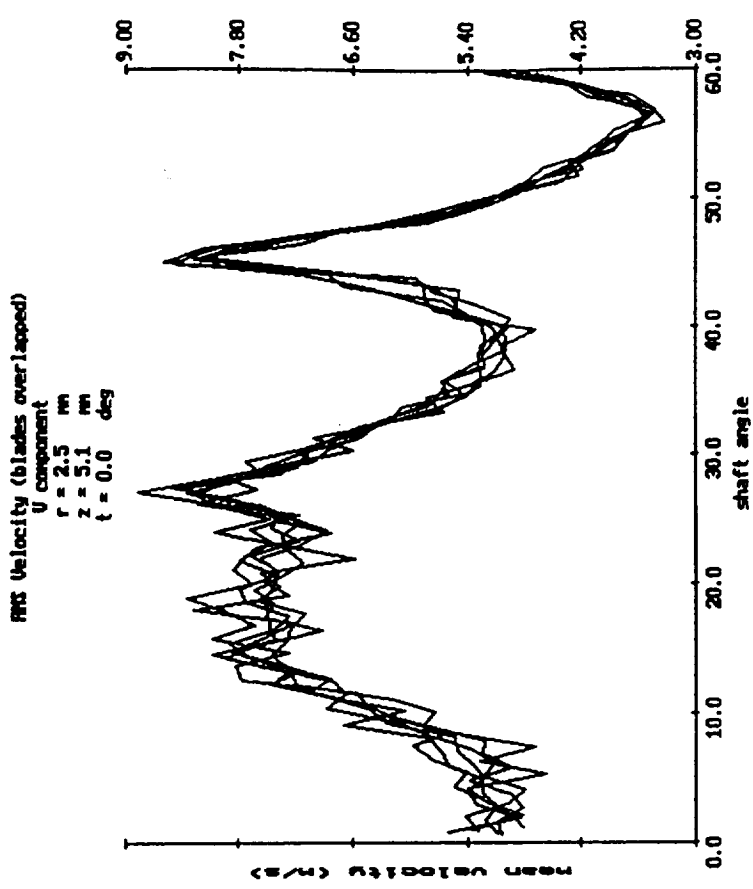


Fig. 13. Continued.

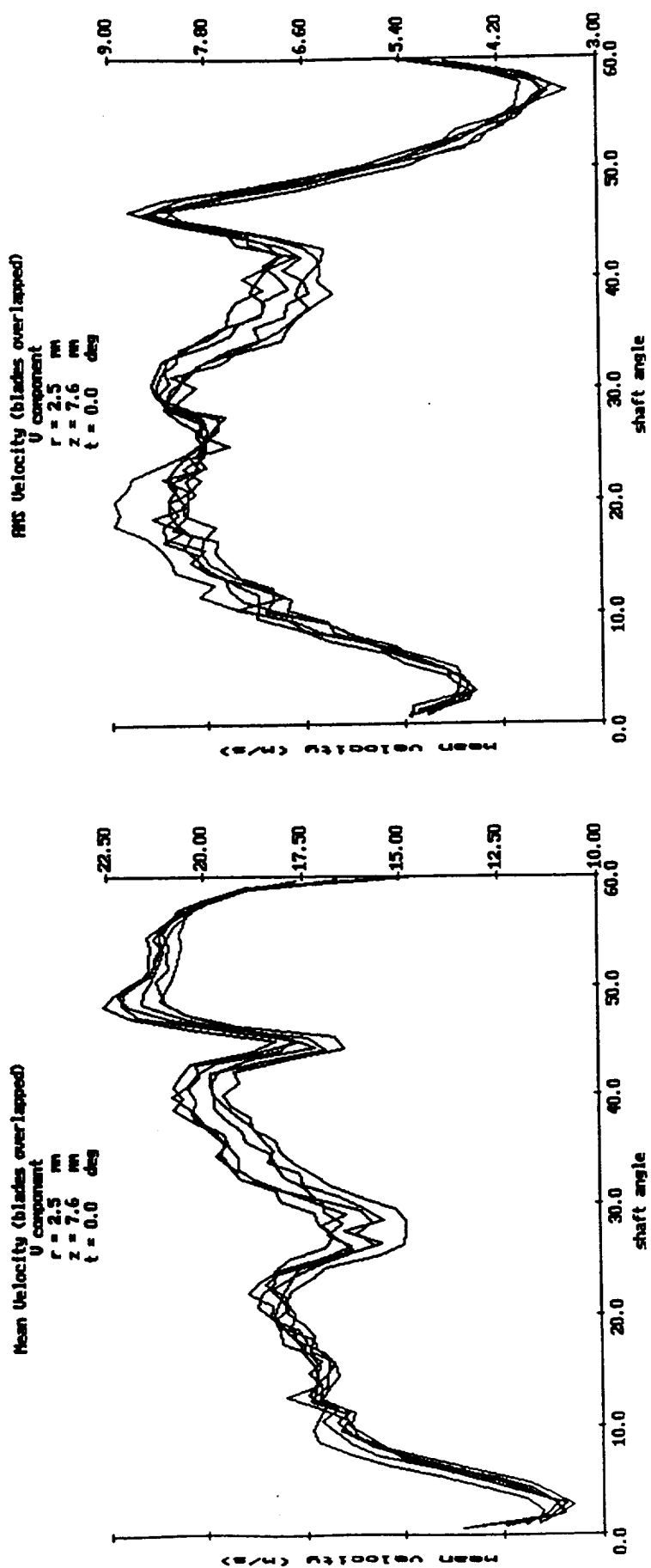


Fig. 13. Continued.

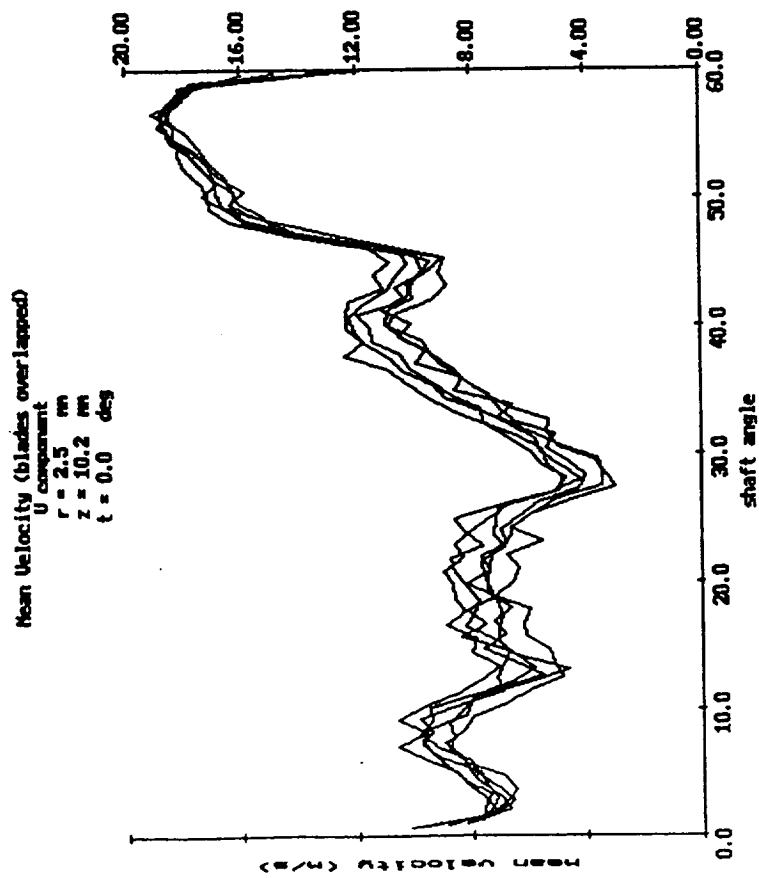
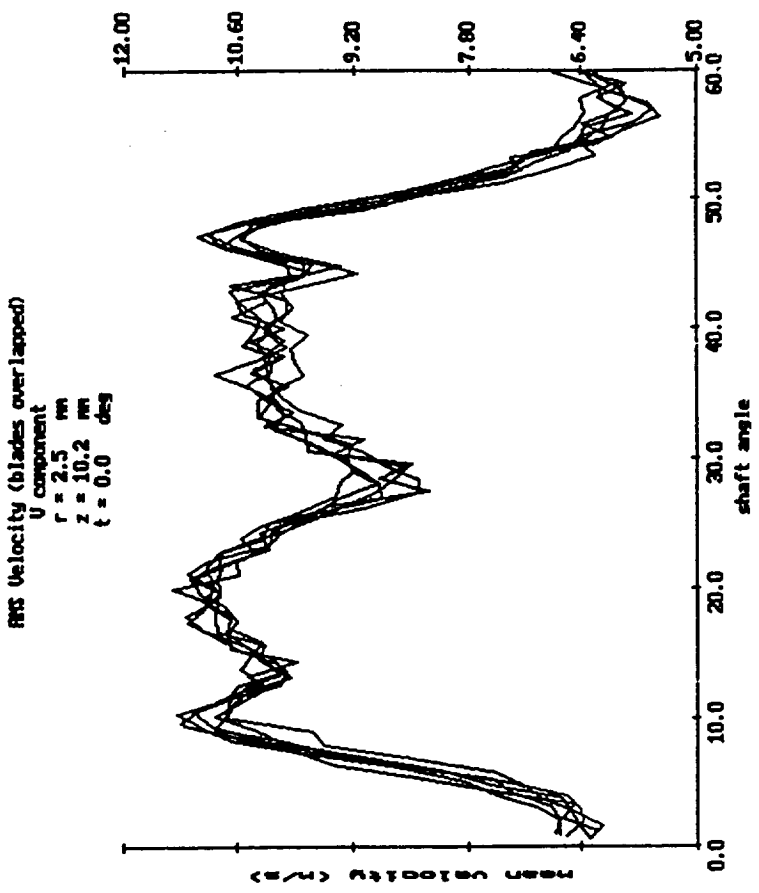


Fig. 13. Continued

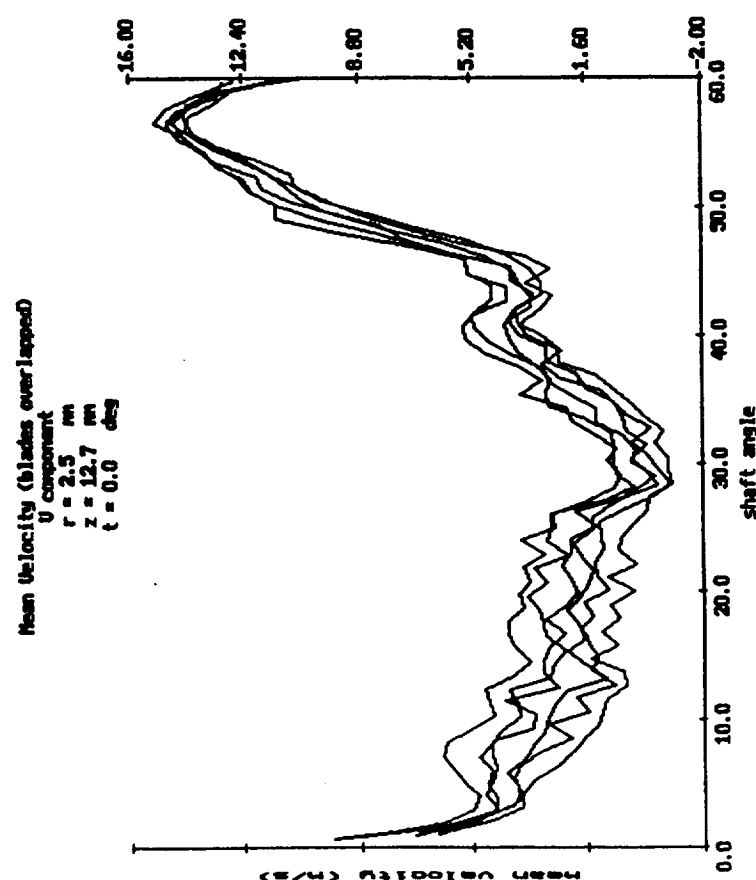
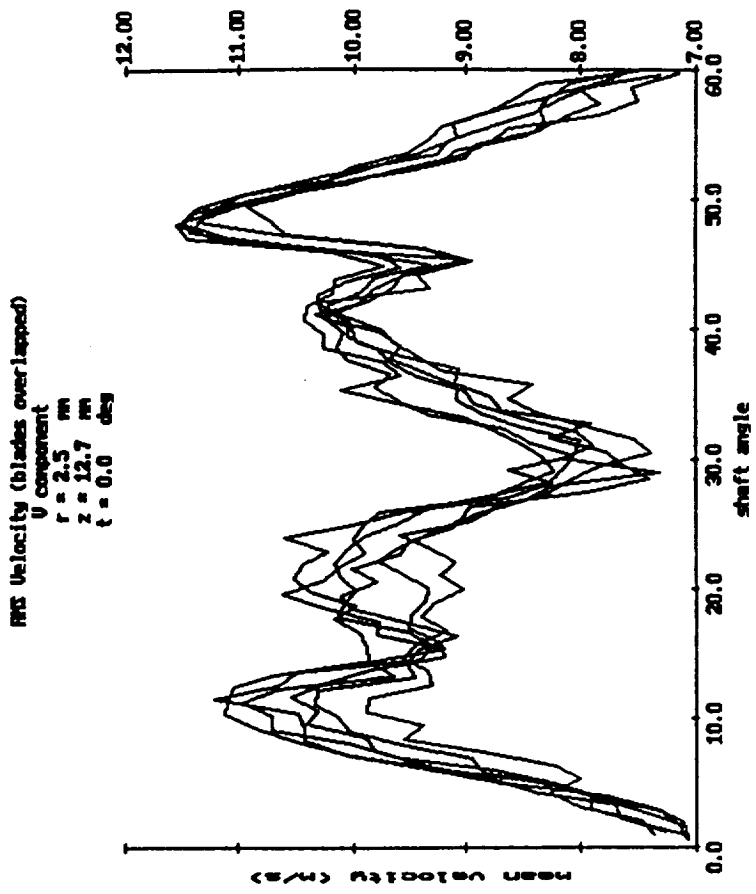
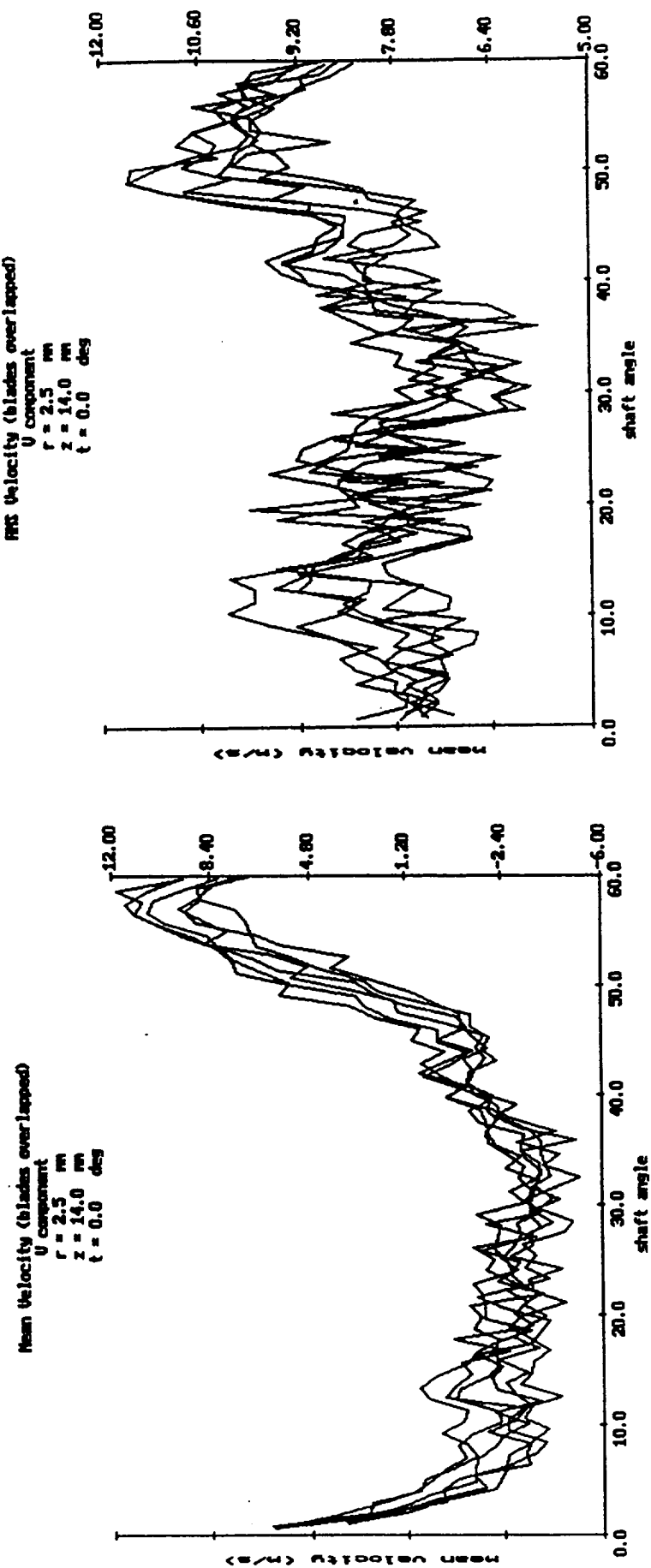


Fig. 13. Continued.



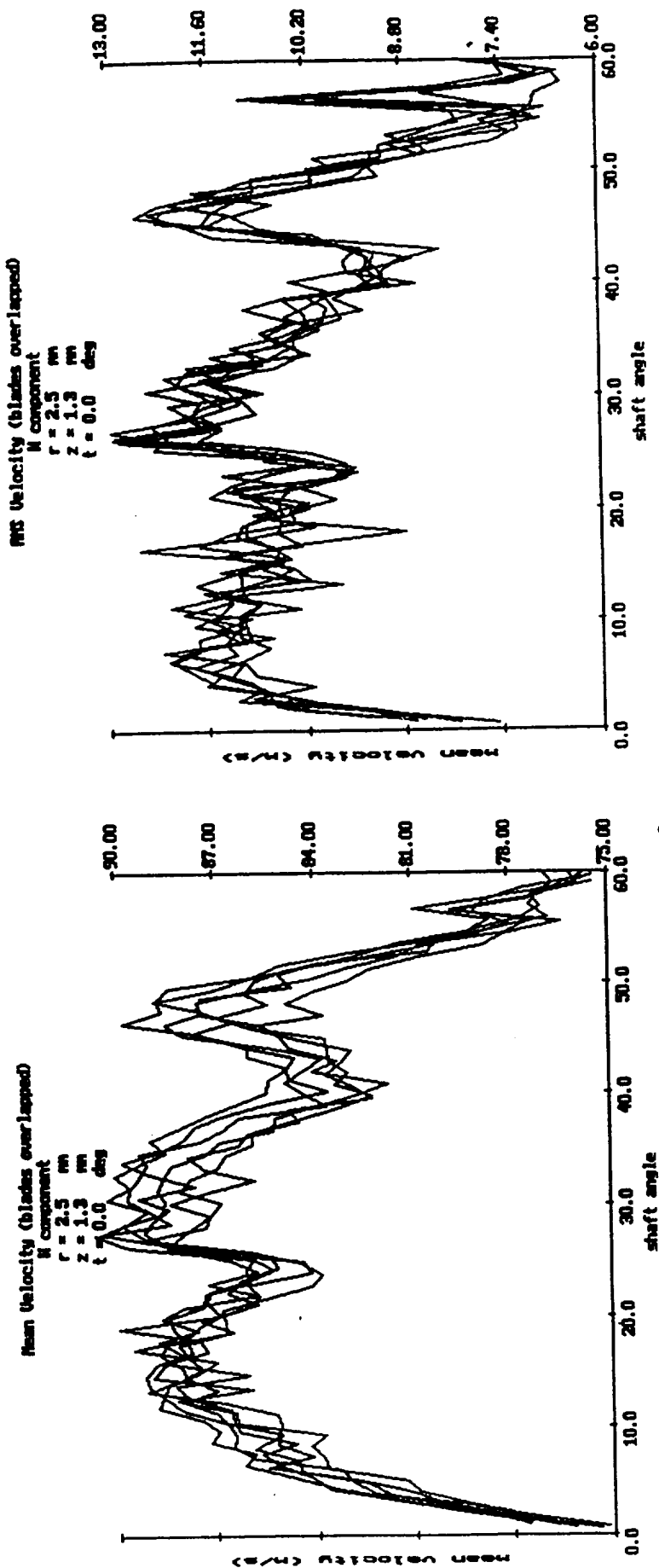


Fig. 14. Ensemble-averaged Tangential Velocities across the Diffuser  
Width at 2.5 mm Downstream of the Impeller Outlet.

ORIGINAL PAGE IS  
OF POOR QUALITY

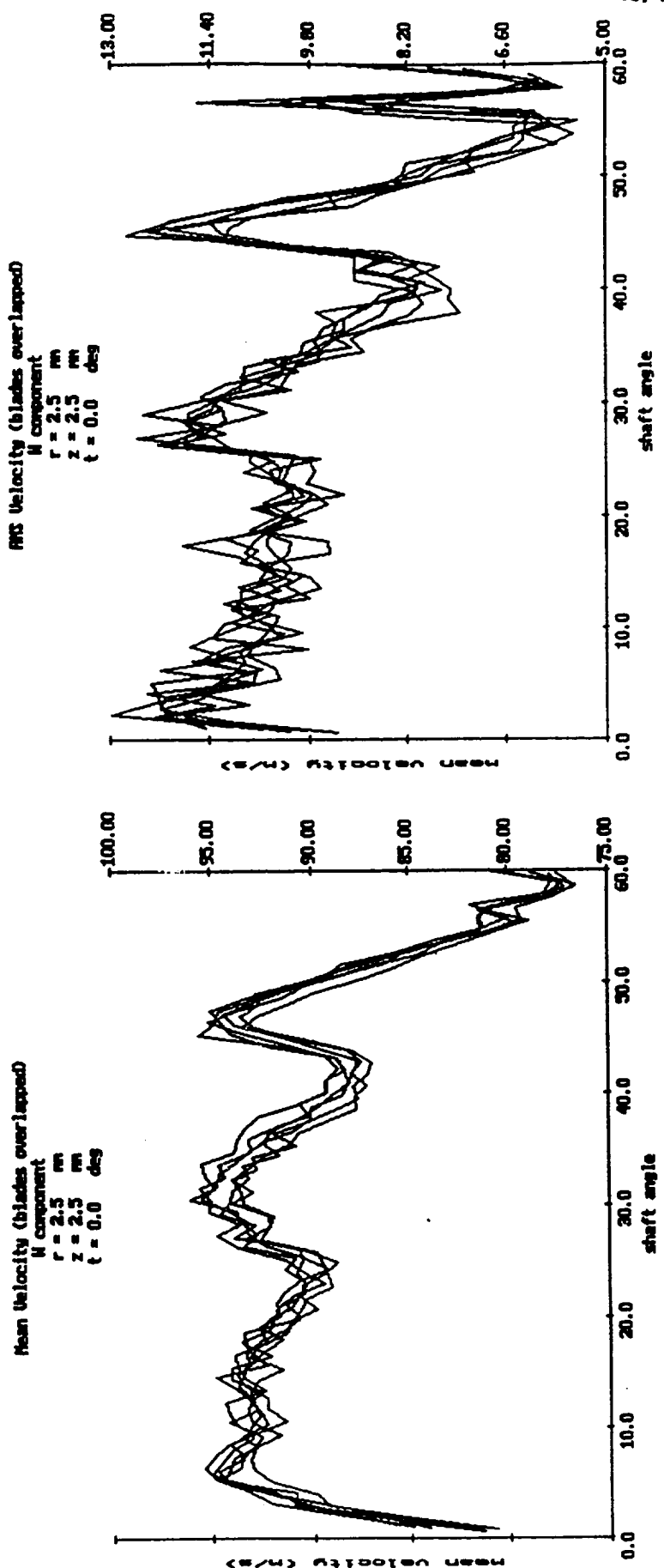


Fig. 14. Continued.

ORIGINAL PAGE IS  
OF POOR QUALITY

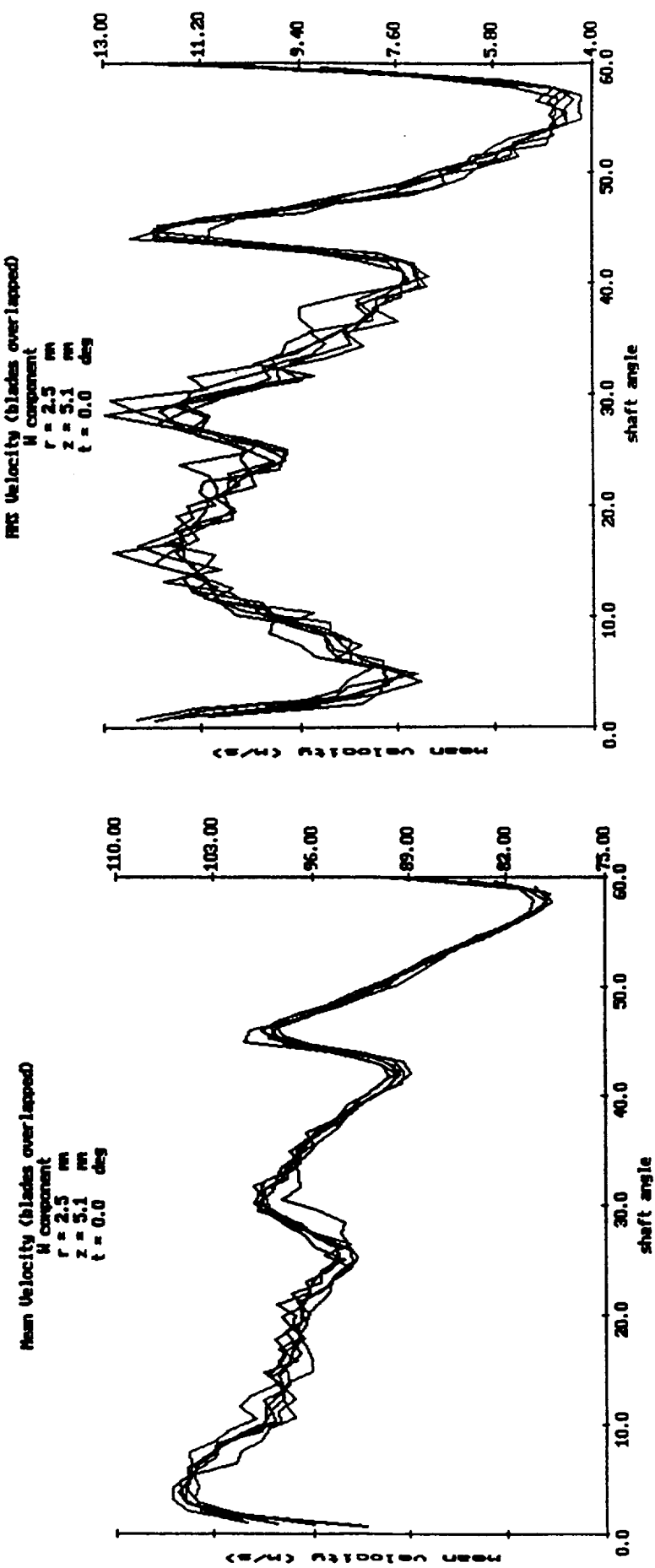


Fig. 14. Continued.

ORIGINAL PAGE IS  
OF POOR QUALITY

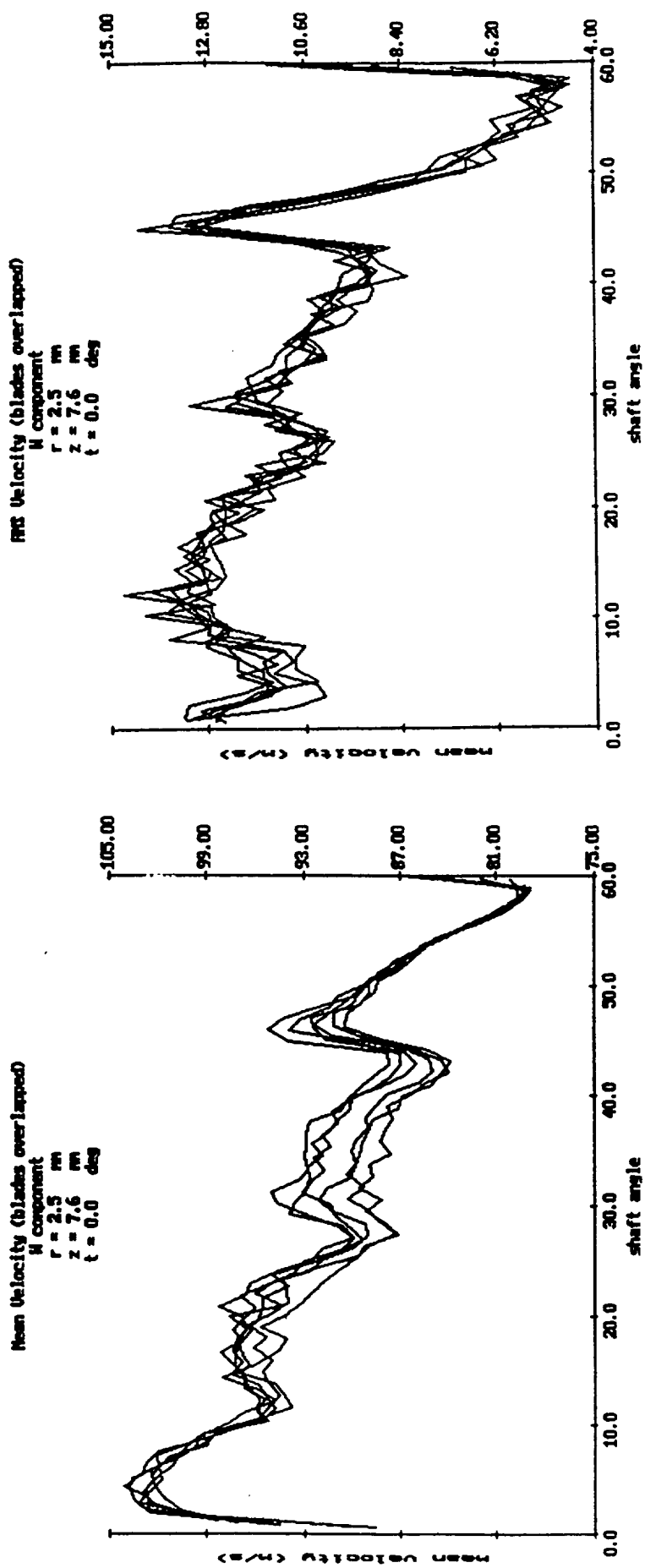


Fig. 14. Continued.

ORIGINAL PAGE IS  
OF POOR QUALITY

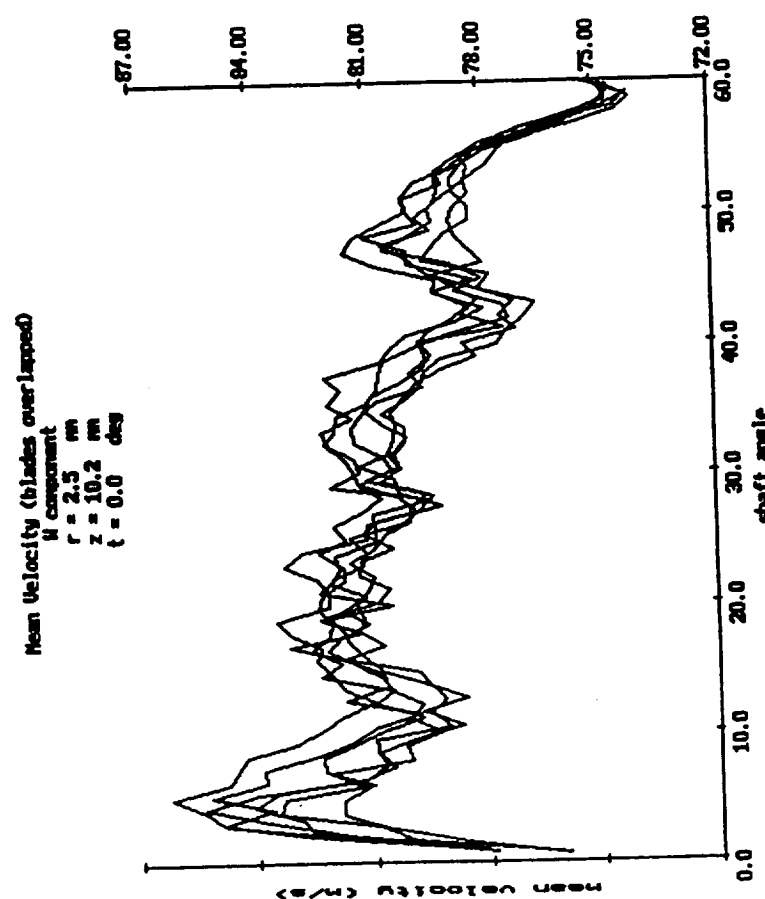
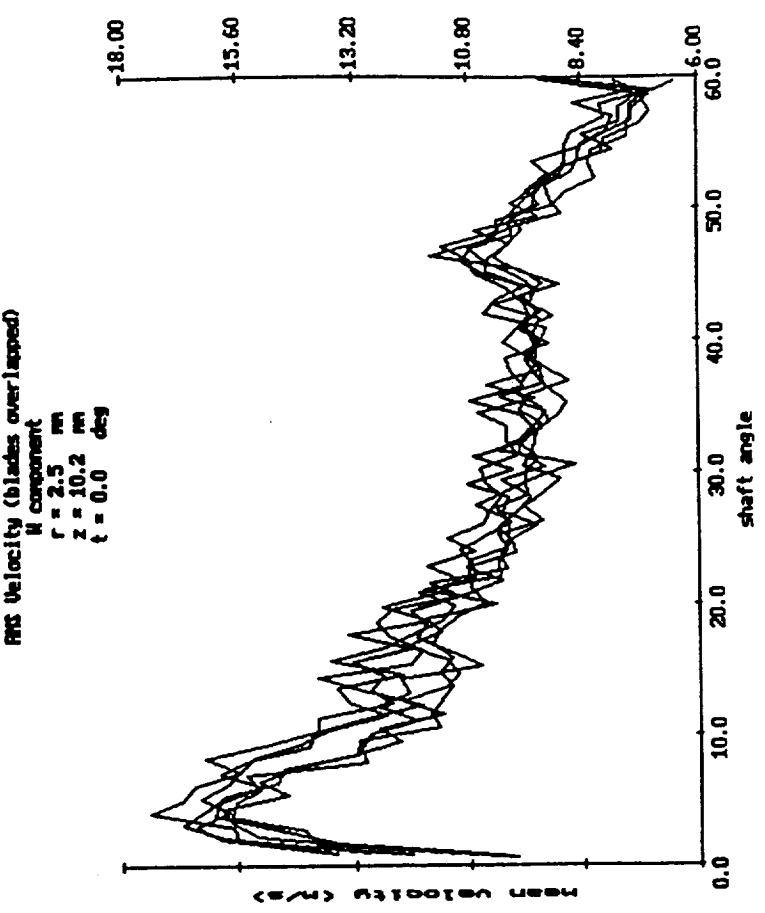


Fig. 14. Continued.

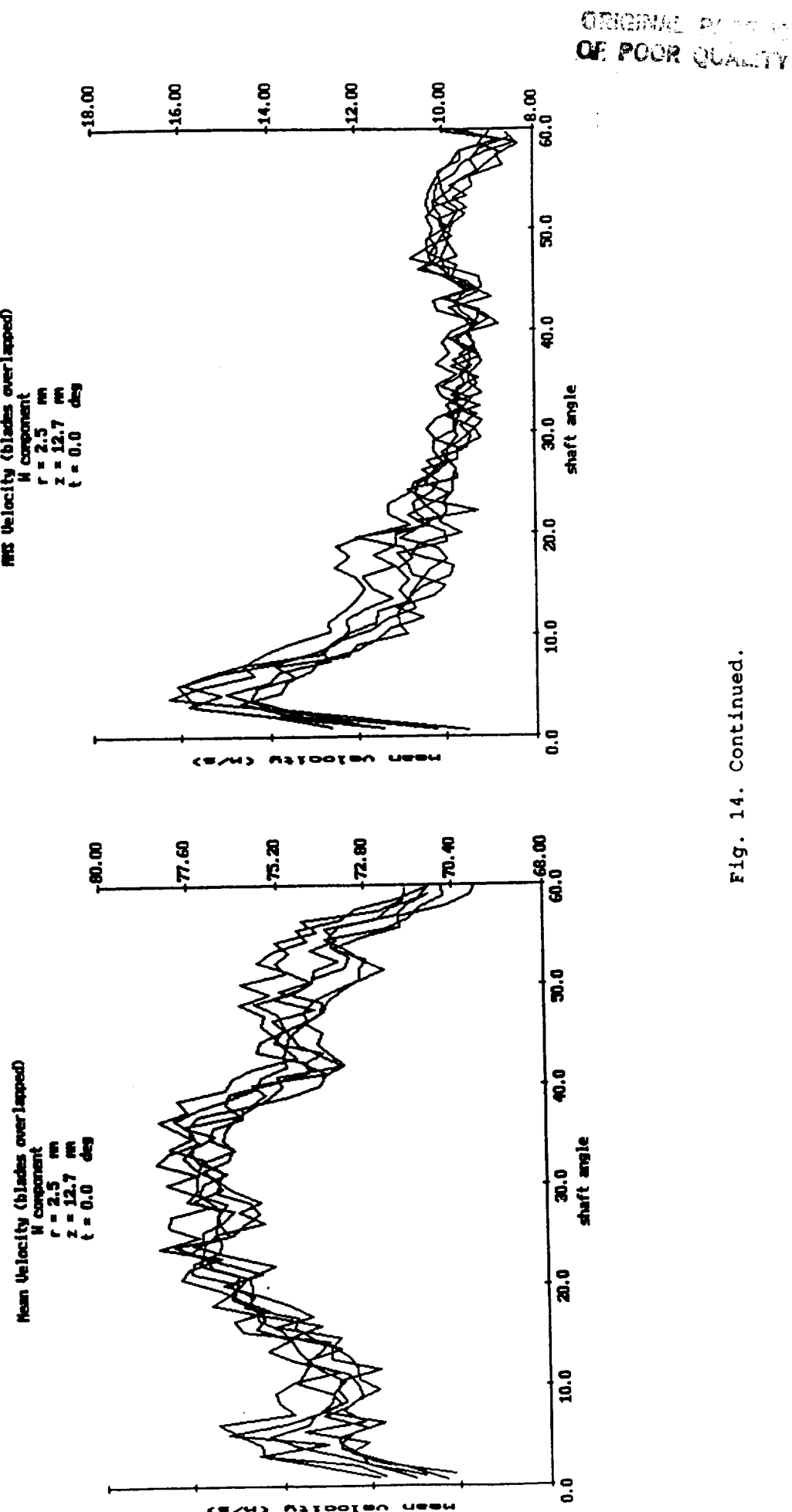


Fig. 14. Continued.

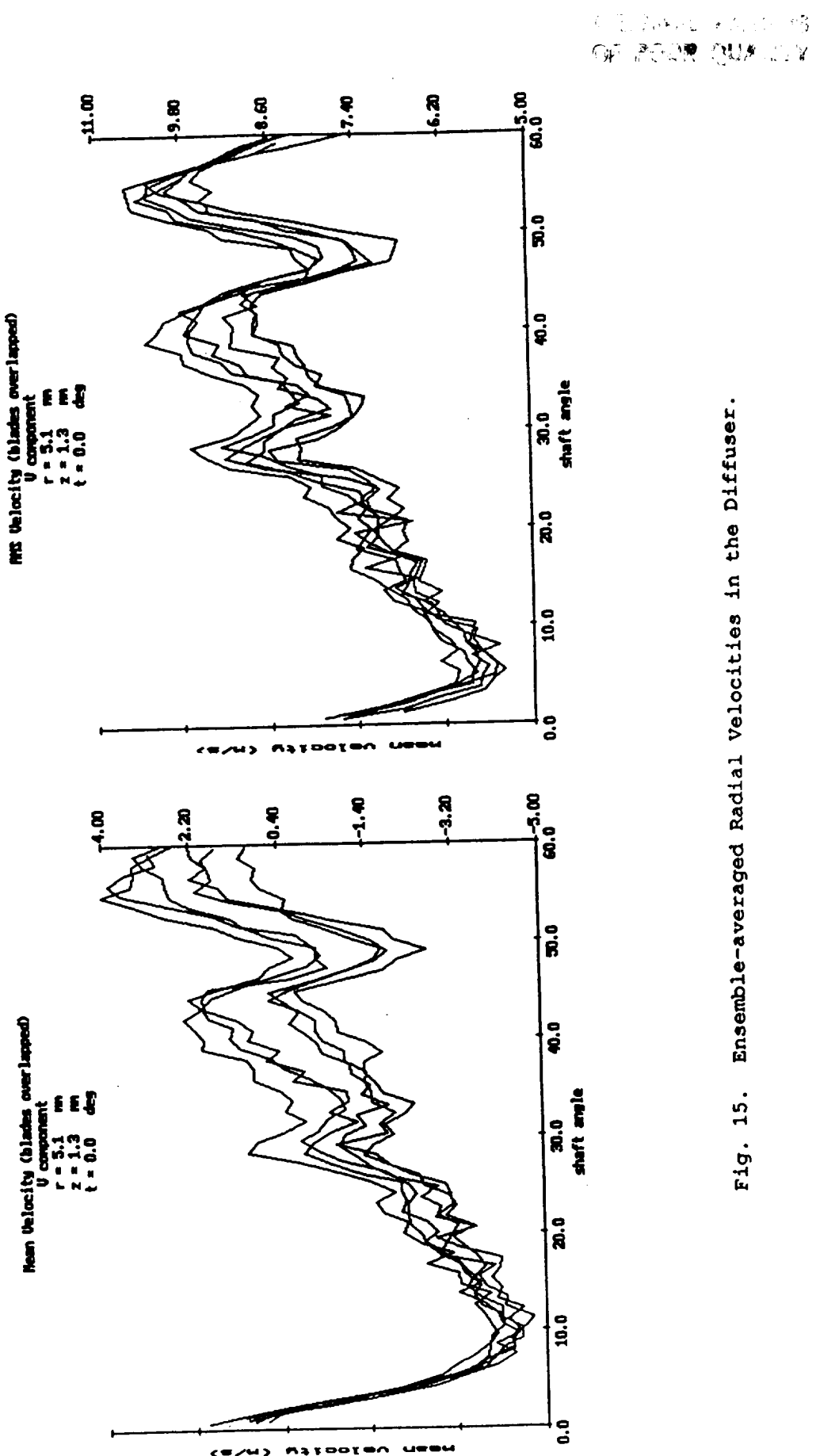


Fig. 15. Ensemble-averaged Radial Velocities in the Diffuser.

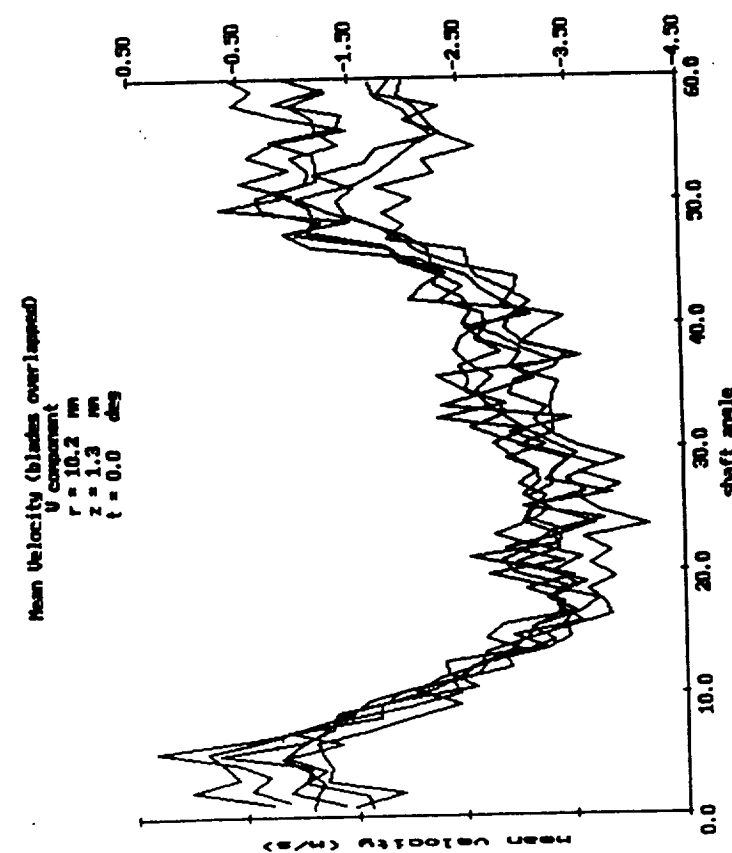
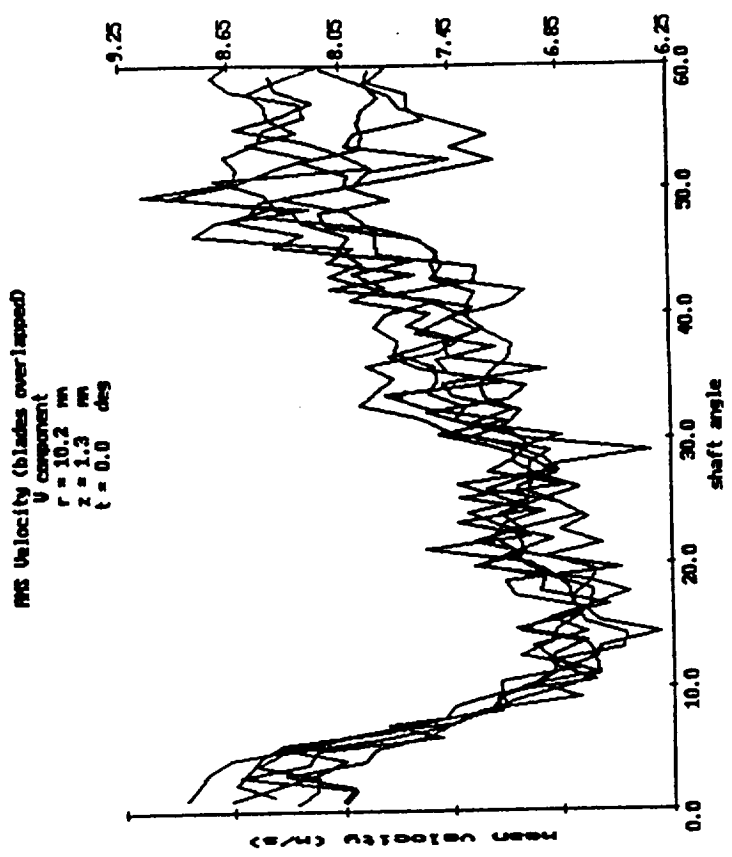


Fig. 15. Continued.

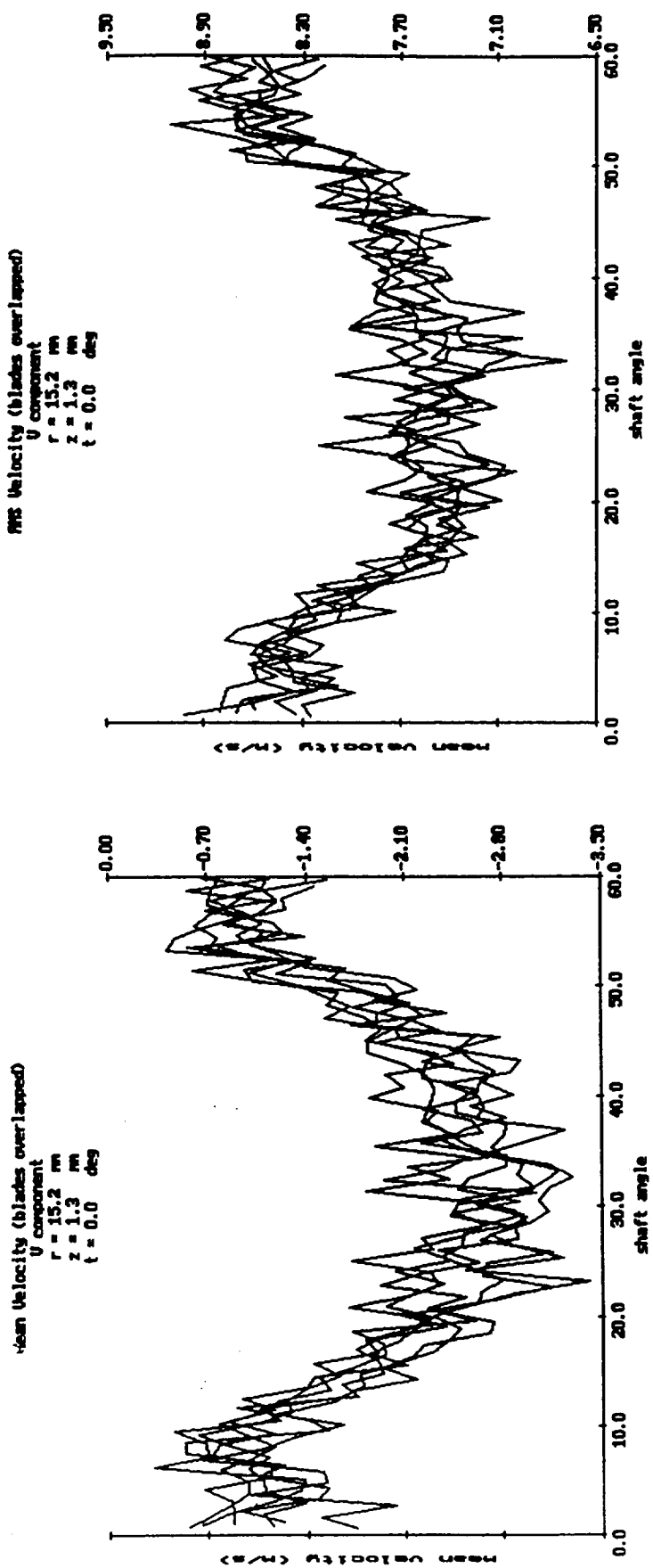


FIG. 15. Continued.

OPTIONAL PAGE IS  
OF POOR QUALITY

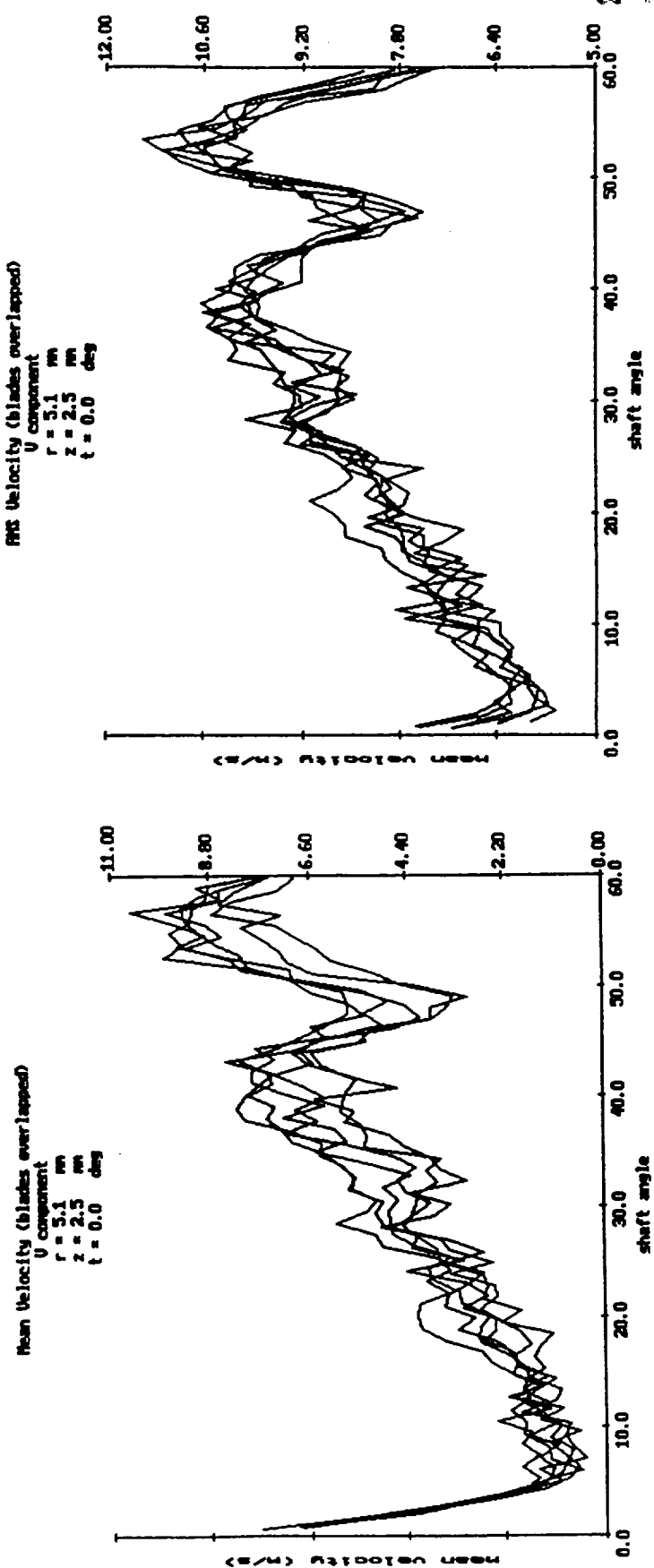


Fig. 15. Continued.

ORIGINAL PAGE IS  
OF POOR QUALITY

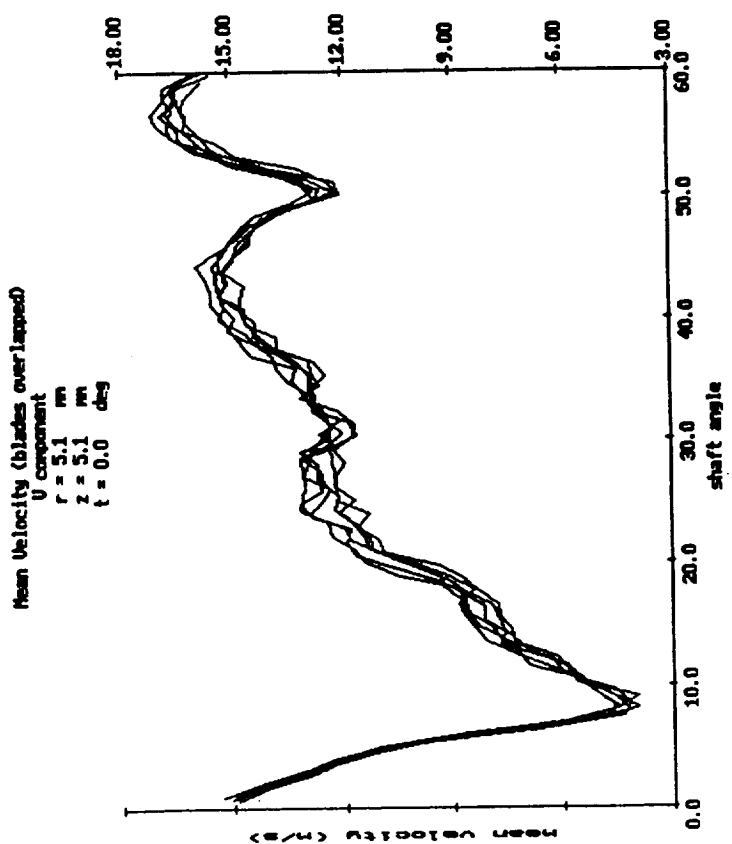
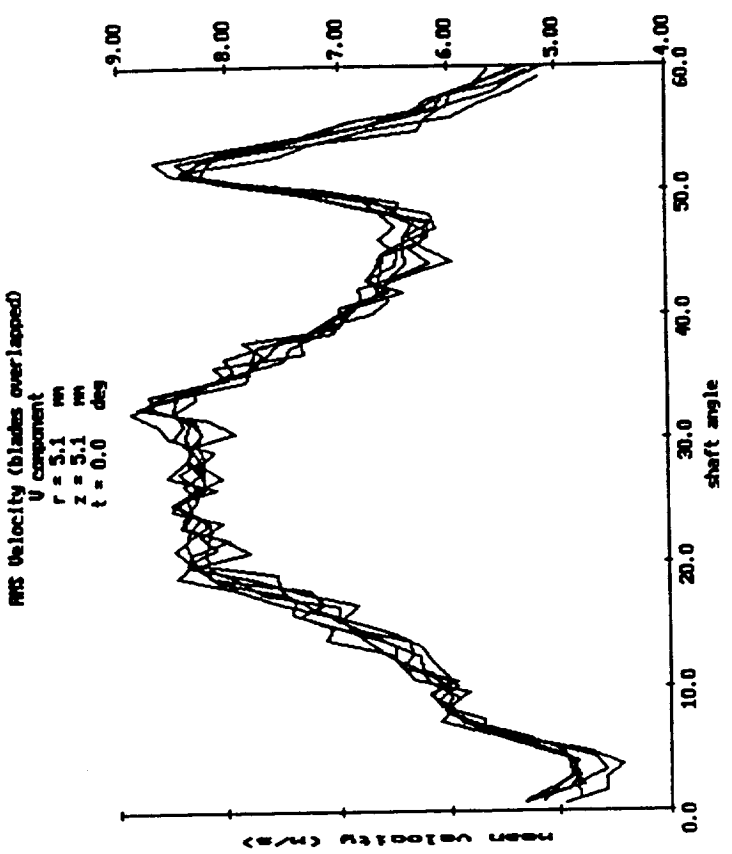


Fig. 15. Continued.

THIS PAGE IS  
OF POOR QUALITY

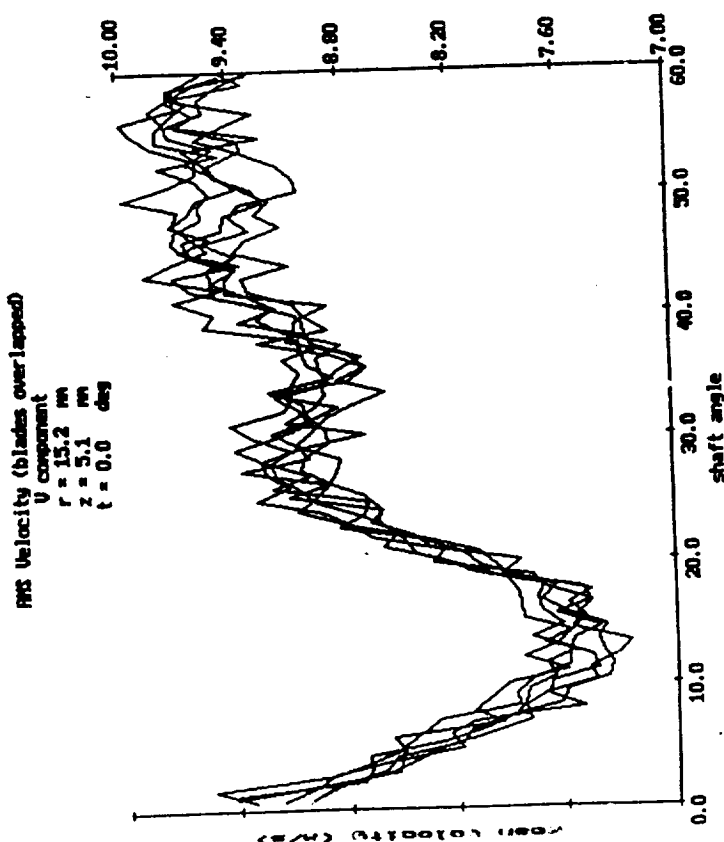
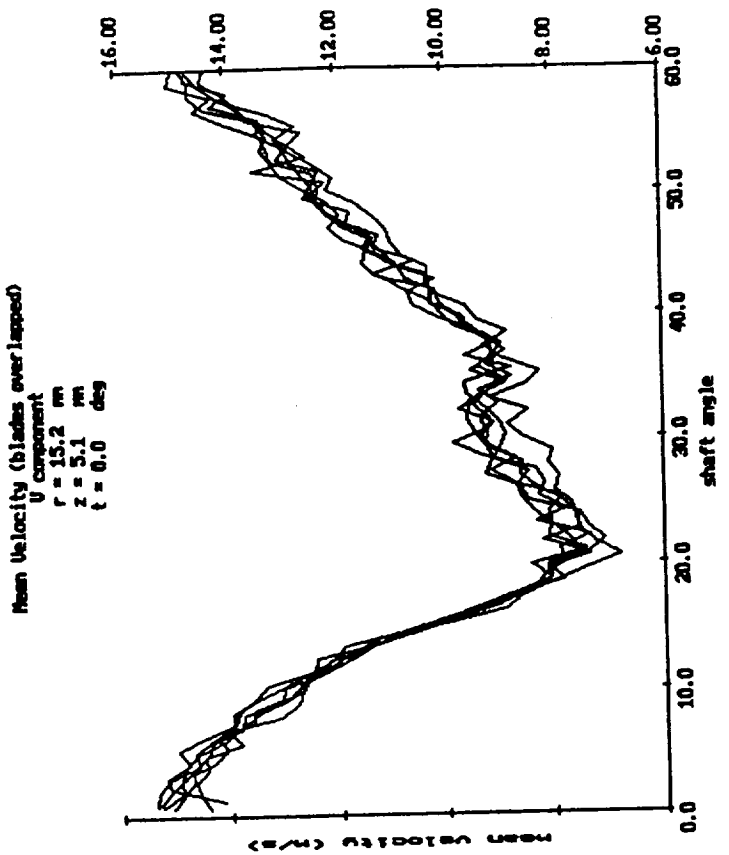


Fig. 15. Continued.

ORIGINAL PAGE IS  
OF POOR QUALITY

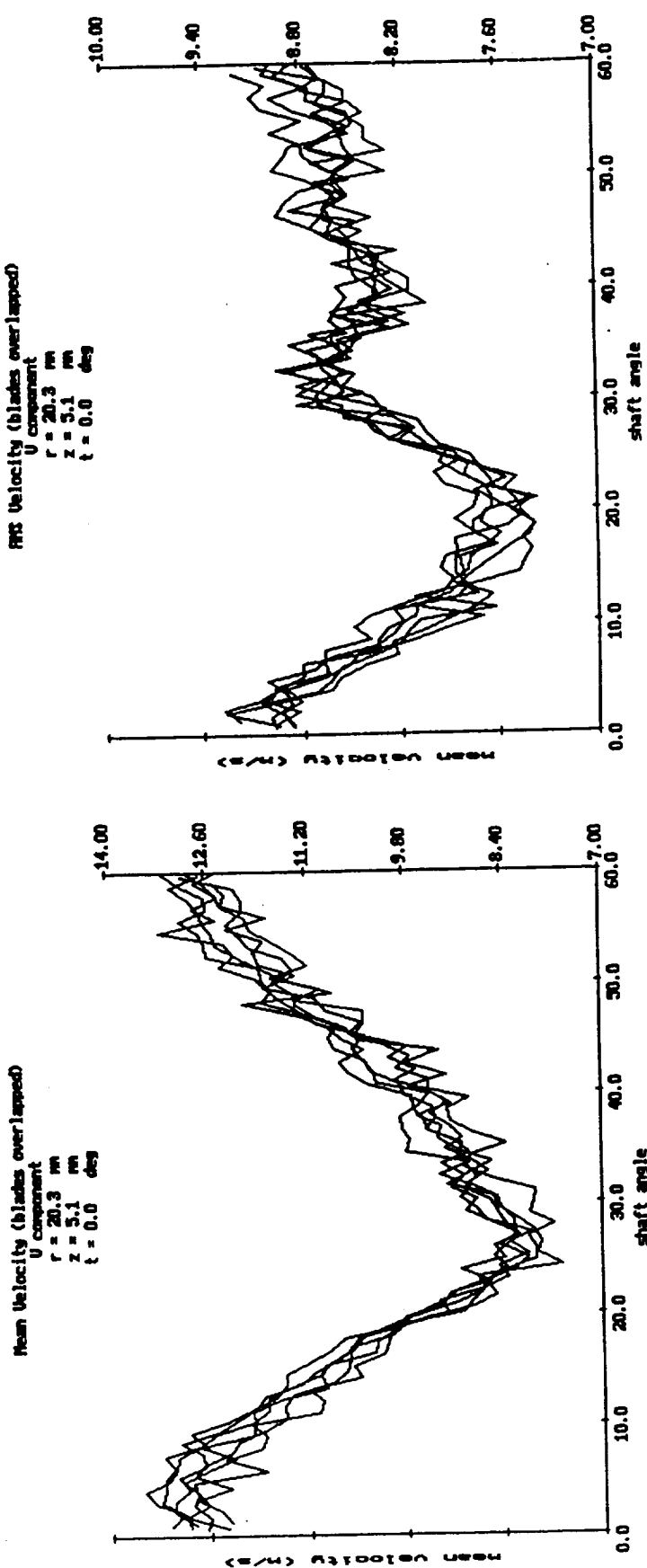


Fig. 15. Continued.

ORIGINAL PAGE IS  
OF POOR QUALITY

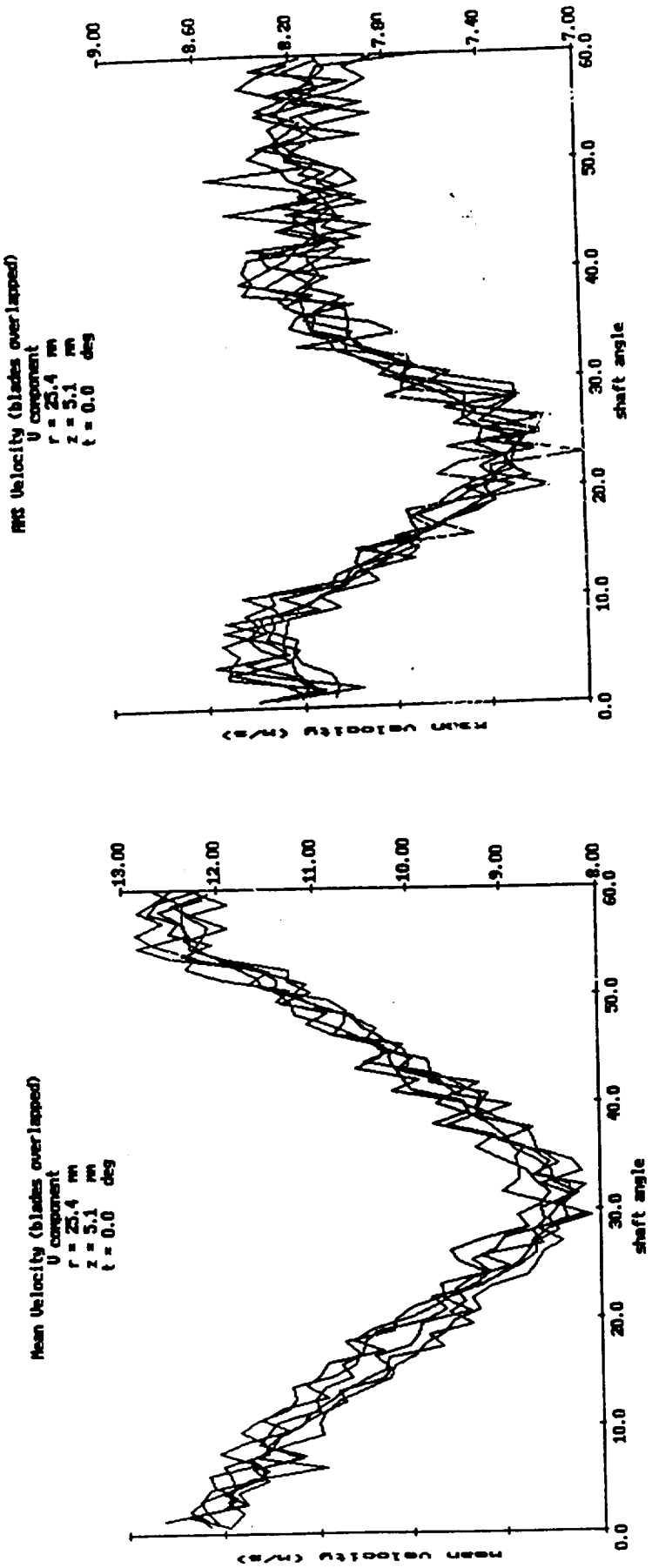


Fig. 15. Continued.

ORIGINAL PAGE IS  
OF POOR QUALITY

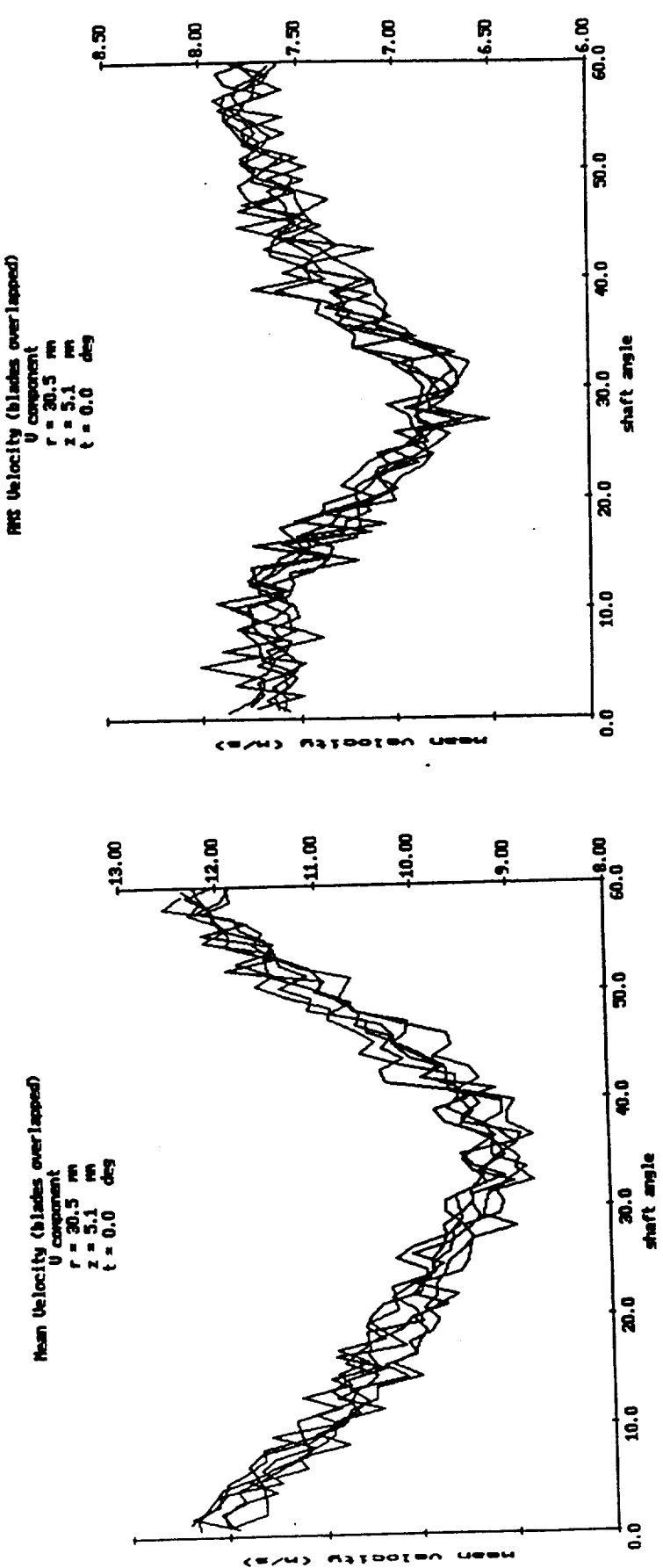


Fig. 15. Continued.

ORIGINAL PAGE IS  
OF POOR QUALITY

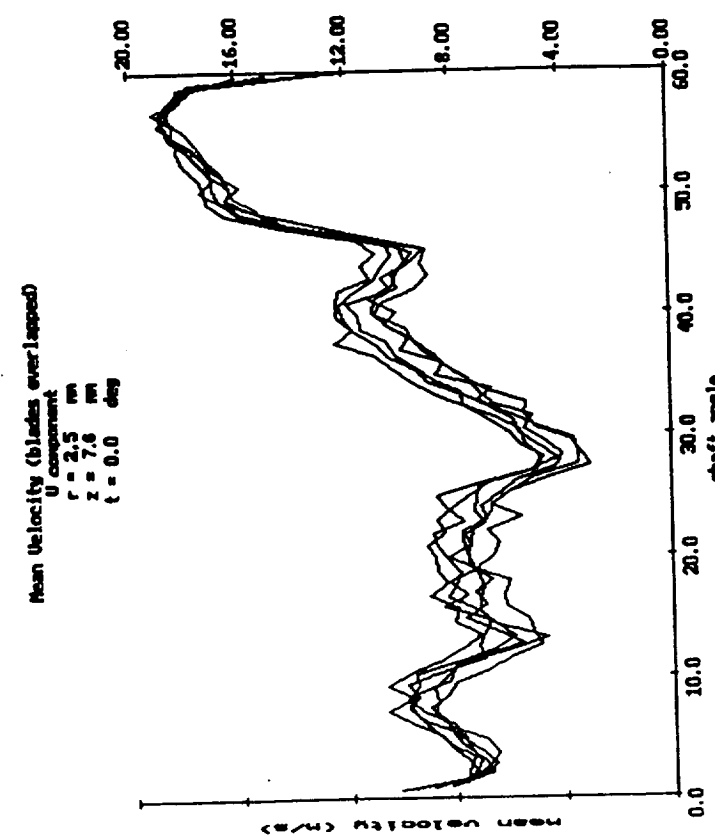
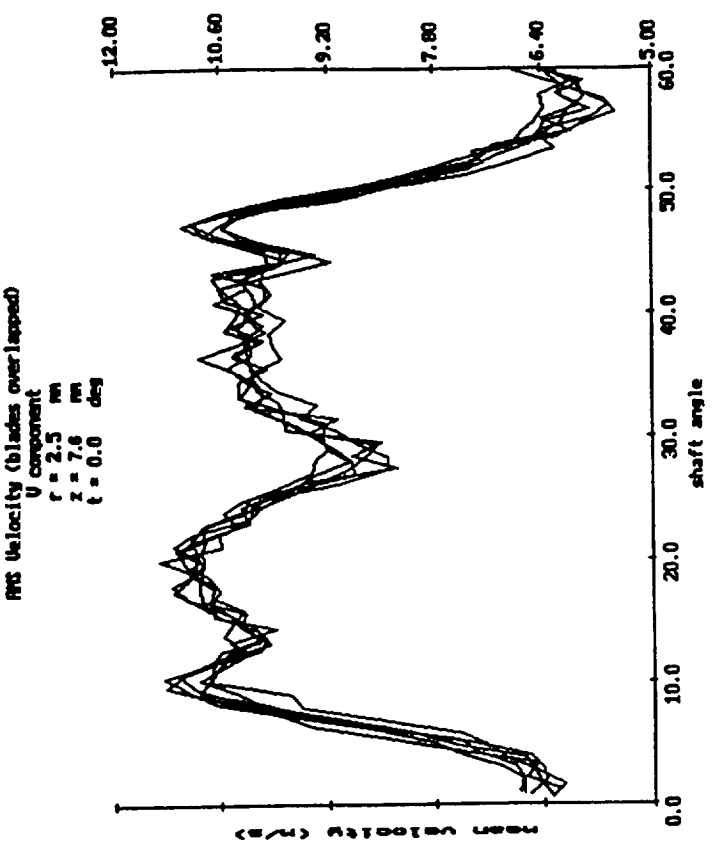


Fig. 15. Continued.

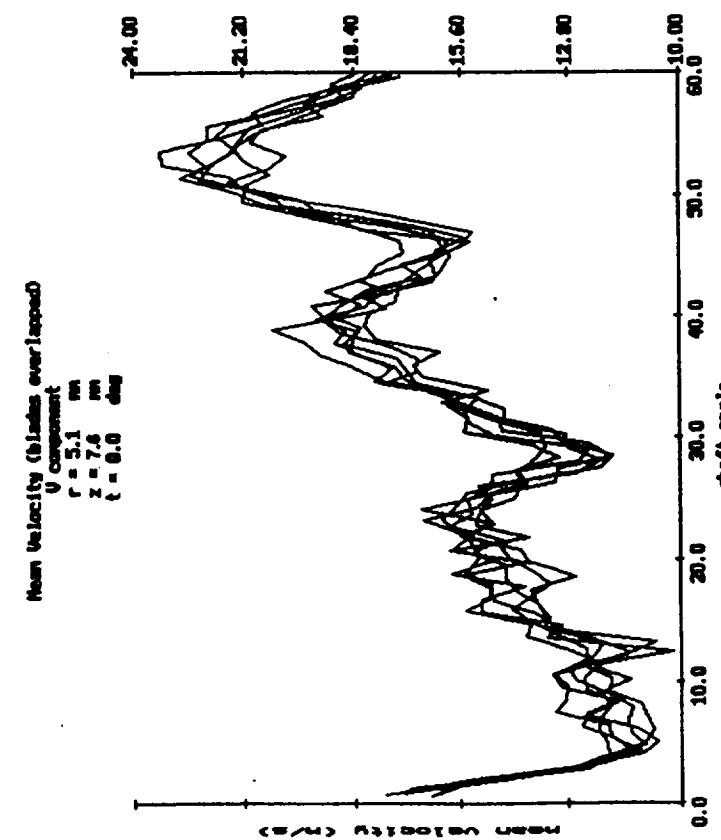
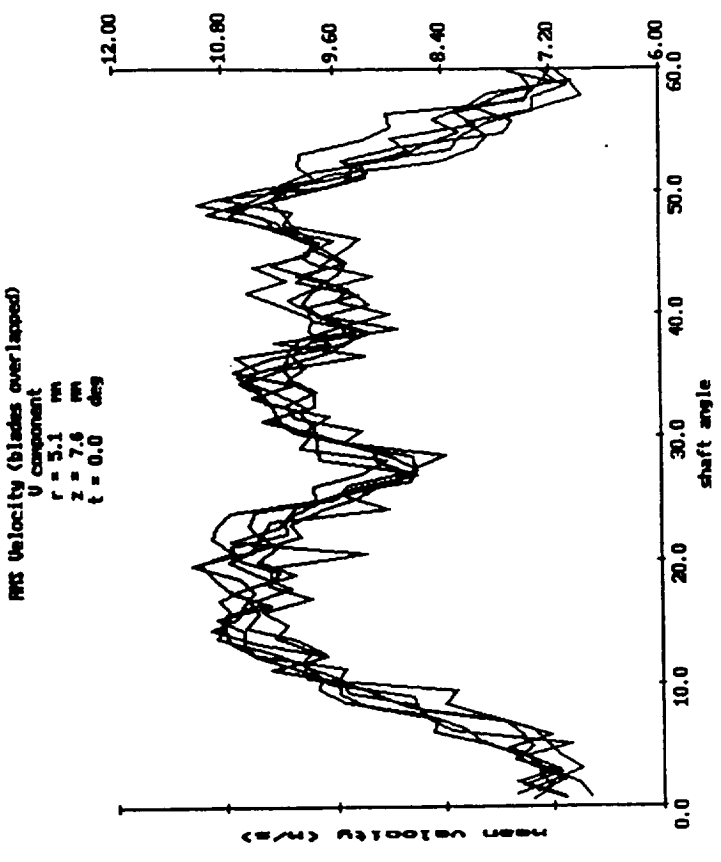


Fig. 15. Continued.

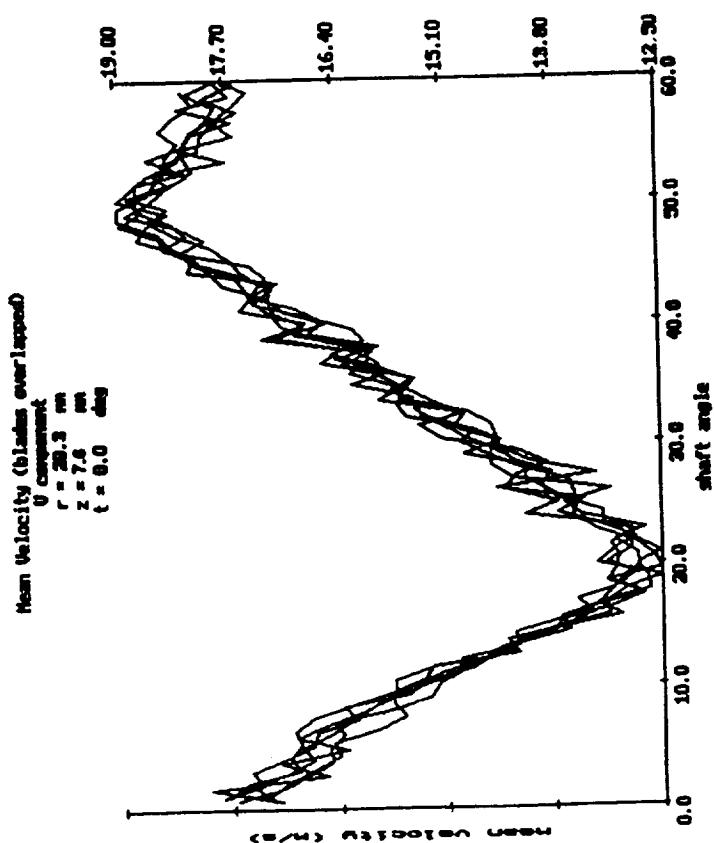
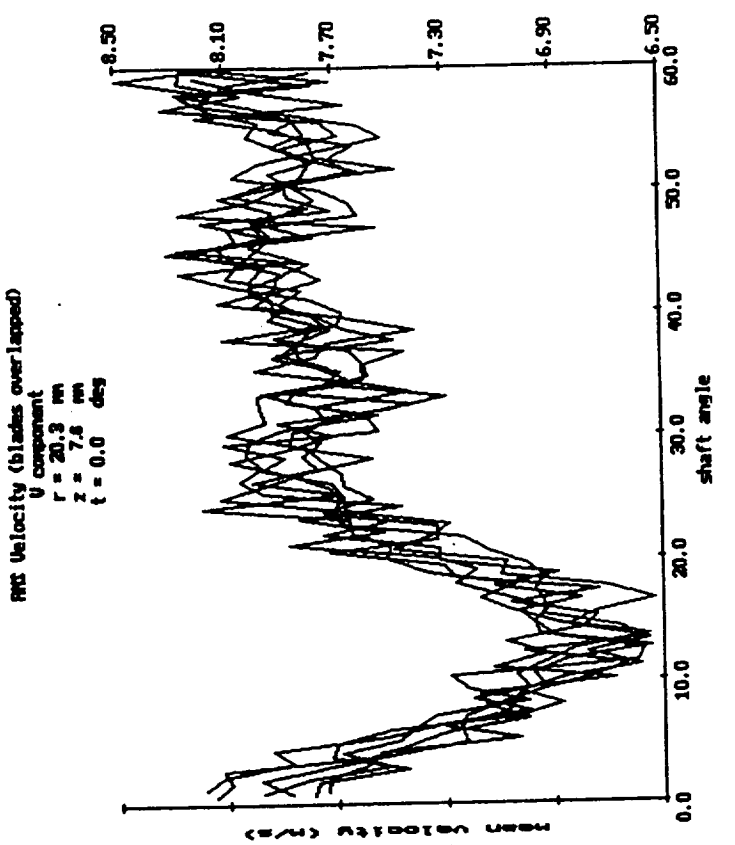


Fig. 15. Continued.

ORIGINAL PAGE IS  
OF POOR QUALITY

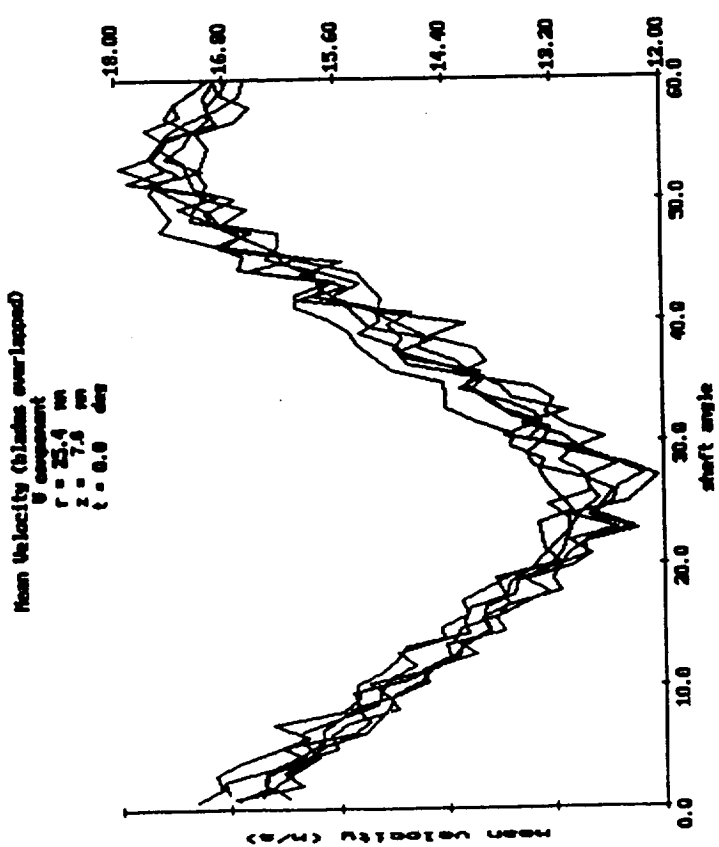
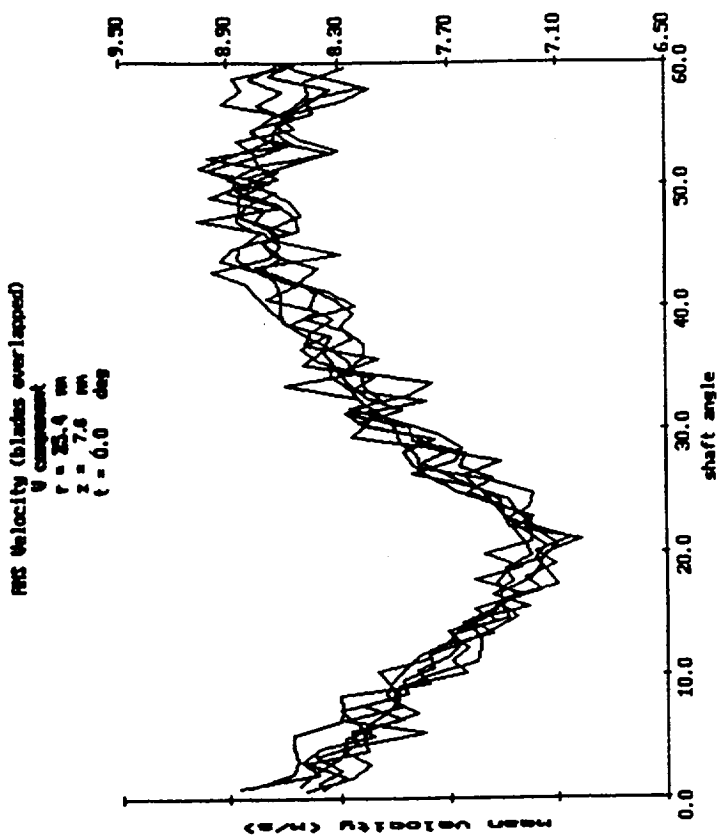


Fig. 15. Continued.

ORIGINAL PAGE IS  
OF POOR QUALITY

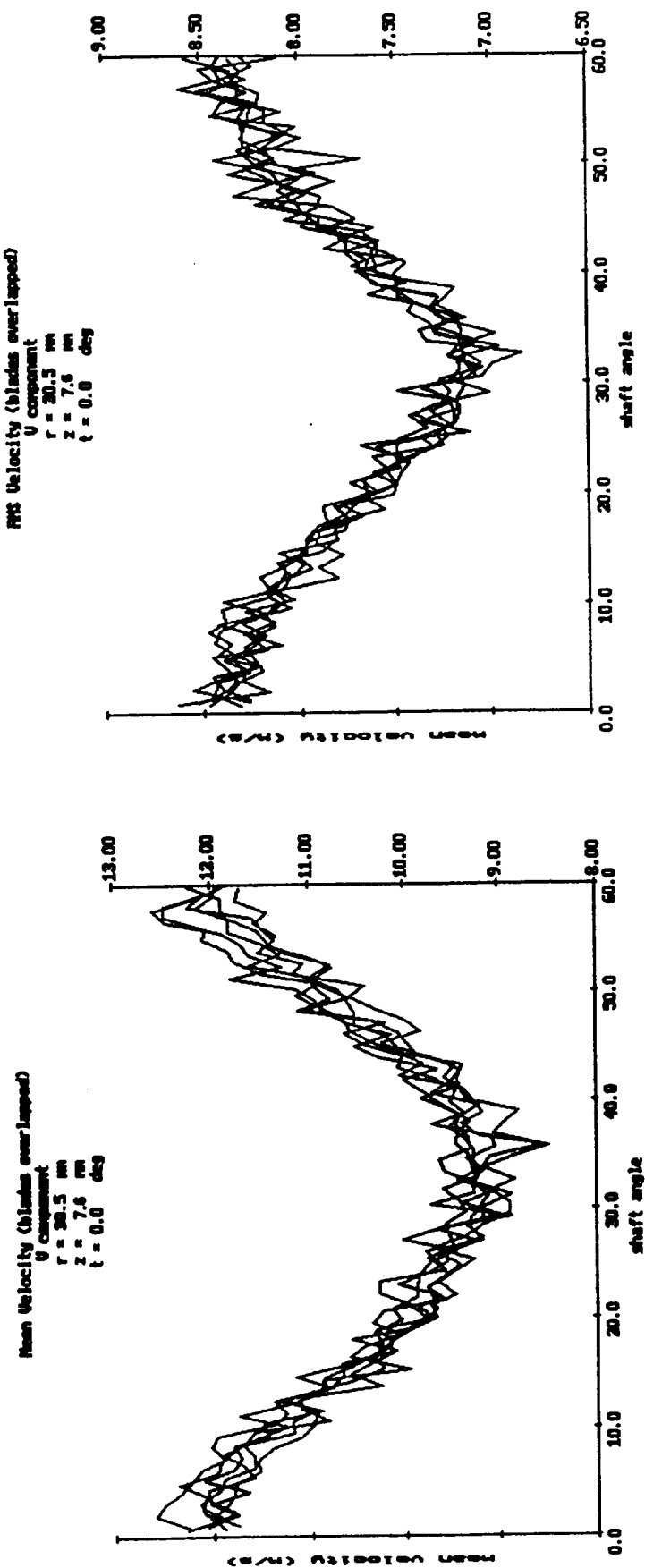


Fig. 15. Continued.

ORIGINAL PAGE IS  
OF POOR QUALITY

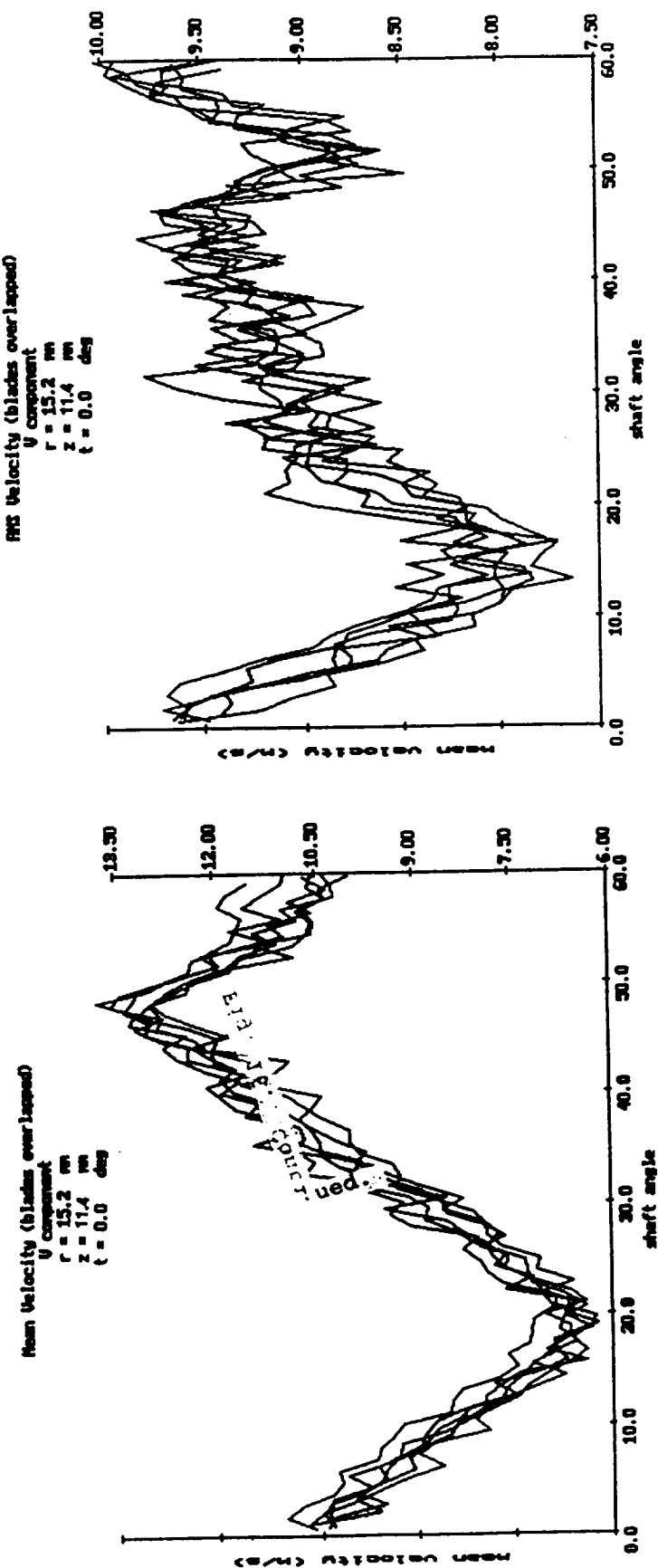


Fig. 15. Continued.

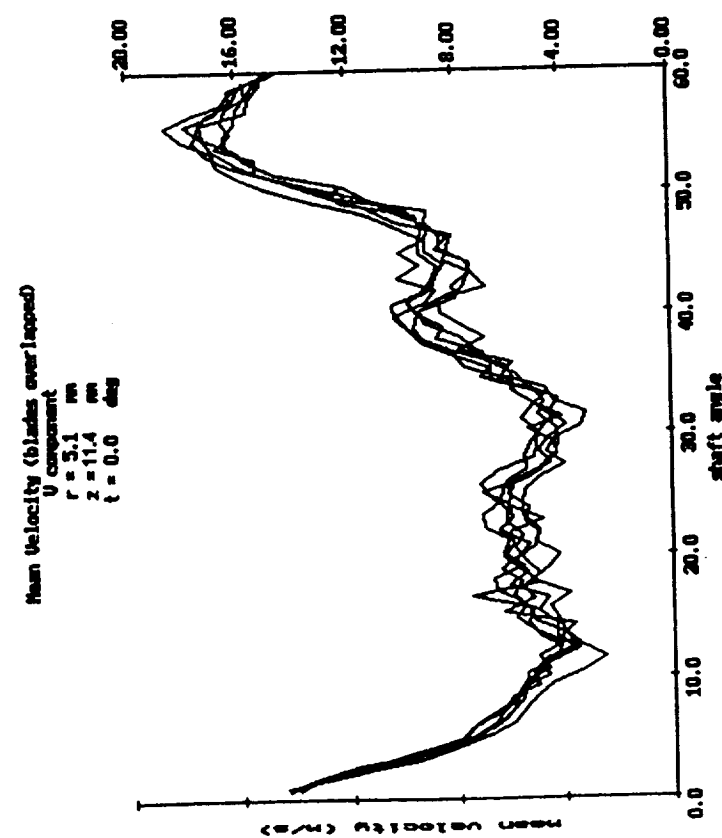
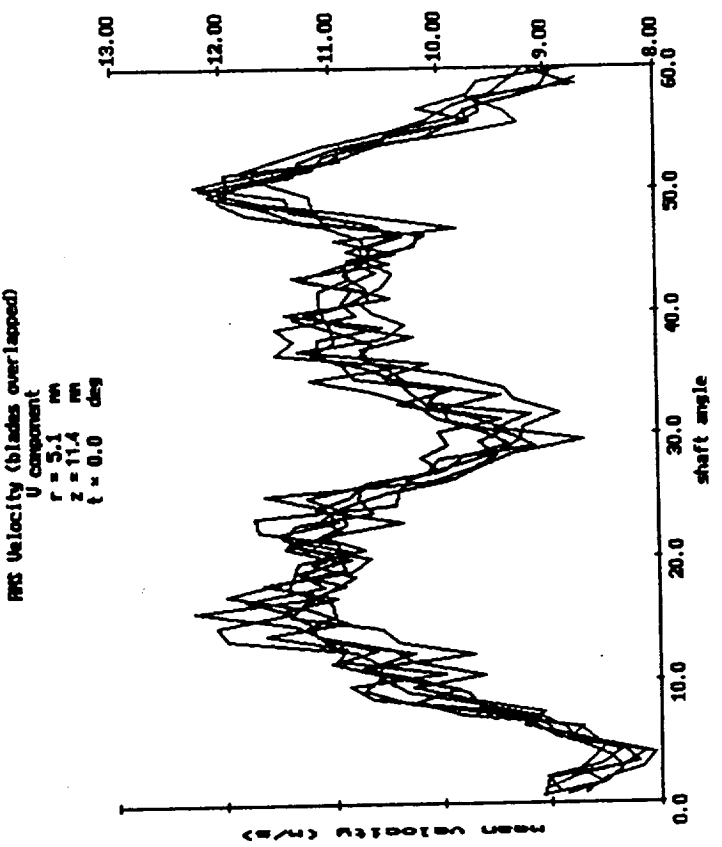


Fig. 15. Continued.

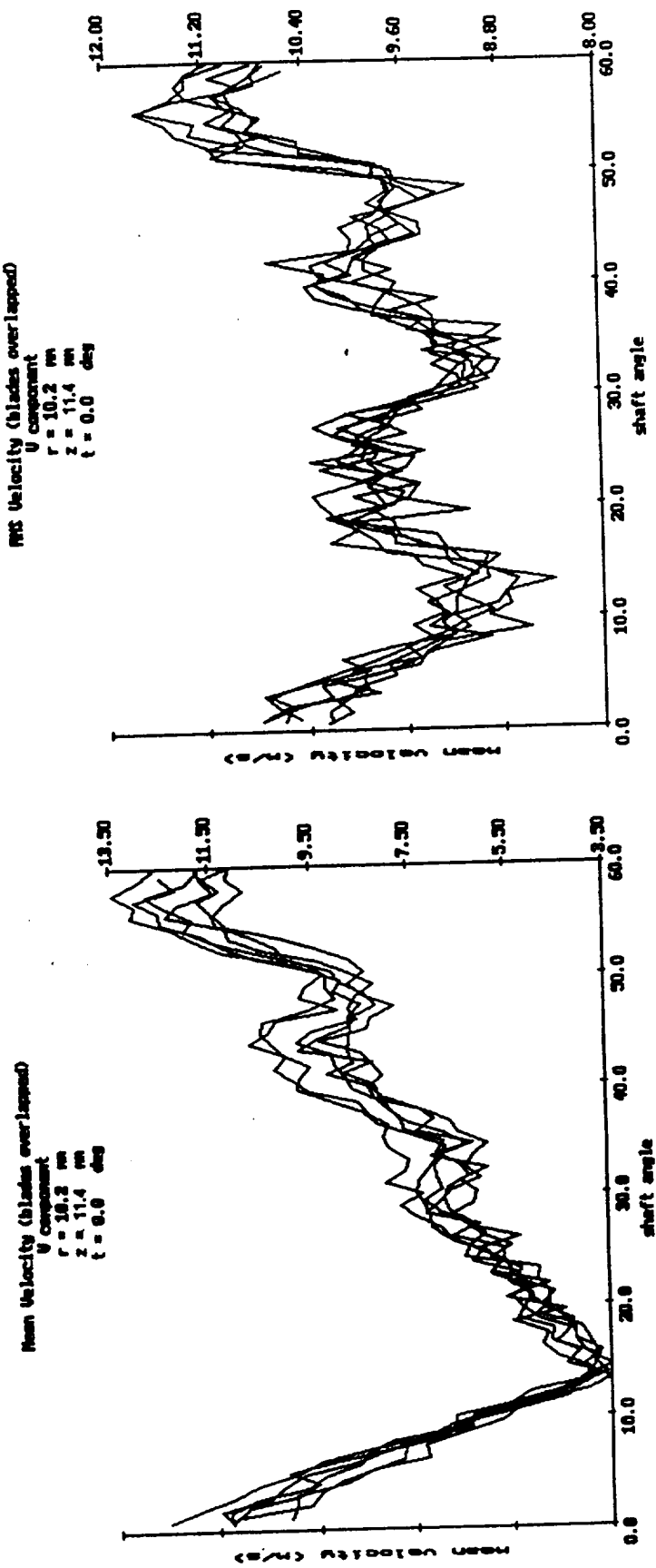


Fig. 15. Continued.

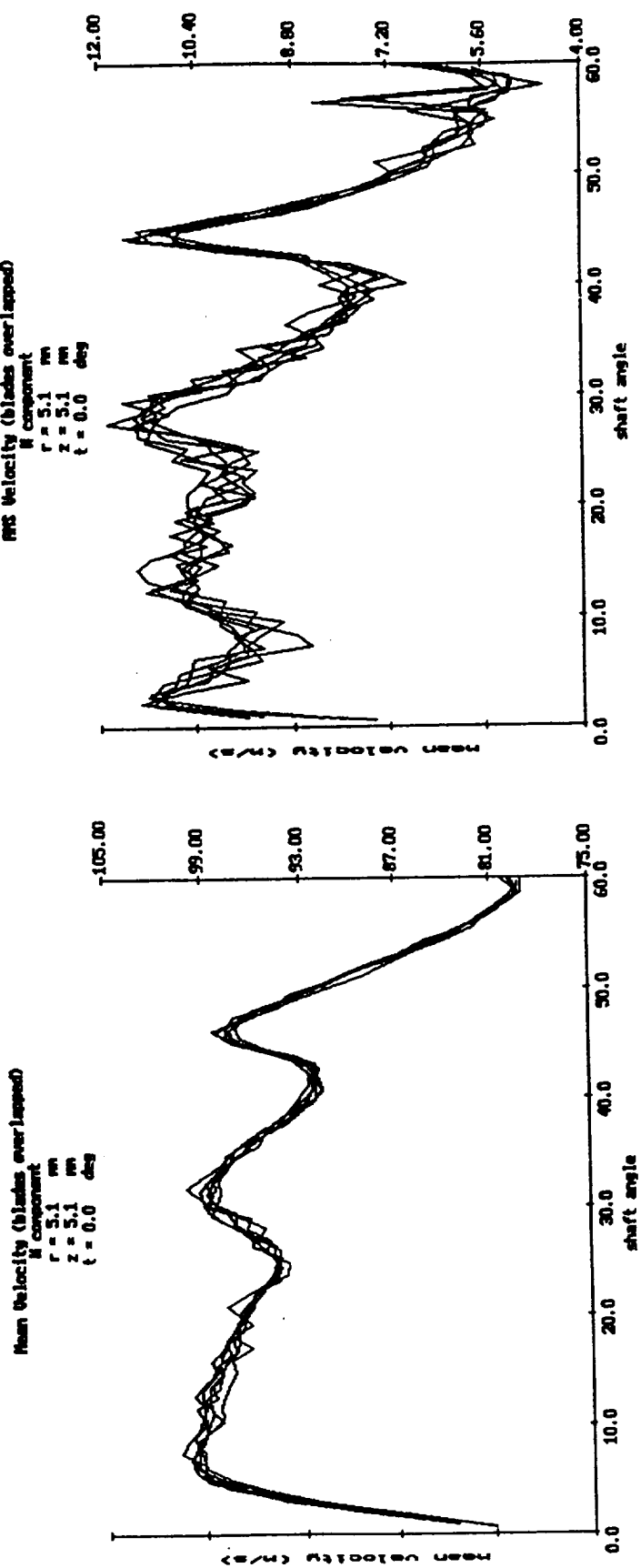


Fig. 16. Ensemble-averaged Tangential Velocities in the Diffuser.

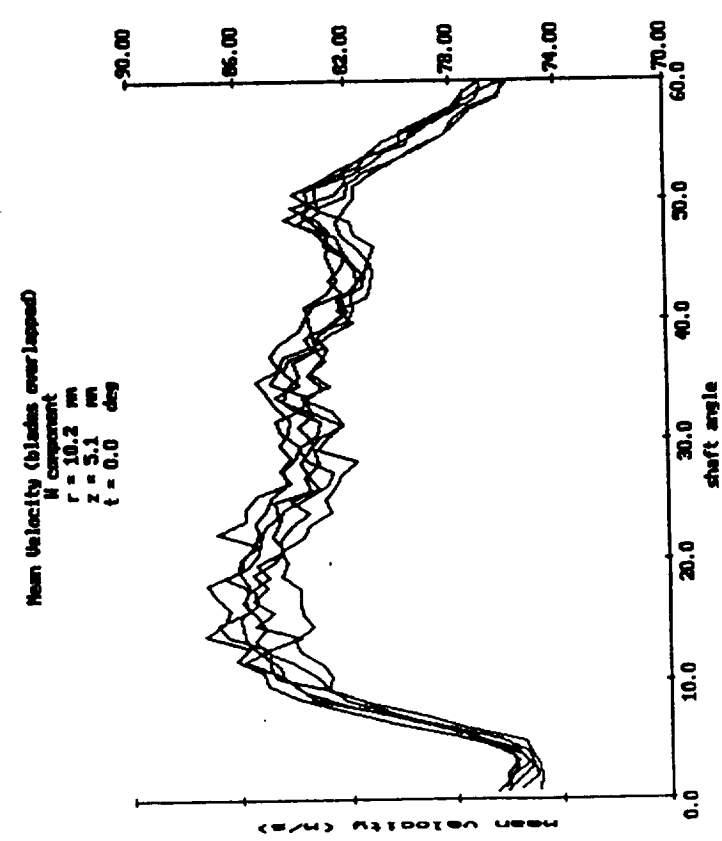
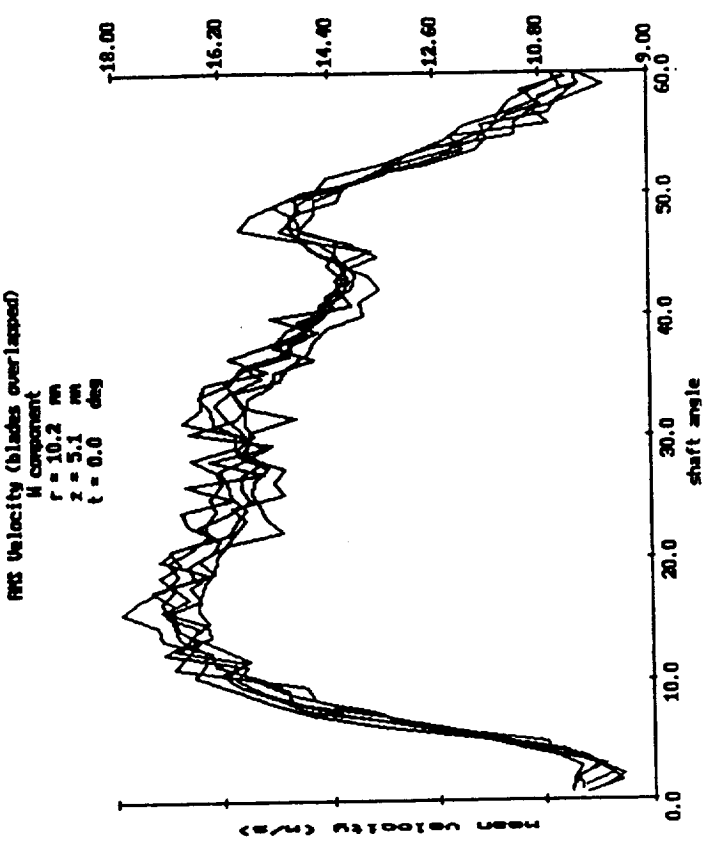


Fig. 16. Continued.

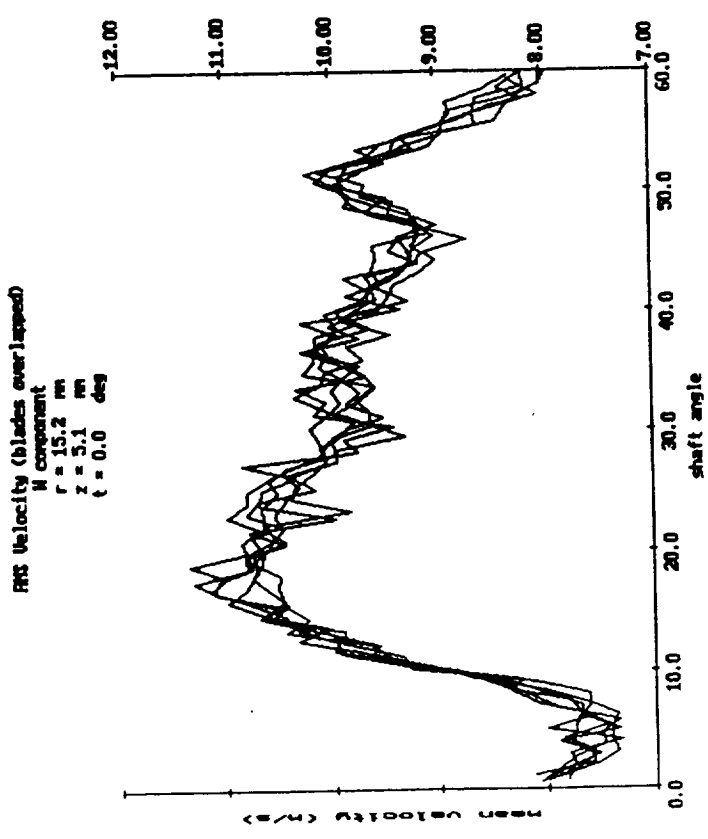
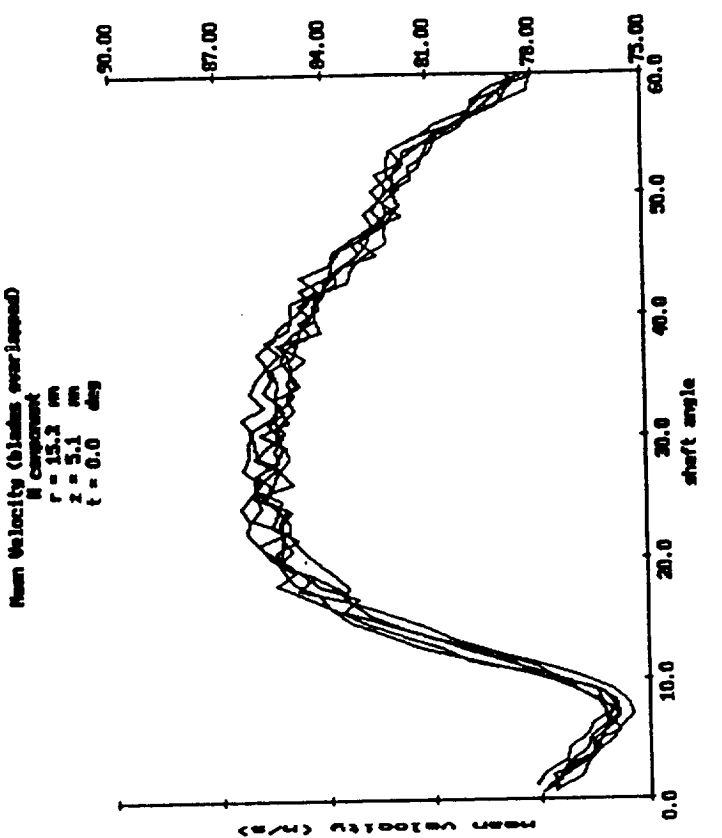


Fig. 16. Continued.

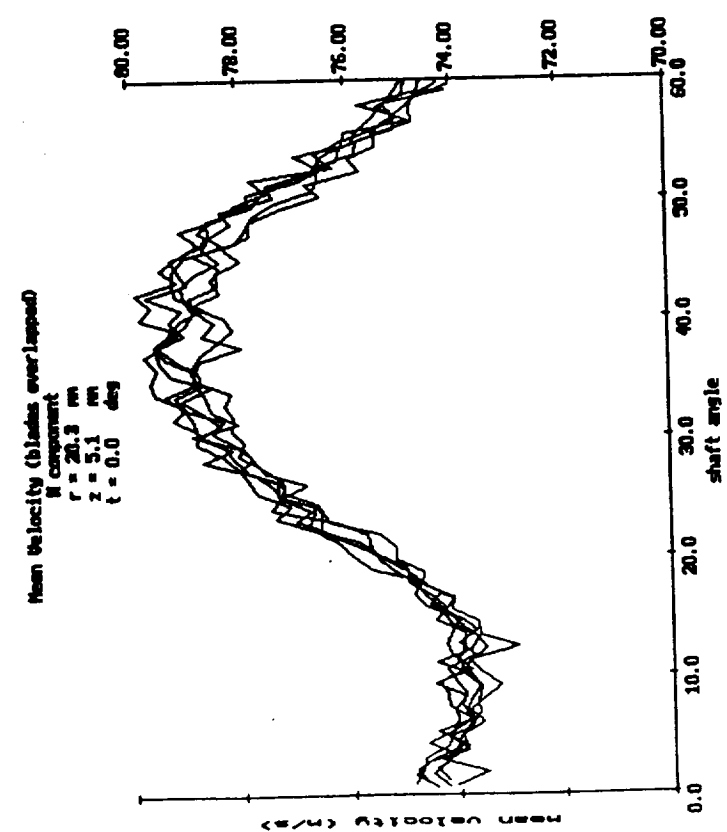
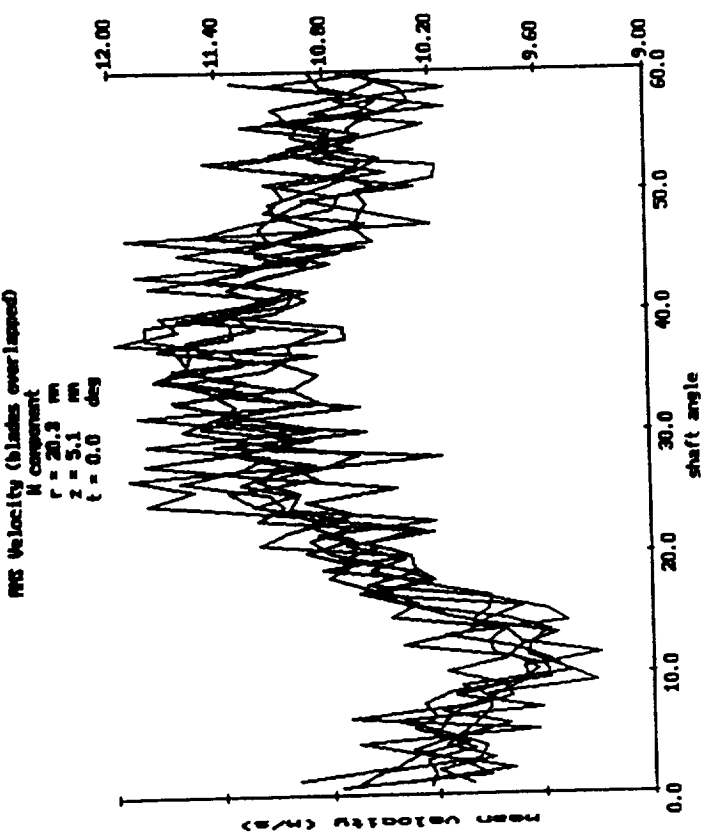


Fig. 16. Continued.

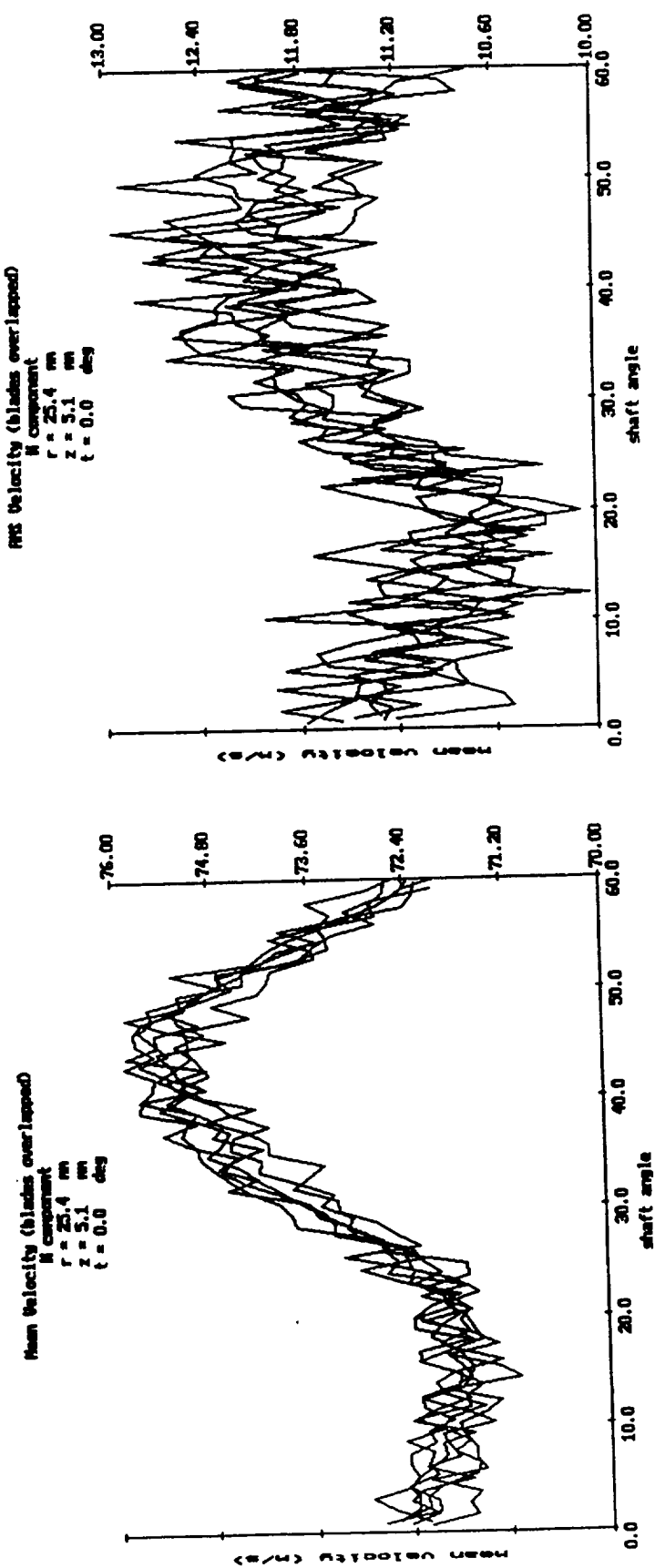


Fig. 16. Continued.

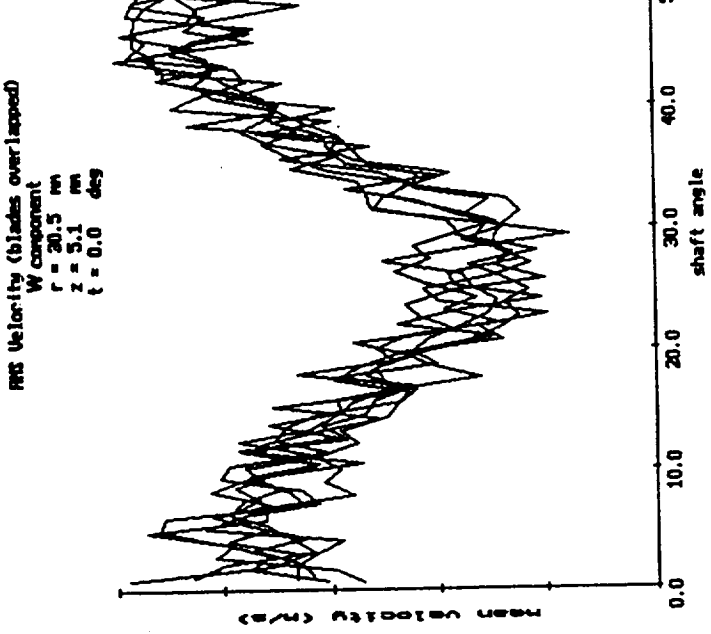
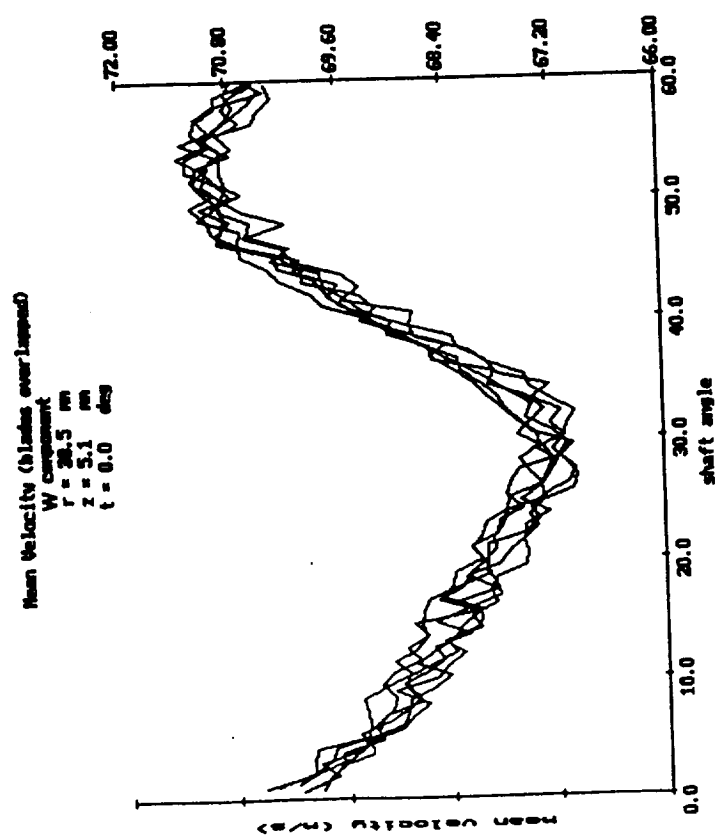


Fig. 16. Continued.

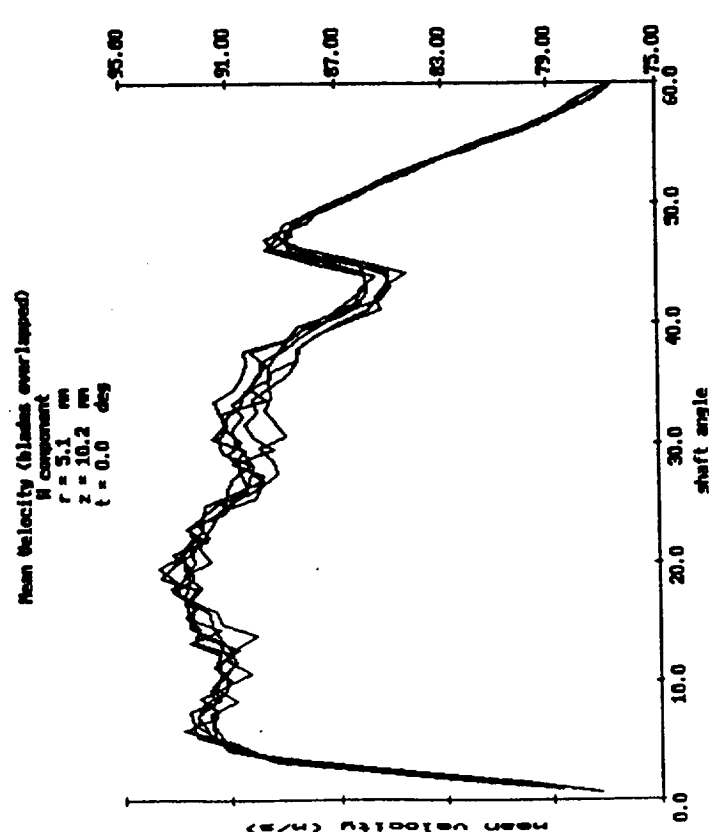
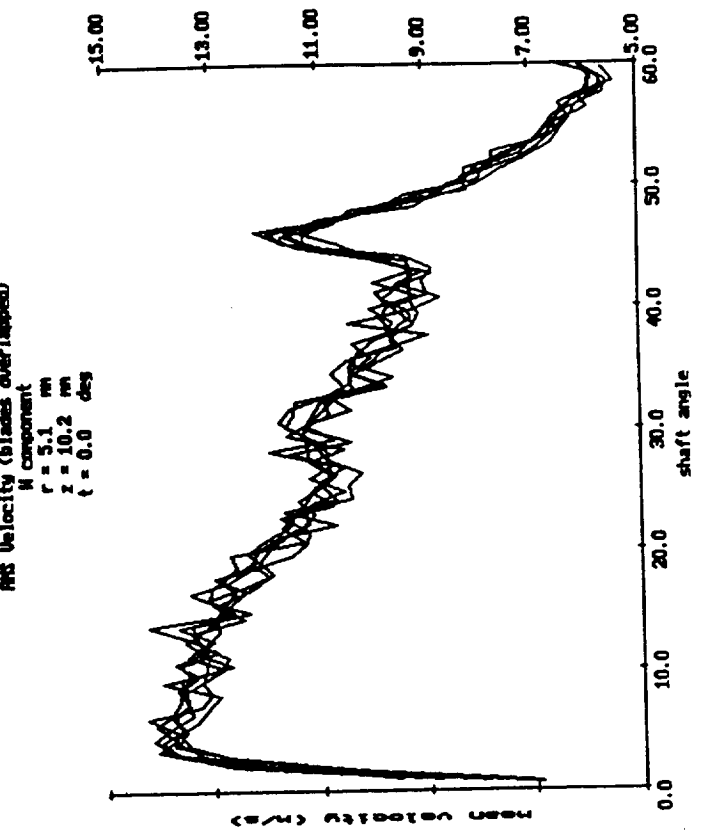


Fig. 16. Continued.

ORIGINAL PAGE IS  
OF POOR QUALITY

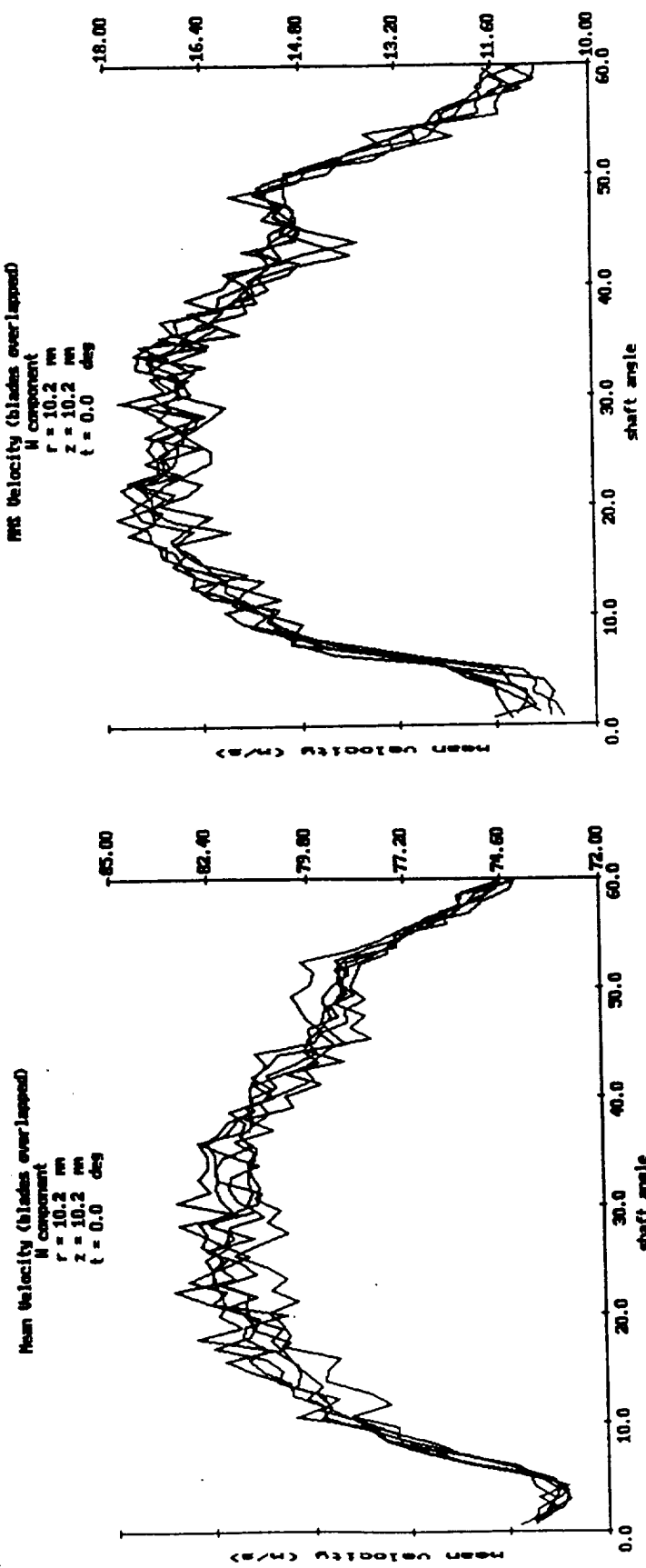


Fig. 16. Continued.

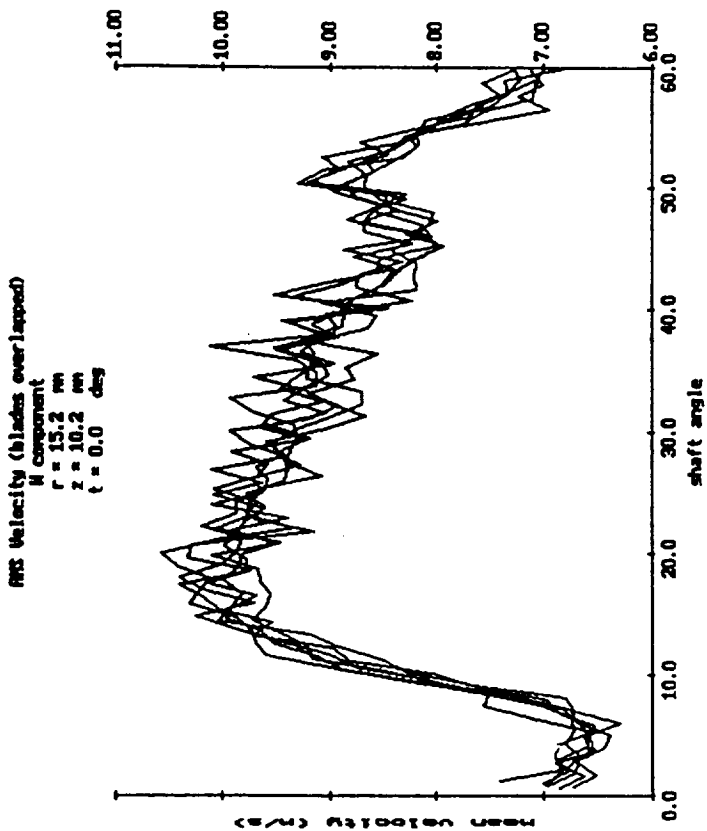
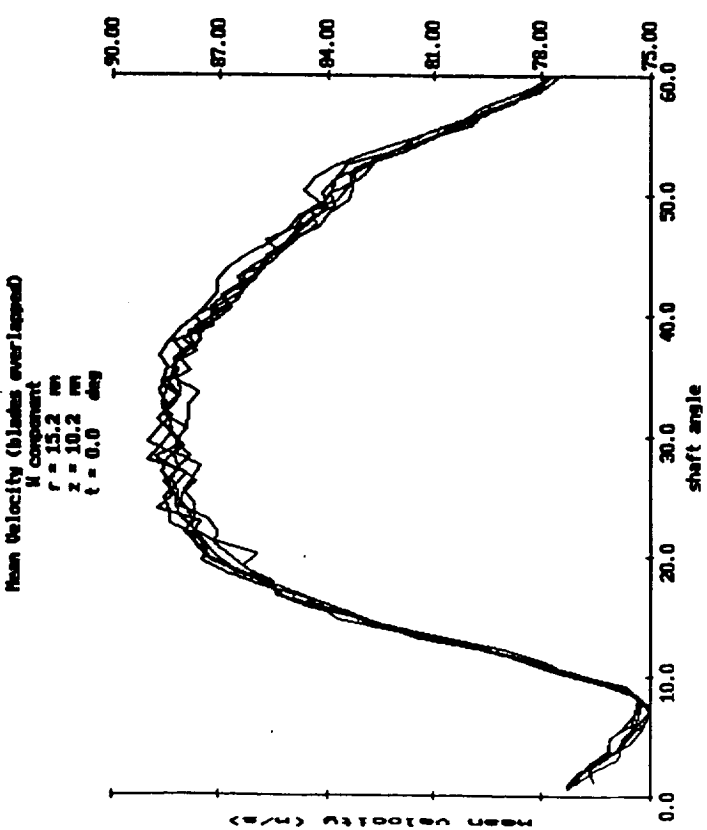


Fig. 16. Continued.

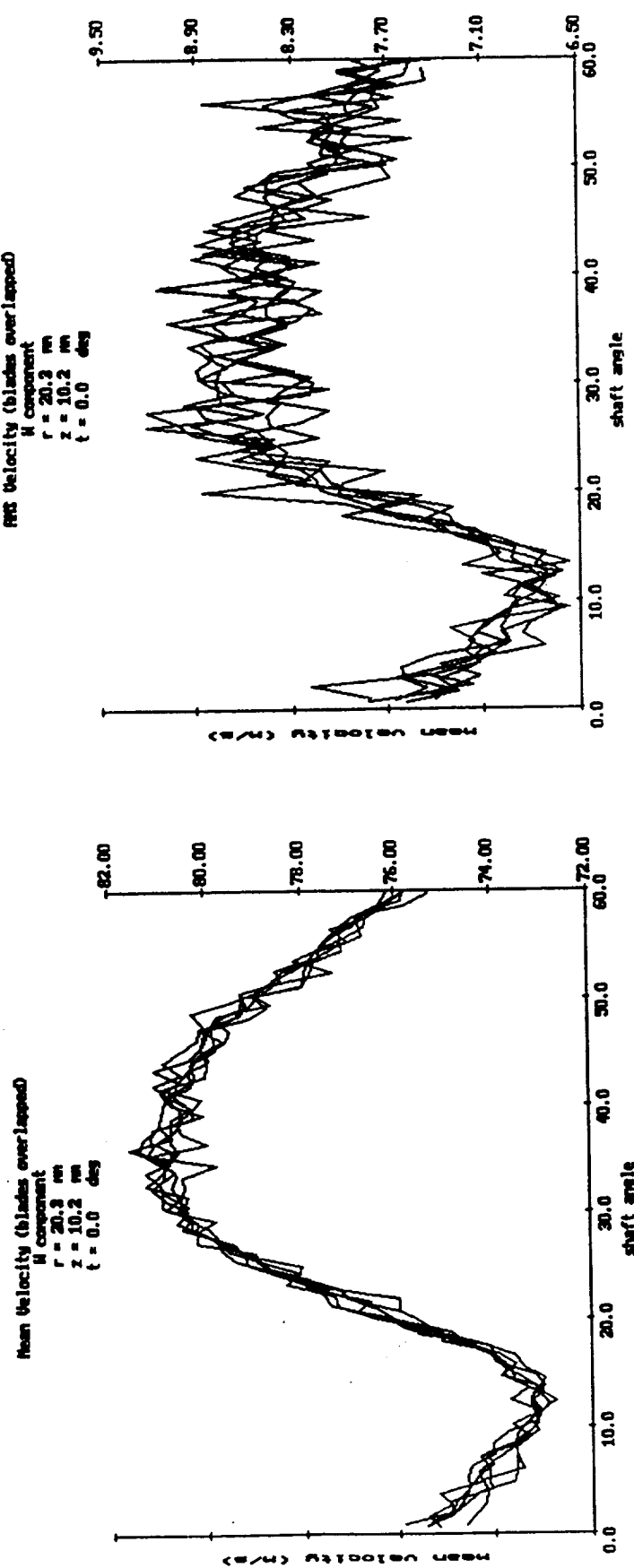


Fig. 16. Continued.

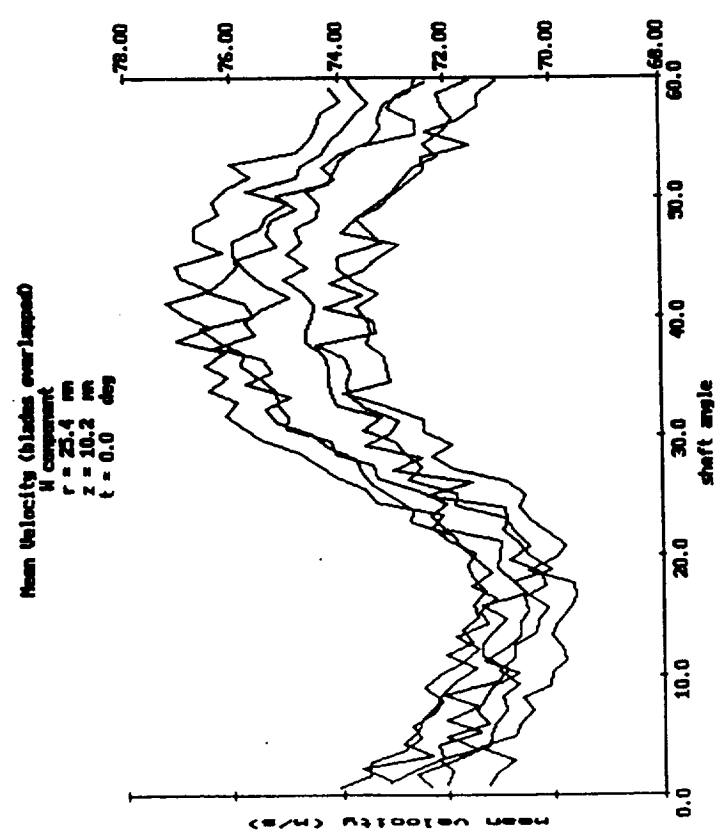
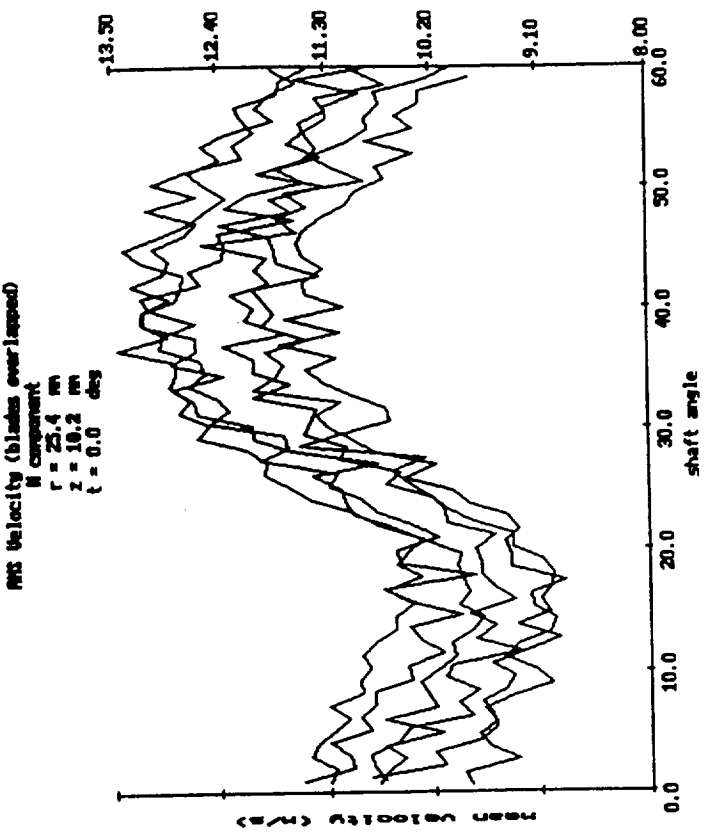


Fig. 16. Continued.

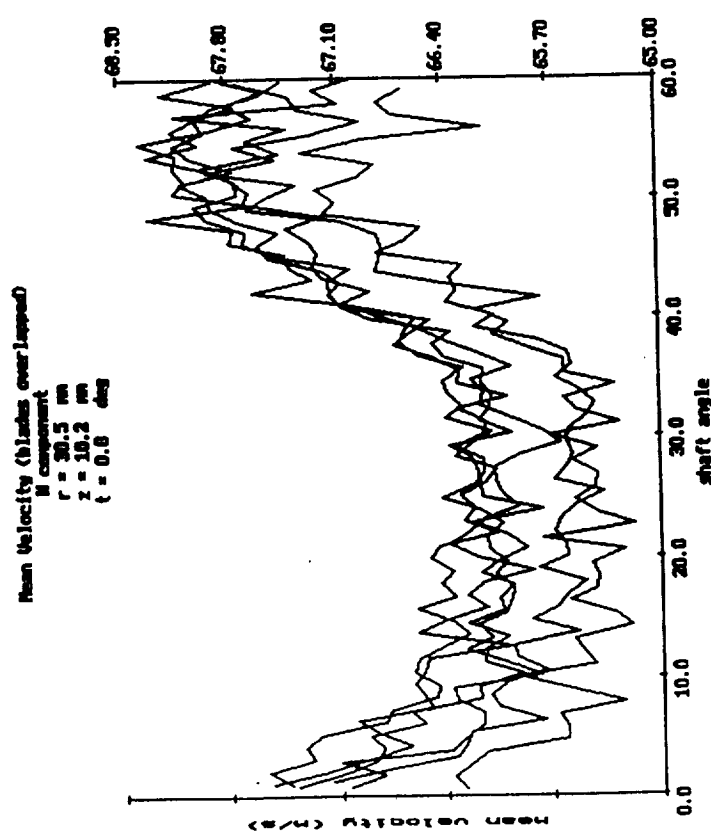
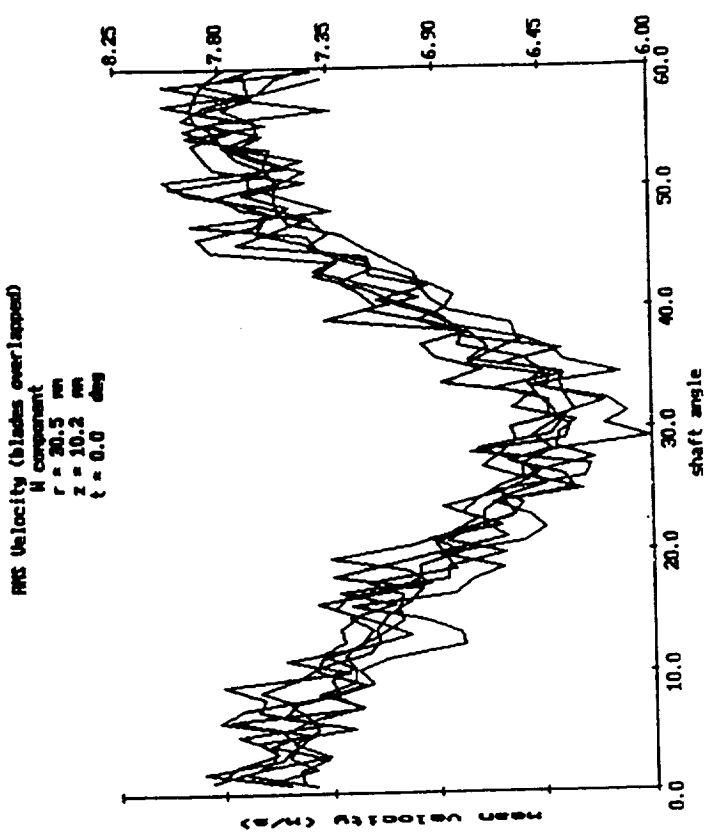


Fig. 16. Continued.

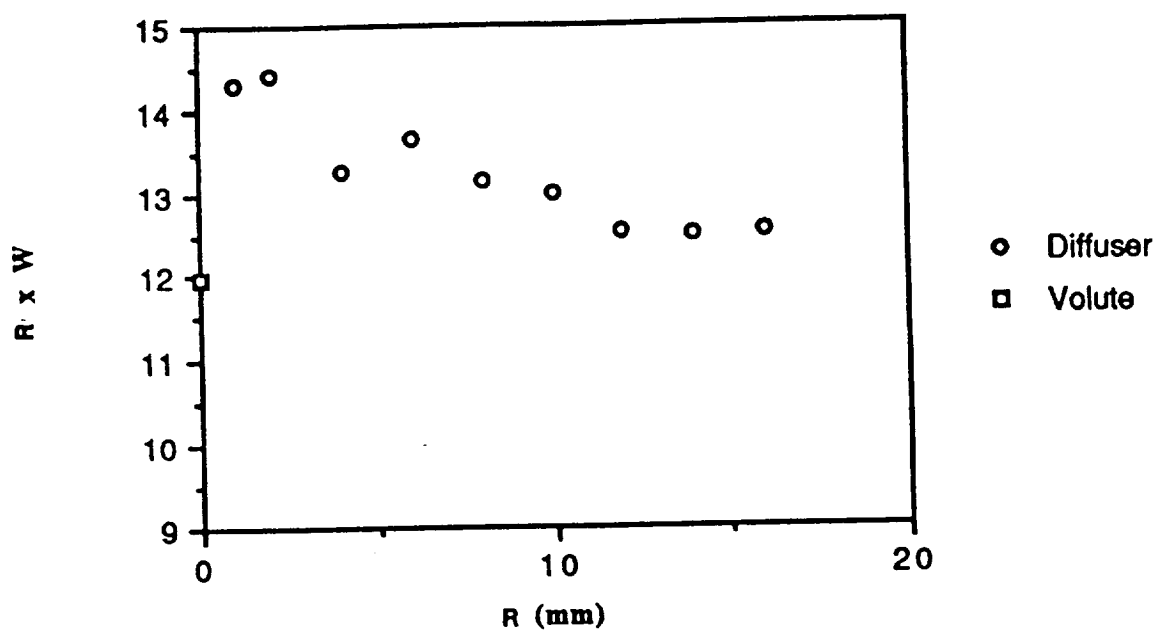


Fig. 17. A Plot of  $R$  times the Revolution-averaged Tangential Velocity versus  $R$ .

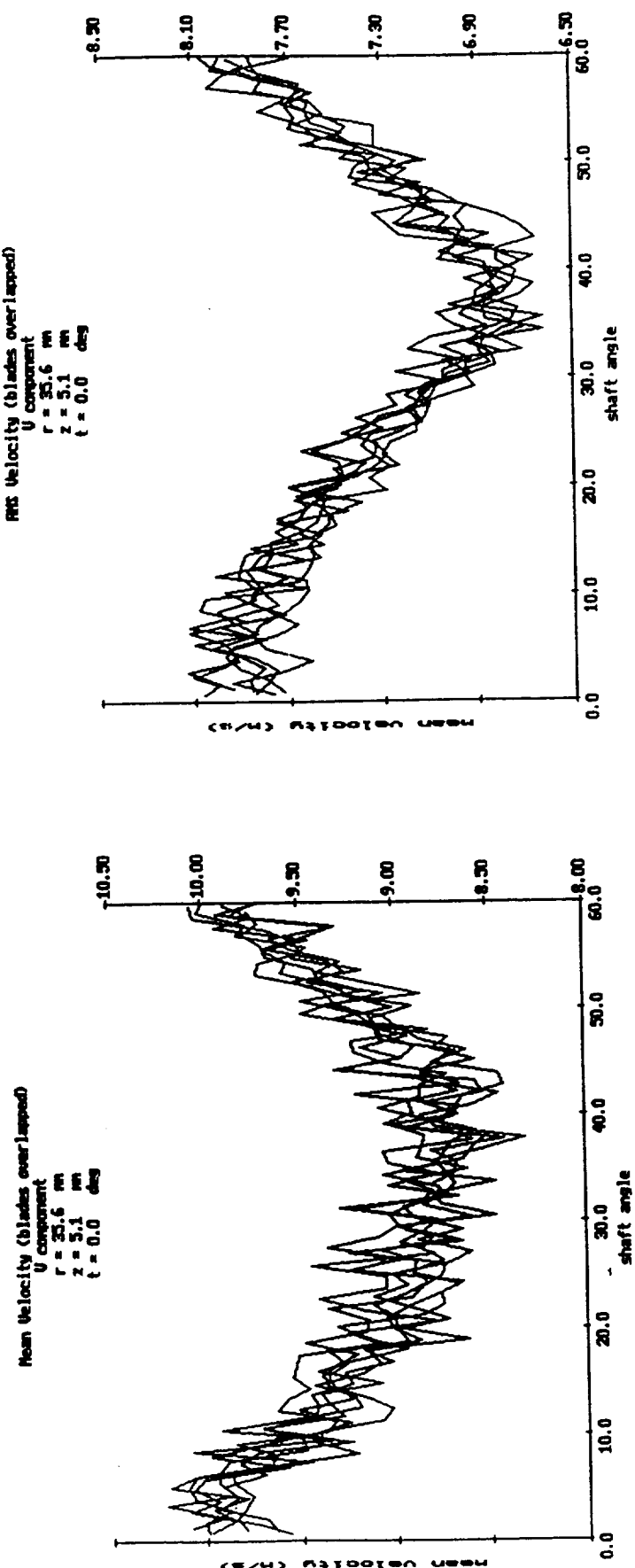


Fig. 18. Ensemble-averaged Radial velocities in the Turn-around Region.

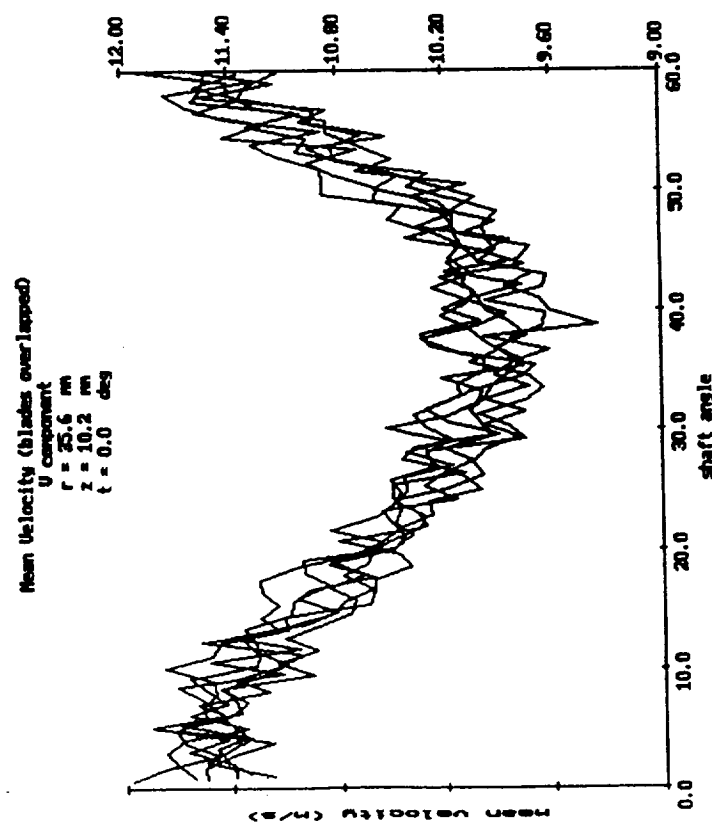
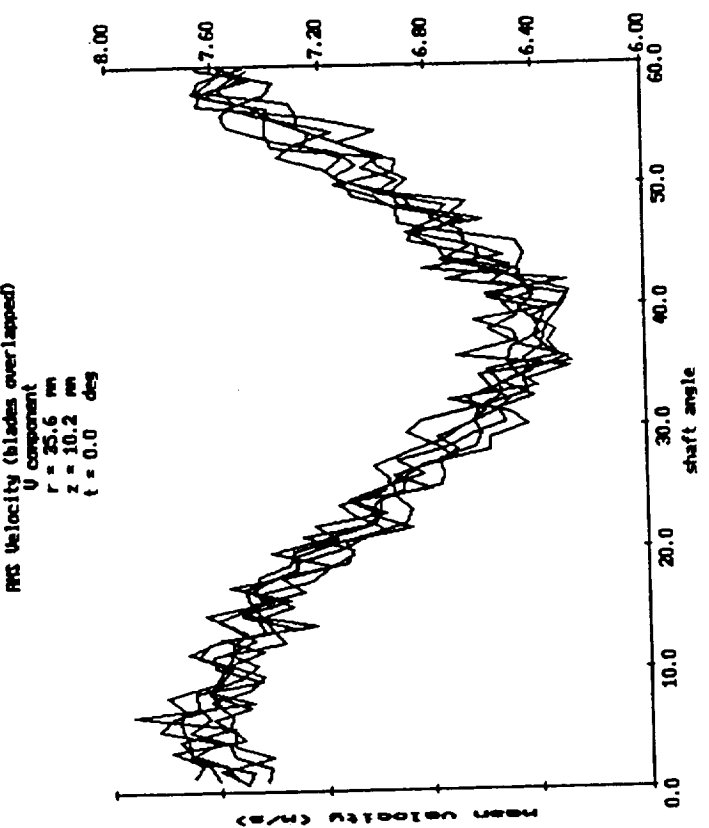


Fig. 18. Continued.

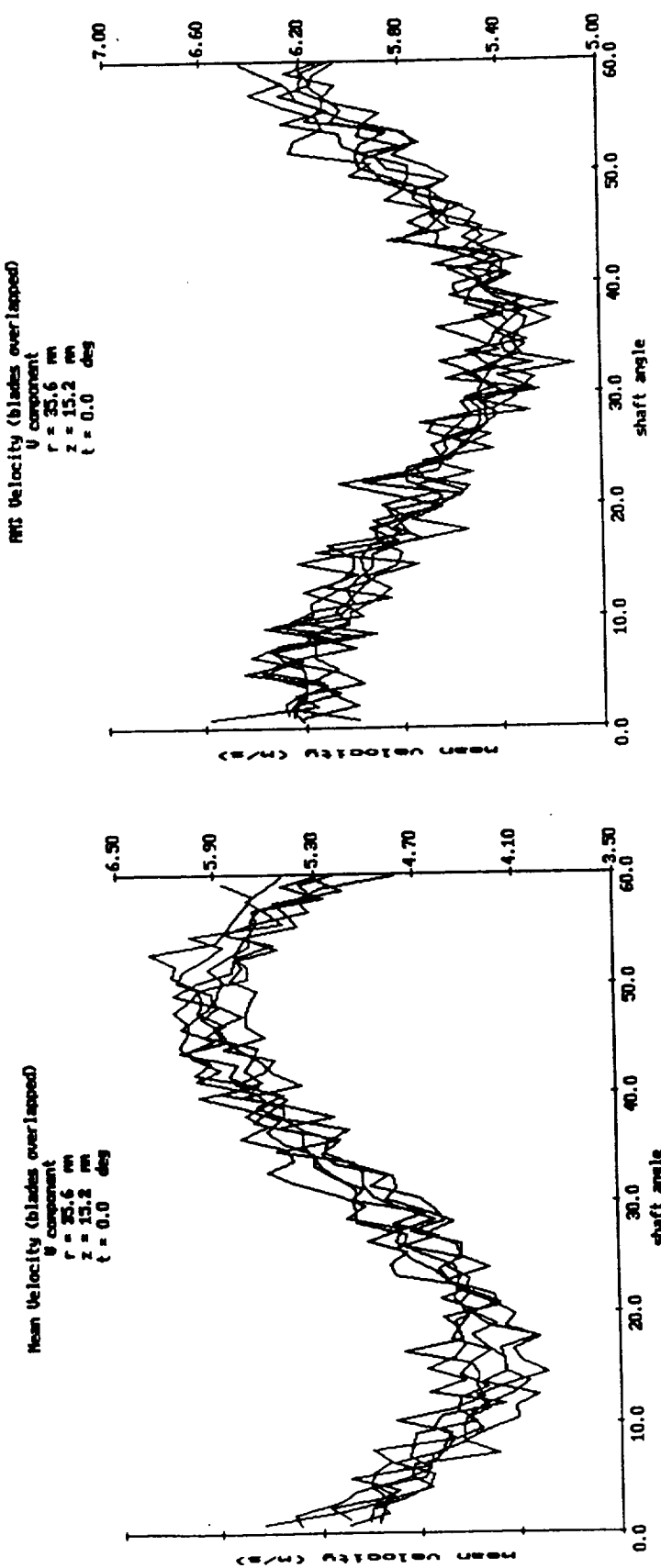


Fig. 18. Continued.

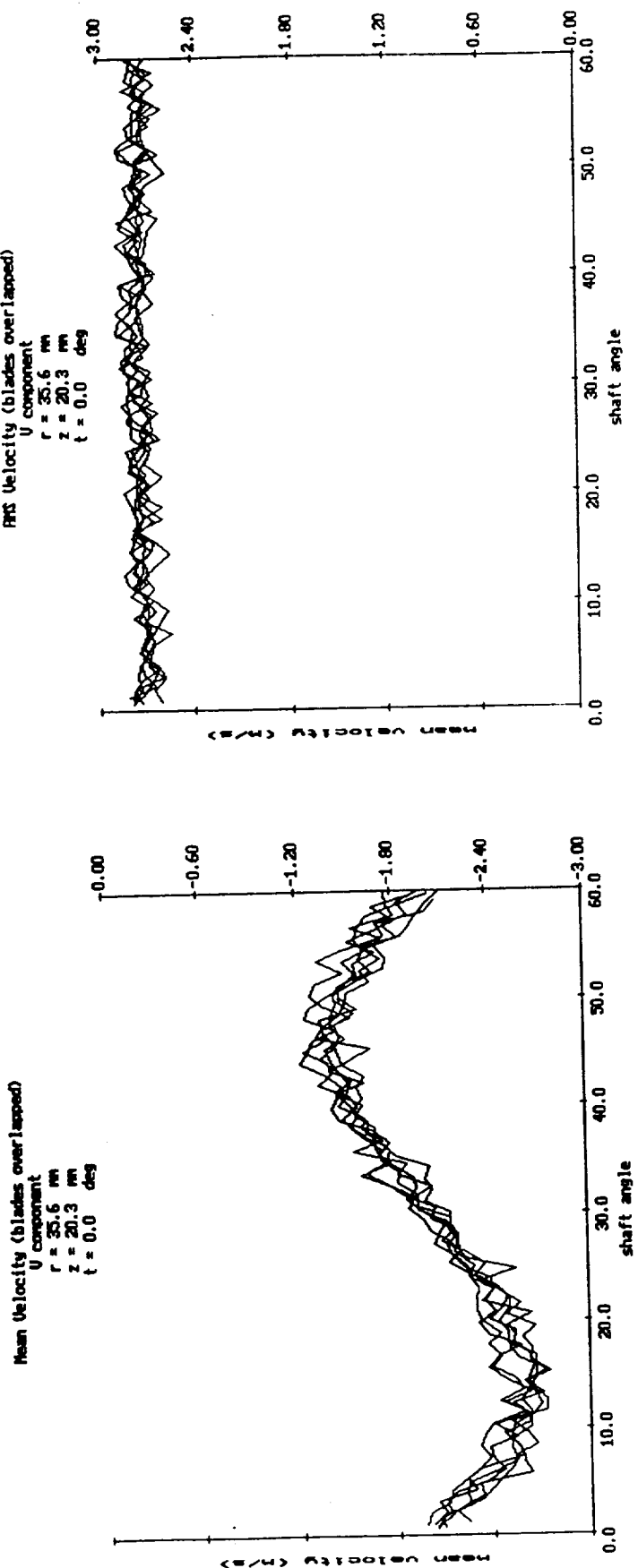


Fig. 18. Continued.

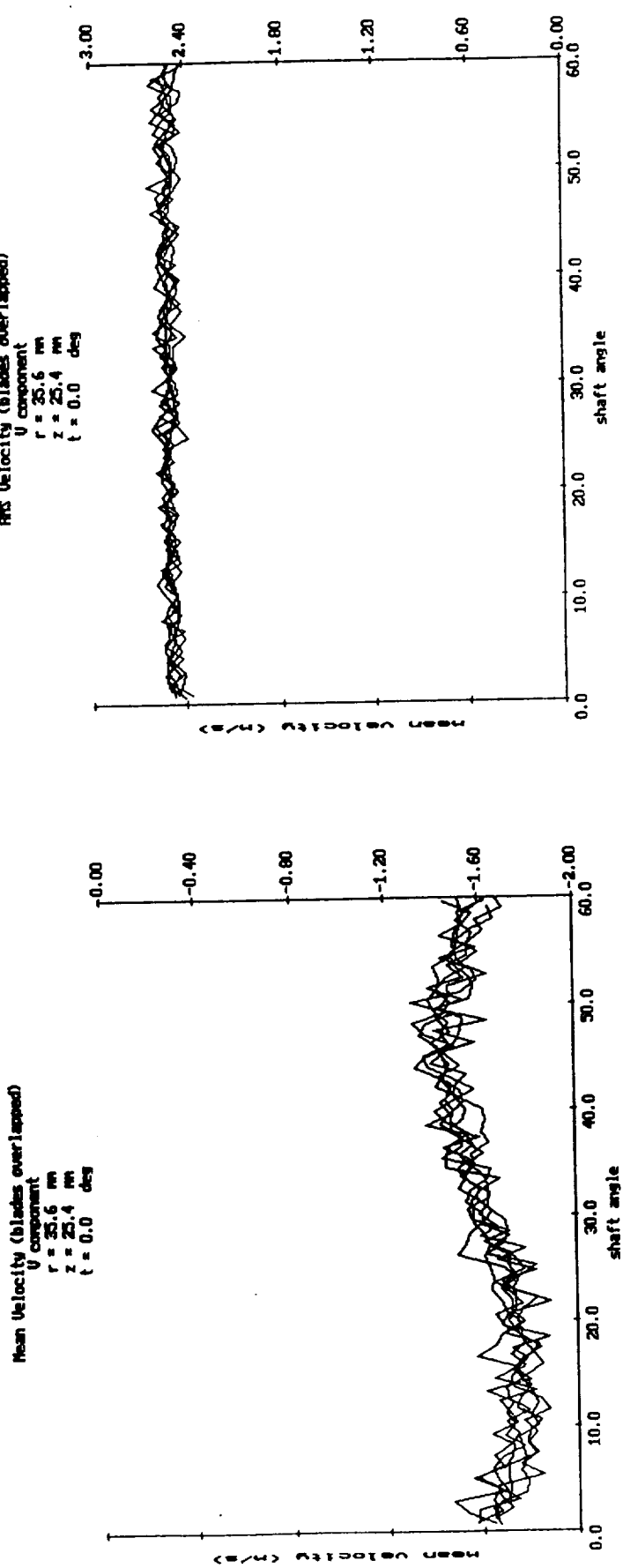


Fig. 18. Continued.

ORIGINAL PAGE IS  
OF POOR QUALITY

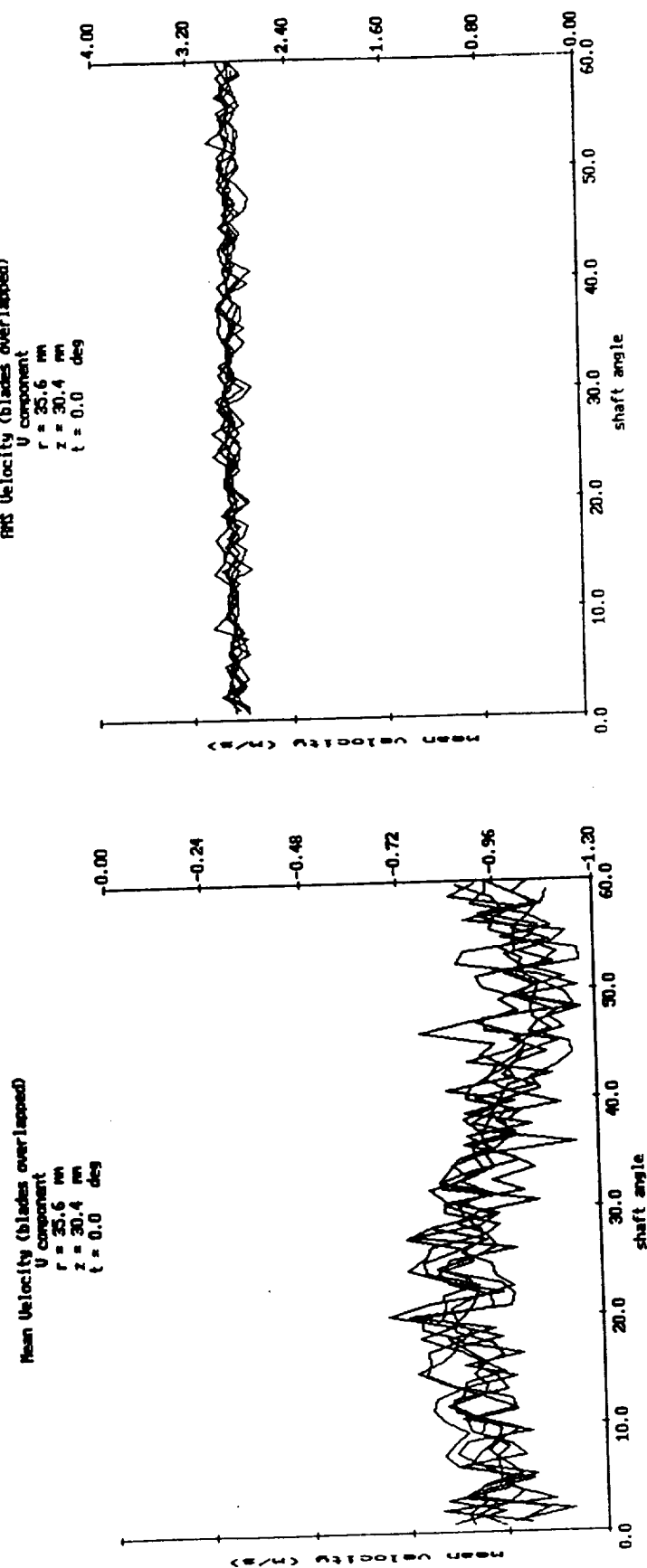


Fig. 18. Continued.

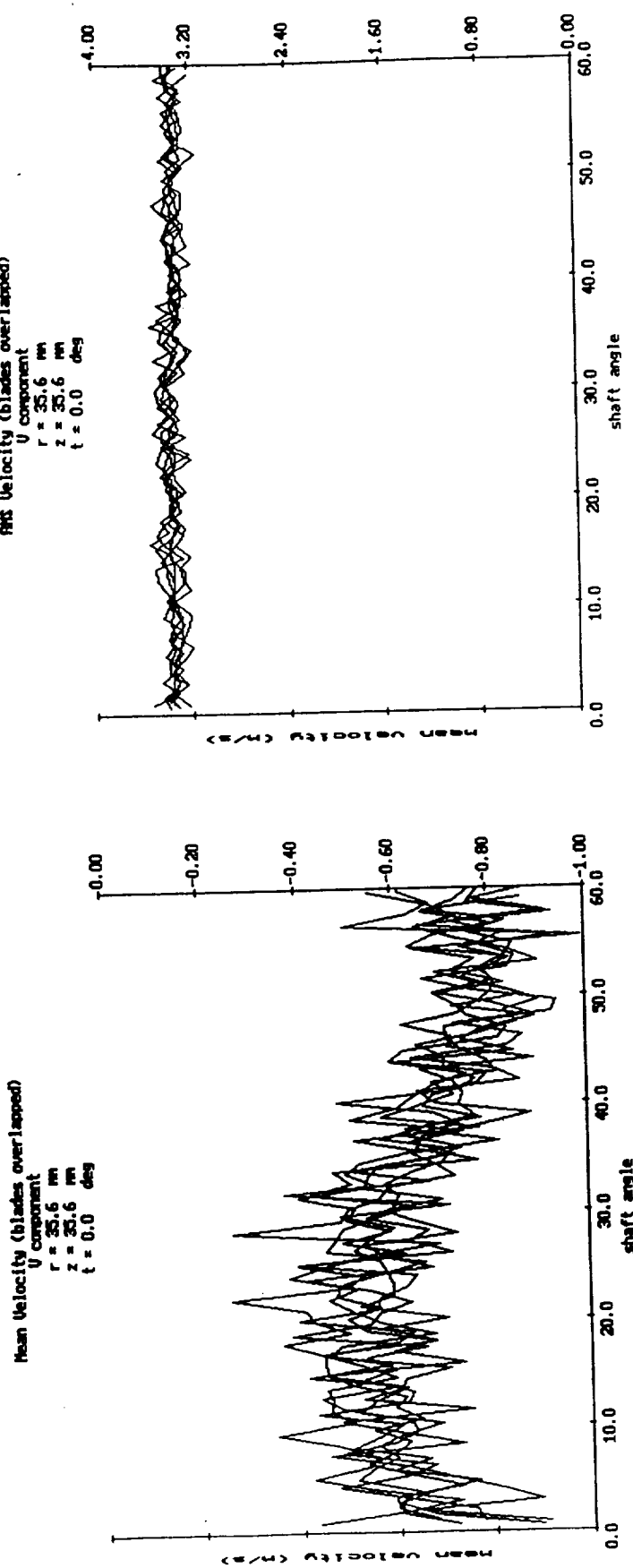


Fig. 18. Continued.

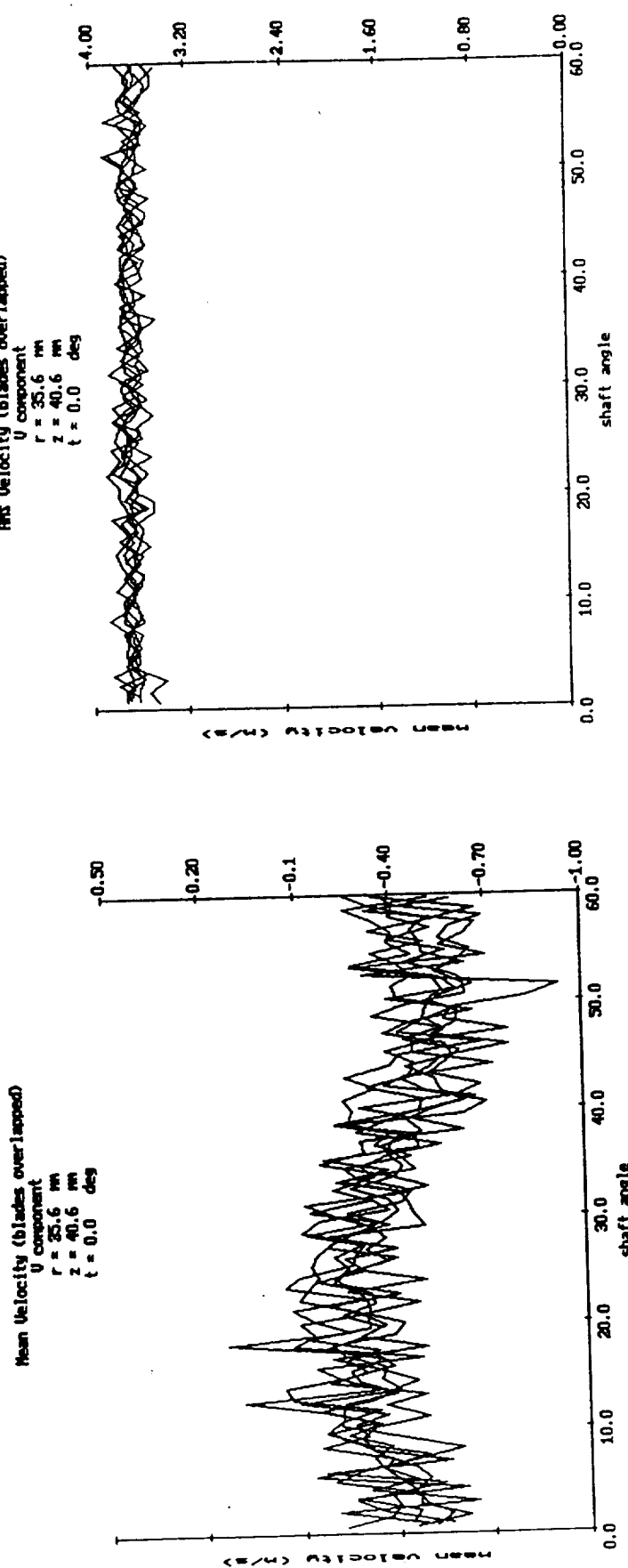


Fig. 18. Continued.

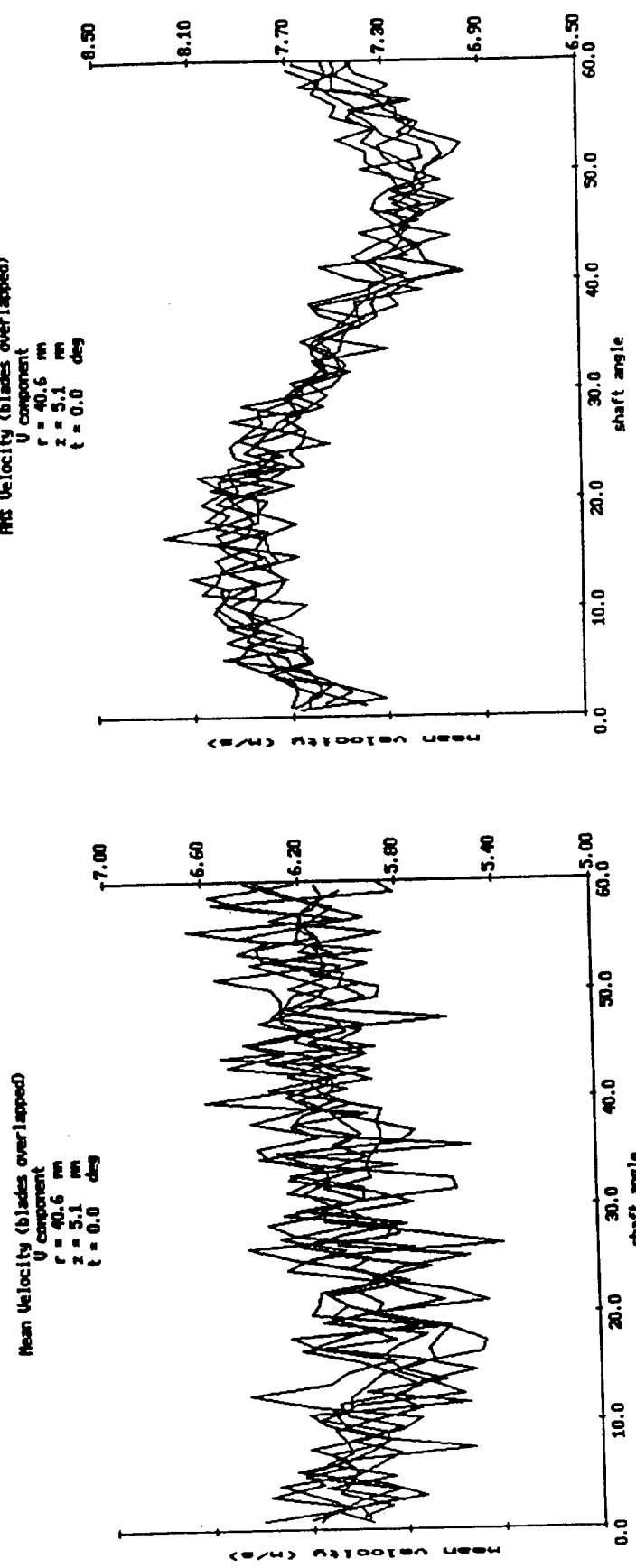


Fig. 18. Continued.

ORIGINAL PAGE IS  
OF POOR QUALITY

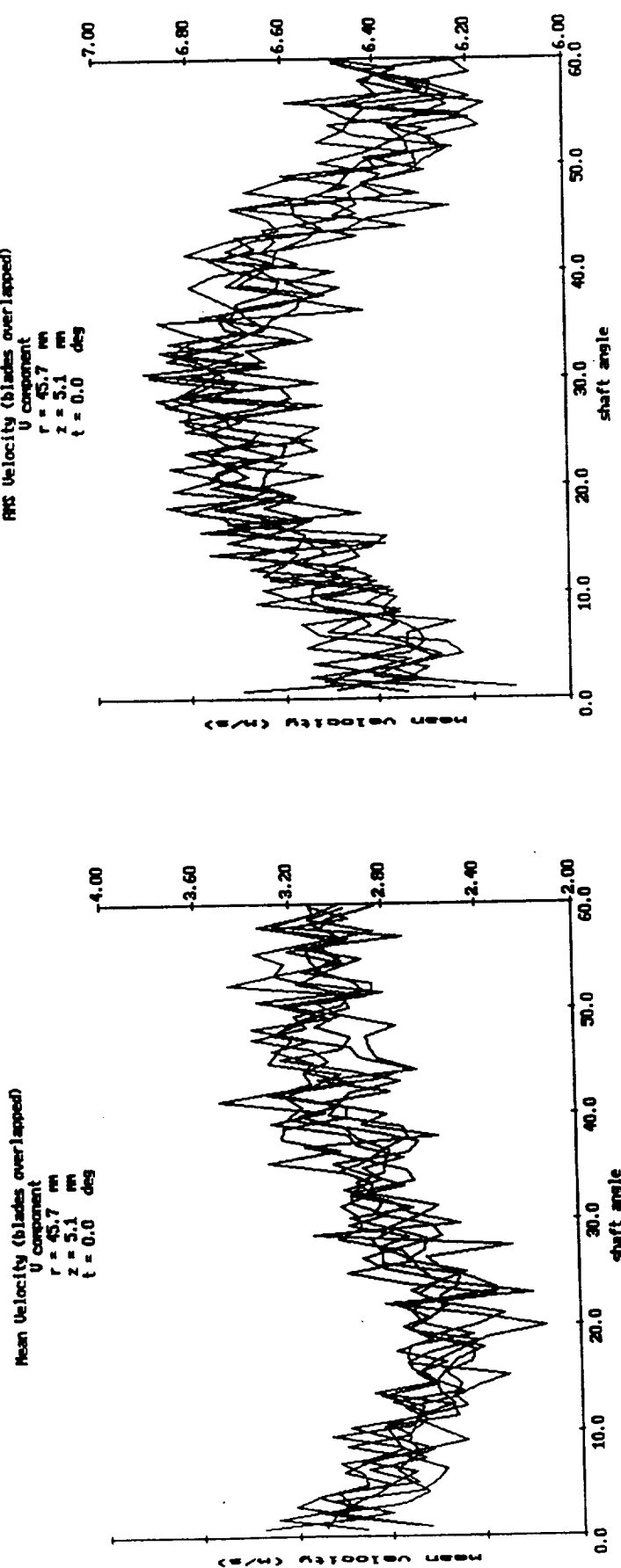


Fig. 18. Continued.

ORIGINAL PAGE IS  
OF POOR QUALITY

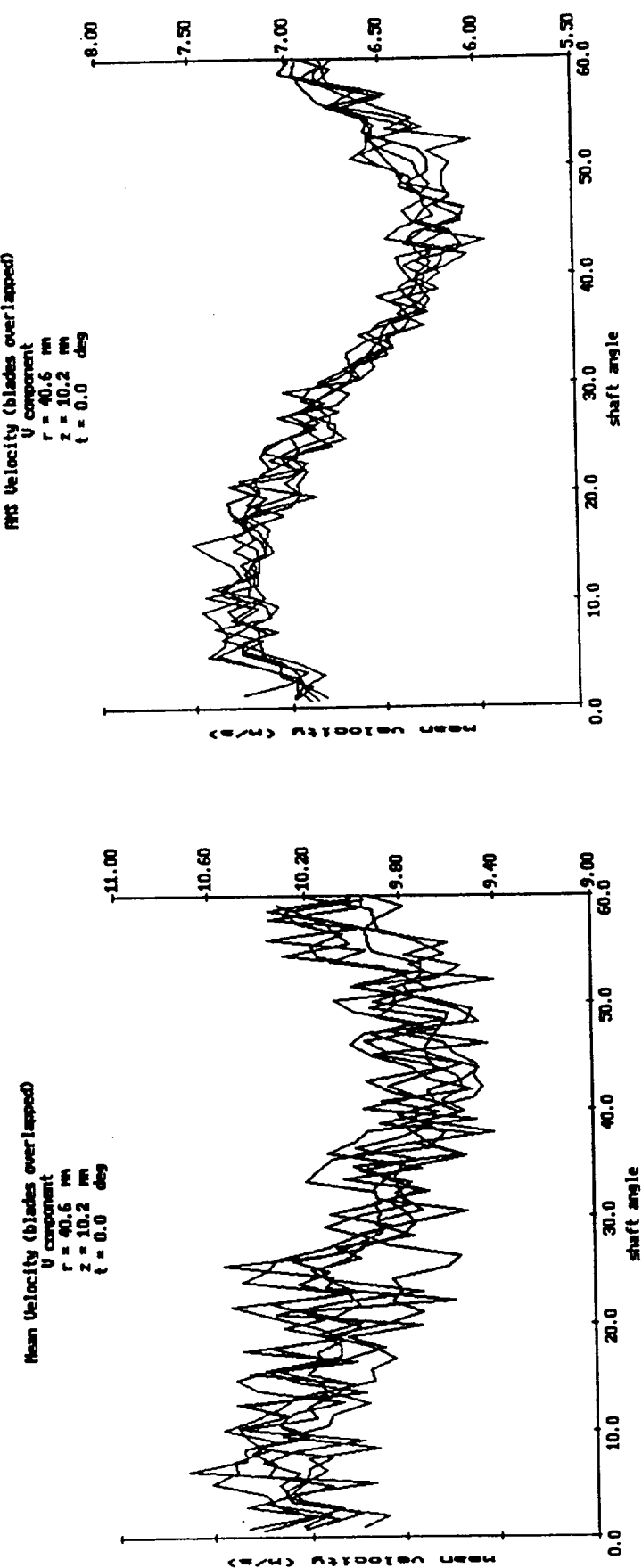


Fig. 18. Continued.

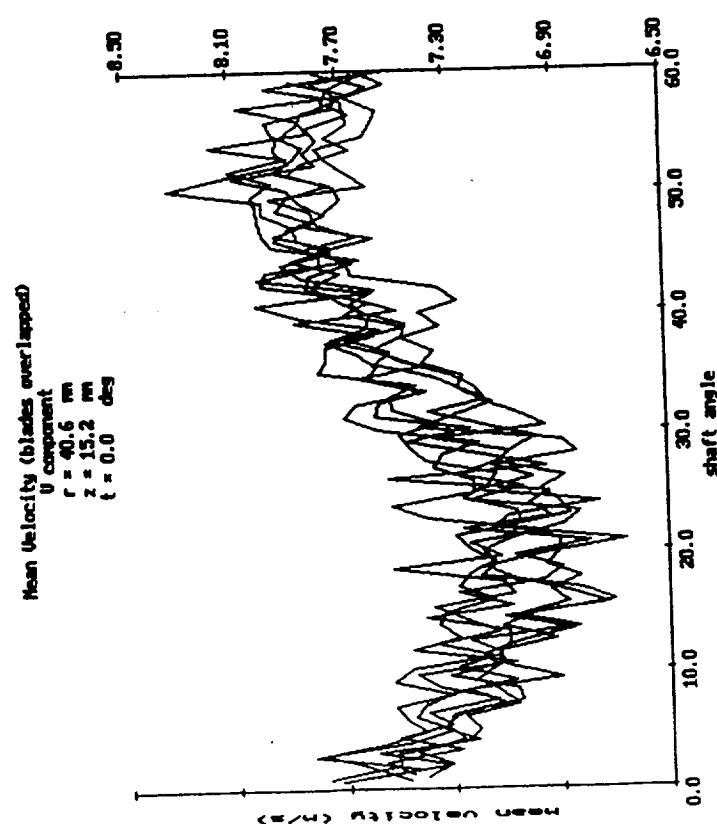
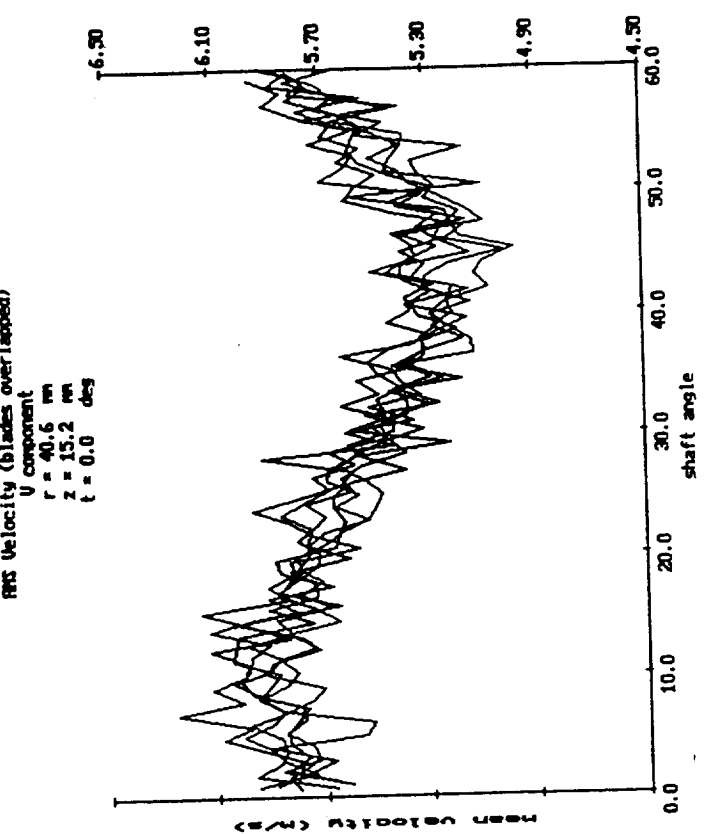


Fig. 18. Continued.

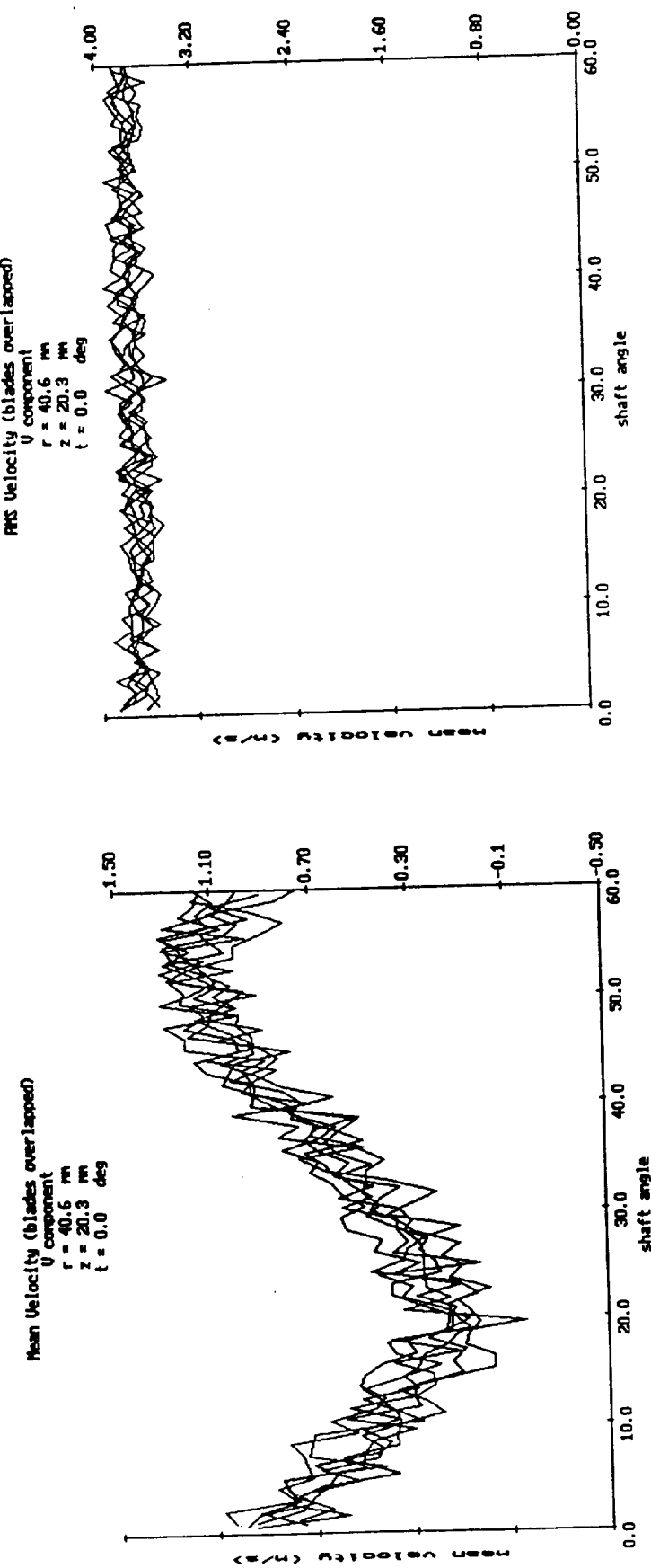


Fig. 18. Continued.

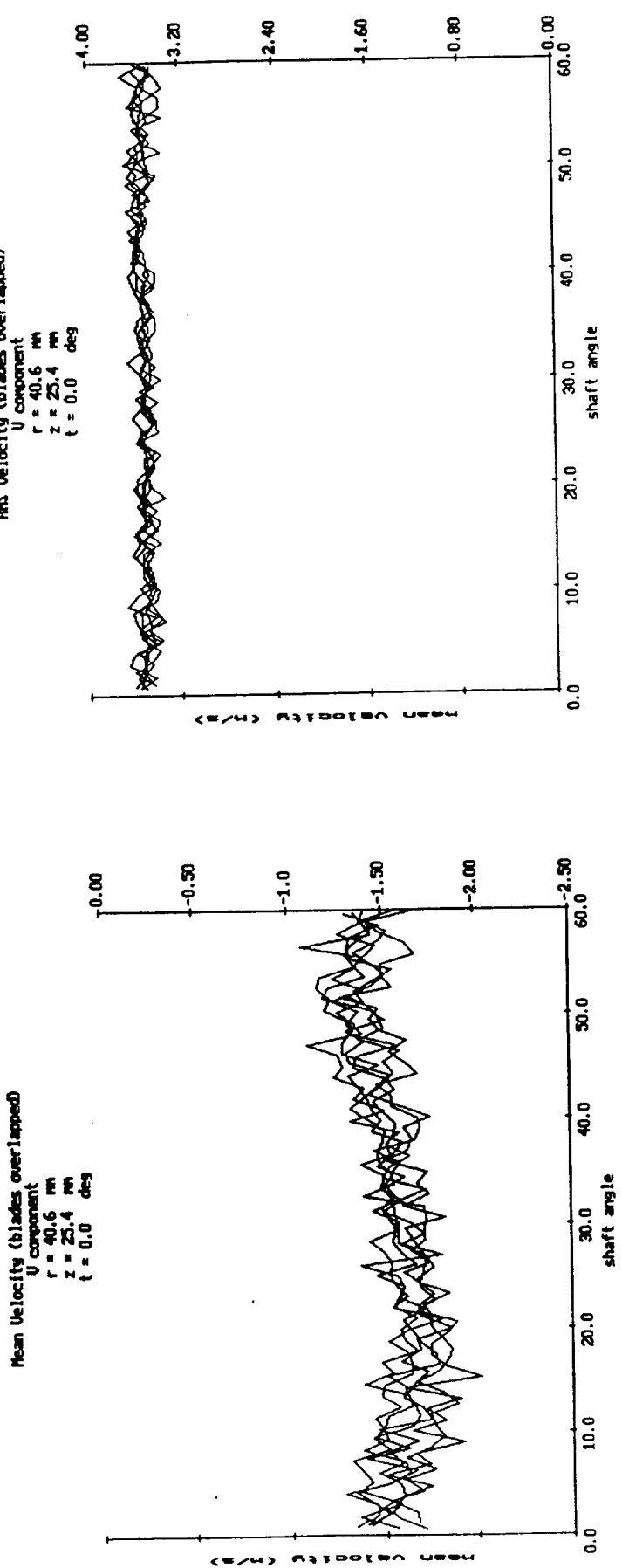


Fig. 18. Continued.

ORIGINAL PAGE IS  
OF POOR QUALITY

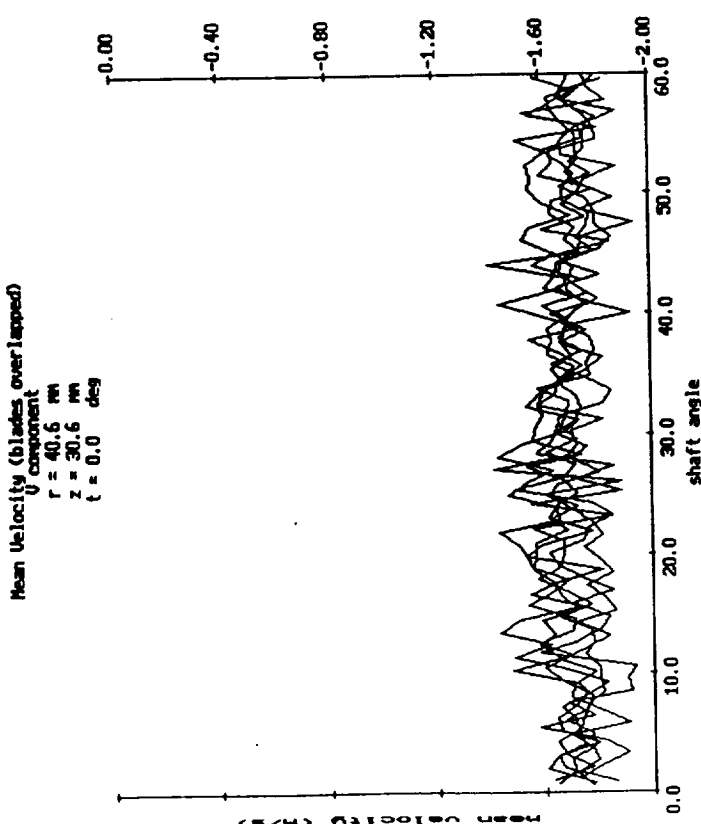
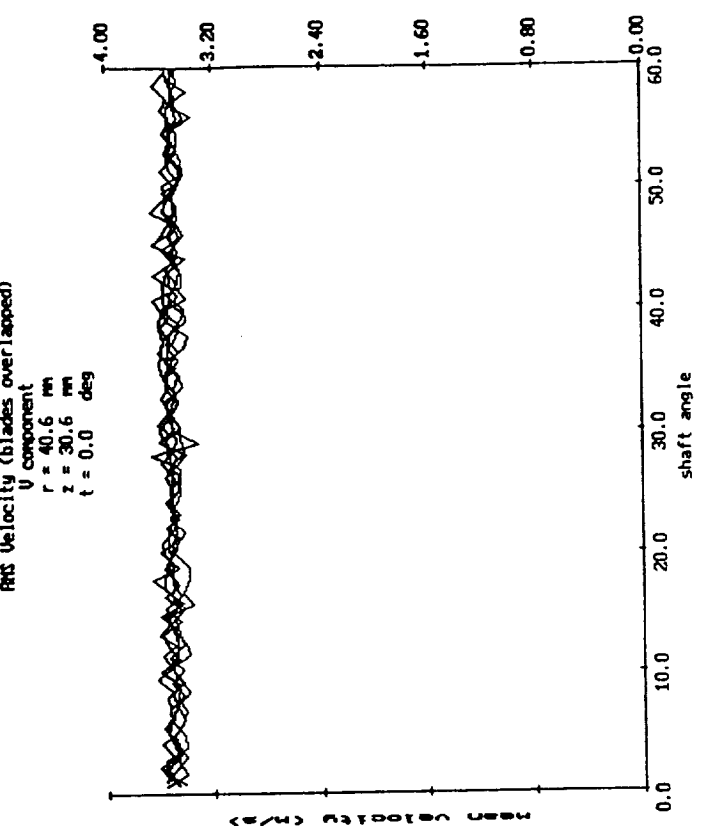


Fig. 18. Continued.

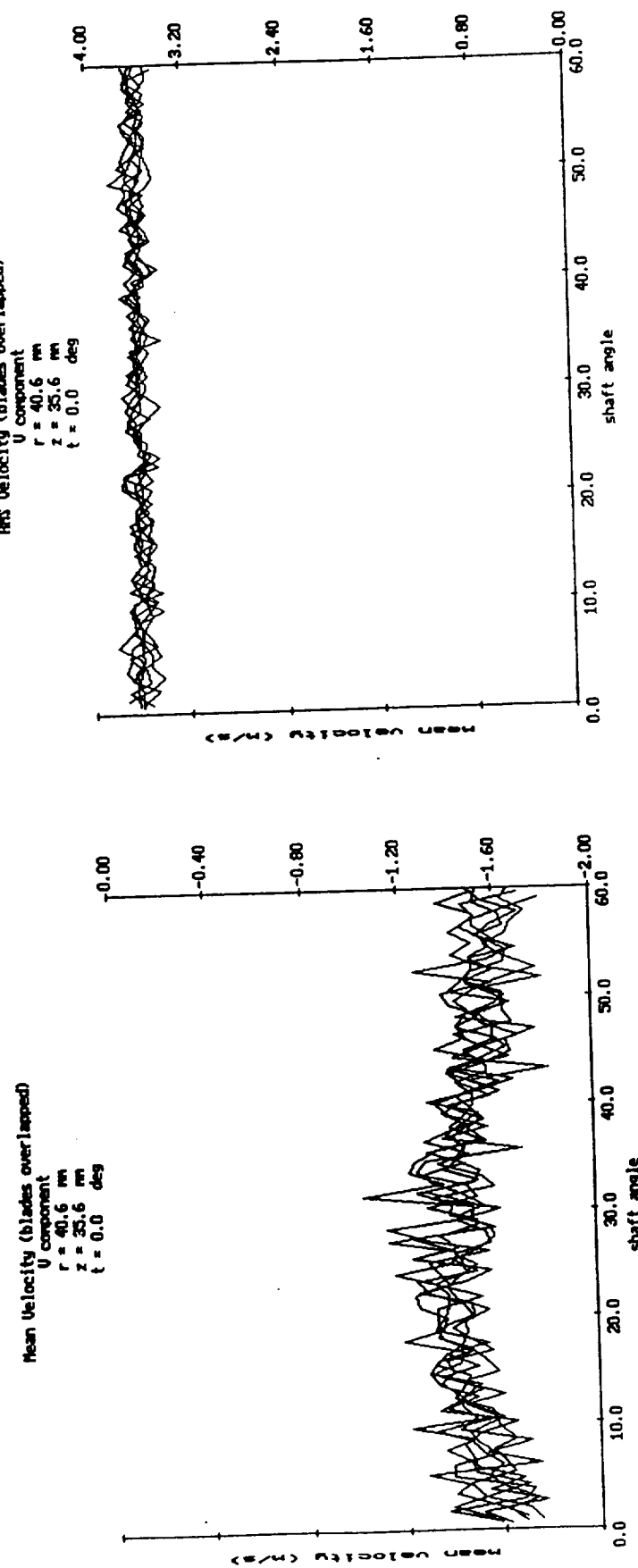


Fig. 18. Continued.

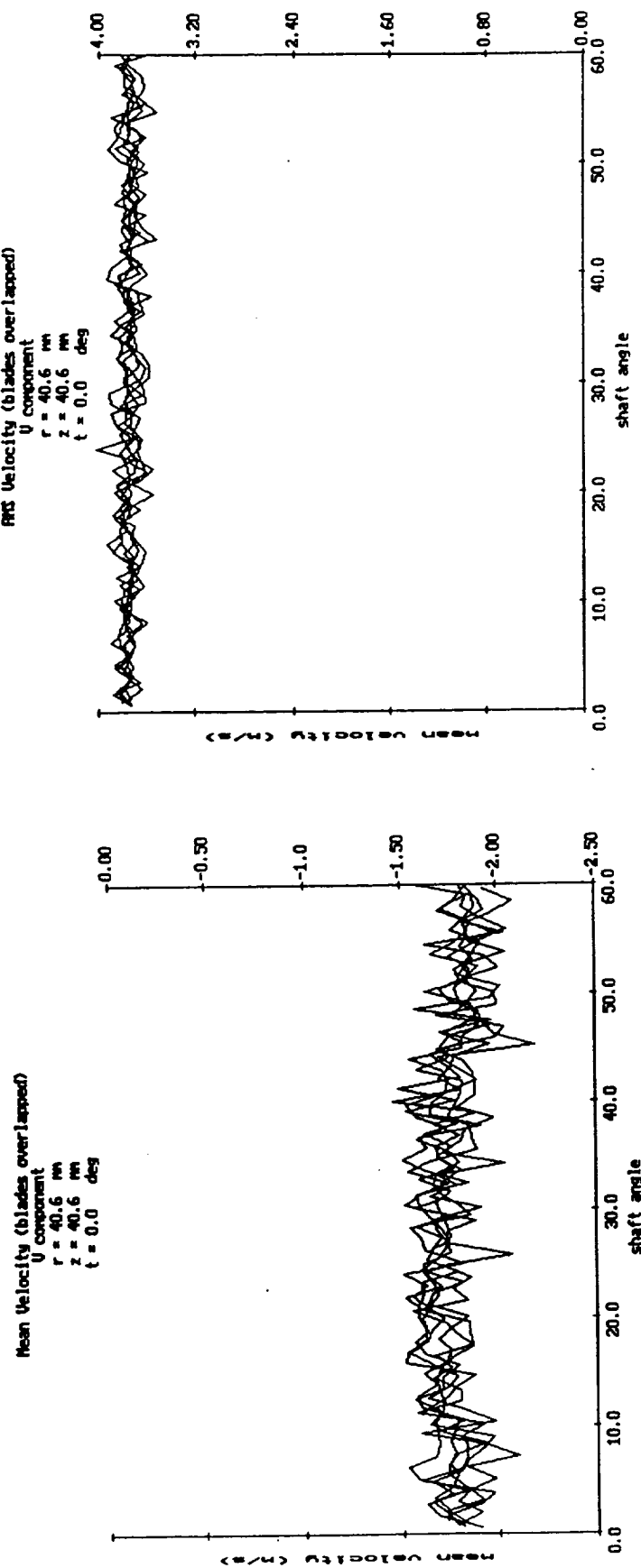


Fig. 18. Continued.

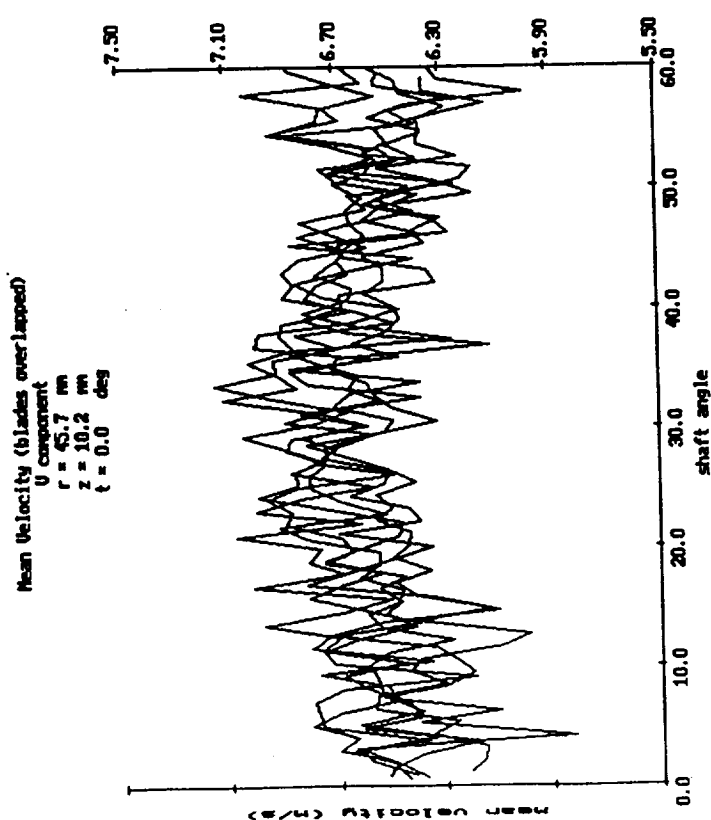
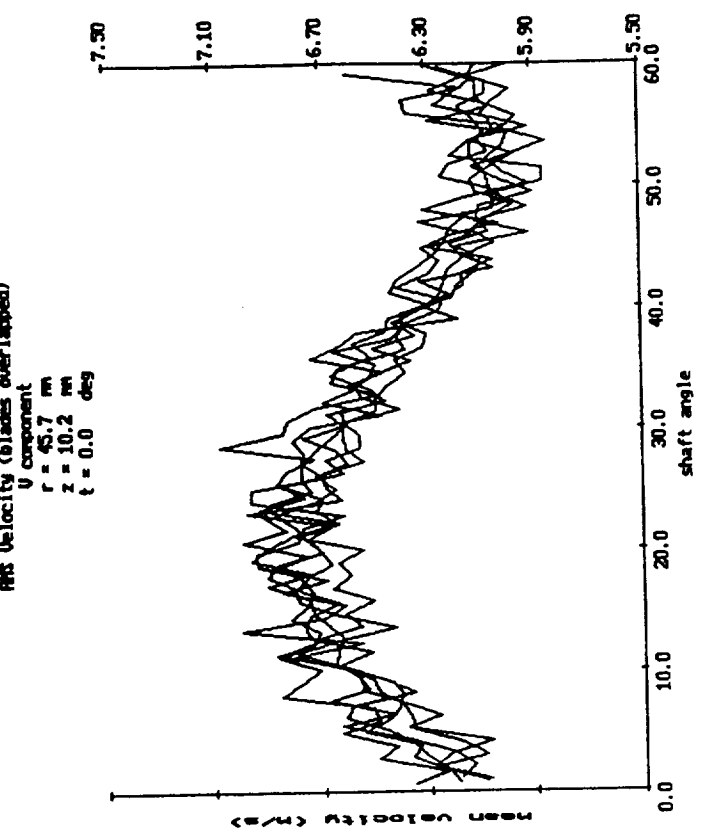


Fig. 18. Continued.

ORIGINAL PAGE IS  
OF POOR QUALITY

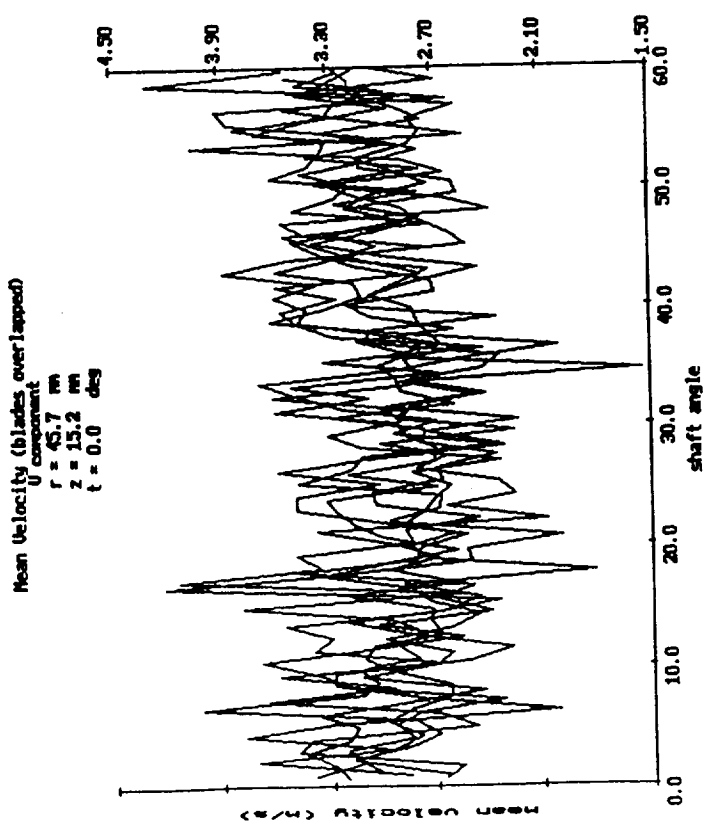
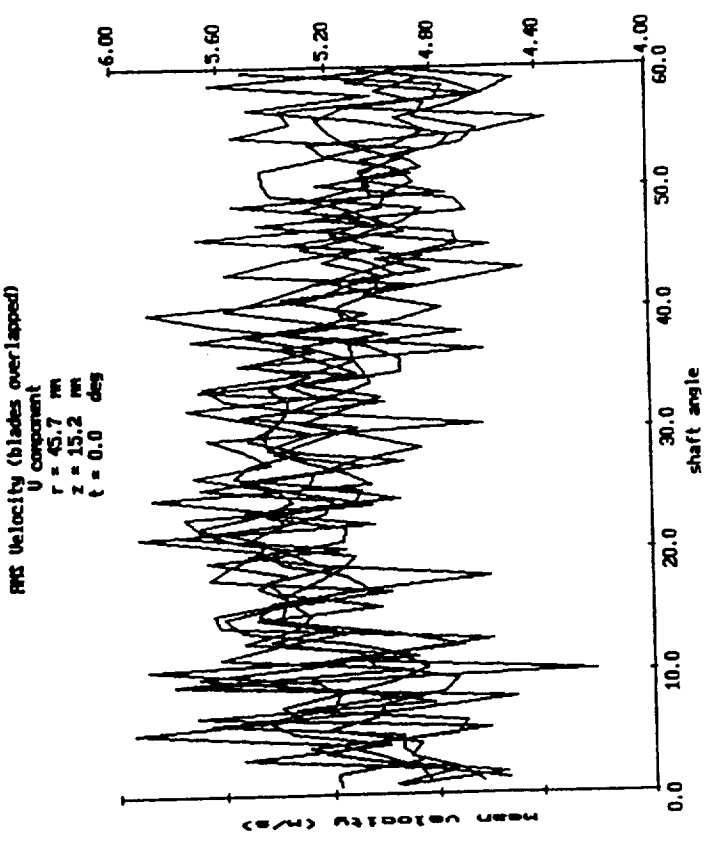


Fig. 18. Continued.

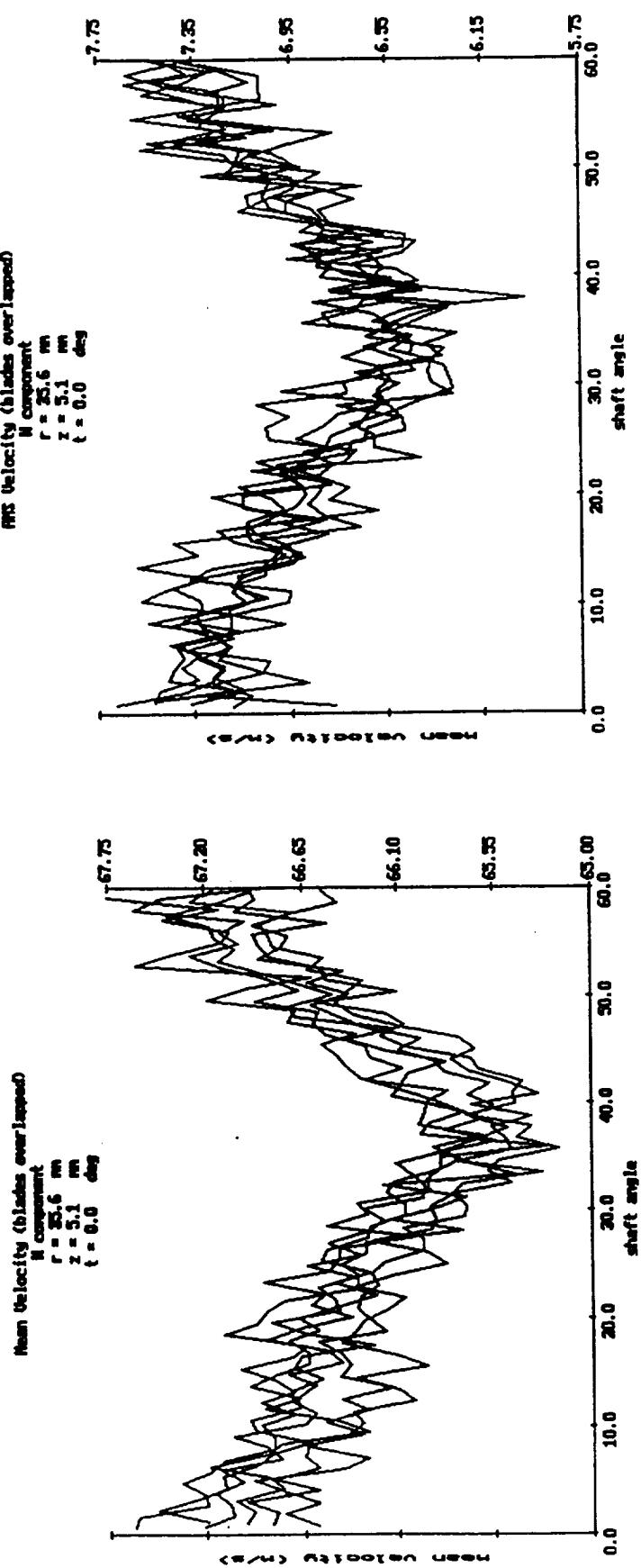


Fig. 19. Ensemble-averaged Tangential Velocities in the Turn-around Region.

ORIGINAL PAGE IS  
OF POOR QUALITY

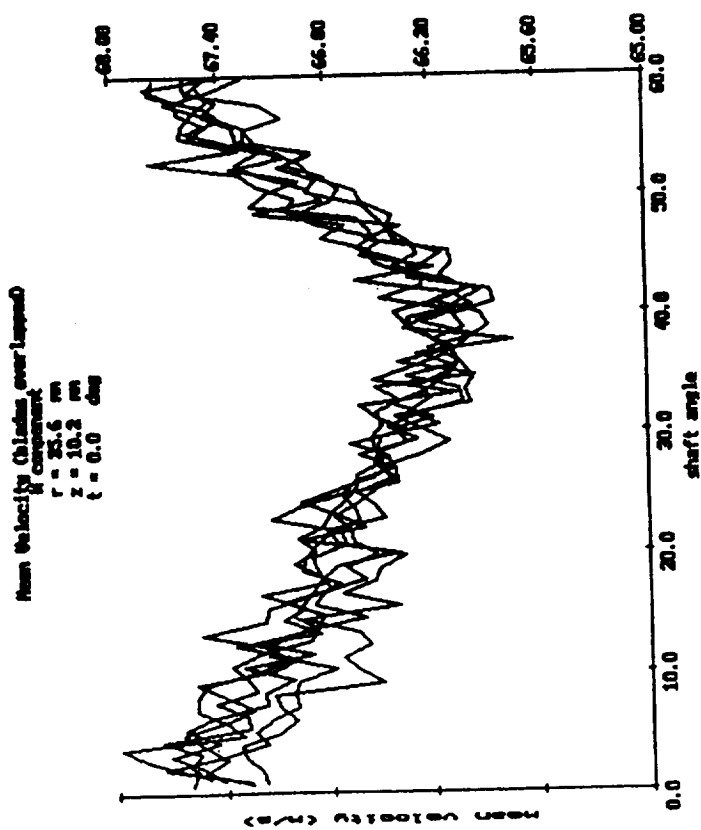
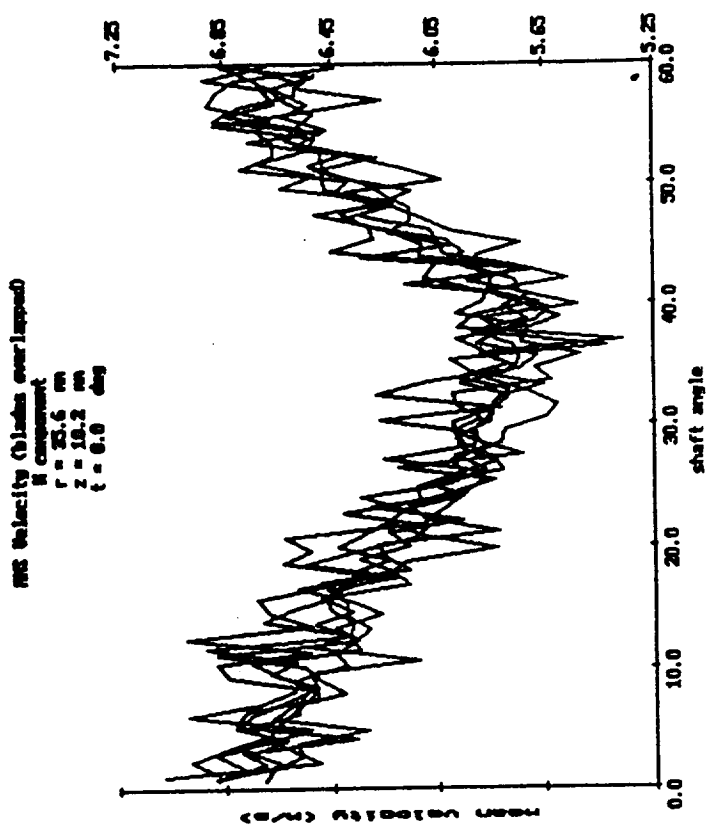


Fig. 19. Continued.

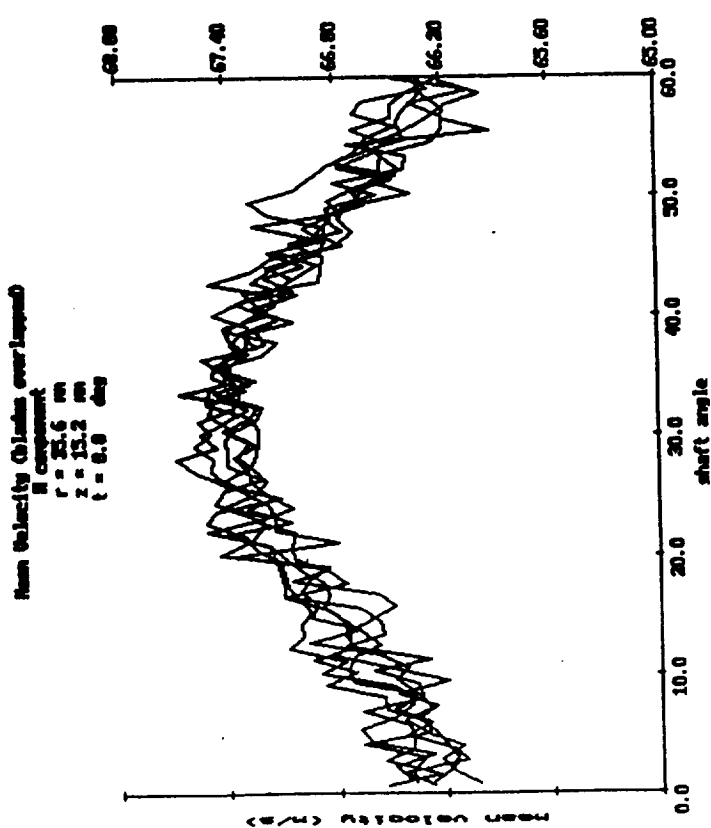
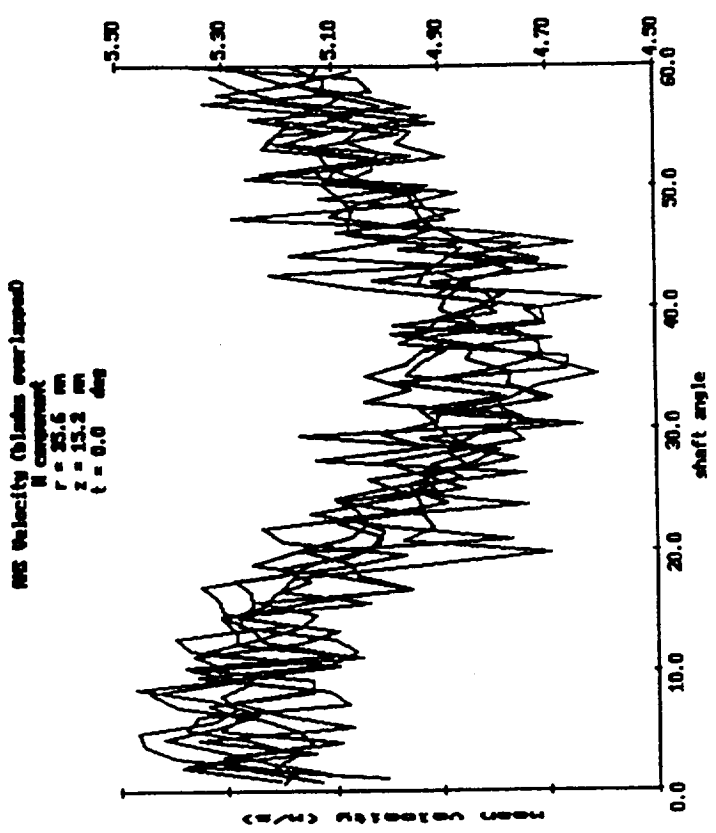


Fig. 19. Continued.

ORIGINAL PAGE IS  
OF POOR QUALITY

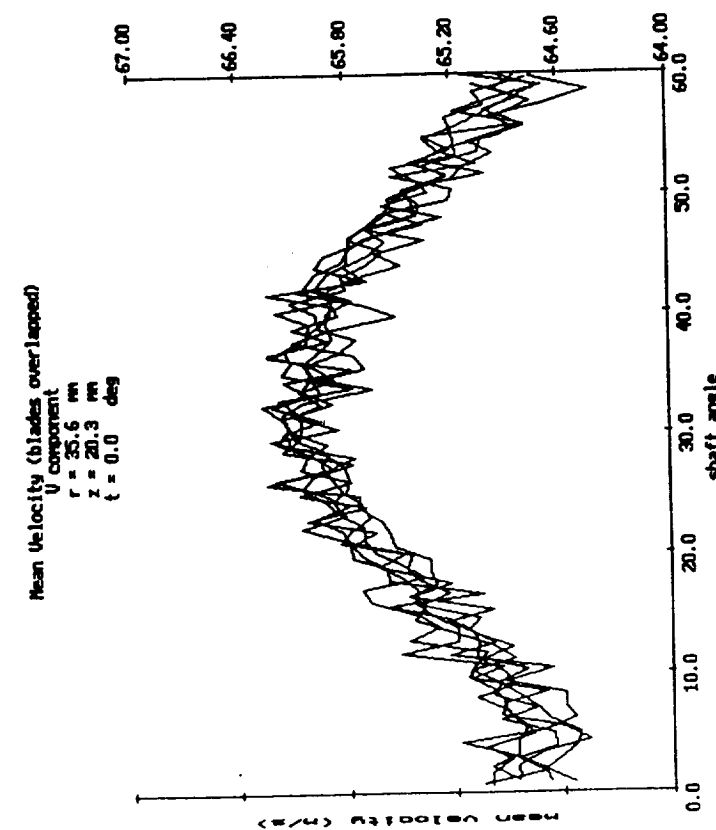
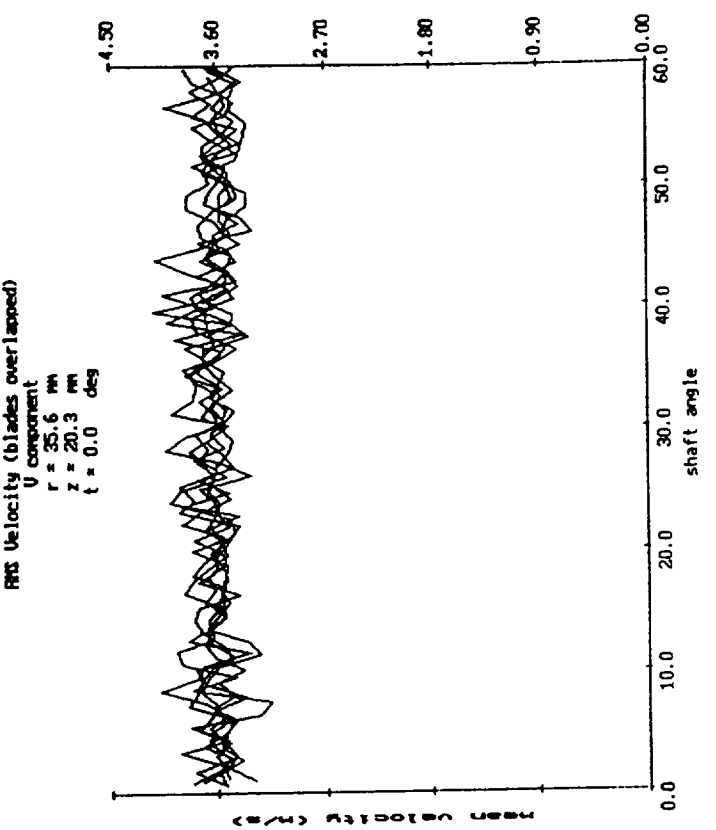


Fig. 19. Continued.

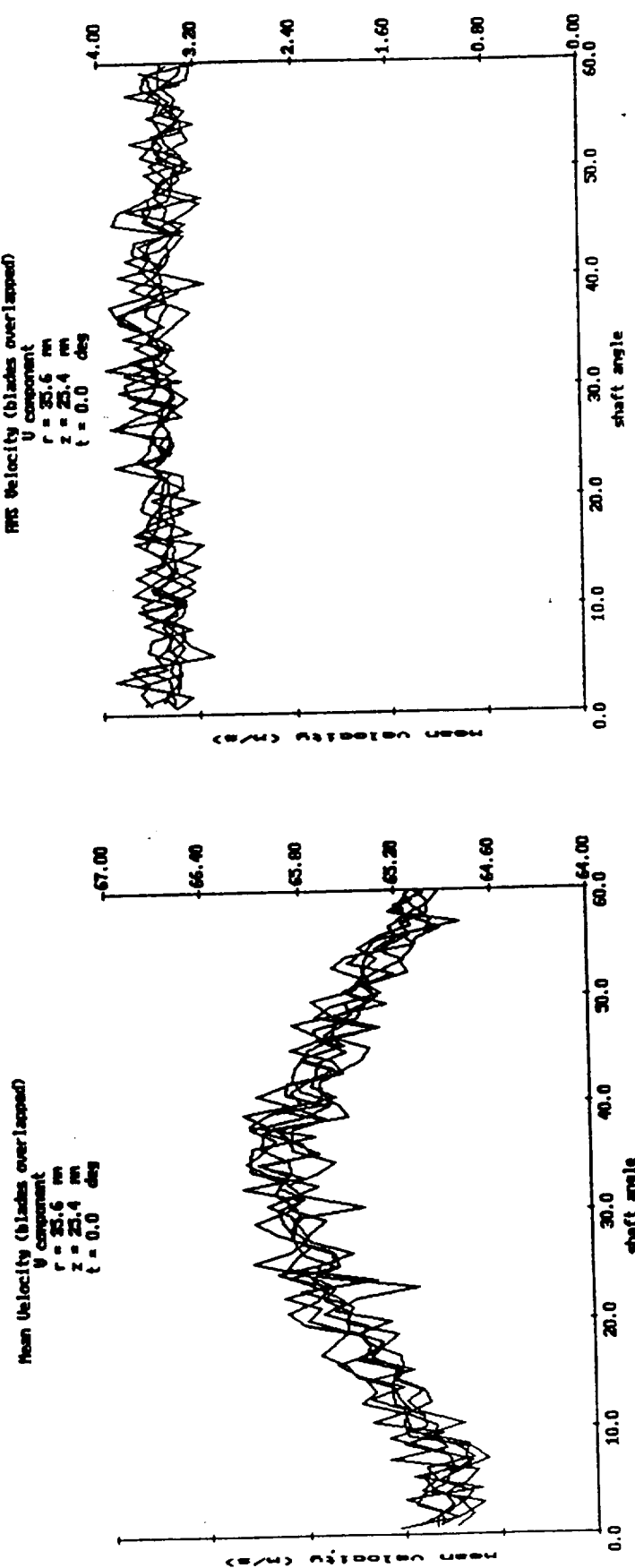


Fig. 19. Continued.

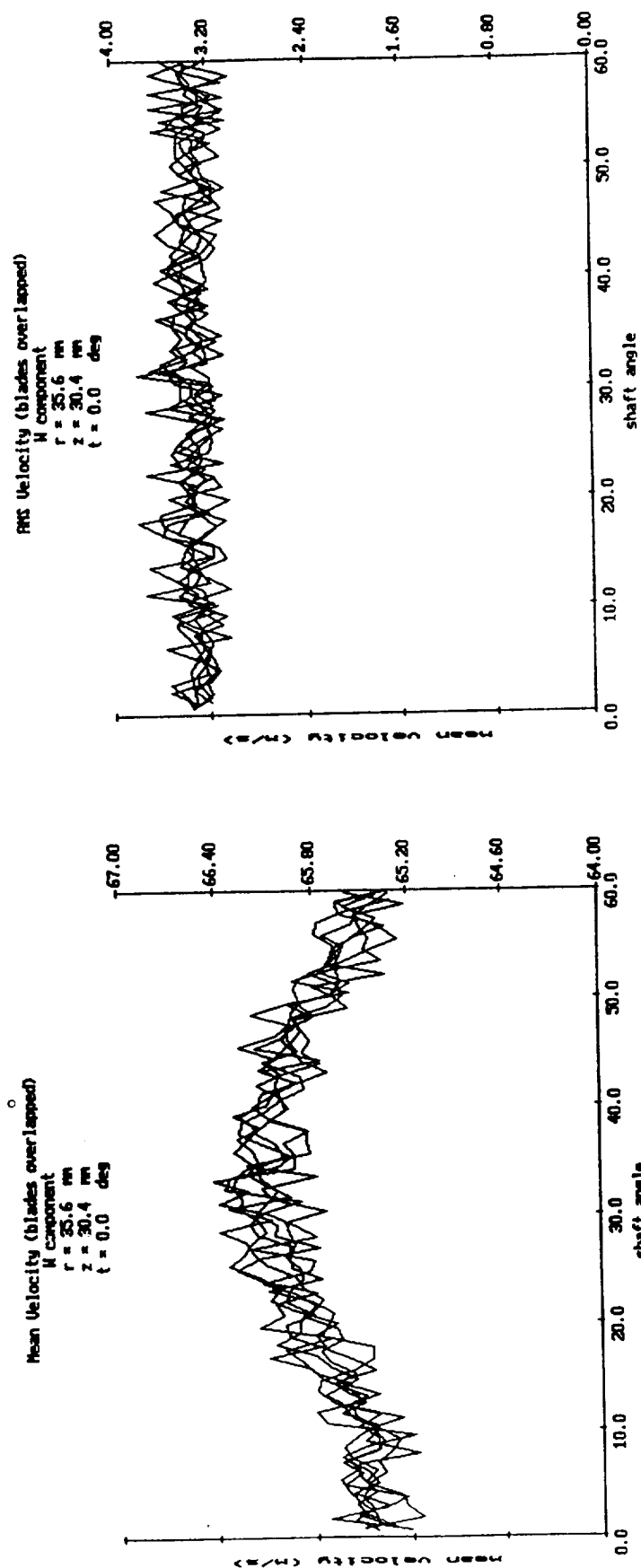


Fig. 19. Continued.

ORIGINAL PAGE IS  
OF POOR QUALITY

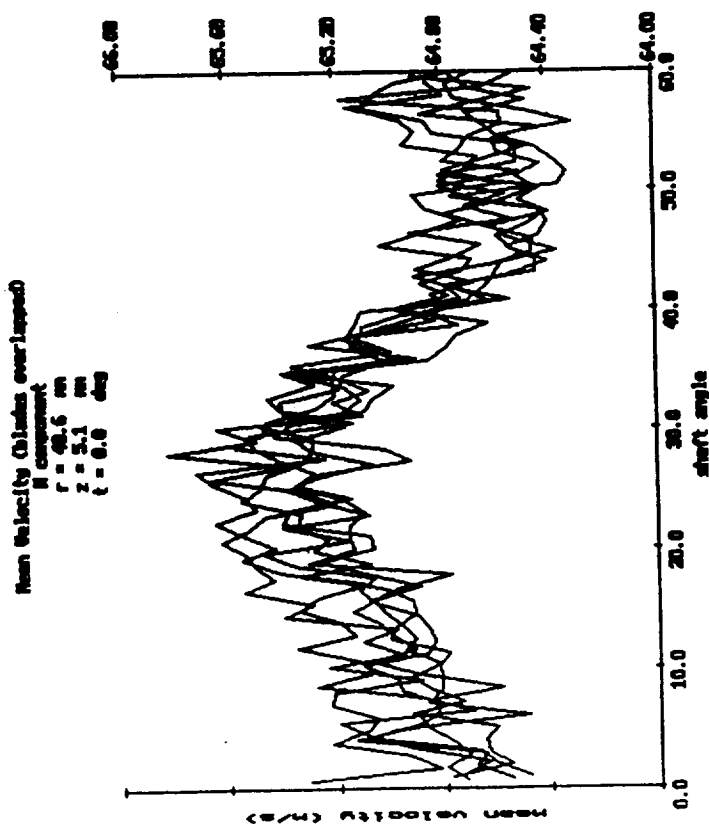
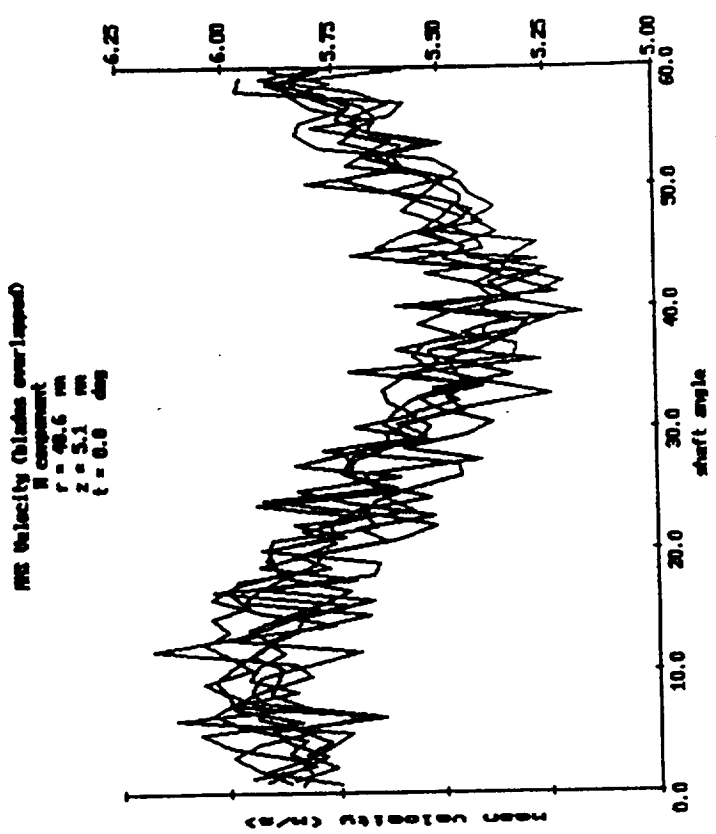


Fig. 19. Continued.

ORIGINAL PAGE IS  
OF POOR QUALITY

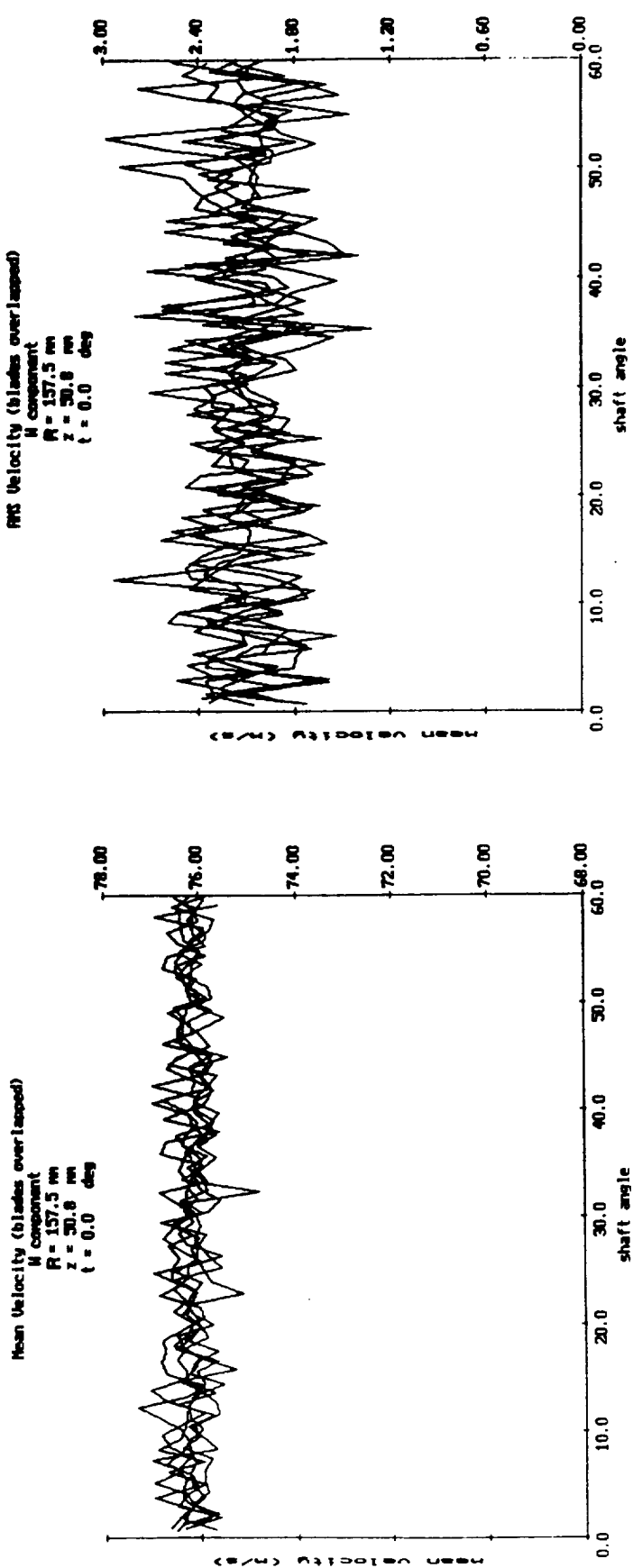


Fig. 20. Ensemble-averaged Tangential velocities in the Volute.

**Report R91-900065-F**

**APPENDIX A**

**IMPERIAL COLLEGE OF SCIENCE, TECHNOLOGY & MEDICINE**  
Mechanical Engineering Department, Fluids Section  
Exhibition Road, London SW7 2BX, UK

**DESIGN AND PRELIMINARY FLOW FIELD EVALUATION OF THE SSME  
HIGH PRESSURE FUEL TURBOPUMP RESEARCH RIG**

by

**C. Vafidis and J.H. Whitelaw**

Final Report to Scientific Research Associates Inc.  
NASA MSFC Contract NAS8-36186

February 1990

FS/90/02

## ABSTRACT

The principles and details for the design of a test rig simulating the first stage of the High Pressure Fuel Turbopump of the Space Shuttle Main Engine are reported, together with preliminary flow field measurements obtained in the model turbopump volute. The results indicate lower flow capacity of the model turbopump than that predicted by similarity analysis from the HPFTP data, which is mainly attributed to simplifications introduced in the volute configuration. The performance of the laser velocimeter system developed for this study is found satisfactory and the velocity field measurements indicate minor only effects of impeller rotational speed on the diffuser flow structure in the speed range of 4260-7680 rpm.

## INTRODUCTION

One of the main components of the Space Shuttle Main Engine (SSME) hardware is the hydrogen fuel supply pump to the main combustor. This is a radial three-stage high pressure turbopump, (HPFTP) powered by a 1,600 kW axial turbine at 37,000rpm. The critical operation of the fuel pump together with the extreme operating conditions makes its performance and reliability essential for the flight safety and engine downtime. Problems of pump components cracking have been identified and attributed to excessive unsteady aerodynamic loads. Further to that, off-design operation performance of the turbopump is not well known and its improvement, together with that at design conditions, is thought to be necessary.

Improvement of the turbopump loading and performance characteristics requires understanding of the unsteady aerodynamics of the interaction between impeller and diffuser, and this can be accomplished by coordinated experimental and numerical flow analysis investigations in relevant flow configurations. The experimental results will provide the necessary insight into the physics of the flow and, at the same time, the validation data for the assessment of the parallel numerical simulation efforts. The results of the numerical studies can in turn be used to guide further experiments with modified diffuser geometries with the further target of improving the operational characteristics of the turbopump.

The experimental approach followed here focuses on the flow characteristics of the first stage of the turbopump as a function of inlet and outlet conditions and diffuser geometry. Since the HPFTP consists of three geometrically similar stages, this simplification is thought to be acceptable. A further simplification concerns the working fluid which in this simulation is air instead of hydrogen. The first task of this work was to design and build an experimental facility to accommodate the actual flight impeller of the first stage of the HPFTP in a flexible test rig in order to allow detailed flow measurements to be obtained by laser Doppler velocimetry at the inlet to the impeller and inside the diffuser. The second task was to develop and test a suitable anemometer system to perform the measurements. A feasibility study for this

work has already been carried out in a high speed (30,000 rpm) turbocharger test rig and reported in Report FS/87/36.

The present report is divided in two parts. The first deals with the design considerations and technical details of the turbopump rig. The second part deals with the performance of the test facility and presents a sample of preliminary flow measurements.

## PART 1: TEST RIG DESIGN CONSIDERATIONS

### 1- *Geometric and Flow Similarity*

A line drawing of the SSME High Pressure Fuel Turbopump assembly is shown in Figure 1. It consists of a scroll-shaped entry stage equipped with guide vanes at its exit and followed by three radial compressor stages, with the last one discharging into a collector volute. From the geometry of the turbopump it is clear that each of the three stages has different inlet or exit conditions. The design objective for the test rig under consideration here, is the capability of simulating the inlet and outlet conditions of the first stage only.

The geometry of the first two stages is identical and consists of a 12" diameter enclosed (shrouded) impeller with six main (full) and two splitter (partial) blades in each passage, shown in Figure 2, and an axisymmetric vaned diffuser volute, shown in Figure 3. Once the decision to make use of the flight impeller was made, the geometric scale of the test facility was necessarily defined to actual size. It remained to establish the best possible flow similarity between the research turbopump and the flight hardware, the main difference being that of working fluid. The flow similarity involves matching of the flow coefficient, blade tip Mach number and Reynolds number, but practical considerations limit the matching in the first two parameters, provided that the test rig Reynolds number ensures fully turbulent flow.

The HPFTP performance baseline data were provided by MSFC and are summarised in Table 1 under the heading "Flight". Similarity of tip Mach number between model and flight hardware implies a model rotational speed of 8690 rpm. The expected flow coefficient similarity yields for the model an air mass flow rate of 0.63 lbm/s (1029 kg/hr), provided that the inlet and outlet conditions to the impeller are similar between flight and model hardware, while, under the same assumptions, the expected discharge pressure will be 16.5 psia. The scaling of power requirements also suggests that at the Mach matching speed of 8690 rpm the model pump will consume 4.78 hp.

**TABLE 1**  
**HPFTP Baseline Operating Conditions**

|  | <u>Flight</u> | <u>Model</u> |
|--|---------------|--------------|
| Inlet pressure, psia                   | 220           | 14.5         |
| Discharge pressure, psia               | 2458          | 16.55        |
| Inlet temperature, °R                  | 42.41         | (526)        |
| Discharge temperature, °R              | 62            | (540)        |
| Inlet density, lbm/ft <sup>3</sup>     | 4.2784        | 0.07         |
| Discharge density, lbm/ft <sup>3</sup> | 4.659         |              |
| Inlet flowrate, lbm/s                  | 162.59        | 0.63         |
| Discharge flowrate, lbm/s              | 162.59        | 0.63         |
| Pump efficiency                        | 0.76          |              |
| Pump horsepower, hp                    | 22110         | 4.78         |
| Pump speed, rpm                        | 36742         | 8690         |
| Pump tip speed, ft/s                   | 1924          | 455          |
| Speed of sound, ft/s                   | 4778          | 1130         |
| Tip Mach number                        | 0.4           | 0.4          |
| Pump head coefficient                  | 1.71          |              |
| Pump flow coefficient                  | 0.179         |              |

Similar analysis for off-design speeds of 4000 and 12000 rpm gives the operating parameter estimates summarised in Table 2, below:

**TABLE 2**  
**Flight and Model Operating Conditions**

|                       | <u>Flight</u>        | <u>Model</u>        |                     |                     |
|-----------------------|----------------------|---------------------|---------------------|---------------------|
|                       |                      | min                 | match               | max                 |
| Mach number           | 0.4                  | 0.18                | 0.4                 | 0.56                |
| Mass flow rate, lbm/s | 162.59               | 0.29                | 0.63                | 0.87                |
| Speed, rpm            | 36742                | 4000                | 8690                | 12000               |
| Reynolds number       | 1.26x10 <sup>7</sup> | 1.3x10 <sup>4</sup> | 2.8x10 <sup>4</sup> | 3.9x10 <sup>4</sup> |
| Pressure rise, psi    | 2228                 | 0.4                 | 2.0                 | 3.8                 |
| Pump power, hp        | 22110                | 0.5                 | 4.8                 | 12.6                |

This preliminary analysis proved that the simulation of the HPFTP operation with air instead of hydrogen as a working fluid is feasible, with the only technical constraint of relatively high speed and moderate power requirements from the driving device. This should ideally be a DC motor with a thyristor speed controller in order to allow continuously variable and regulated speed. However, DC motors above 6000 rpm with power outputs of the order

of 10 hp are not readily available. The alternative solution would be a standard 3000 rpm motor of 15 hp output coupled with an orbital step-up gearbox to achieve the 12000 rpm target. Careful consideration of the financial implications indicated that the best cost effective solution would be to design the test rig for a maximum rotational speed of 12000 rpm but, in the first stages, to drive it with a DC motor capable of 7.8 kW (10.4 hp) at a speed of 8000 rpm. Provisions, however, have been made for the motor control equipment to be able to accommodate the power requirements of the motor/gear box arrangement at 12000 rpm.

## *2- Inlet and Outlet Conditions*

Understanding of the impeller/diffuser aerodynamics is expected to benefit from simple inlet and outlet conditions, even if they are not representative of the flow situation in the actual flight turbopump. It was decided to, initially, eliminate the scroll entry stage upstream of the first stage of the turbocompressor as well as the impeller and volute of the second stage. The simplest possible inlet and outlet conditions correspond to inlet from atmosphere and discharge into a long annular duct. Inlet from atmosphere implies the use of a bell-mouth shaped entry section while the presence of the annular duct necessitates the introduction of a collector volute at its end in order to direct the discharge flow into a pipe and metering device. The inlet bell-mouth geometry was made identical to that of the exit of the inlet scroll of the flight hardware, albeit without the guide vanes. The geometry of the annular duct downstream of the first stage volute was dictated by the outlet dimensions of the volute and was made 10 hydraulic diameters long in order to minimise the upstream effect of the collector scroll.

The geometry of the diffuser volute was simplified even further by eliminating the vanes and by slightly altering the geometry of its walls to enable better access for LDV velocity measurements. These simplifications are bound to affect the performance of this stage of the turbocompressor but they provide a well-defined reference geometry for the study of impeller/diffuser interaction and for the assessment of numerical simulations. The simplified test rig is shown schematically in Figure 4a and represents the basic flow configuration. All parts of interest, such as the volute and inlet bell-mouth, were manufactured in clear cast acrylic in order to enable optical access for LDV measurements.

The basic test rig has been designed in a way that further additions of flight hardware can be incorporated in order to simulate more closely the HPFTP geometry. Figures 4b-d show examples of modifications which have been considered in the design of the test rig. The inlet to the first stage impeller can be modified by introducing guide vanes into the currently installed bell-mouth. Alternatively, the inlet conditions may be altered to represent a pipe flow with or without vane-induced swirl. There is also provision for installing a replica of the scroll-shaped entry stage which can be manufactured in clear cast acrylic to enable laser velocimetry studies to be conducted with identical inlet conditions to those of the HPFTP and inside the entry stage. Provision also has been made for the installation of the actual second stage

volute downstream of the first stage to simulate the proper outlet conditions. A useful alternative operating mode of the test rig is also shown in Figure 4d, whereby the downstream collector scroll is modified into a suction pump. This configuration may allow elementary studies of the flow field within the volute of the first stage in the absence of impeller-induced flow effects. The arrangements of Figures 4b-d clearly indicate that the closer to the flight configuration the rig geometry is, the more restricted the access for LDV flow studies becomes. This provides further justification to the decision of initially simplifying the flow configuration as much as permissible.

A further consideration in the design of the basic test rig was the gap and clearance similarity between the impeller exit and volute as well as in the labyrinth seals. The former were arranged identical to the actual configuration but the labyrinth seal gaps had to be doubled. This was necessary because of the relative radial flexibility of the acrylic volute and is not expected to influence the leakage flow similarity significantly, particularly when the much lower pressures in the test rig are taken into account.

### *3- Structural Design Considerations*

The primary concern for the design of the basic test rig was the provision of ample optical access at the inlet to the impeller and inside the diffuser and volute. Given the dimensions of the volute, the use of high quality glass or similar material was excluded. The next best candidate considered was high impact polycarbonate (Lexan) but this had also to be excluded because of poor optical properties and machinability difficulties. It was decided to make use of thick section Transpalite clear cast acrylic which presents moderate mechanical but superior optical properties, combined with low cost. The volute, shown in Figure 4e, was cast, machined, polished and thermally treated in two pieces, joined together with studs between two spider-shaped aluminium flanges. The splitting line of the volute is such that enables future insertion of simple geometry vanes in the radial diffuser.

The length of the annular duct downstream of the volute was dictated by fluid mechanics considerations in order to minimise the upstream effect of the collector scroll. This caused the length of the driving shaft to increase disproportionately and to cause concern for possible shaft whirl. A simple shaft analysis, however, indicated that the critical speed of the final assembly is well above 18000 rpm. This was achieved by the sizing of the shaft as well as the bearings selection. The initially selected ball and roller bearings, shown in Figure 4, were replaced by one matched pair of pre-loaded high precision angular contact (spindle) bearings (Fafnir 2MM9108WIDUL) in "O" arrangement near the impeller and a single spring-loaded spindle bearing at the floating end of the shaft. The final shaft assembly is shown in Figure 5. This arrangement, apart from increasing the stiffness of the shaft and improving the axial positioning accuracy of the impeller, also enables the test rig to run with oil or even grease lubrication, instead of the initially selected oil mist lubrication, up to speeds higher than 19000 rpm.

The simultaneous determination of the angular position of the impeller with the LDV measurements called for a high resolution and high frequency response shaft encoder device. Given the 12" diameter of the impeller any uncertainty in terms of angular position would be magnified at the impeller tip. This led to the decision to mount the shaft encoder on the shaft of the test rig rather than at the end of the driving device, taking into account the necessary intervention of a flexible coupling between them. This arrangement called for a hollow encoder disc with the encoder head mounted on the body of the test rig. The encoder selected was the Teledyne 8709-2048-MA with two tracks of 2048 lines per revolution giving angular resolution of 0.175°. Considering the 500 kHz frequency response of the reading head, the selected encoder is suitable for speeds up to 14600 rpm. The drawback of this device is its sensitivity to alignment between the disc and reading head which can deteriorate with increased shaft vibrations.

The test rig was connected to the DC motor via a high speed flexible coupling, Metastream Type TSK-11, balanced to ISO G2.8. The motor selected was a specially converted Thrige-Titan GK80-12BF9 DC motor capable of 7.8 kW (10.4 hp) at 8000 rpm, driven by a SSD-546 3-phase 2-quadrant thyristor convertor capable of maximum power output of 20 kW (26 hp) in order to accommodate future driving devices at the higher speed of 12000 rpm.

The test rig/motor assembly, views of which are shown in the photographs following Figure 5, has been mounted on a frame and balanced in situ to ISO G2.8 standards. It must be stressed here that the alignment and balancing of the assembly is strongly affected by the flexibility and, therefore, by the mounting method of the supporting frame. It is strongly recommended that the frame is rigidly mounted on a large mass concrete block and the test rig re-aligned and balanced to the same standards before operation at speeds exceeding 4000 rpm.

## PART 2: PRELIMINARY MEASUREMENTS

A number of preliminary tests have been carried out to evaluate the performance of the test rig and the feasibility of obtaining reliable LDV velocity measurements in the speed range of interest. The maximum speed achieved proved to be 7740 rpm, limited by the tachogenerator output reference circuit of the motor controller. This can be increased, if necessary, to 8000 rpm by changing a resistor value in the control unit but was not thought to be necessary since the tip Mach number matching speed is in excess of the rated speed limit of the DC motor. The shaft encoder output pulse trains were also examined and the necessary adjustments to the reading head made to obtain symmetric pulses from both channels. It is during these tests that the sensitivity of the encoder alignment to shaft vibrations was identified and cured with higher quality balancing of the test rig and optimum alignment of the encoder head. The stability of the impeller speed was measured by feeding the shaft encoder pulse train in a 1 ns resolution frequency counter and was found to be better than 0.05% over the whole speed range and to improve with shaft speed.

## **1- Discharge Flowrate Measurements**

The turbopump discharge flowrate was measured by passing the outlet flow from the collector scroll through a 4" pipe equipped with an orifice flow meter device according to BS 1042. The pressure drop across the orifice and the upstream static pressure and temperature were measured over the speed range of the turbopump without throttling its outlet. The results, shown in Figure 6, indicate a linear increase of mass flowrate with rotational speed and a less than linear increase of volume flowrate, calculated with respect to the air density at the measuring device. The volume flowrate was calculated for reasons which will become clear in the discussion of the velocity measurements. These results also suggest that the measured mass flowrate is 60% less than that predicted by the similarity analysis presented in Part 1 of this report. This discrepancy can be attributed to the fact that the similarity analysis predicts the performance of an identical turbopump stage for a different fluid. No account has been taken of the fact that the inlet and outlet conditions to the compressor are not the same to those of the flight hardware and, more importantly, that the geometry of the simplified vaneless volute differs significantly from that of the SSME HPFTP. Further to that, it is not clear if the values of the baseline performance given in Table 1 were obtained under load or not. The present measurements have been obtained in a configuration which presents load (pressure losses) in the collector scroll and flow measurement device of the order of 0.4 psi at maximum flowrate which, when compared with the predicted discharge pressure rise of 1.6 psi at 7740 rpm, are quite significant.

## **2- Velocity field Measurements**

### **2.1- Measurement System**

The laser velocimeter used for these preliminary measurements consisted of an Argon-Ion laser operating at 514 nm with power output of 0.8 W, an optical transmitting unit based on a rotating diffraction grating providing continuously variable frequency shift up to 16 MHz and a photomultiplier light collection unit. The laser beams were directed into the transparent volute by means of a mirror positioned at 45° with respect to the laser axis and the velocimeter was operated in the off-axis back-scatter or 90° scatter modes. Seeding of the flow was performed by silicone oil droplets of 1-3 microns diameter generated in a micro-fog lubricator. The positioning of the outlet pipe of the seeding generator was found to be critical for the velocity data rate and performed optimally when it was streamlined with the inlet flow to the turbopump. Similar arrangement was found to be beneficial in the turbocharger study reported in FS/87/36.

The signal from the photomultiplier was processed in a TSI 1990c counter processor the output of which was interfaced to an IBM/AT compatible computer via a purpose-built DMA card. The same interface card was fed with the 2048 pulses per revolution from the shaft encoder and allowed pairs of velocity measurements with impeller angle information to be stored in the microcomputer. The data acquisition and processing software (tsi\_g), which

was specifically developed for this application, continuously displays the number of valid velocity measurements as a function of shaft angle and allows the measurement to be terminated when a statistically adequate number of data has been acquired in all pre-determined angle windows. The measurements presented below have been obtained with approximately 1000 data per  $1.05^\circ$  (6 encoder pulses) window. This feature of the data acquisition software is particularly useful in rotating turbomachinery investigations since it allows continuous monitoring of the periodic features of the flow. The data processing software is able to analyse the velocity measurements in terms of ensemble averages within variable shaft angle windows and is also capable of overlaying and comparing the ensemble average mean and rms velocity estimates from one blade passage to the next, thus enabling blade-to-blade variations to be studied.

The data processing software supplied with the test rig also features stationary or time-resolved velocity measurement capabilities (tsl\_v) with the option of continuous monitoring of the dynamic PDF and a plotting and printing routine (plot\_g) for post-processing of stored data files.

The shaft encoder output is also processed by a dedicated counter to provide display of the impeller speed, while the same circuitry allows for the adjustment of the index (reference) pulse. This reference pulse can be positioned by a set of thumbwheel switches in any position of the  $360^\circ$  shaft rotation relative to the encoder marker pulse so that it can be adjusted to coincide with a specific angular position ( $t$ ) of the impeller.

The locations in the diffuser and volute where measurements have been obtained for this preliminary study are shown in Figure 7. They correspond to the middle plane of the radial diffuser section and extend over the apex of the volute along a diametral plane of the turbocompressor. The coordinate and sign conventions are also shown in Figure 7. Radial (V) and swirl (W) velocity components were measured for an impeller rotational speed of 4260 rpm (71 Hz) and some measurements are also reported for the same locations for speeds of 6084 rpm (101.4 Hz) and 7680 rpm (128 Hz). For the measurements presented below, the position of the index pulse ( $t=0$ , zero angle reference) was arbitrarily set to 20 pulses from the encoder marker pulse.

## 2.2 LDV Data Rate

Figure 8 shows the sample size per  $1.05^\circ$  averaging window for four measurement locations which also corresponds to the data arrival rate for the specific impeller angular positions. The distinct feature which can be observed is the periodicity of the data arrival rate which corresponds to the impeller rotational frequency multiplied by six, the number of main blades. The deeps of the sample size curves correspond to lower velocity magnitudes and indicate that, for a finite averaging time, smaller number of slow rather than fast seeding particles is observed. This is typical of periodically varying flows and illustrates the "velocity bias" effect that conventional population averaging would introduce in the statistics of such samples. It should be stressed,

however, that the conditional angle-resolved averaging performed here minimises this bias.

The graphs of Figure 8 also show that the flow periodicity induced by the impeller blades is evident even at 35 mm away from the impeller, although with attenuated effect. This will become clearer in the discussion of the corresponding velocity magnitude measurements.

### 2.3 Blade-to Blade Variations

Figure 9 presents swirl and radial mean and turbulent velocity component measurements obtained at four locations and for the three impeller speeds investigated, as indicated on the individual graphs. These measurements, which were obtained throughout the 360° revolution, are presented as six superimposed traces in a 60° window and illustrate the blade-to-blade variability (or periodic repeatability) of the flow. The results clearly indicate that the flow exhibits a very good periodic repeatability, particularly as far as the position of the steep temporal velocity gradients is concerned. This is attributed to the high manufacturing standards of the impeller and is not a usual feature of common high speed turbocompressor impellers (see, for example FS/87/36). Some blade-to-blade flow variations are observed in regions of near constant velocities, mainly in the radial direction. These variations may be attributed to imperfections in the positioning and sizing of the splitter blades, but their relative magnitudes are small.

The above results, apart from confirming the manufacturing standards of the HPFTP impeller, enhance the confidence level of the LDV measurements and of their angular resolution. They also suggest that averaging of velocity data over all six main blade passages, although not recommended, will not introduce a significant error.

### 2.4 Flow in the Radial Diffuser

Radial and swirl velocity measurements were obtained at all measurement locations shown in Figure 7 for an impeller rotational speed of 4260 rpm and the results are shown in the graphs of Figure 10. Each graph is individually labelled as for the measured variable and location.

The radial and swirl velocity measurements obtained in the middle plane of the radial diffuser ( $z=6.5$  mm) and close to the impeller ( $r=2$  mm) exhibit the characteristic blade-to-blade periodicity mentioned in section 2.1 but also present evidence of flow oscillations within a blade passage period which can be attributed to the presence of the two splitter blades in each main passage. They also indicate that the swirl component varies between 44 and 59 m/s (25%), as compared to the blade tip velocity which is 68 m/s for the impeller rotational speed of 4260 rpm, and the radial velocities fluctuate by more than 50% around 9 m/s. Comparison of the swirl and radial velocity magnitudes suggests that the angle of the velocity vector in the  $r-t$  plane also fluctuates around 80° with respect to the impeller radius. It is also seen that the maximum radial velocity occurs when the swirl velocity is minimum and

vice versa indicating that, very close to the exit of the impeller, the velocity vector on the  $r-t$  plane abruptly changes direction from  $75^\circ$  to  $85^\circ$  with respect to the radius as the main blade passes by the measurement location. The turbulent velocity magnitudes also vary accordingly, being higher in regions of steep temporal velocity gradients.

At radial location  $r=5$  mm from the impeller tip, the radial velocities appear higher and the swirl velocities lower than the corresponding ones at  $r=2$  mm, indicating a reduction of the vector angle to around  $700-820$  with respect to the impeller radius. Similar flow features within the impeller blade passage period are observed as at  $r=2$  mm, with the effects of the splitter blades still evident. Turbulence levels are similar to those at  $r=2$  mm but exhibit lower peak values in the regions of steep velocity gradients with average relative intensity values of 40% and 10% in the radial and swirl directions, respectively.

Similar trends are observed in measurement locations  $r=10$  and  $r=15$  mm where the radial velocities keep increasing and the swirl velocities decreasing with radial distance. The characteristic blade-to-blade periodicity is clearly evident but the swirl velocity now fluctuates by only 12% around a mean value of 45 m/s and the radial velocities by 30% around an average value of 12 m/s. Relative turbulence intensities remain of the same order of magnitude as in the previous measurement locations.

By  $r=20$  and  $25$  mm, the mean swirl velocity fluctuations around the average value have been reduced to 10% and the corresponding radial velocity fluctuations to 25%. The flow patterns within a blade passage period have also been smoothed out, indicating that at these locations the presence of the splitter blades is not felt by the flow.

At  $r=35$  mm, which corresponds to the outlet of the radial diffuser, the average flow angle with respect to the impeller radius is  $760$ , although it still varies with impeller rotation angle. Relative turbulence intensities remain of the order of 40% and 10% on the radial and swirl directions, respectively and are still influenced by the impeller angle. It is not before half-way down in the turn-around section of the volute ( $r=40$ ,  $z=20$  mm) that the turbulence magnitudes appear to be independent of impeller rotation, with magnitudes around 1.65-1.7 m/s, while the mean velocities still exhibit their characteristic periodicity at the exit of the turn-around section of the volute, with the exception of the radial velocities which, anyhow, are near-zero.

At  $r=35$ ,  $z=40$  mm, which is the last measurement location in the volute middle plane, the velocity vector angle in the  $r-t$  plane is very near  $880$  with respect to the impeller radius, suggesting the presence of a net swirl motion inside the volute, which should be kept responsible for the increased losses and reduced discharge capacity of the turbopump, discussed in section 1 of Part 2. These results indicate that, if the discharge flowrate of the turbopump were to be increased for this rotational speed, the incorporation of guide vanes in the radial diffuser would be mandatory.

The presentation of the above preliminary data also indicates that the amount of data generated by the measurement system is very large and their interpretation not straightforward. It is worth mentioning that each graph from those of Figure 10 contains information from over 400,000 individual realisations. The interpretation of the results will benefit from a presentation software, probably of the type of "animated" vector plots, which would be able to cope with the large amount of acquired information.

### 2.5 Effect of Impeller Speed

Figure 11 presents data of mean and turbulent radial and swirl velocity components, obtained at locations  $z=6.5$ ,  $r=10$ , 20 and 30 mm for an impeller rotational speed of 6084 rpm. The velocity scales have been selected to match those of the corresponding measurements of Figure 10 based on a linear increase of velocity magnitudes with impeller speed. As can be seen from a comparison between the corresponding graphs, the flow features are very similar for the two impeller speeds, particularly as far as the swirl velocity variation with impeller rotational angle is concerned. The mean velocity magnitudes in the radial direction do not appear to scale with rotational speed but the swirl velocities scale fairly well. The scaling of the swirl velocities is considerably improved if the scaling factor is taken as the volume flowrate at a given speed rather than the speed itself. The impeller speed ratio is  $6084/4260=1.428$ , while the volume flowrate ratio for the two speeds, as deduced from Figure 6, is 1.345. The angle of the velocity vector on the  $r-t$  plane is, again, of the order of 80°. The turbulent velocities increase in-line with the mean velocity gradients and follow similar patterns to those at the lower speed.

The results of the swirl velocity measurements obtained for impeller speed of 7680 rpm are shown in Figure 12 and exhibit similar behaviour to those of the lower speeds, both in terms of characteristic flow features and scaling with volume flowrate.

It can be concluded that, for the impeller speed range investigated, the flow field structure in the radial diffuser was not substantially affected by rotational speed. This may allow the study of the flow in this basic simulation of the SSME HPFTP rig to be conducted in relatively low speeds, particularly since the turbopump flow coefficient similarity does not appear feasible without the introduction of guide vanes in the diffuser volute.

## CONCLUSIONS

The principles and details for the design of a test rig simulating the first stage of the High Pressure Fuel Turbopump of the SSME, together with preliminary measurements of the performance and flow field inside the model turbopump volute have been reported. The main conclusions of this study can be summarised as follows:

- 1) The test rig design and construction satisfies the required specifications in terms of operating characteristics and optical accessibility for laser velocimetry studies.
- 2) The flow coefficient of the turbopump rig was less than that predicted by the similarity analysis performed on the basis of the HPFTP flight data, primarily due to simplifications in the volute geometry.
- 3) The LDV measurement system performed satisfactorily in terms of reliability and accuracy in the speed range of interest.
- 4) The blade-to-blade flow repeatability was very good due to the high manufacturing standards of the SSME HPFTP impeller.
- 5) The flow inside the diffuser and volute of the turbopump has been studied for an impeller rotational speed of 4260 rpm and the results suggest that the lack of guide vanes in the diffuser/volute arrangement allows the development of high swirl velocities at the expense of the radial velocities, thus reducing significantly the flow capacity of the model turbopump.
- 6) The flow field inside the radial diffuser was studied for rotational speeds up to 7680 rpm and the results revealed minor only effects of impeller speed on the overall flow structure.

## LIST OF FIGURES

Fig. 1 The SSME High Pressure Fuel Turbopump

Fig. 2 HPFTP first stage impeller

Fig. 3 HPFTP first stage diffuser volute

Fig. 4 Basic geometry of the test rig

Fig. 5 Details of the final shaft assembly

Fig. 6 Discharge flowrate of the turbopump

Fig. 7 Measurement locations and sign conventions

Fig. 8 Variation of sample size per  $10^6$  window as a function of measurement location

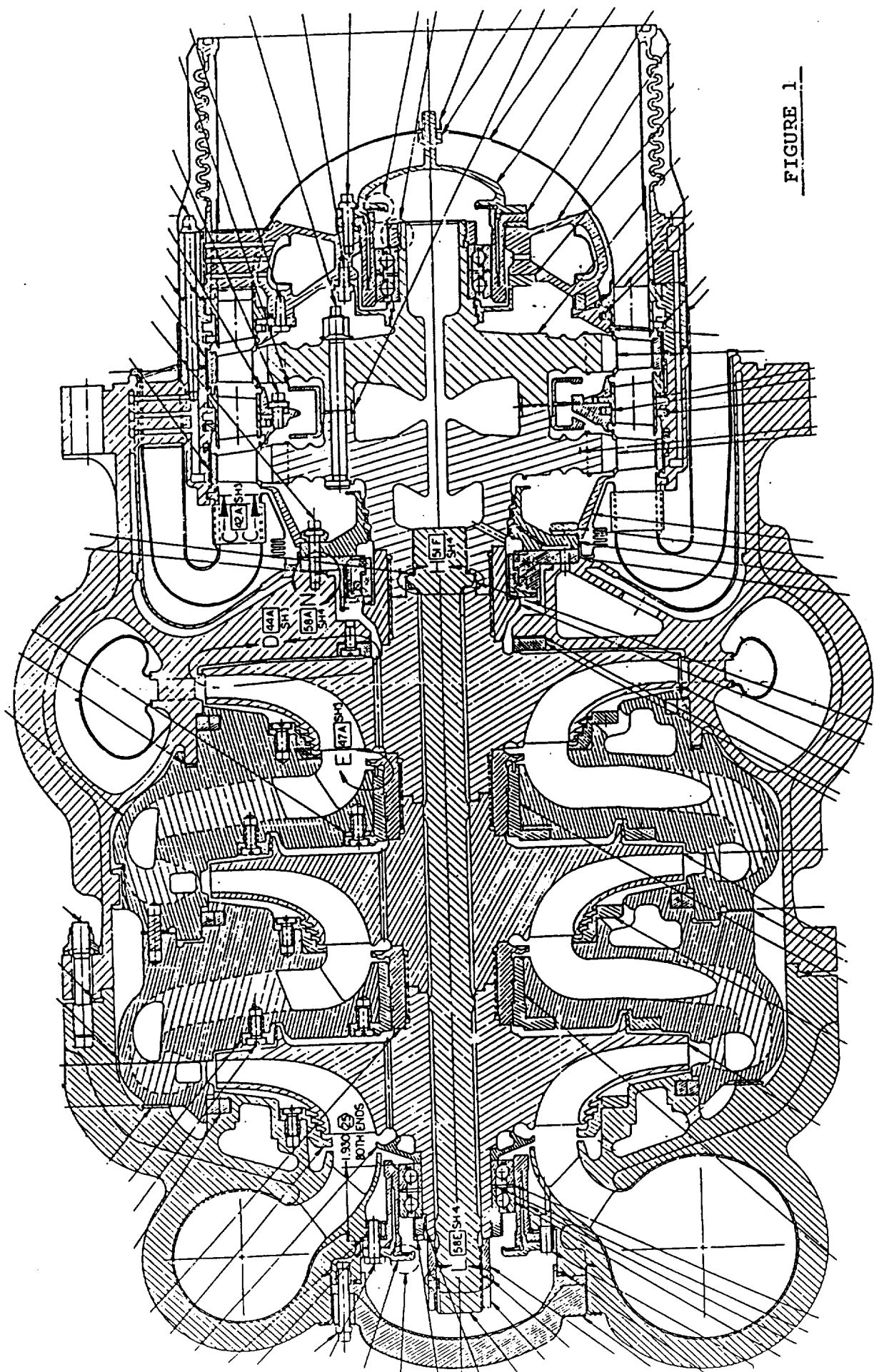
Fig. 9 Comparison of mean and turbulent velocity magnitudes in six  $60^\circ$  intervals of a revolution, for various velocity components, measurement locations and impeller rotational speeds.

Fig. 10 Variation of mean and turbulent radial and swirl velocity components in the middle plane of the radial diffuser as a function of impeller rotation. Turbopump rotational speed: 4260 rpm.

Fig. 11 Variation of mean and turbulent radial and swirl velocity components in the middle plane of the radial diffuser as a function of impeller rotation. Turbopump rotational speed: 6084 rpm.

Fig. 12 Variation of mean and turbulent swirl velocity component in the middle plane of the radial diffuser as a function of impeller rotation. Turbopump rotational speed: 7680 rpm.

**FIGURE 1**



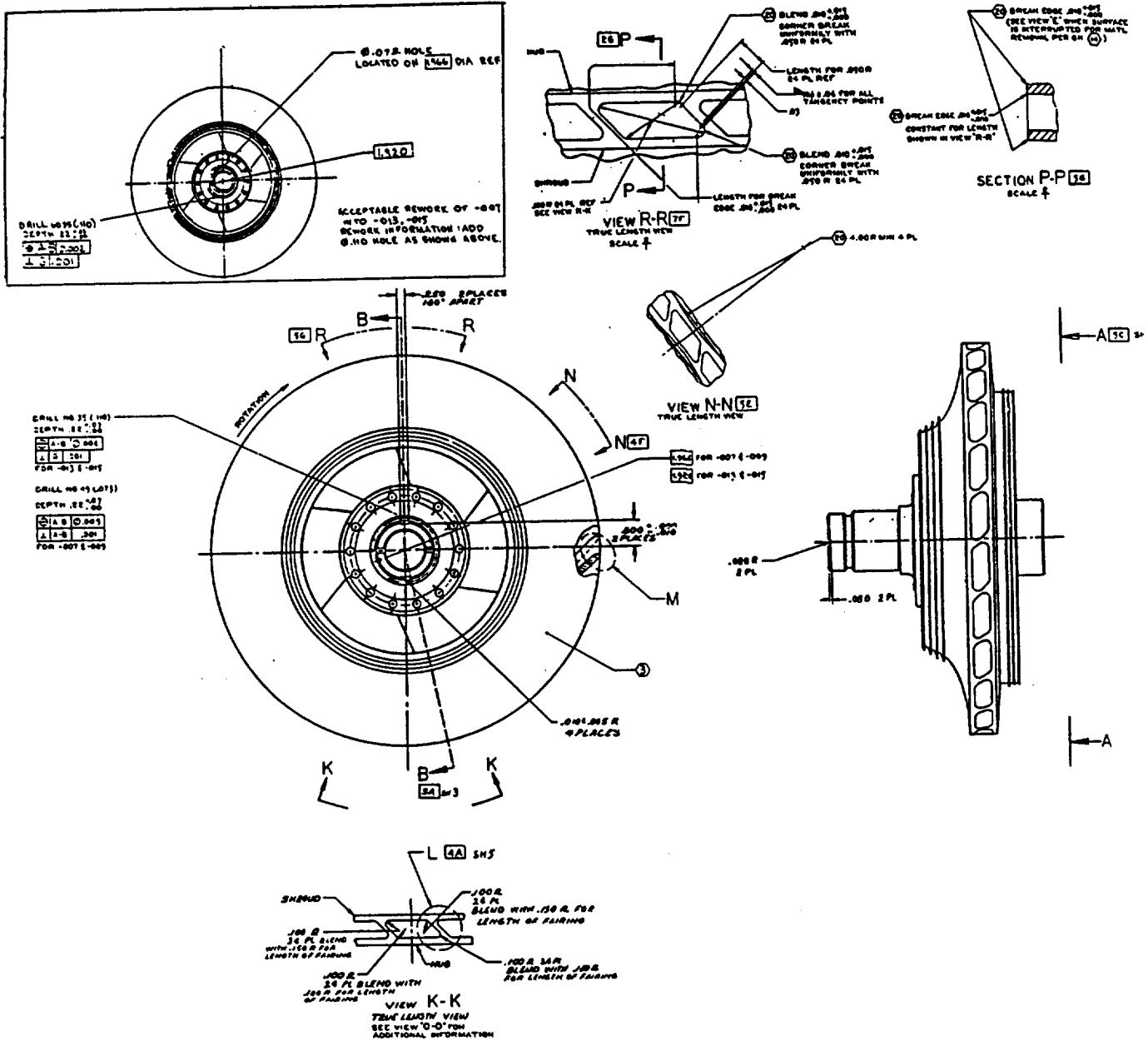
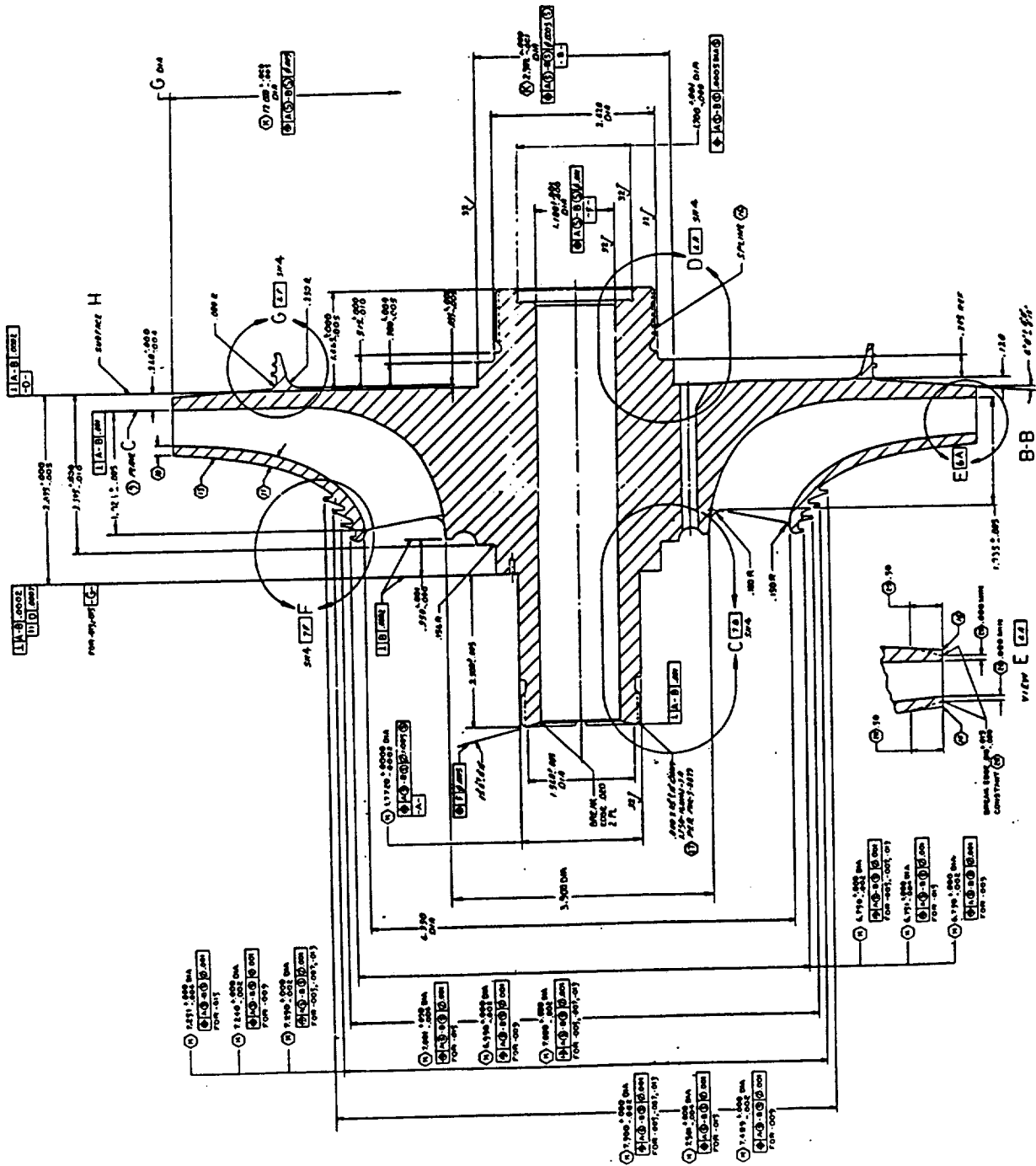
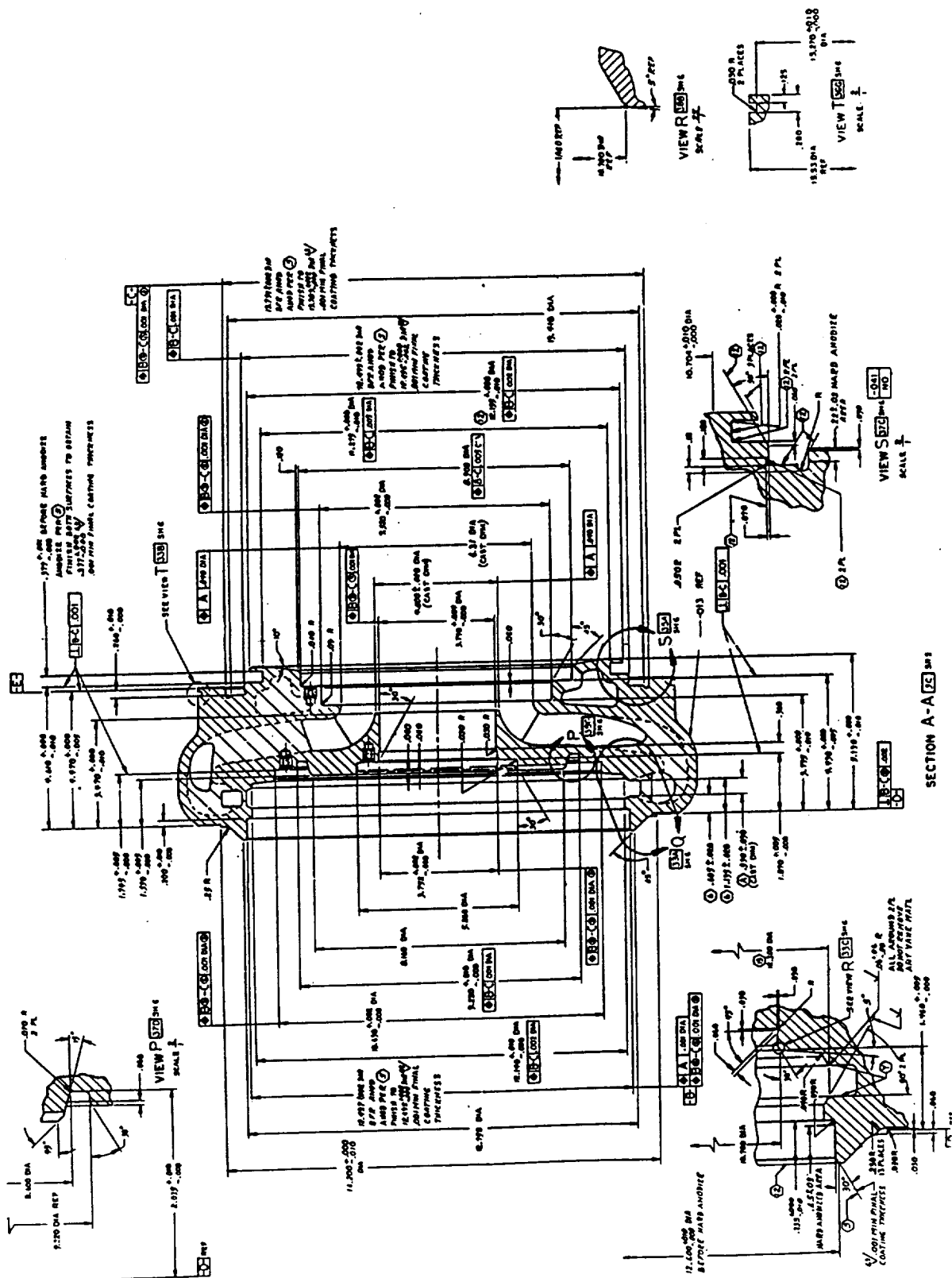


FIGURE 2a

**FIGURE 2b**



ORIGINAL PAGE IS  
OF POOR QUALITY



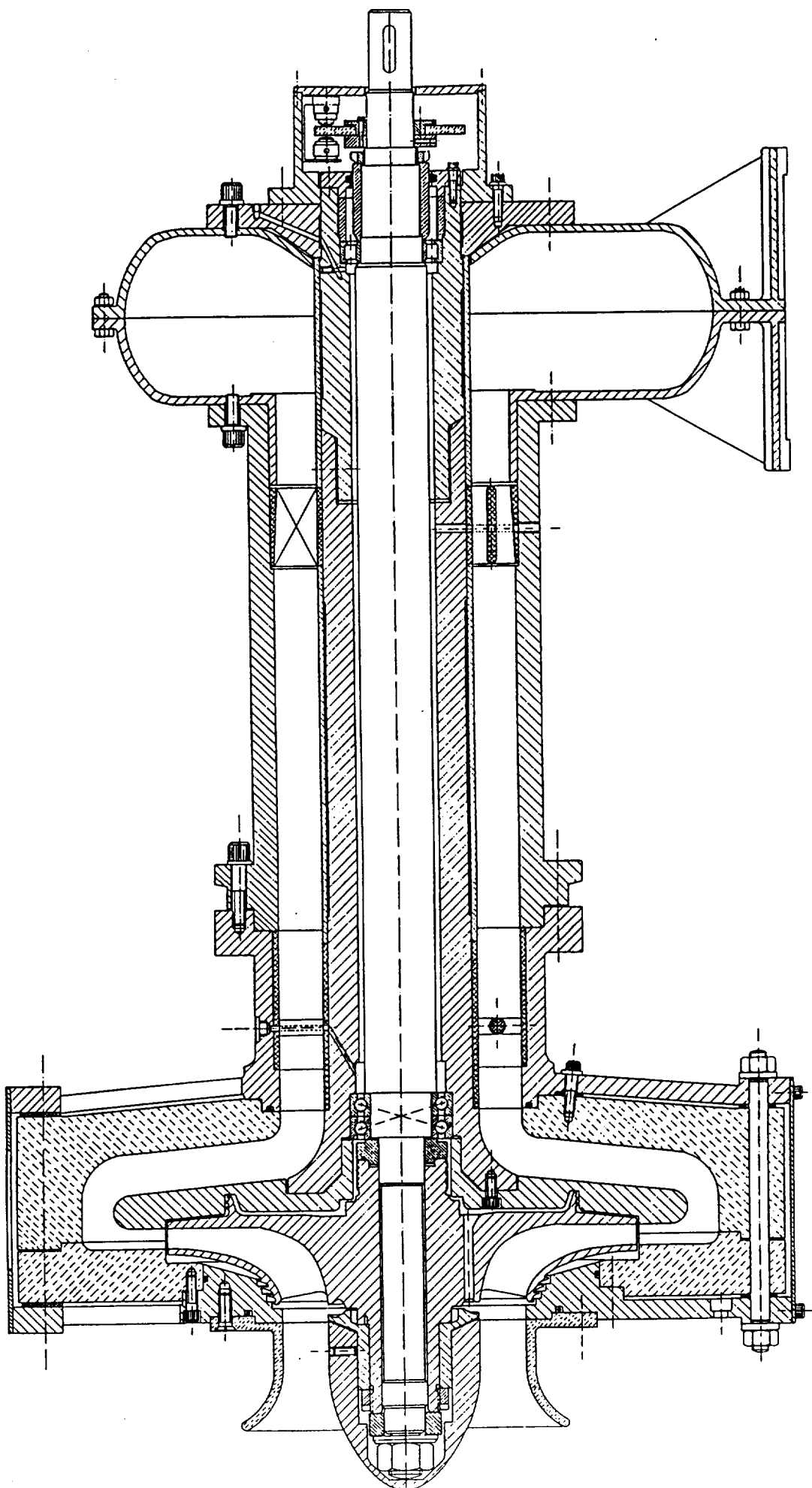


FIGURE 4a

ORIGINAL DRAWING IS  
OF POOR QUALITY

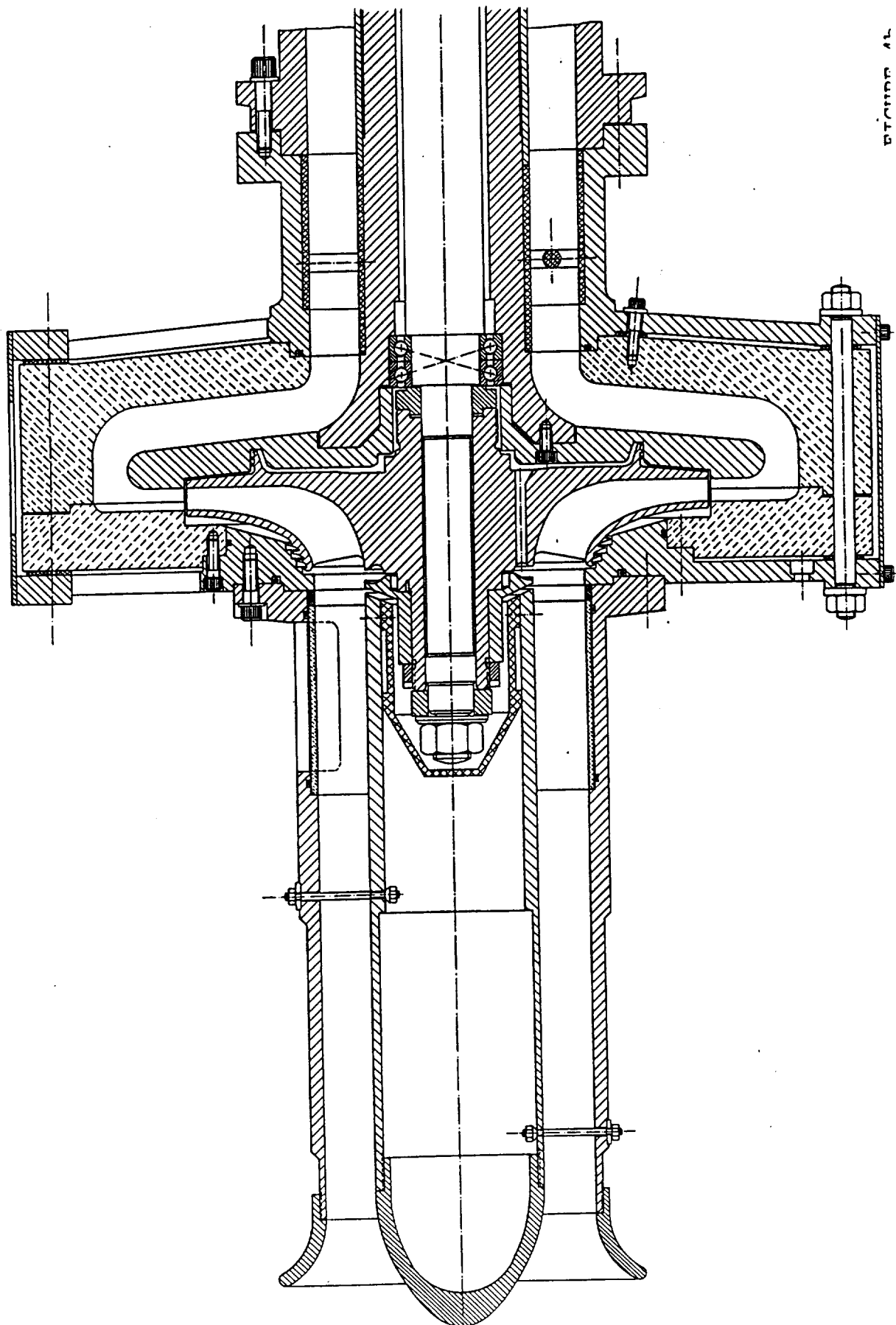


FIGURE 4C

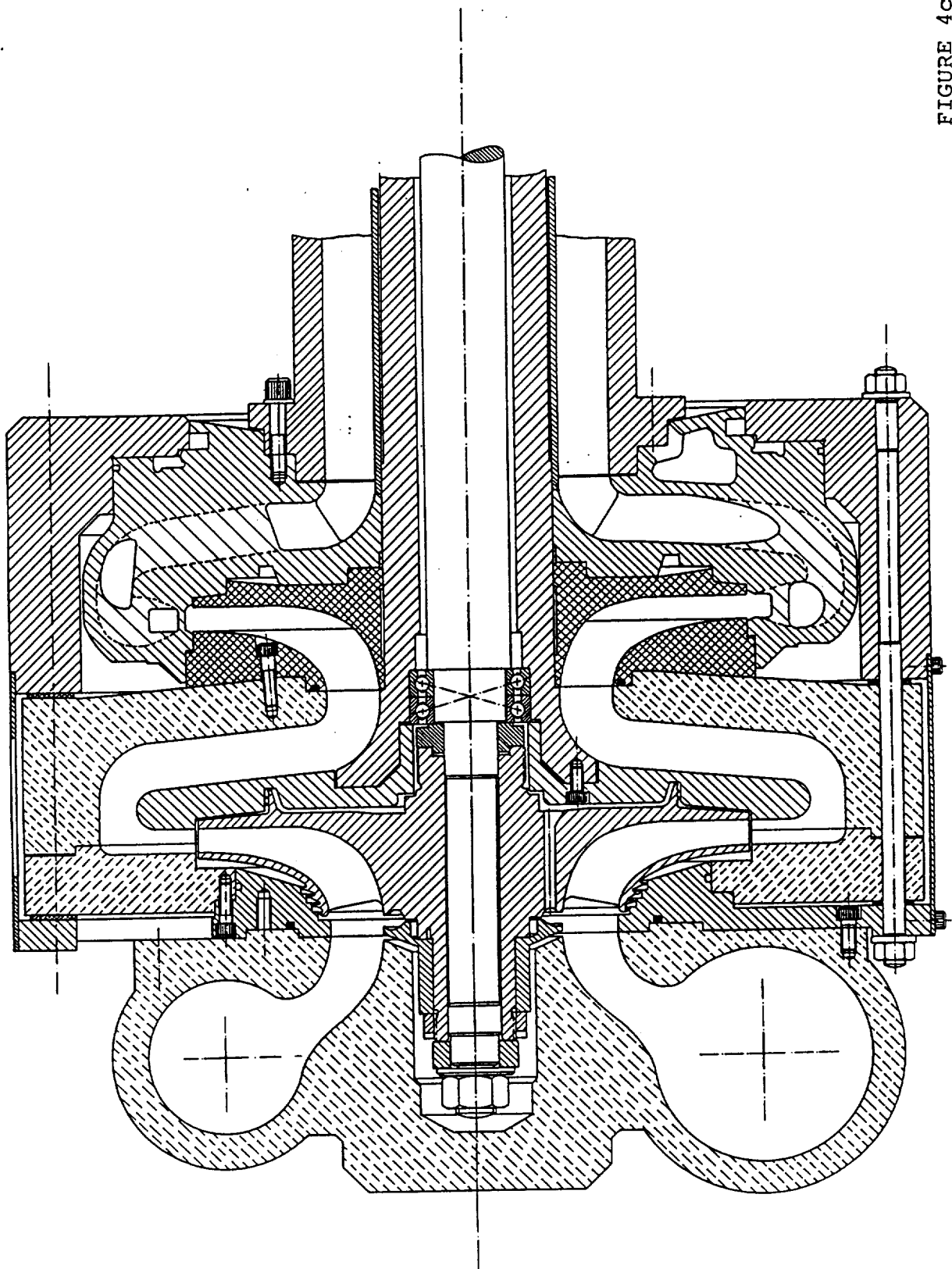
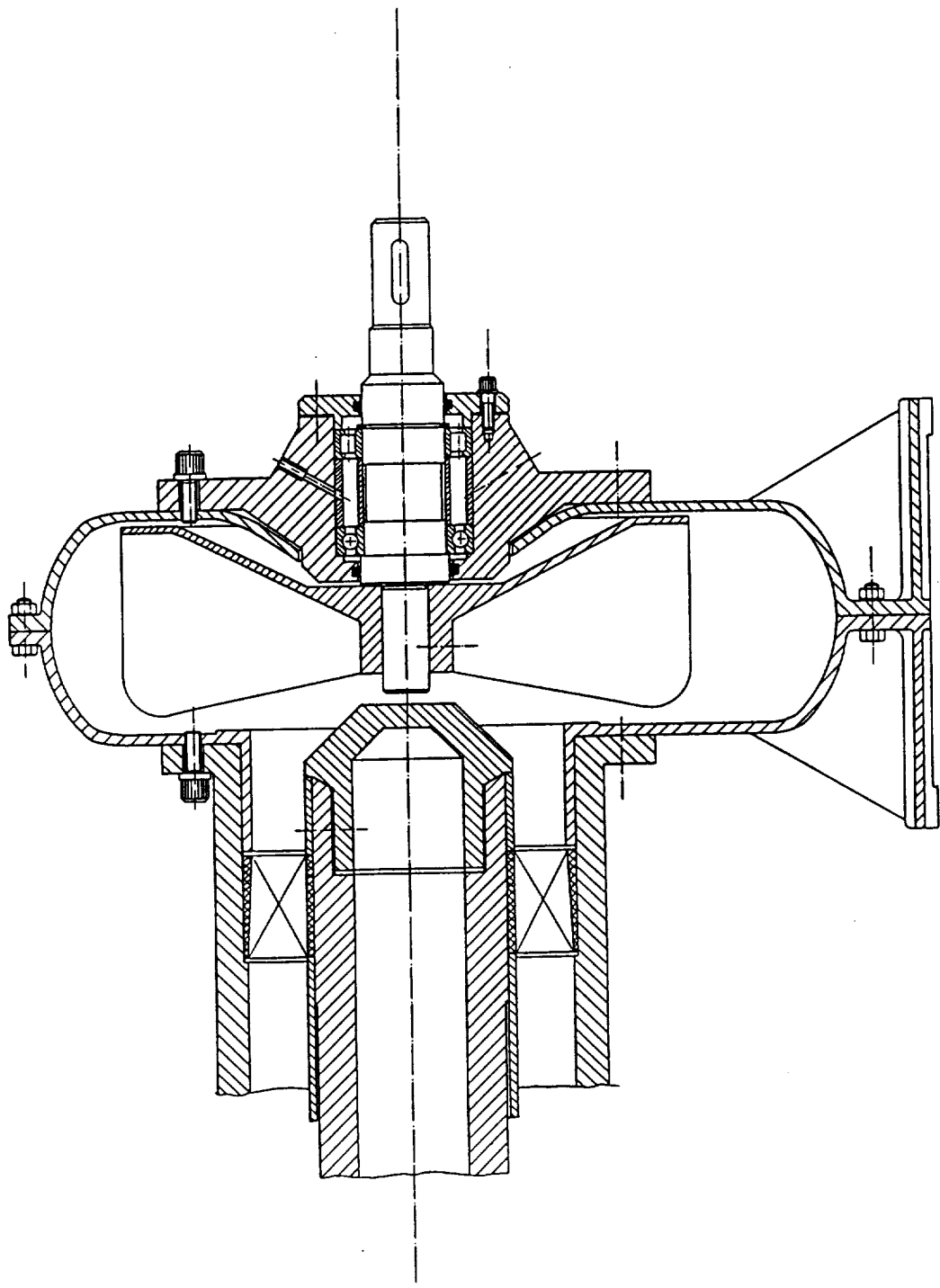


FIGURE 4d



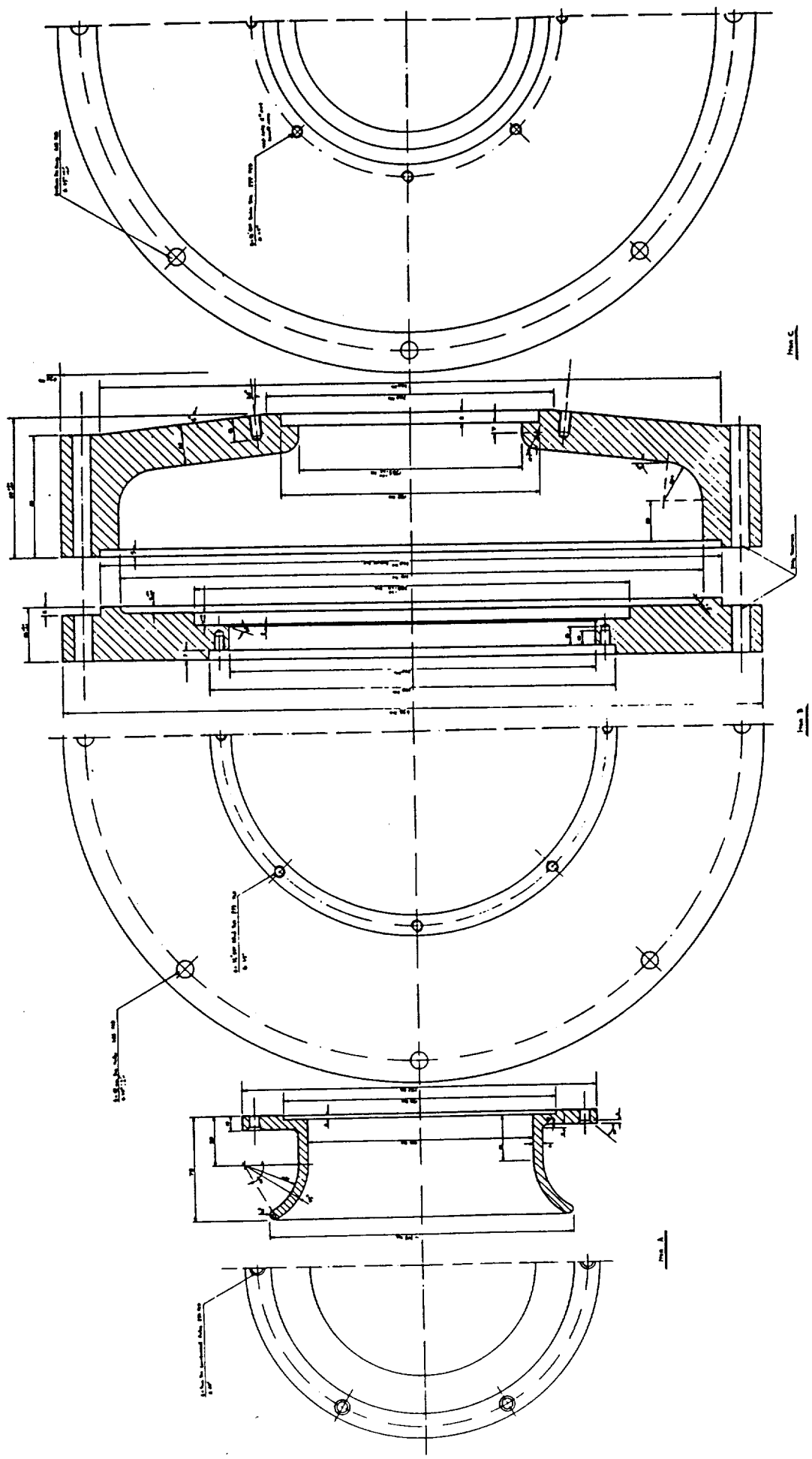
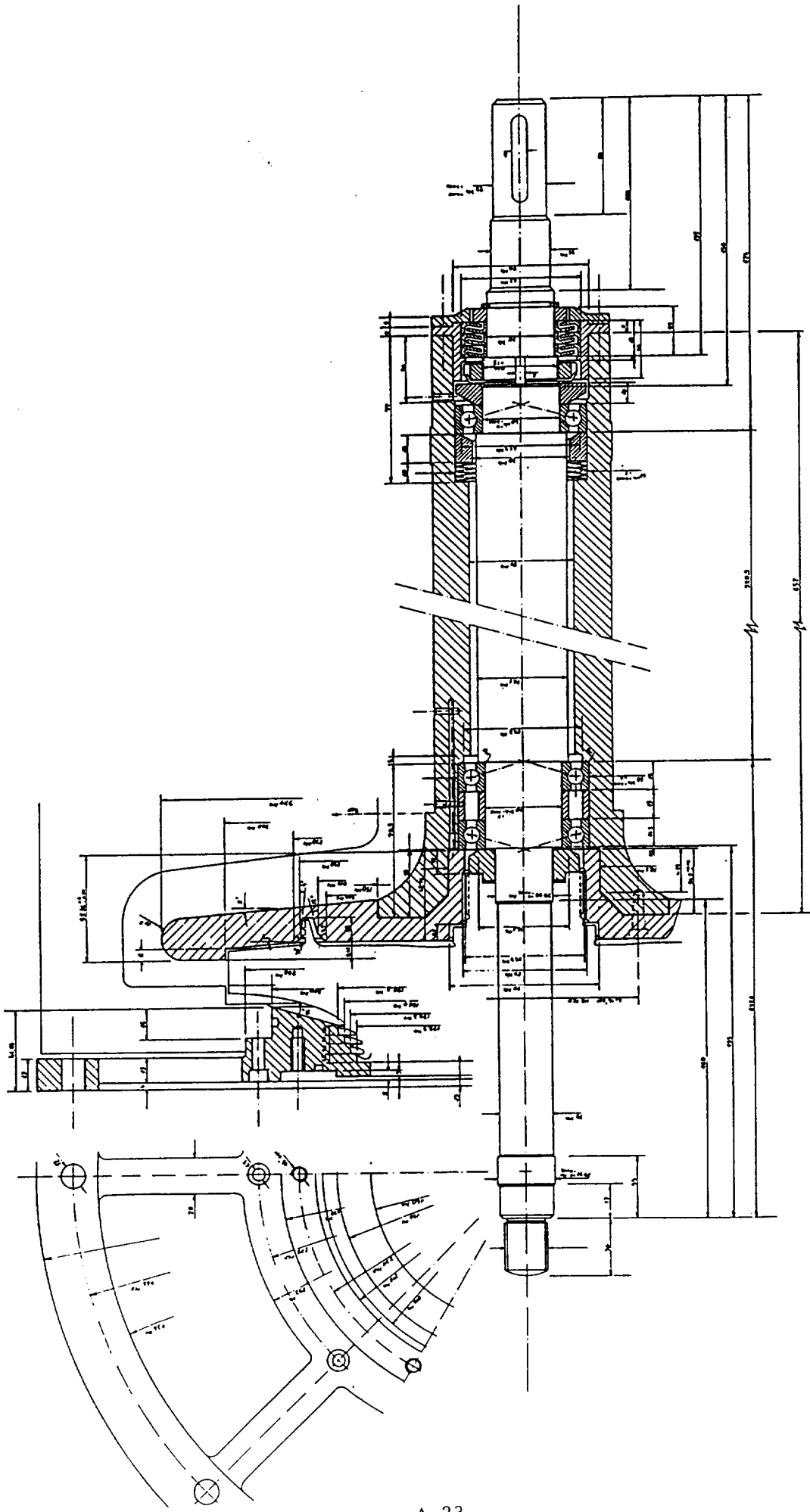


FIGURE 4e

FIGURE 5



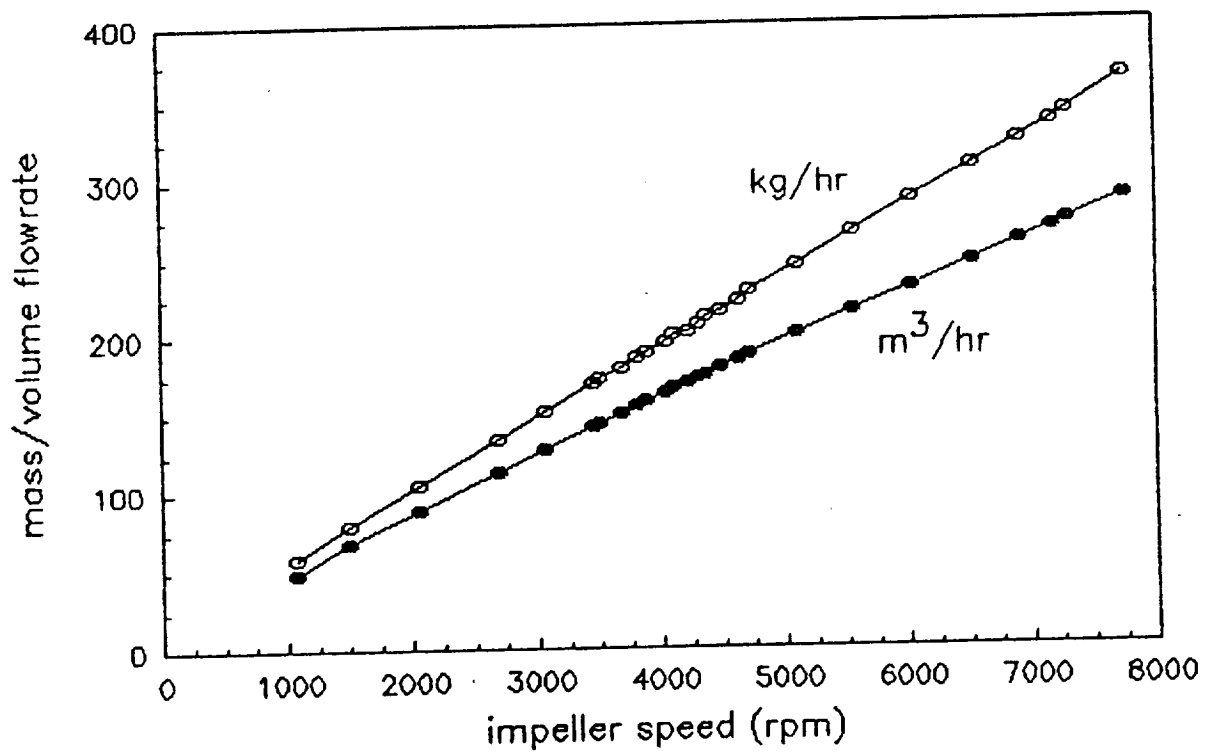
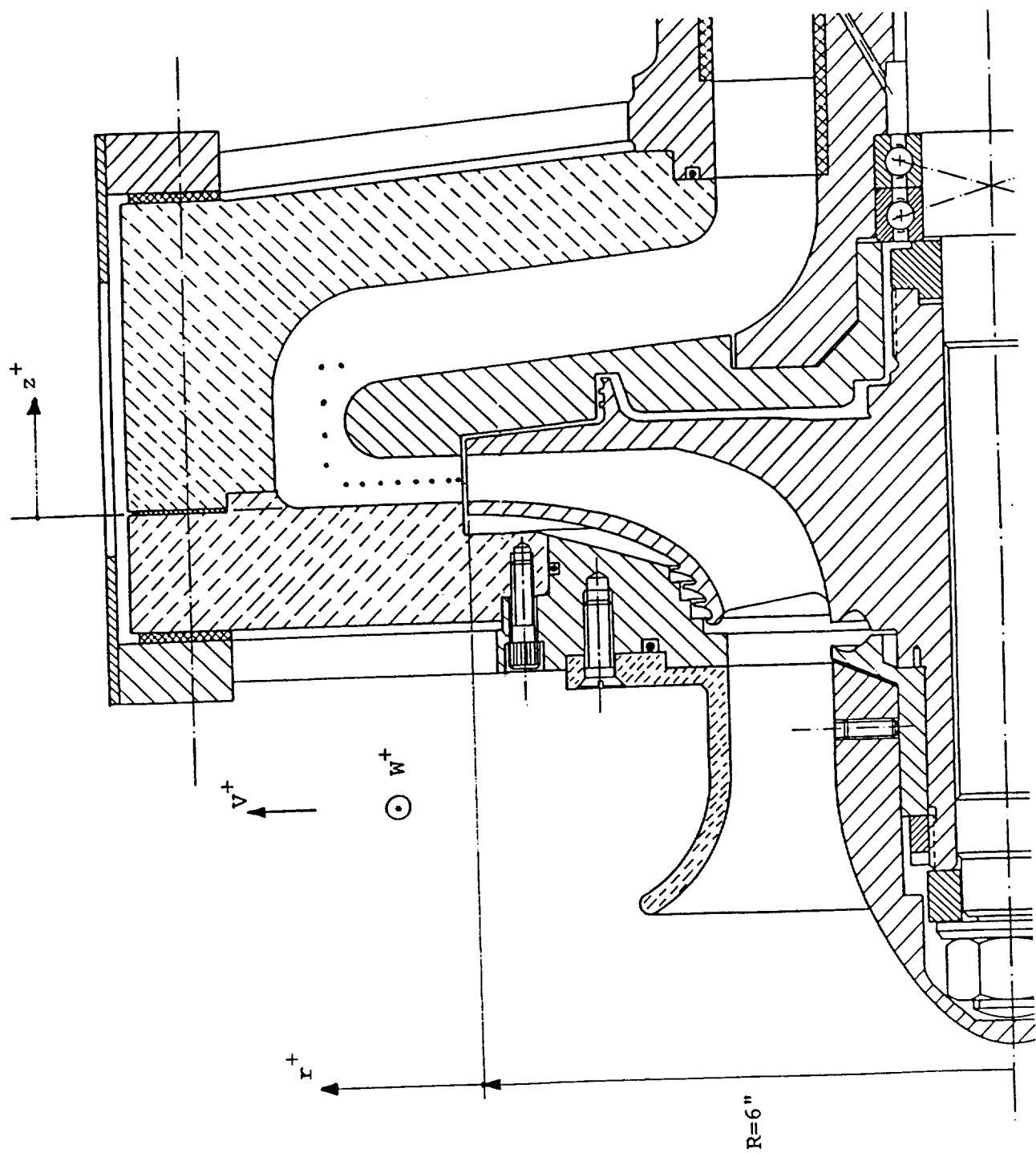
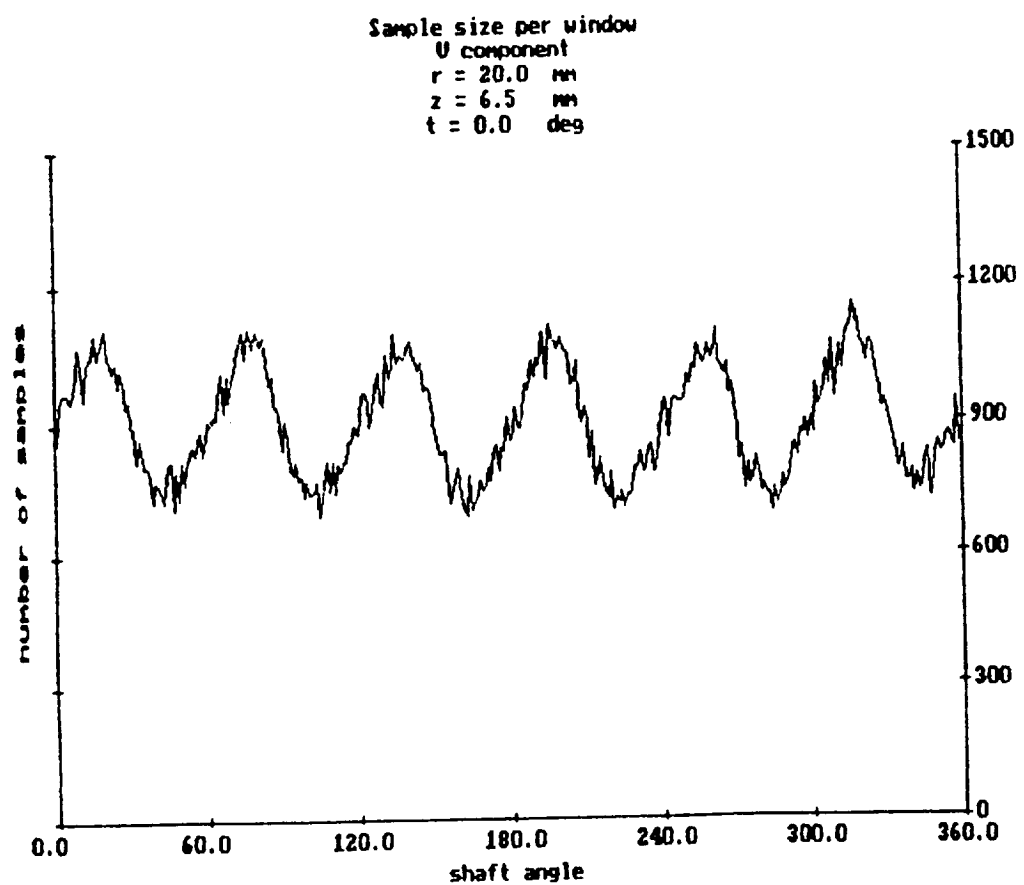
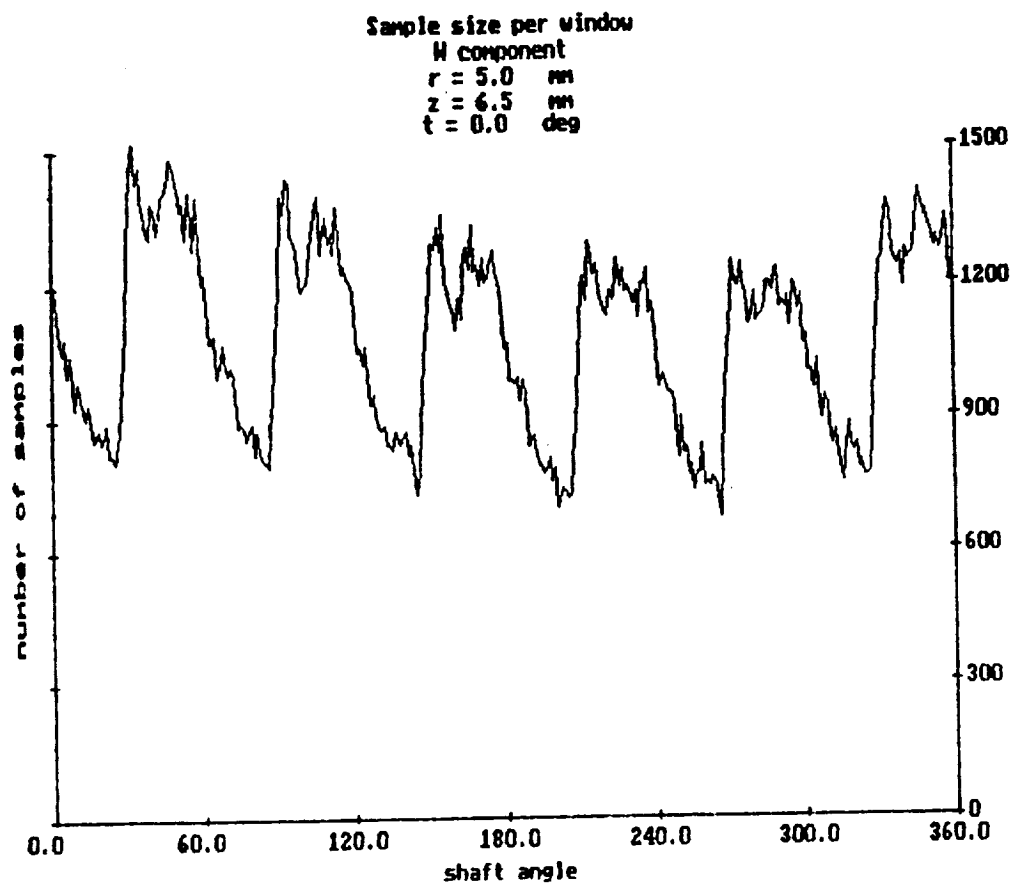
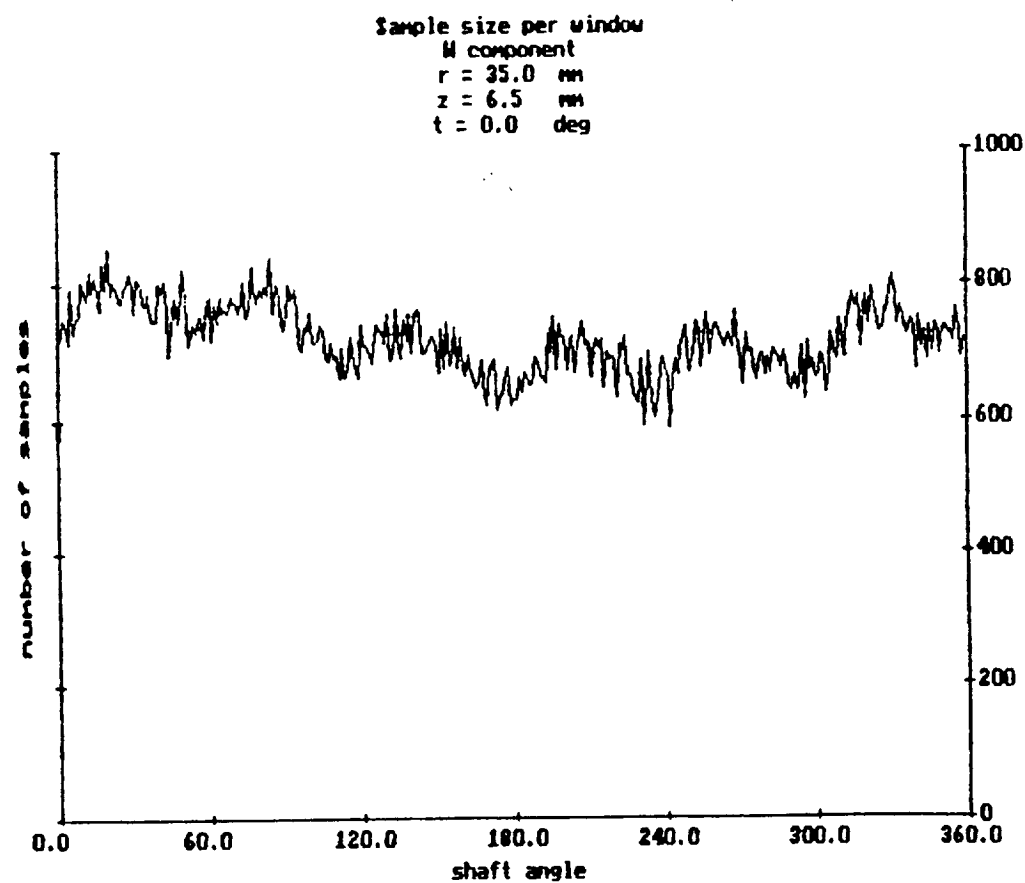
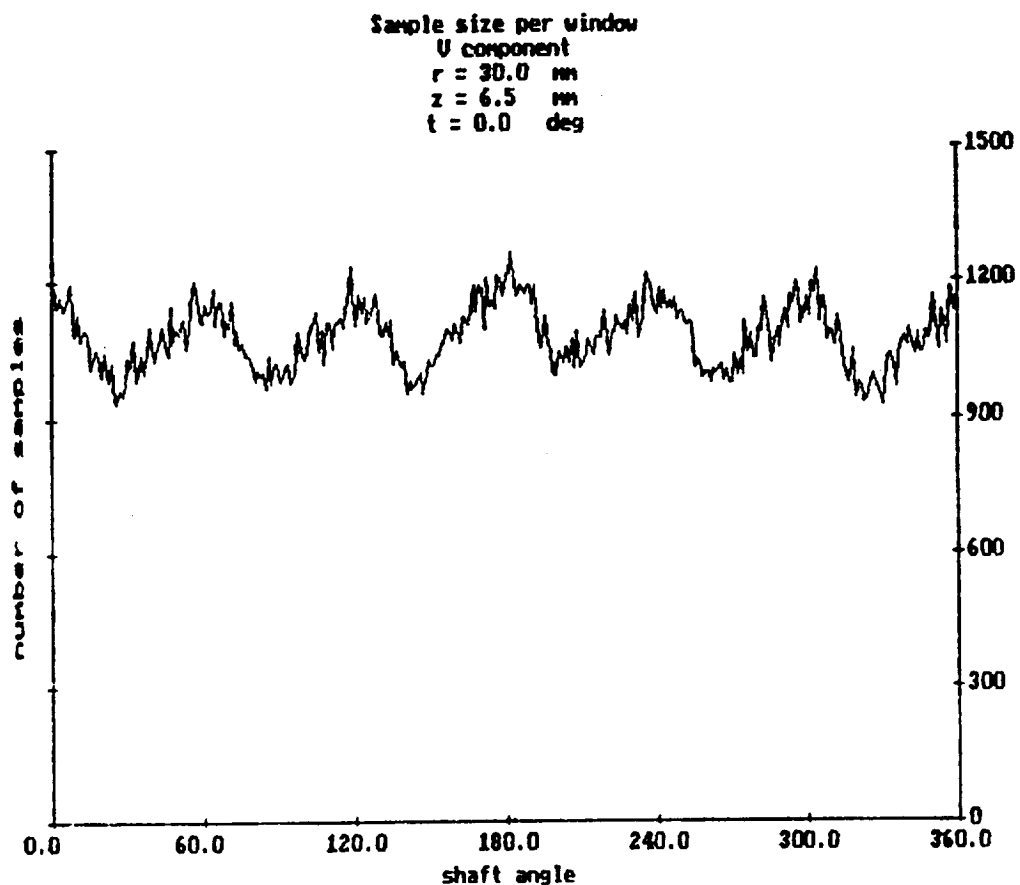


FIGURE 6



**FIGURE 8**





**FIGURE 9**

Mean Velocity (blades overlapped)

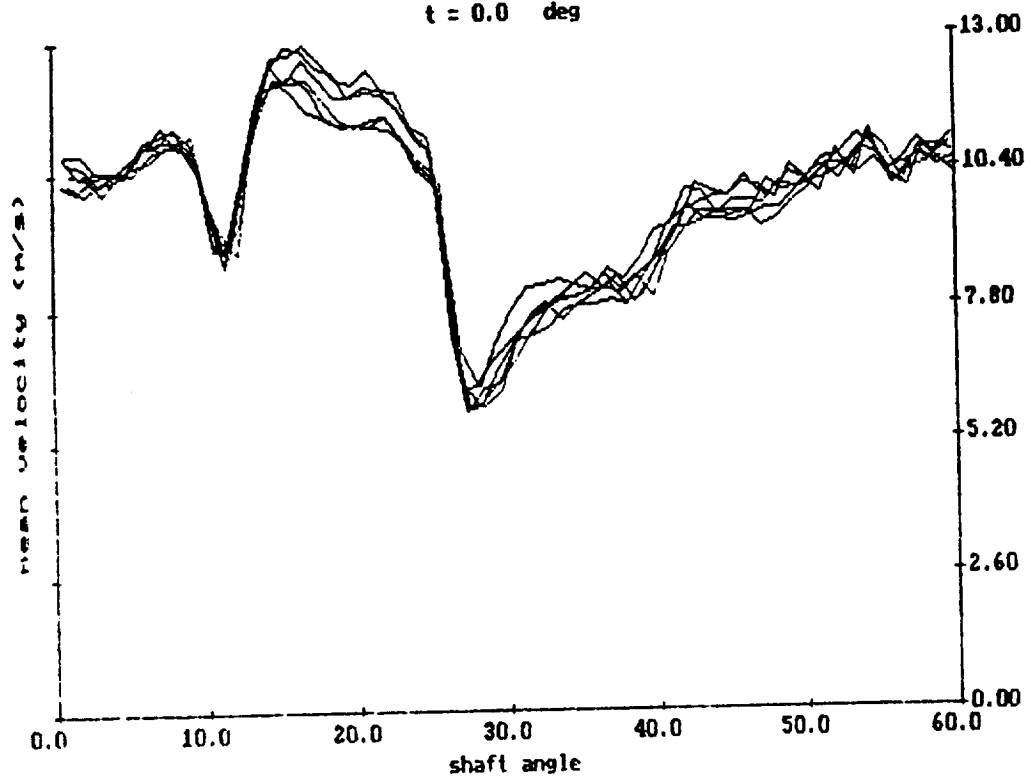
4260 rpm

U component

r = 2.0 mm

z = 6.5 mm

t = 0.0 deg



Mean Velocity (blades overlapped)

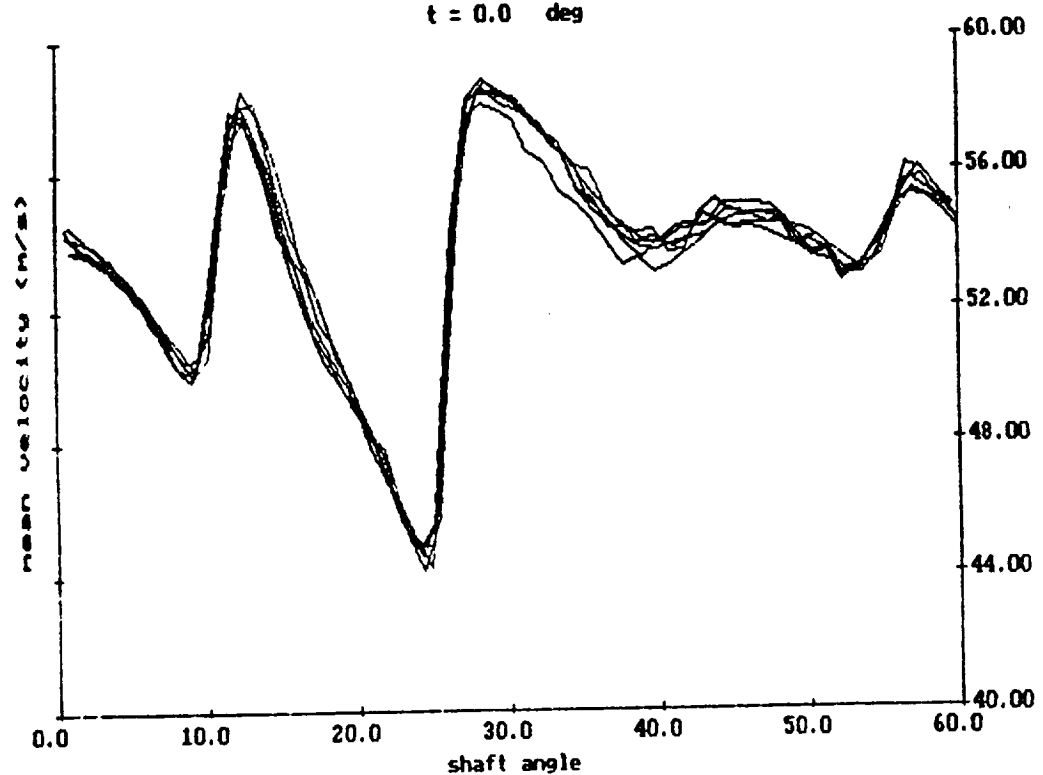
W component

r = 2.0 mm

z = 6.5 mm

t = 0.0 deg

4260 rpm



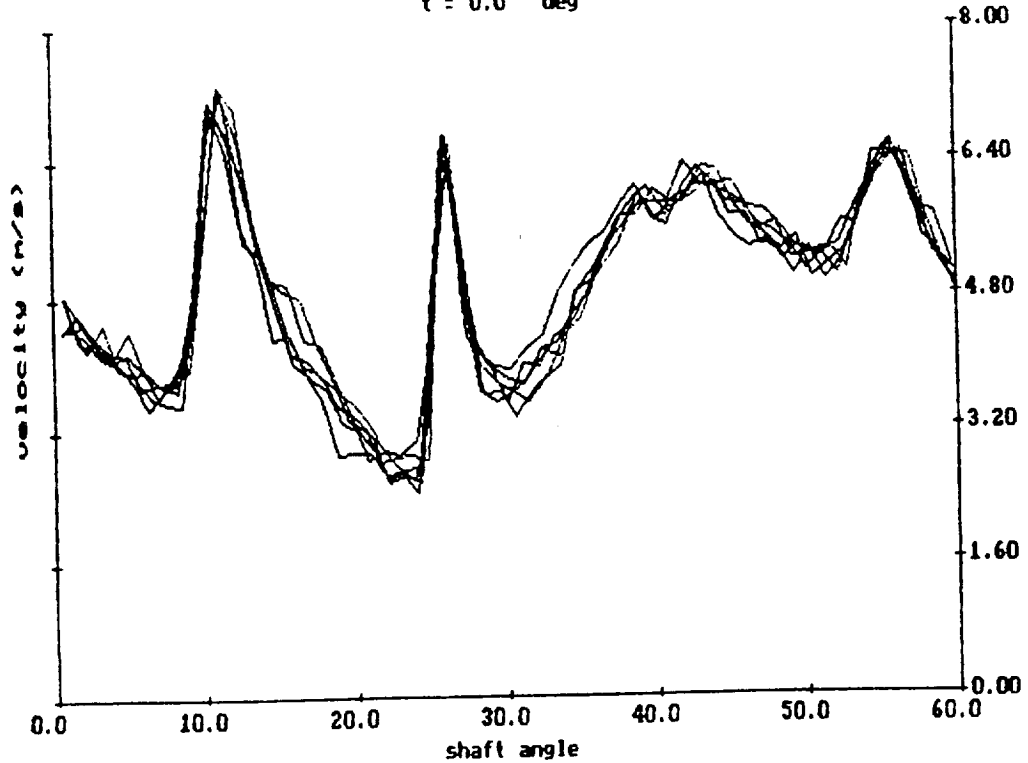
RMS Velocity (blades overlapped)

W component

r = 2.0 mm

z = 6.5 mm

t = 0.0 deg



Mean Velocity (blades overlapped)

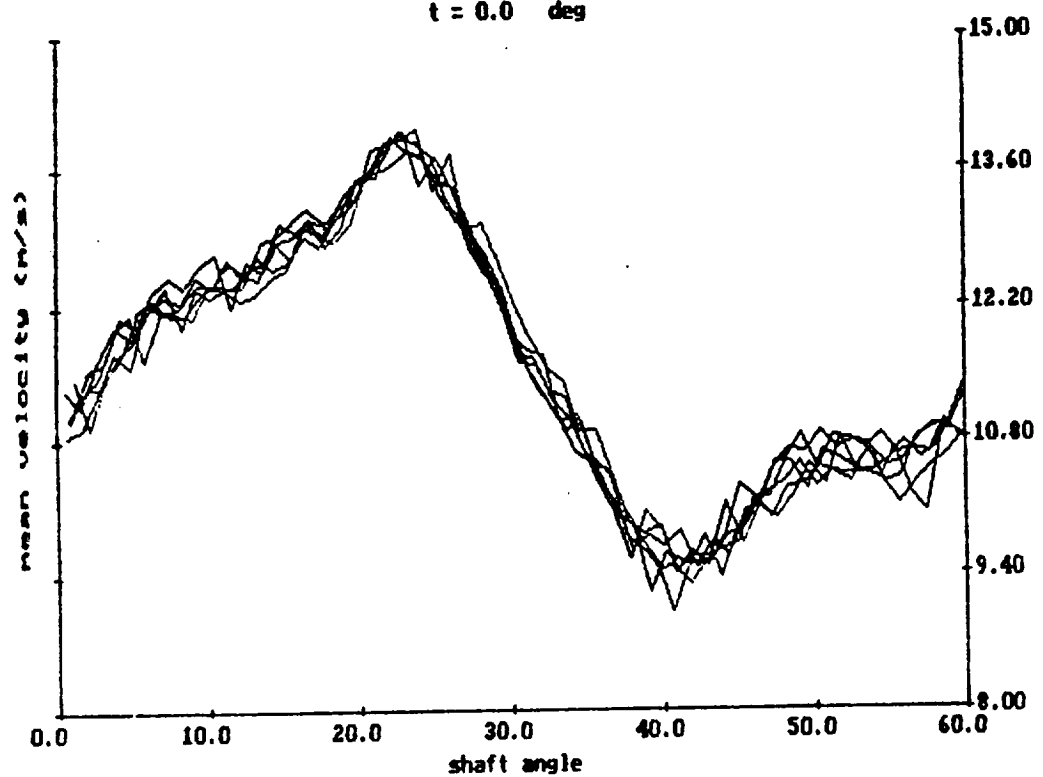
$U$  component

$r = 15.0$  mm

$z = 6.5$  mm

$t = 0.0$  deg

4260 rpm



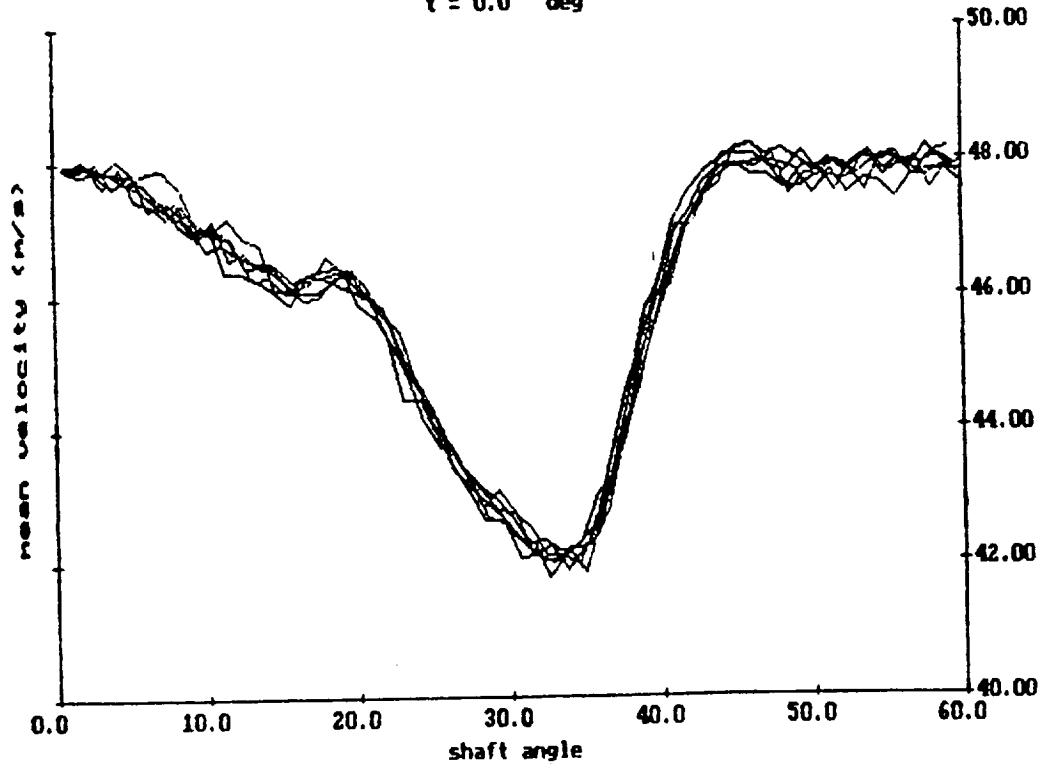
Mean Velocity (blades overlapped)

$W$  component

$r = 15.0$  mm

$z = 6.5$  mm

$t = 0.0$  deg



Mean Velocity (blades overlapped)

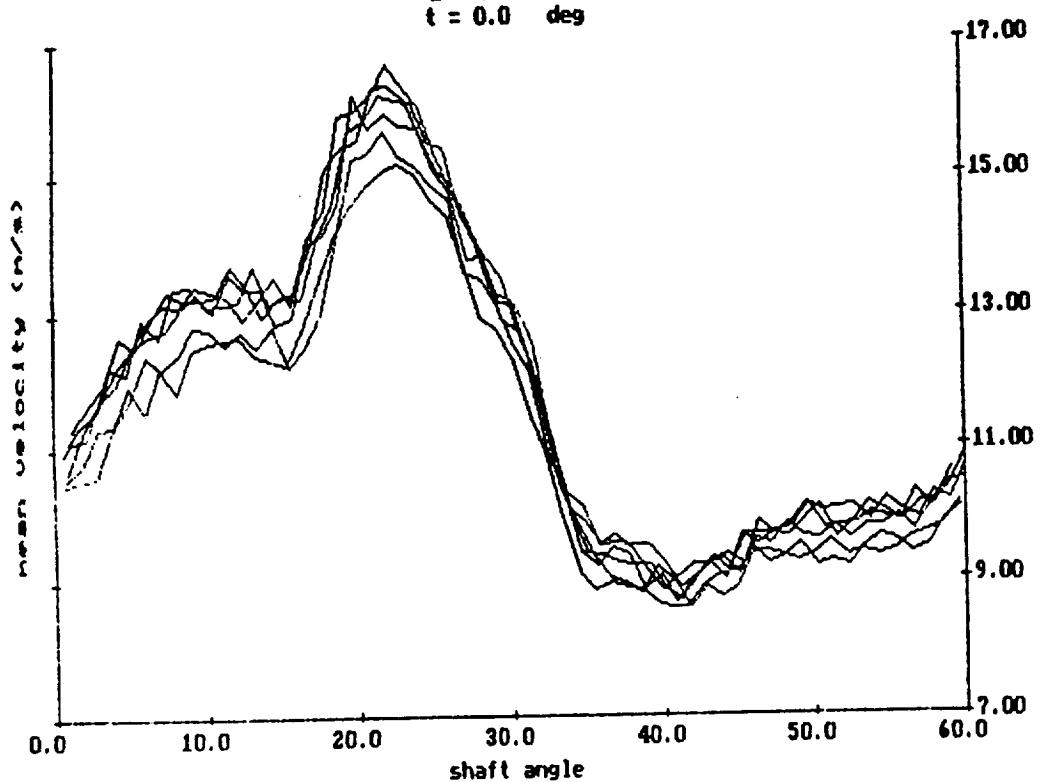
*U* component

*r* = 10.0 mm

*z* = 6.5 mm

*t* = 0.0 deg

6084 rpm



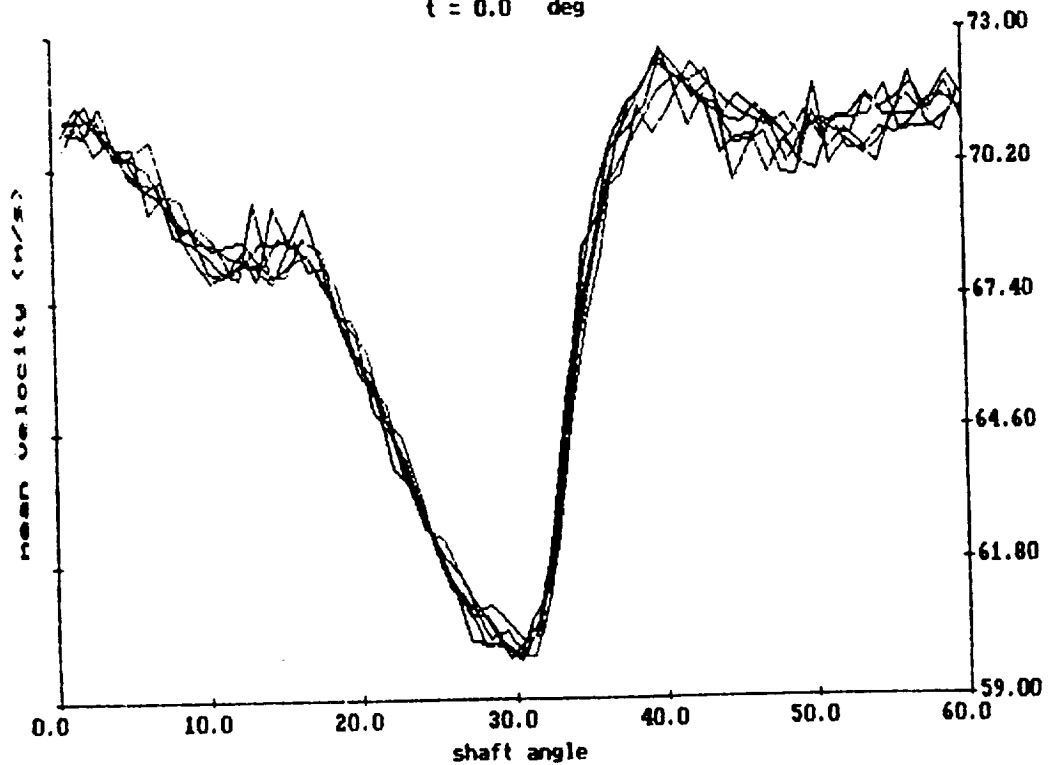
Mean Velocity (blades overlapped)

*W* component

*r* = 10.0 mm

*z* = 6.5 mm

*t* = 0.0 deg



Mean Velocity (blades overlapped)

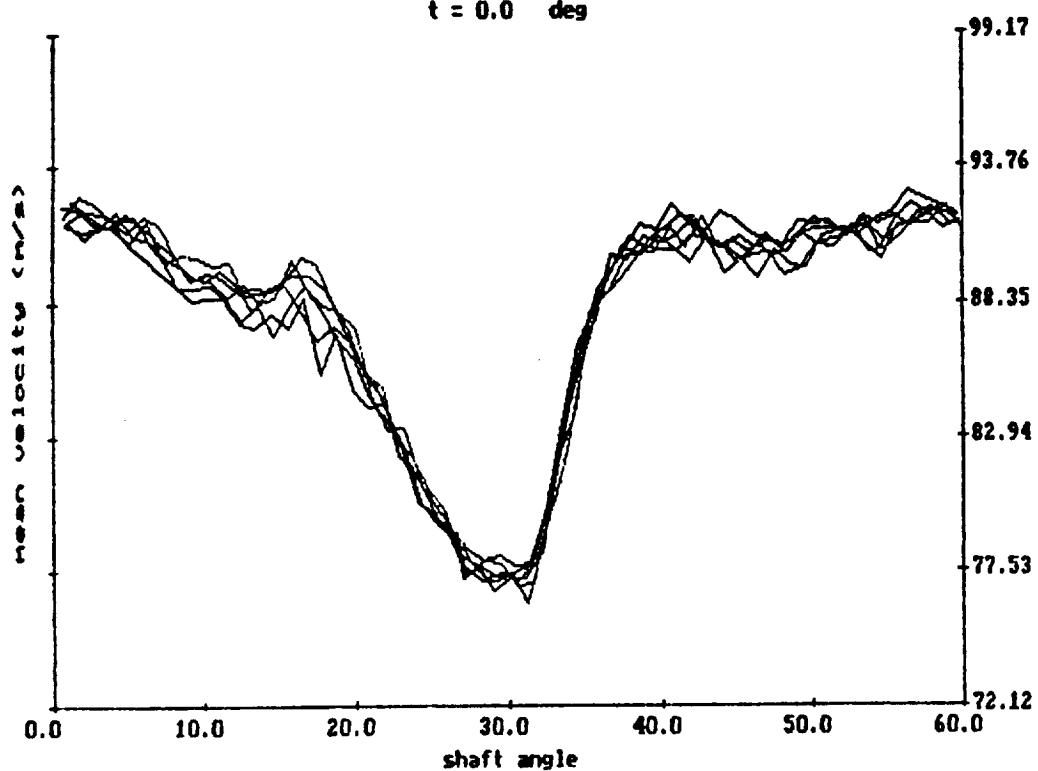
W component

r = 10.0 mm

z = 6.5 mm

t = 0.0 deg

7680 rpm



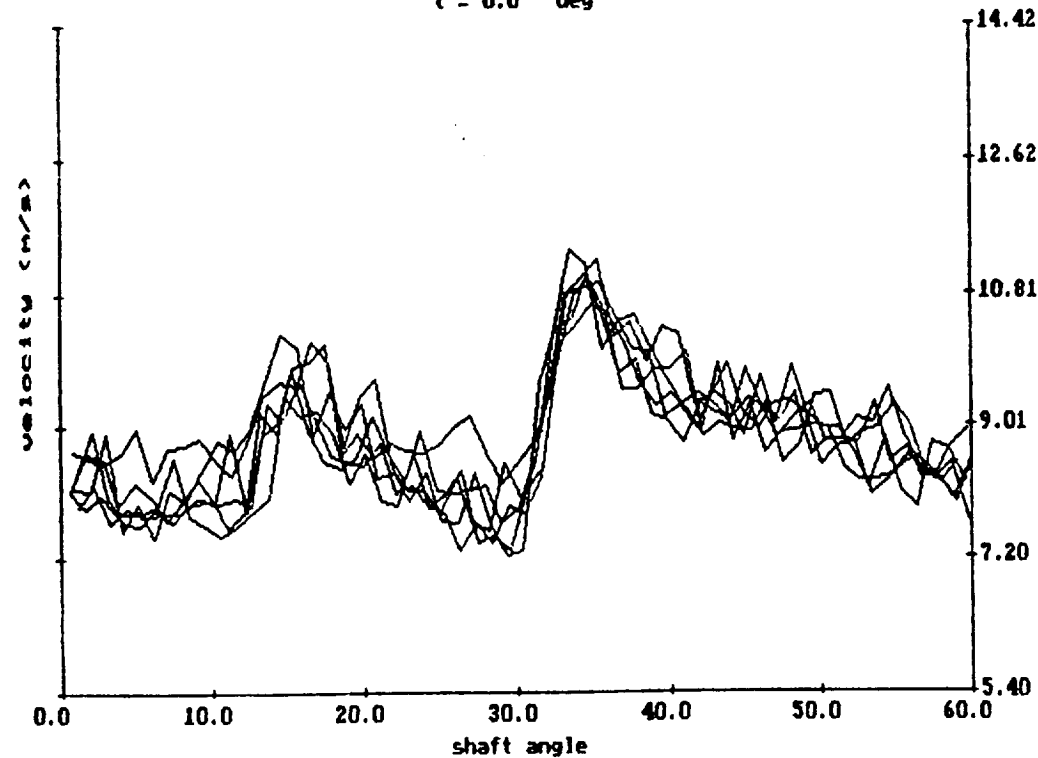
RMS Velocity (blades overlapped)

W component

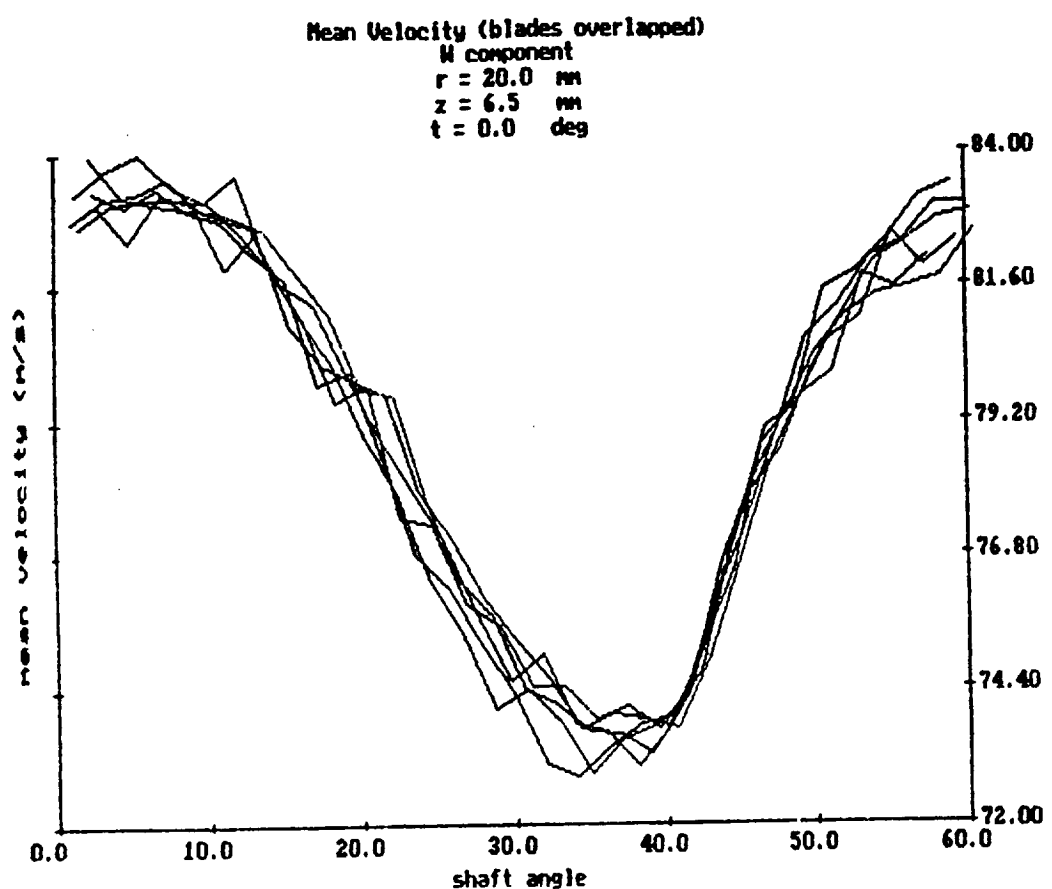
r = 10.0 mm

z = 6.5 mm

t = 0.0 deg

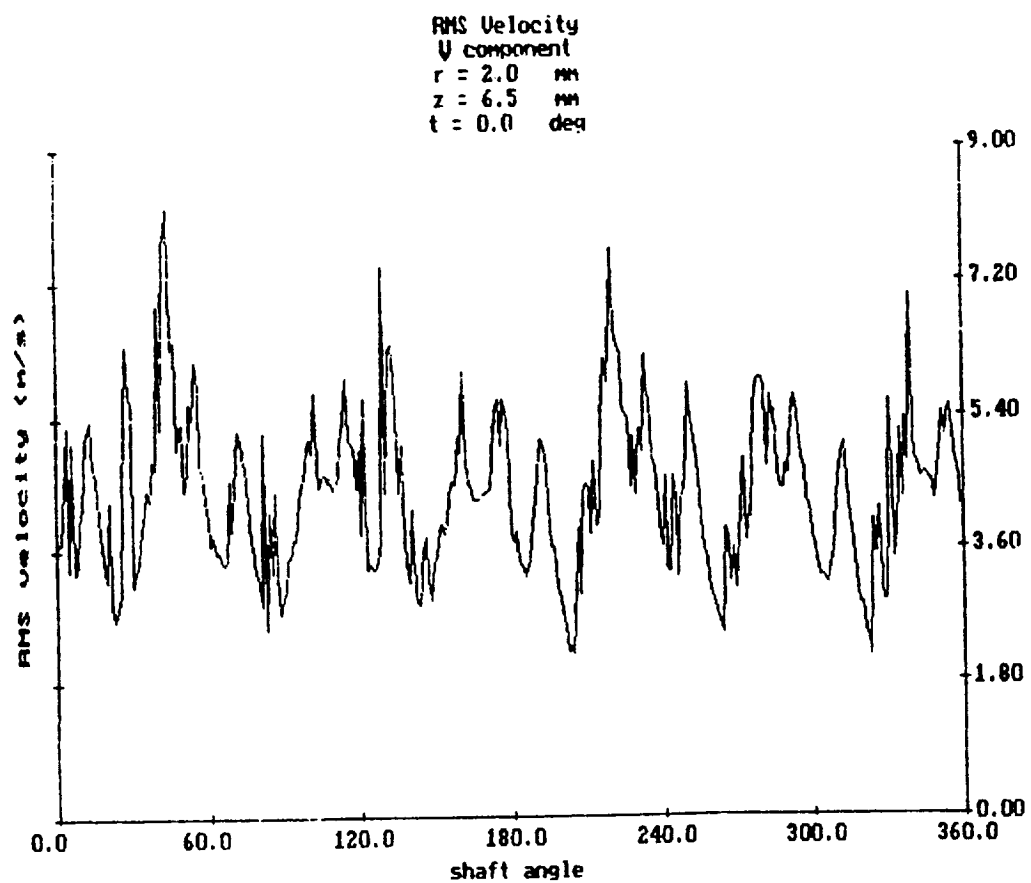
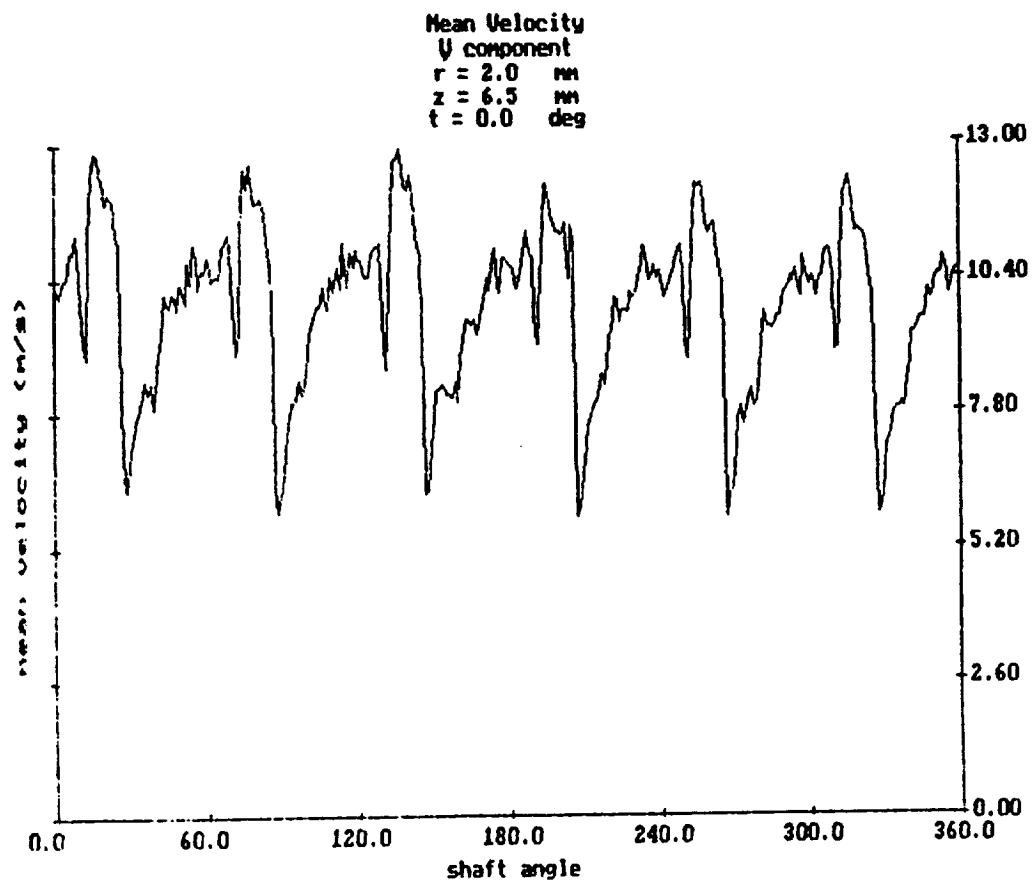


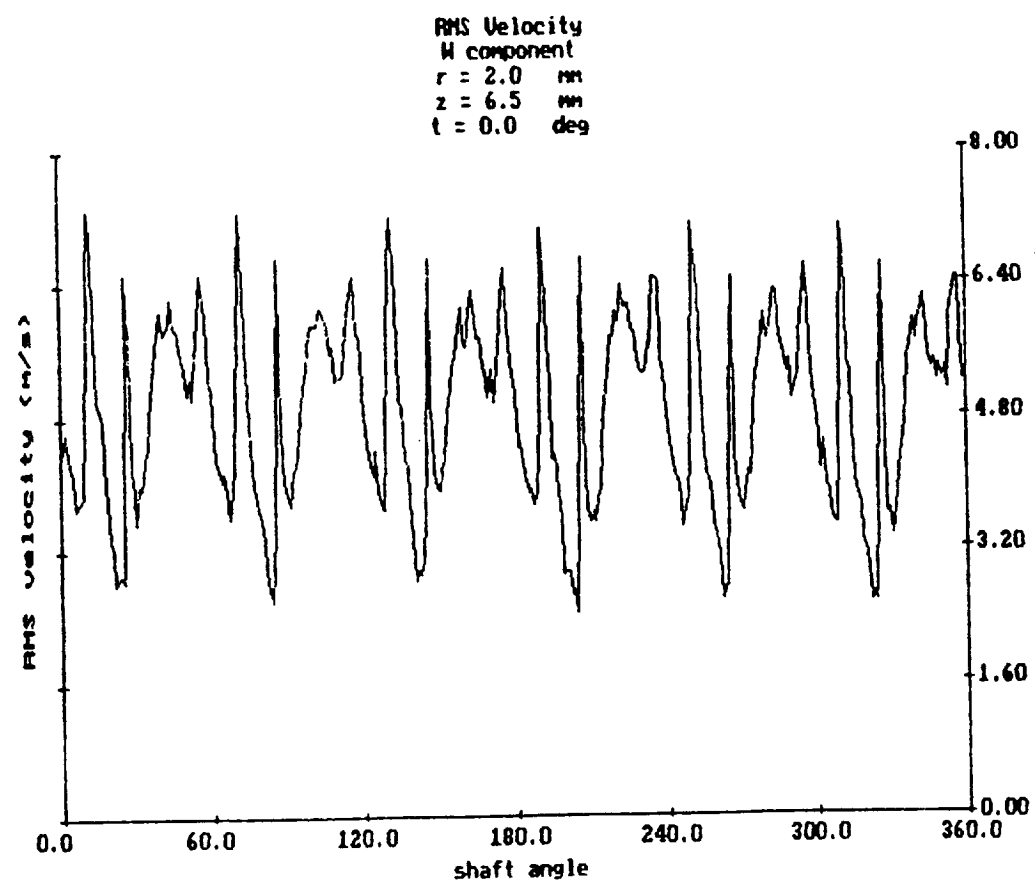
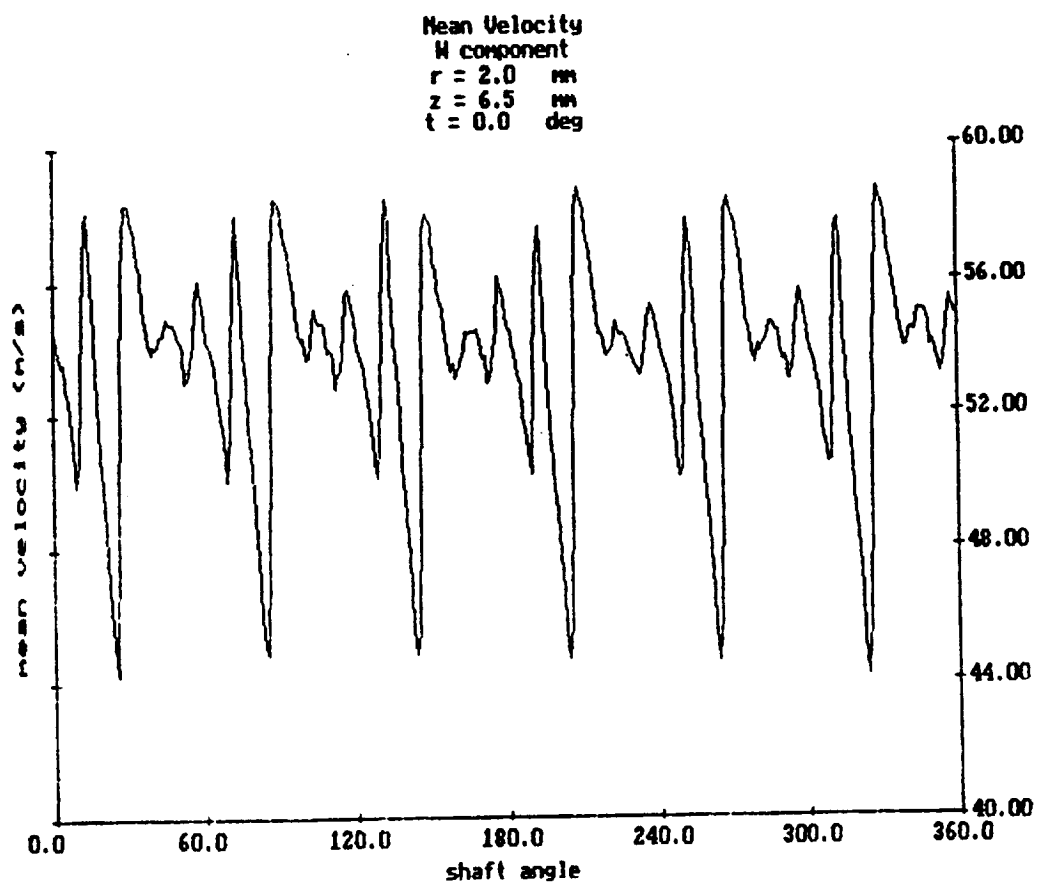
7680 rpm

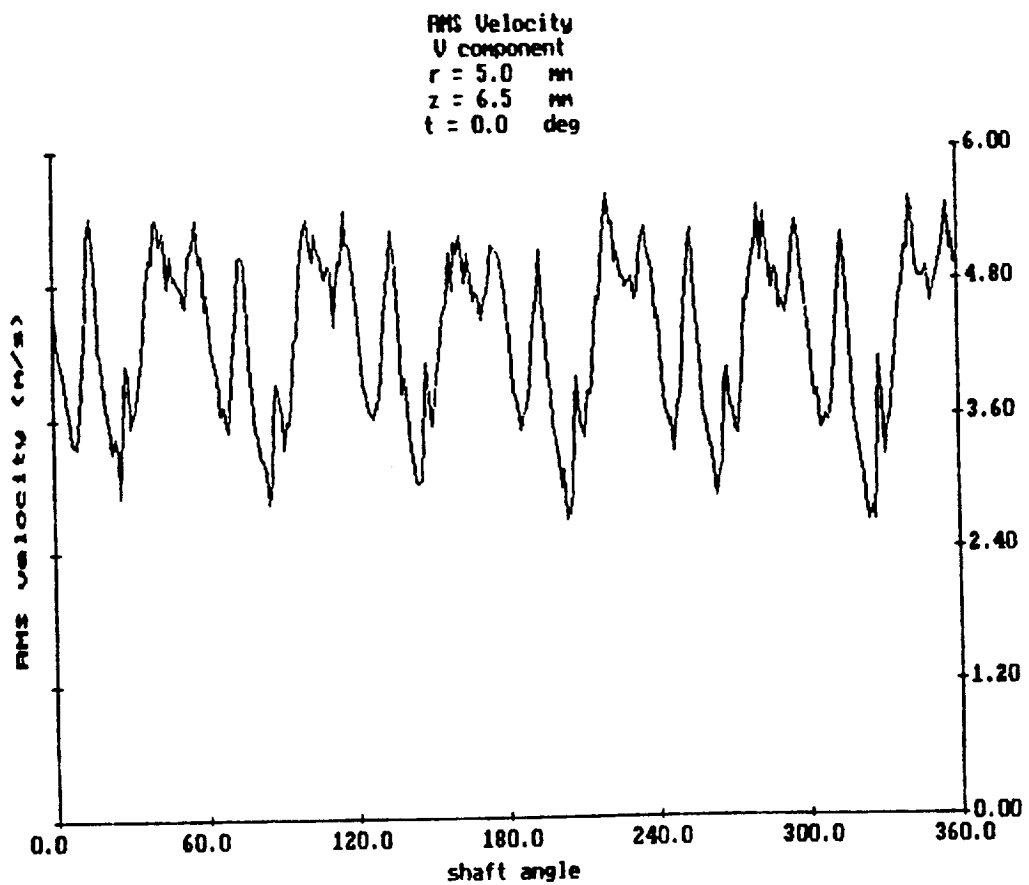
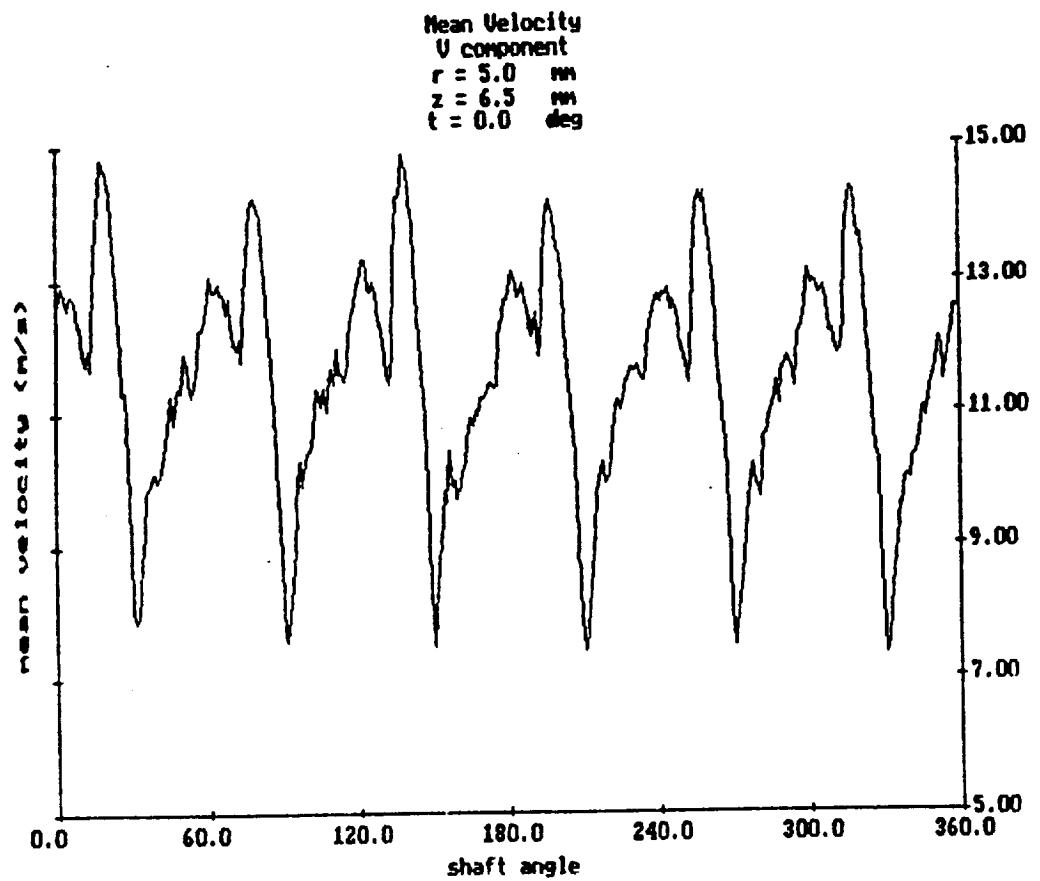


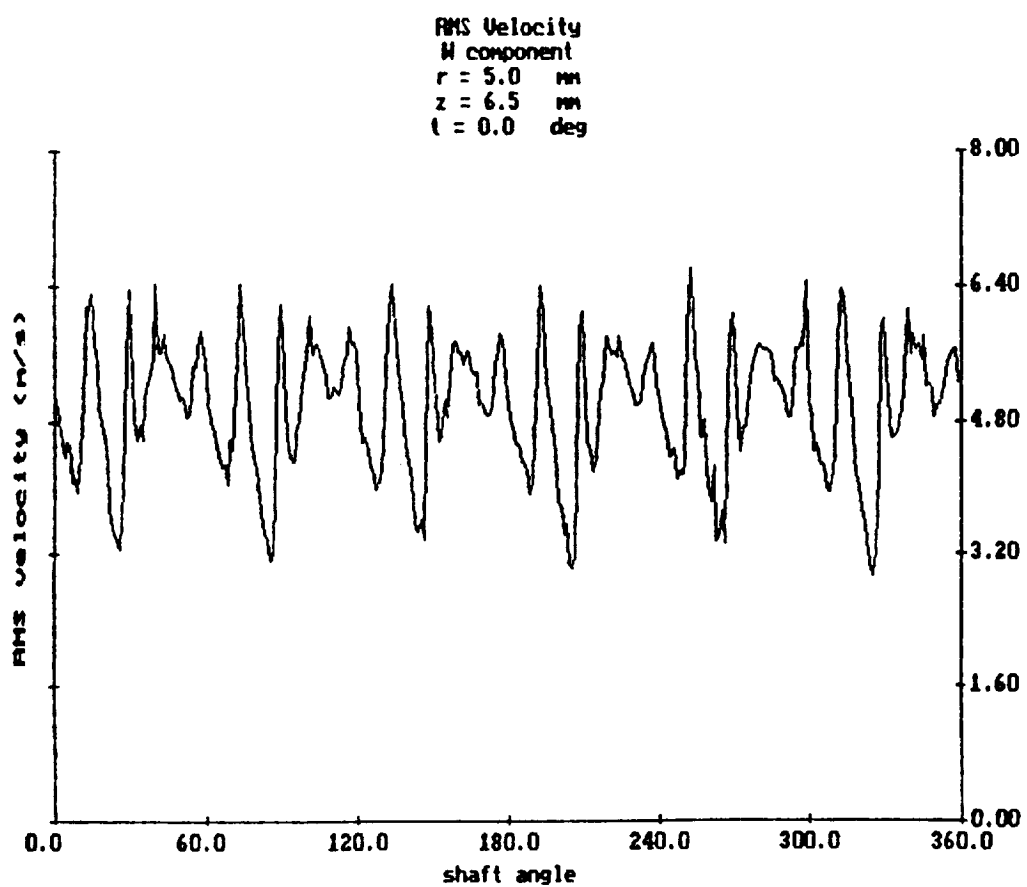
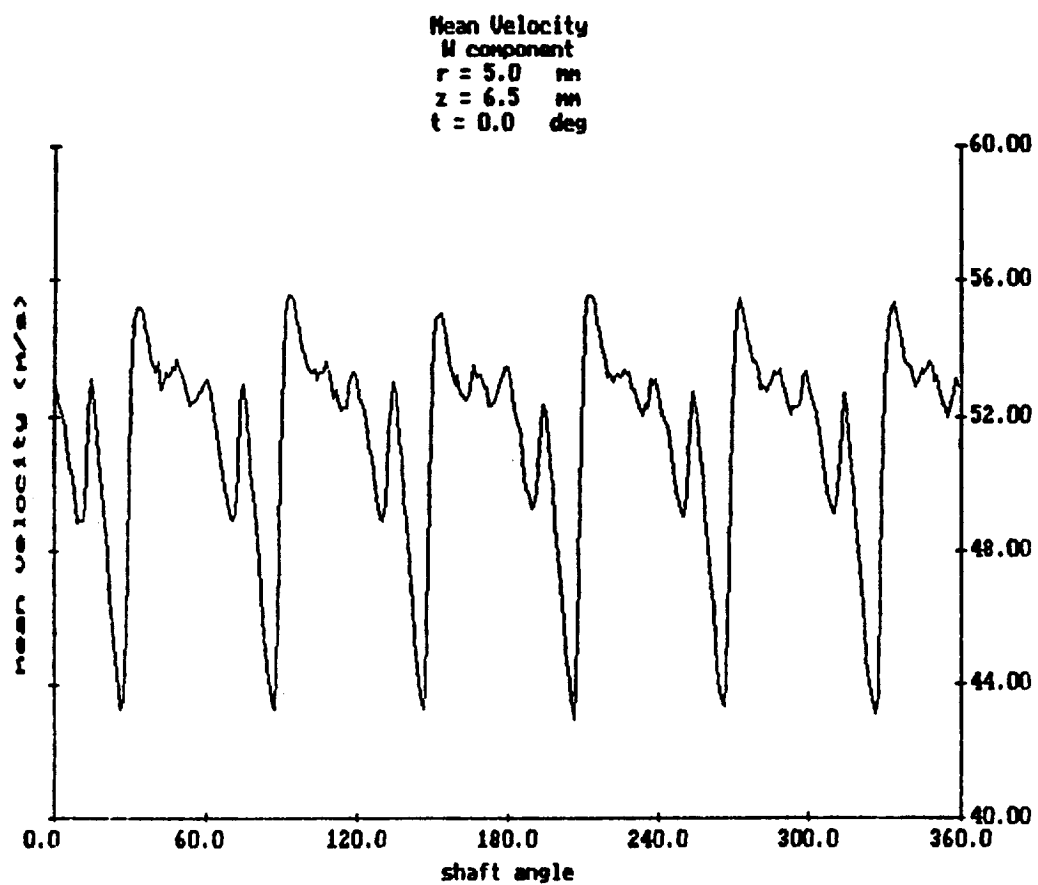
**FIGURE 10**

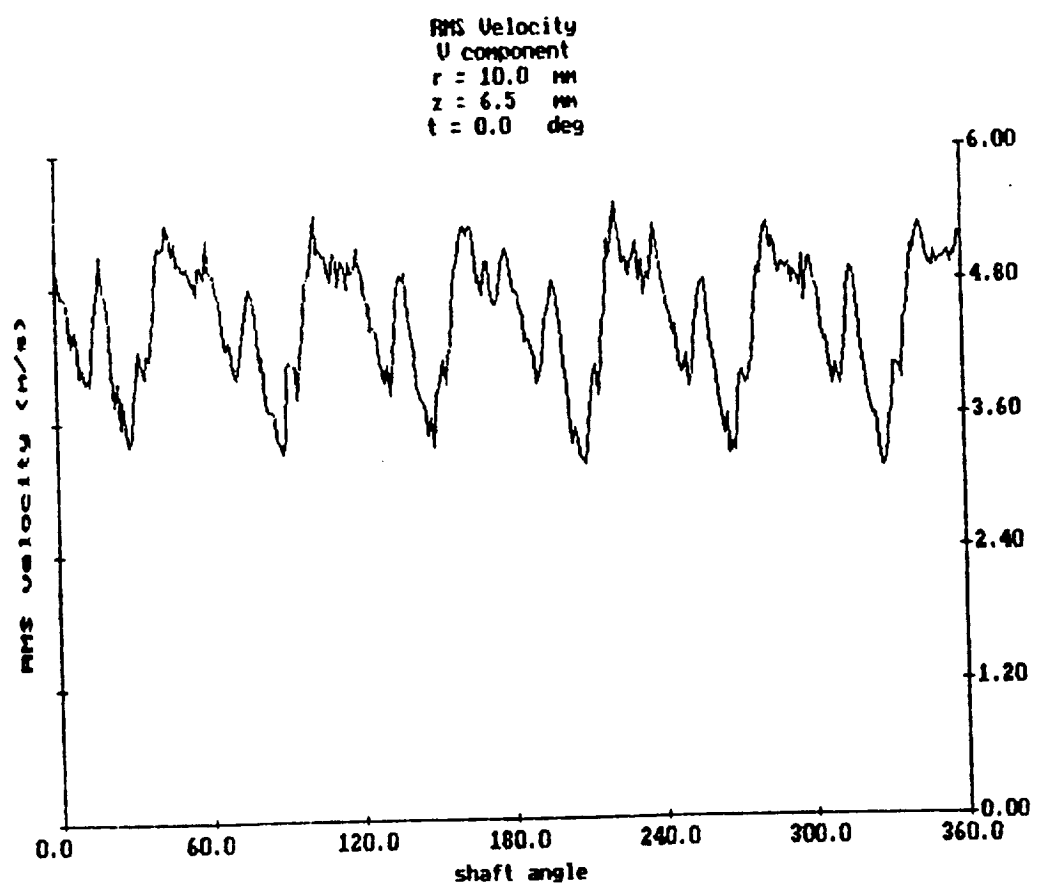
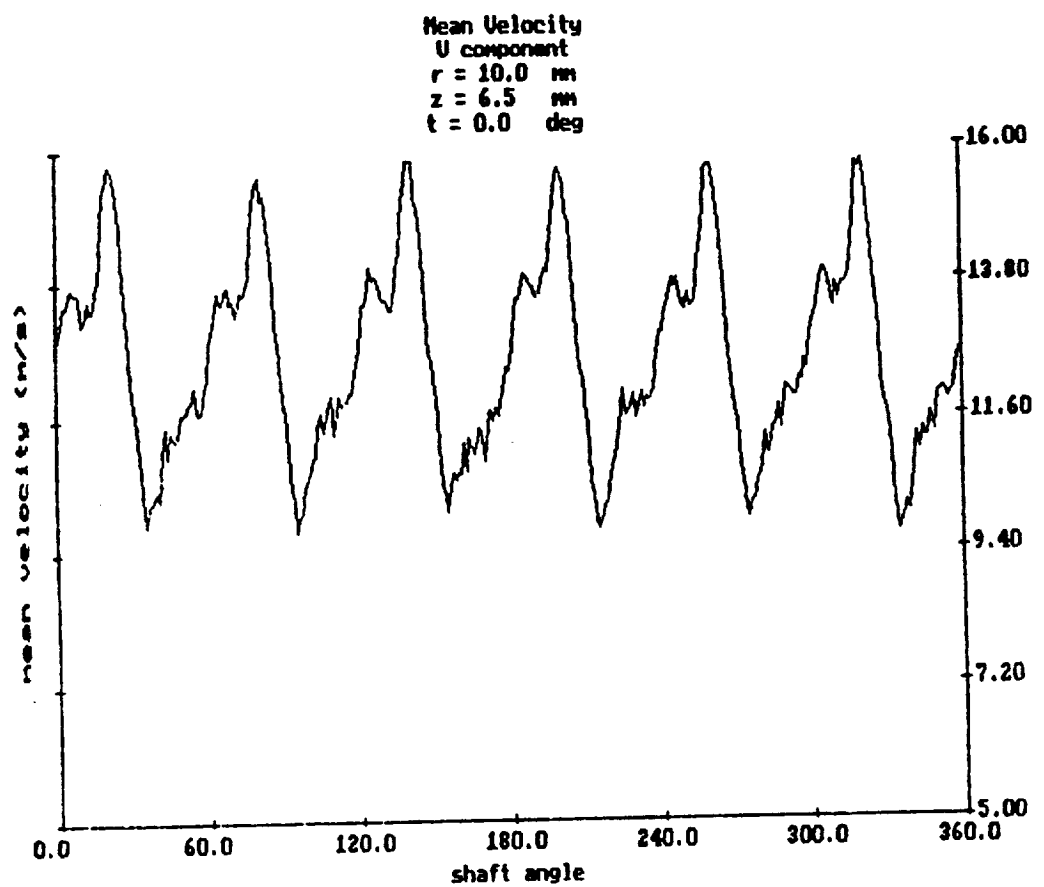
**4260 RPM**

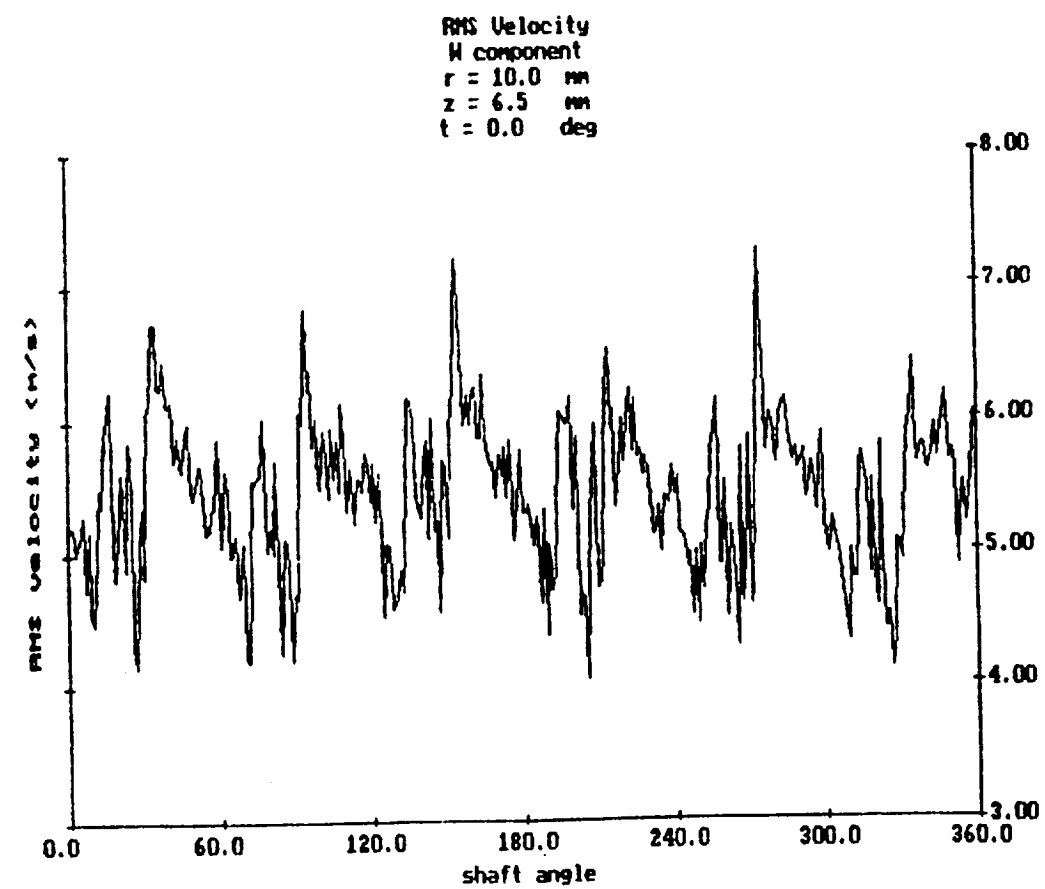
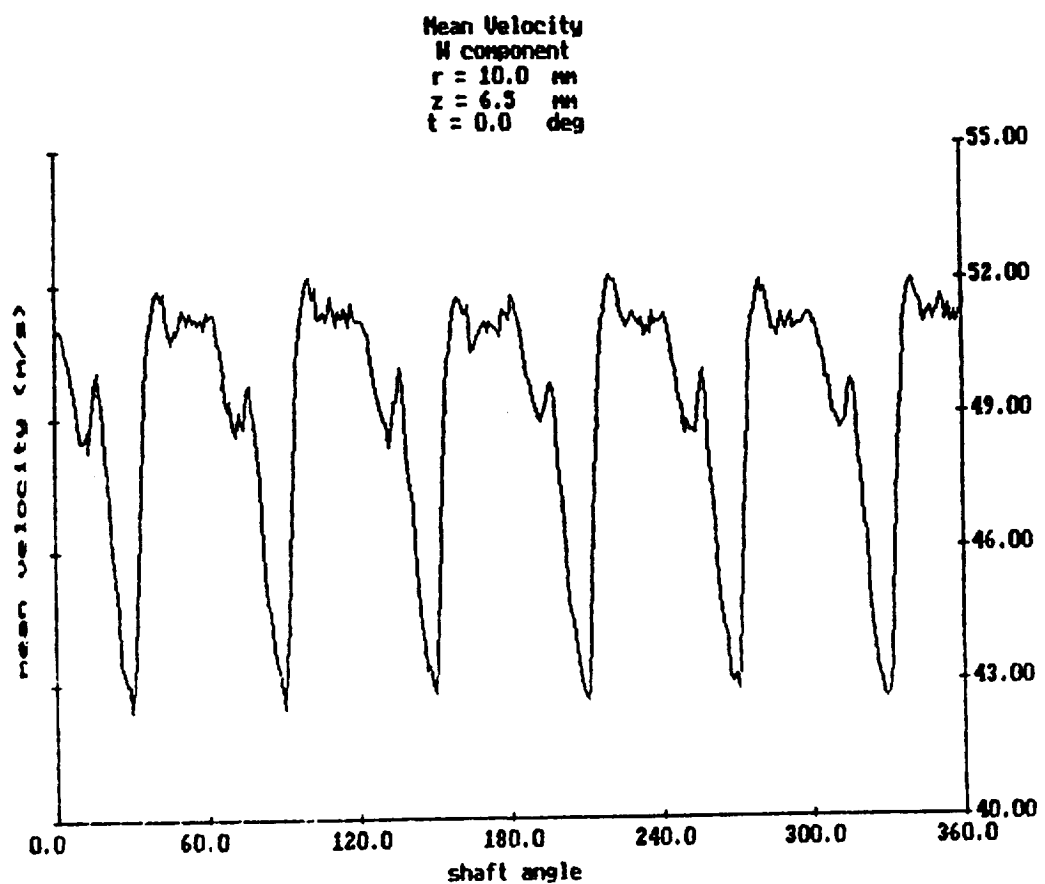


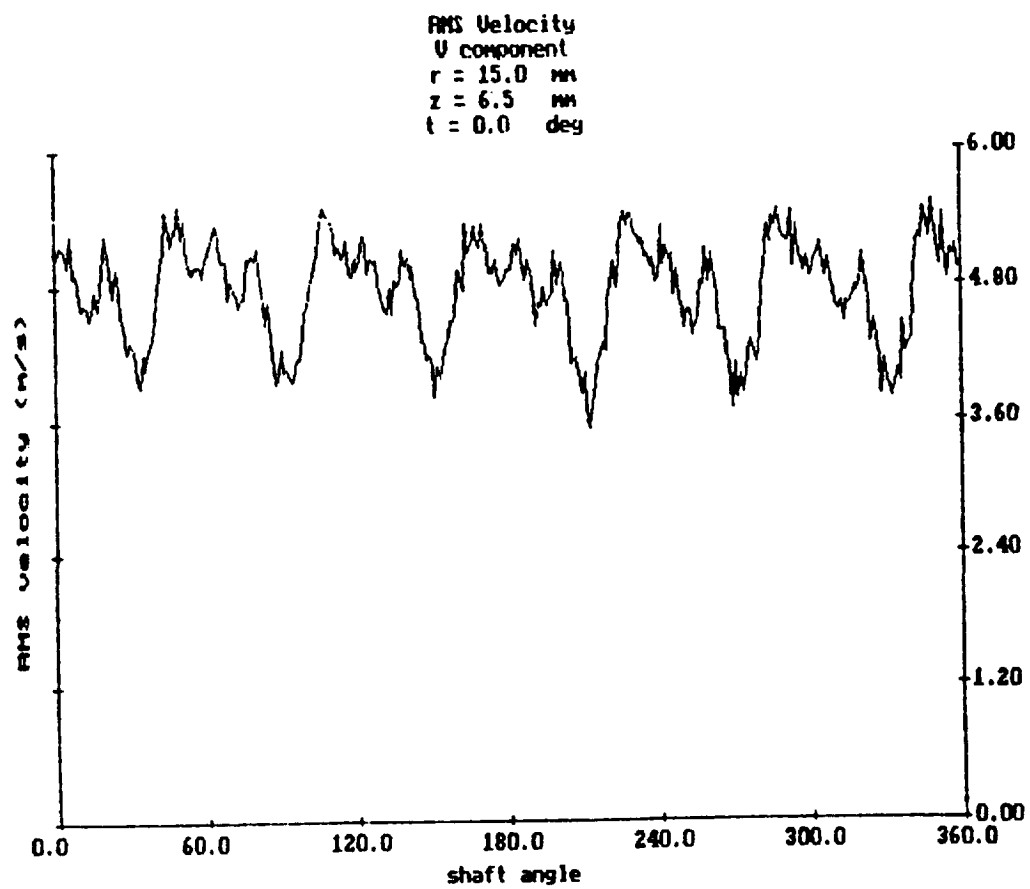
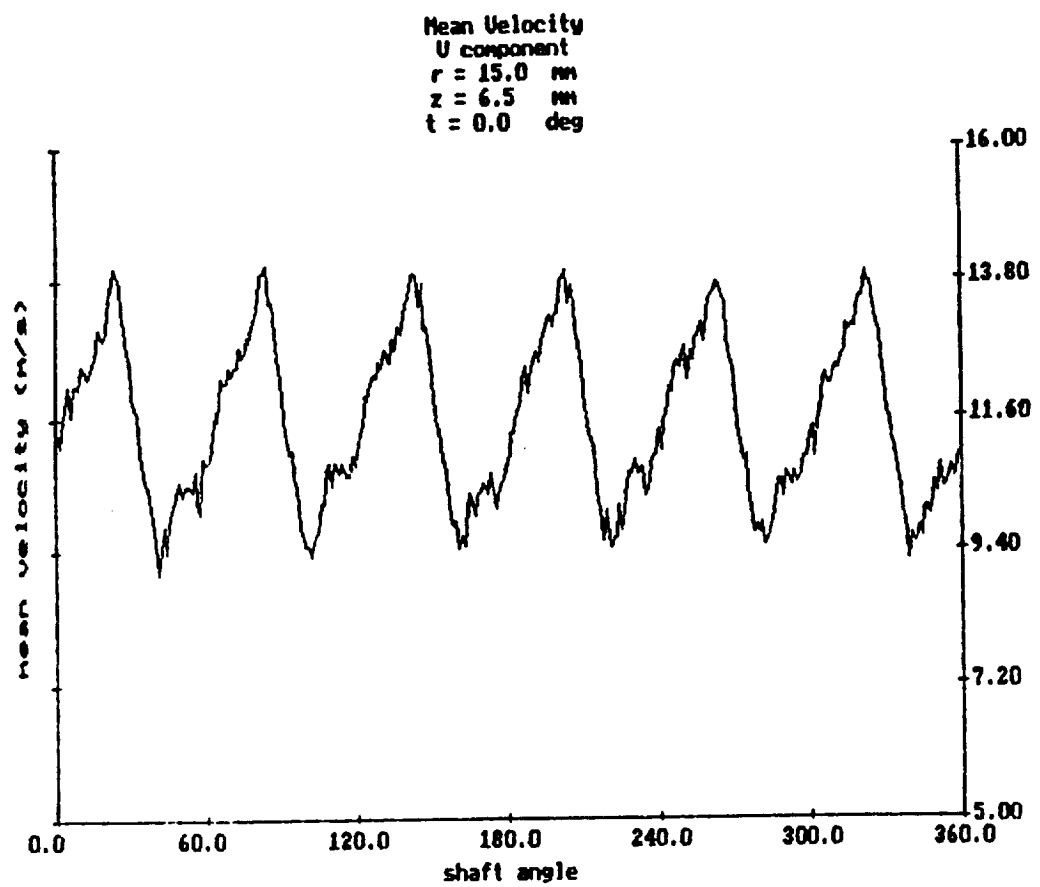


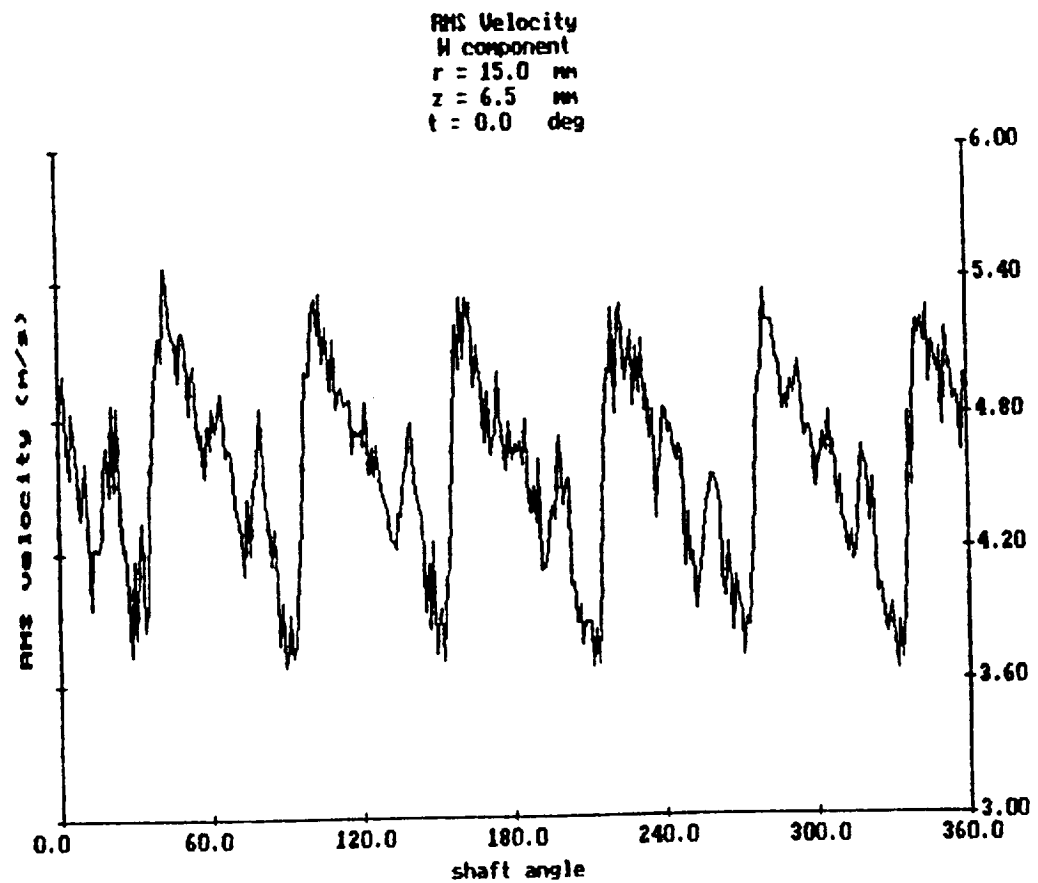
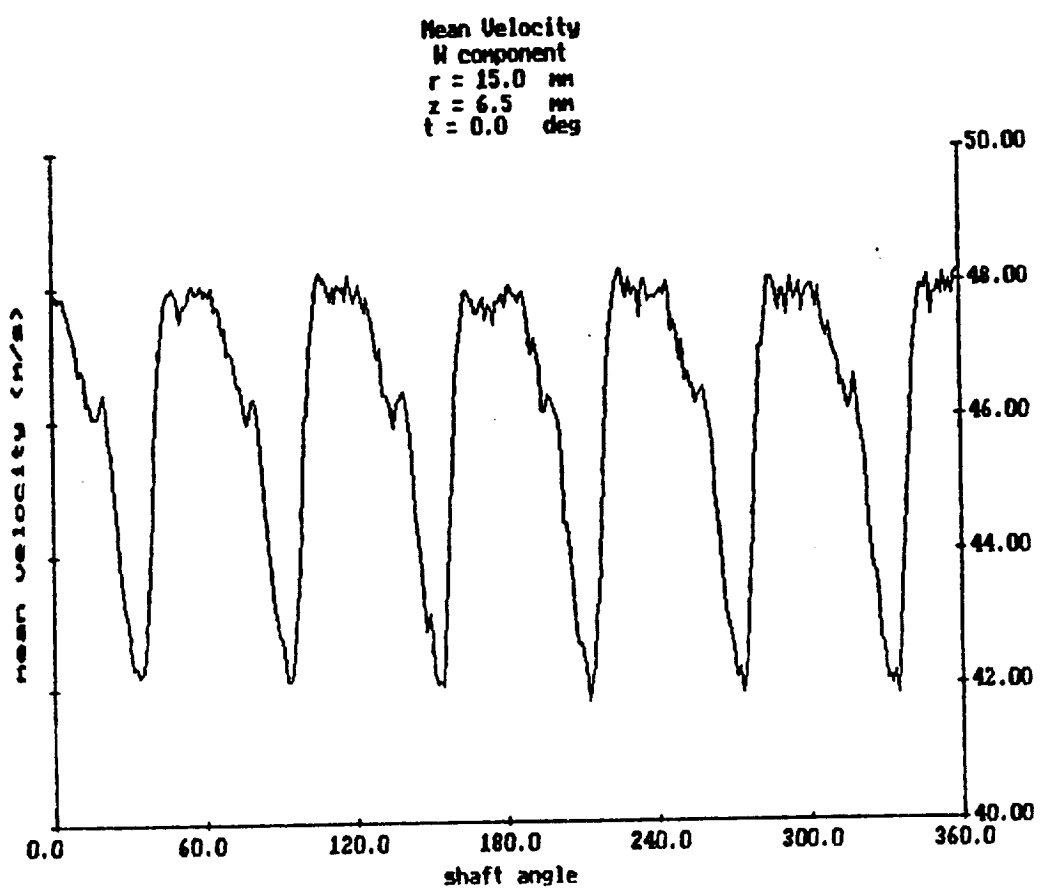




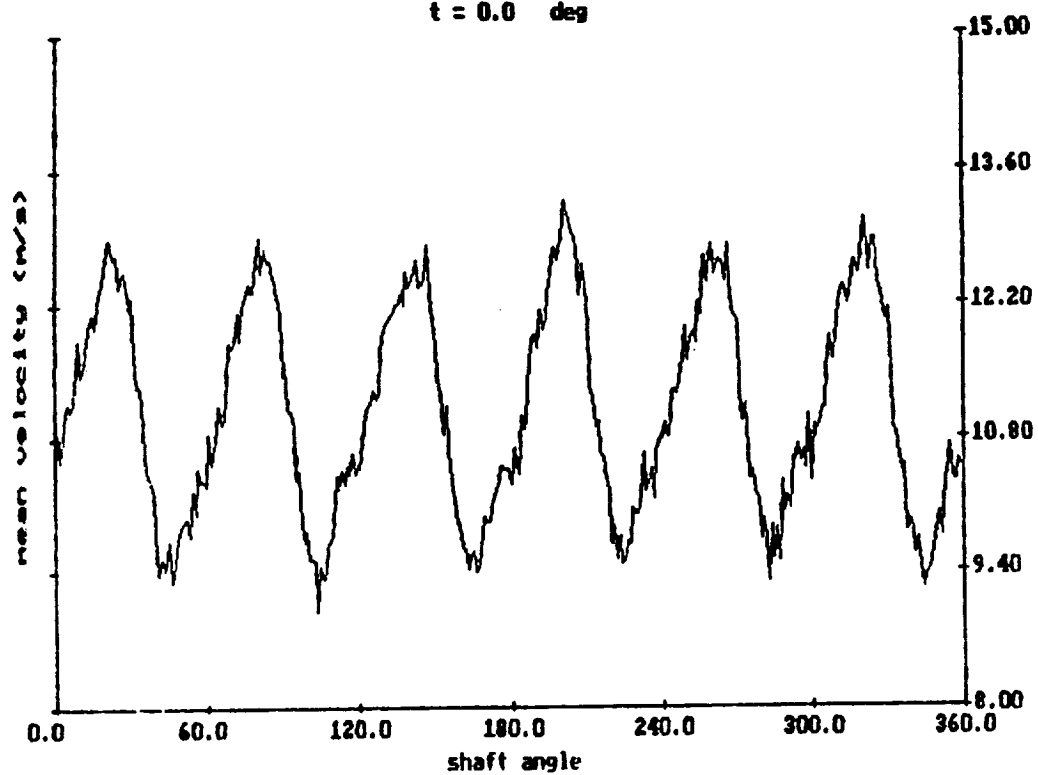


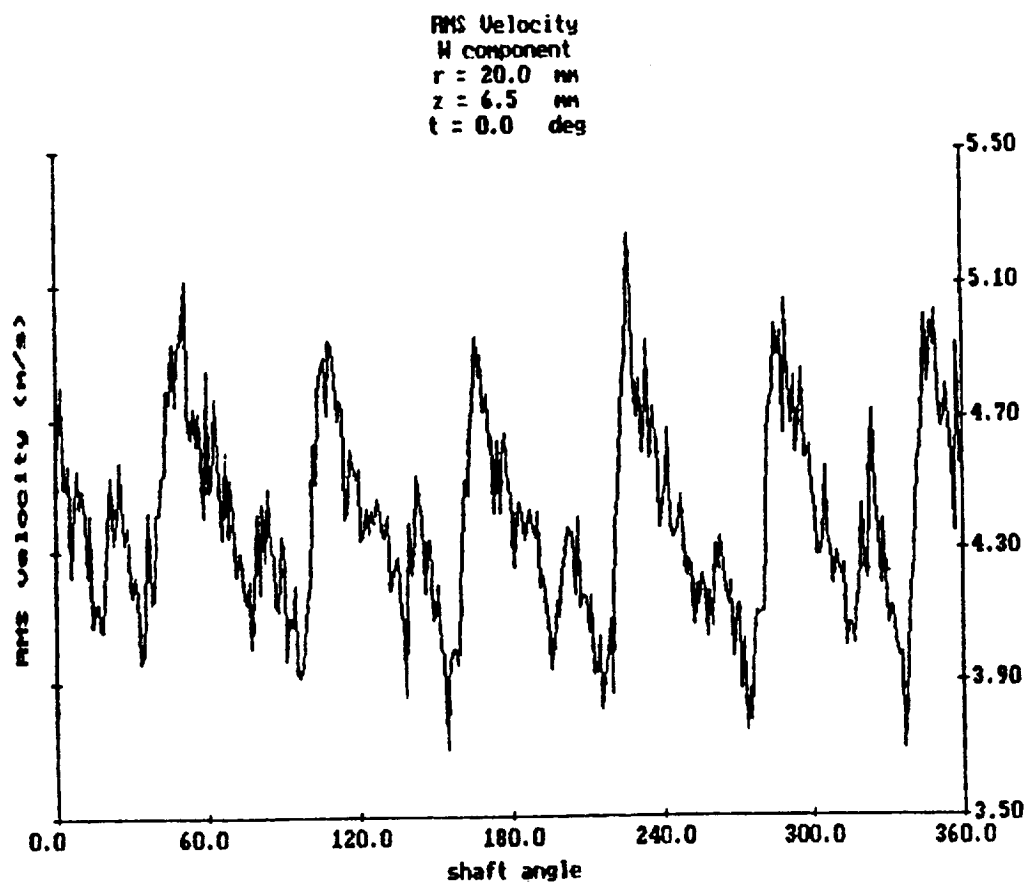
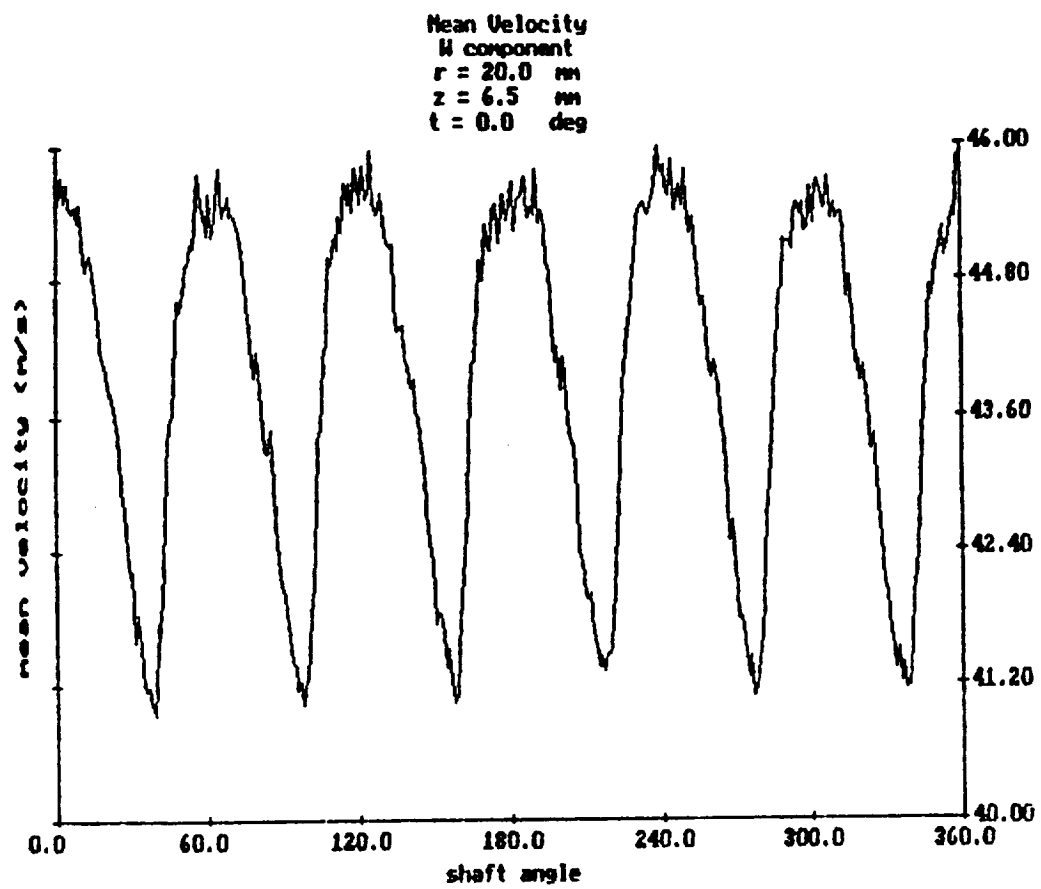


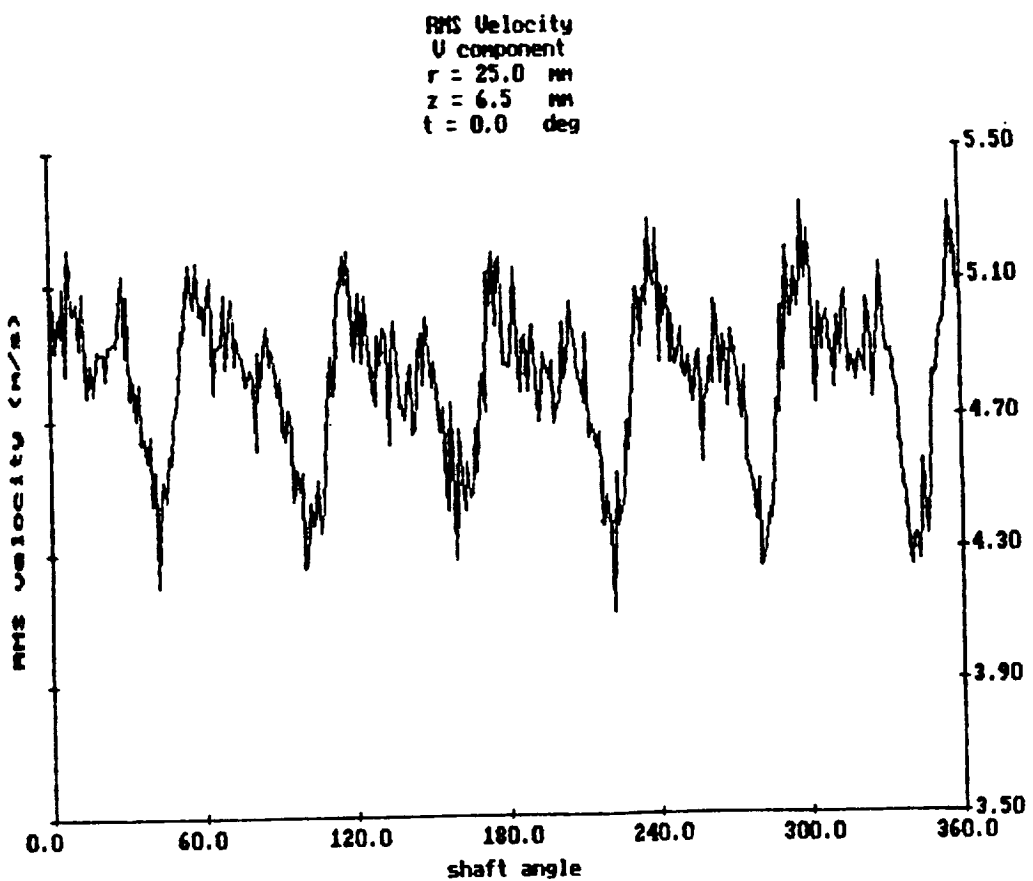
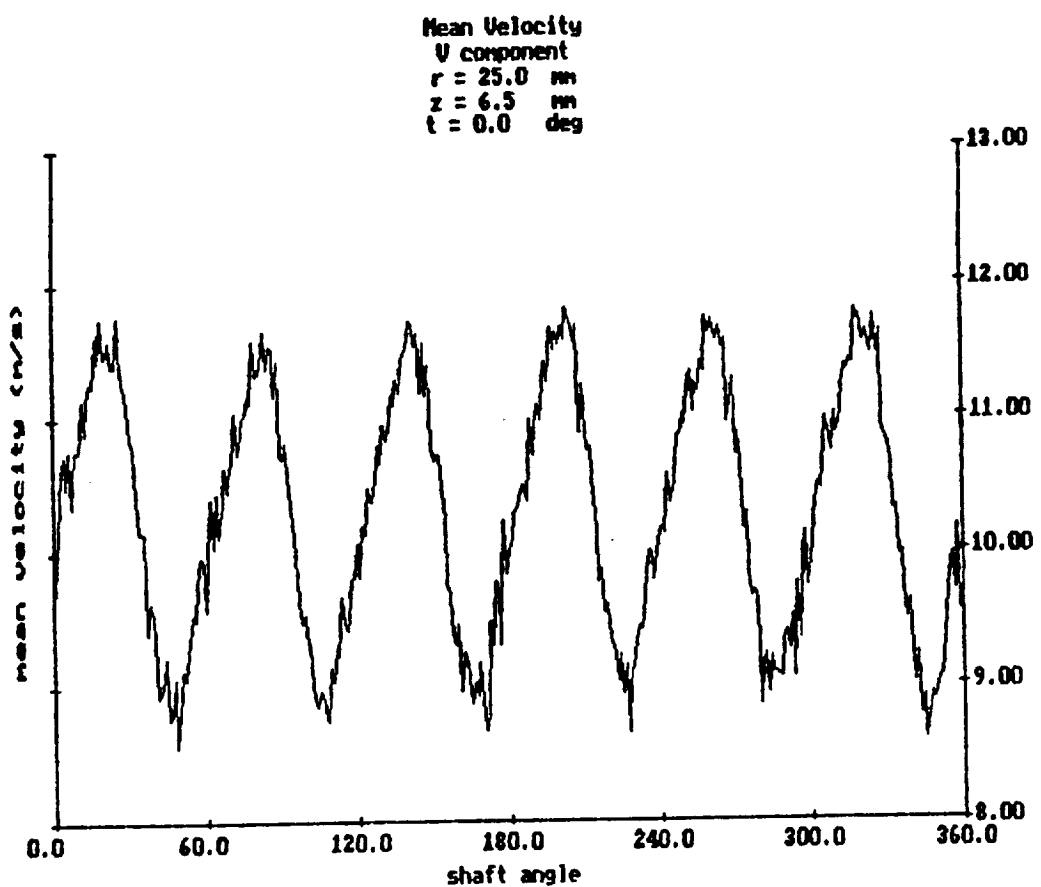


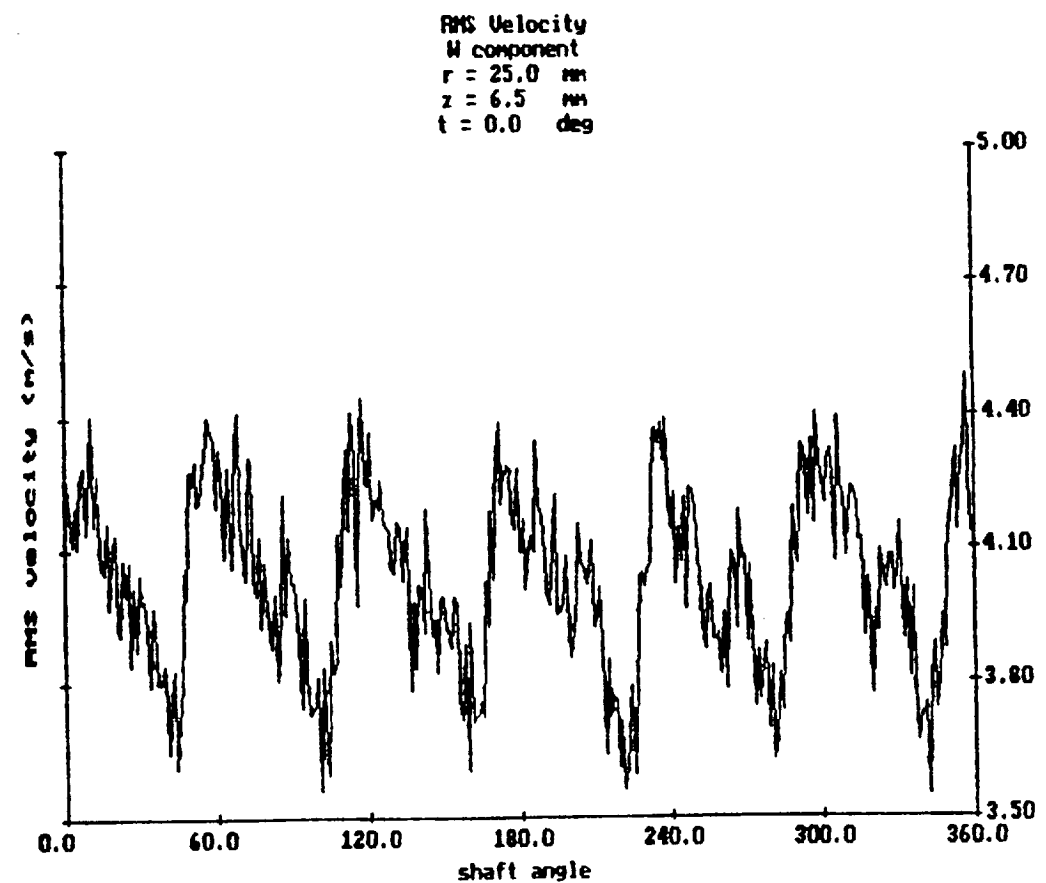
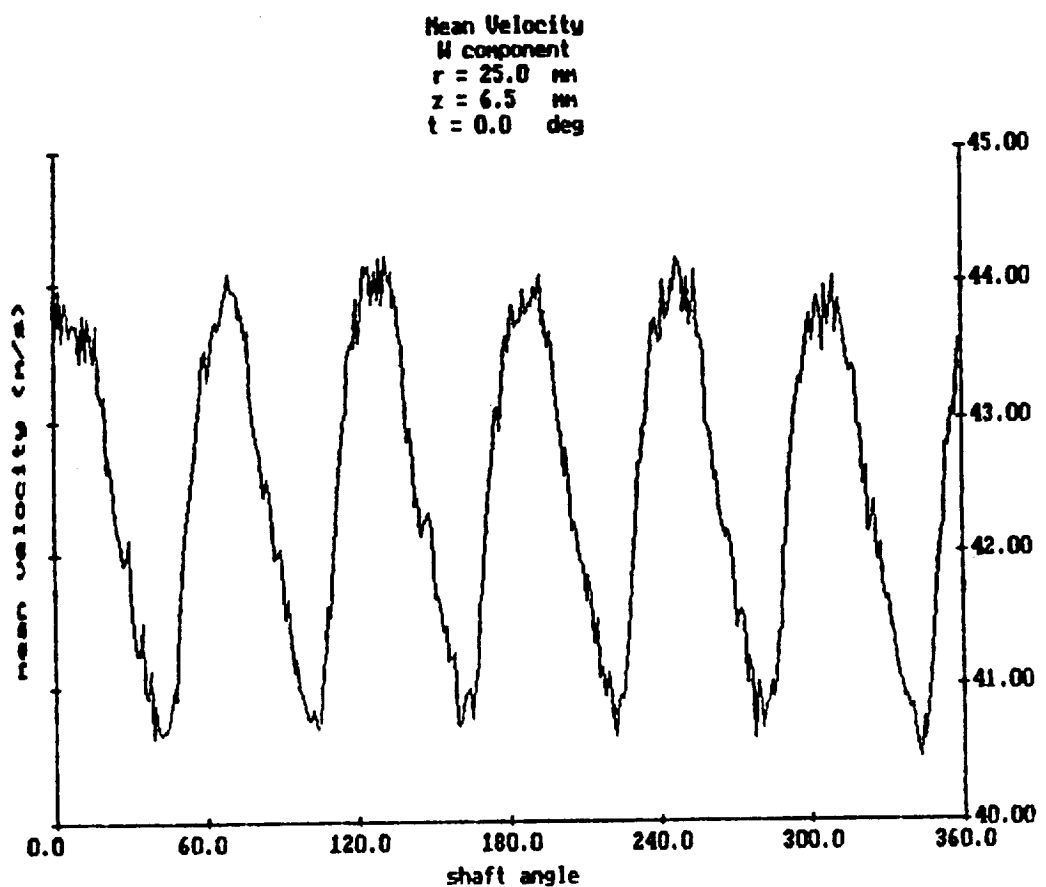


Mean Velocity  
V component  
 $r = 20.0$  mm  
 $z = 6.5$  mm  
 $t = 0.0$  deg

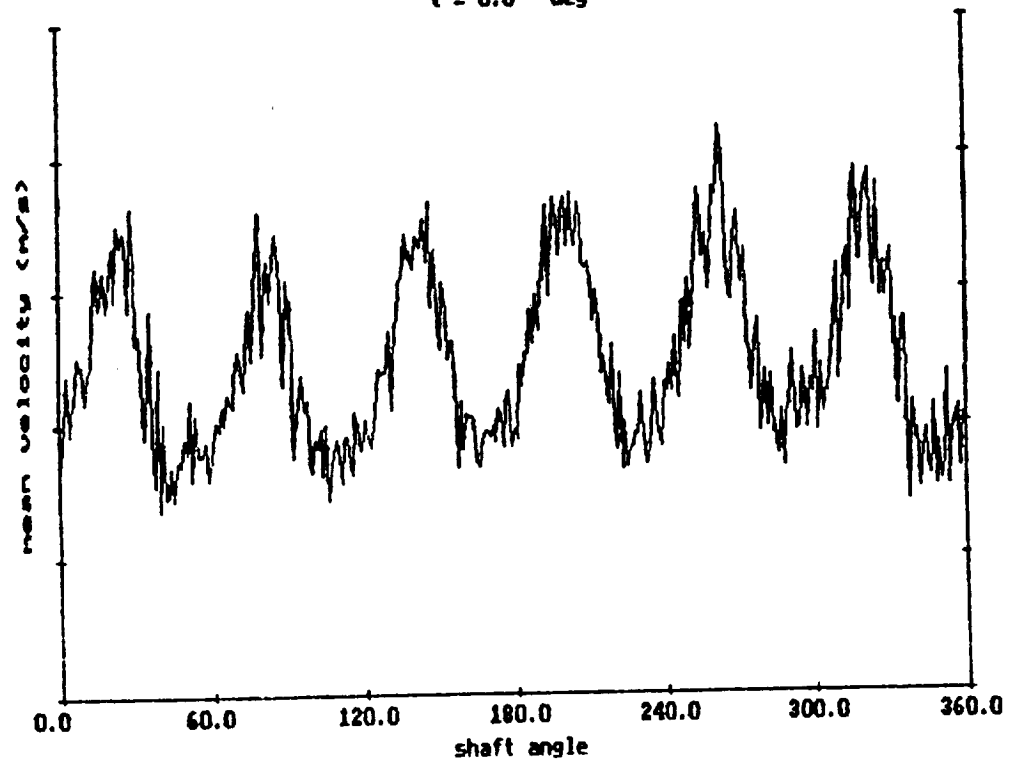




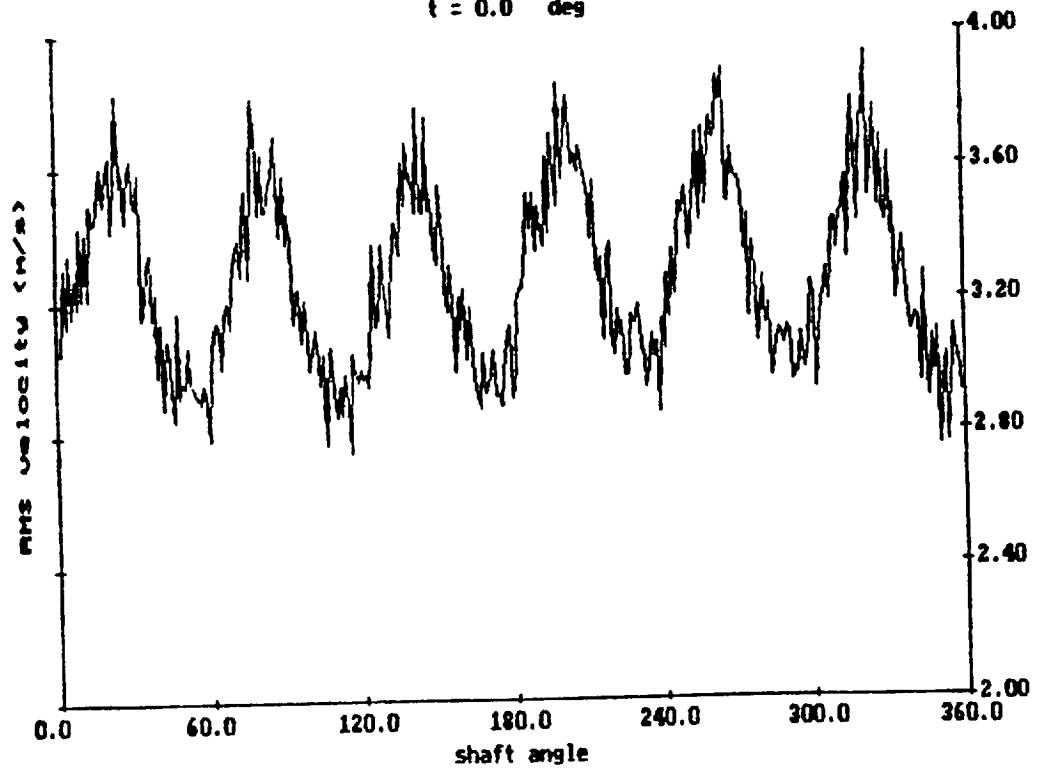


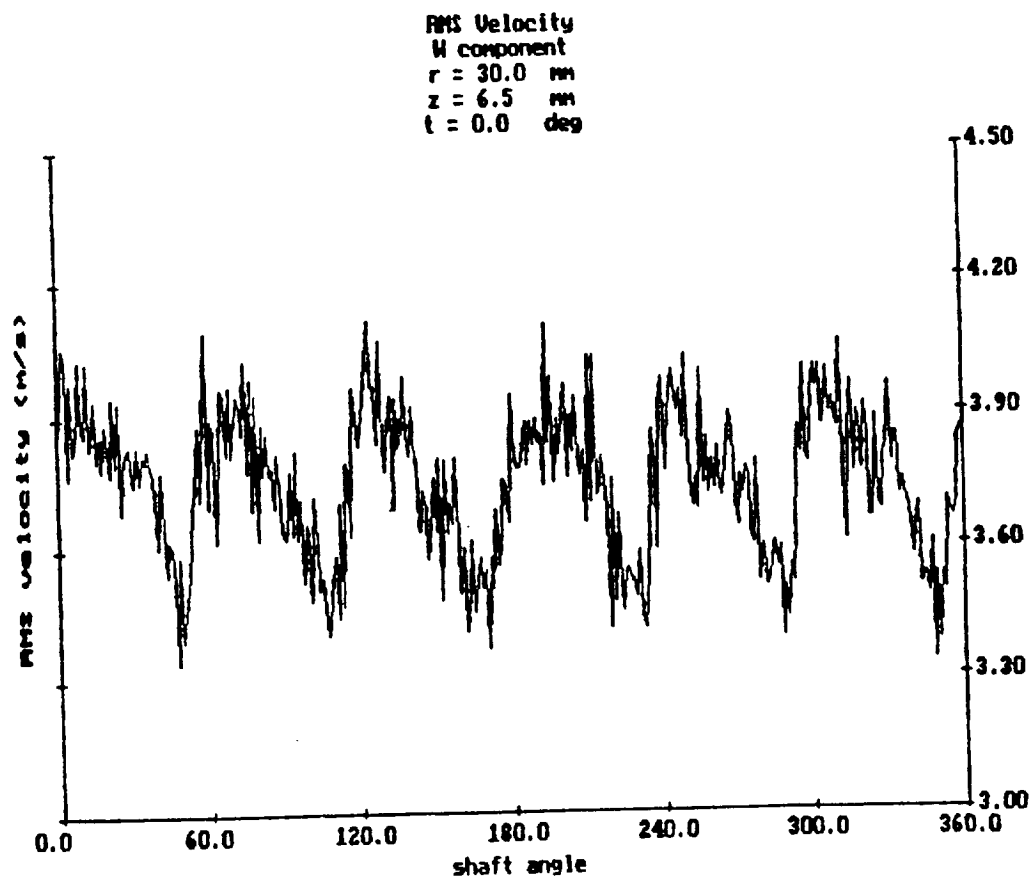
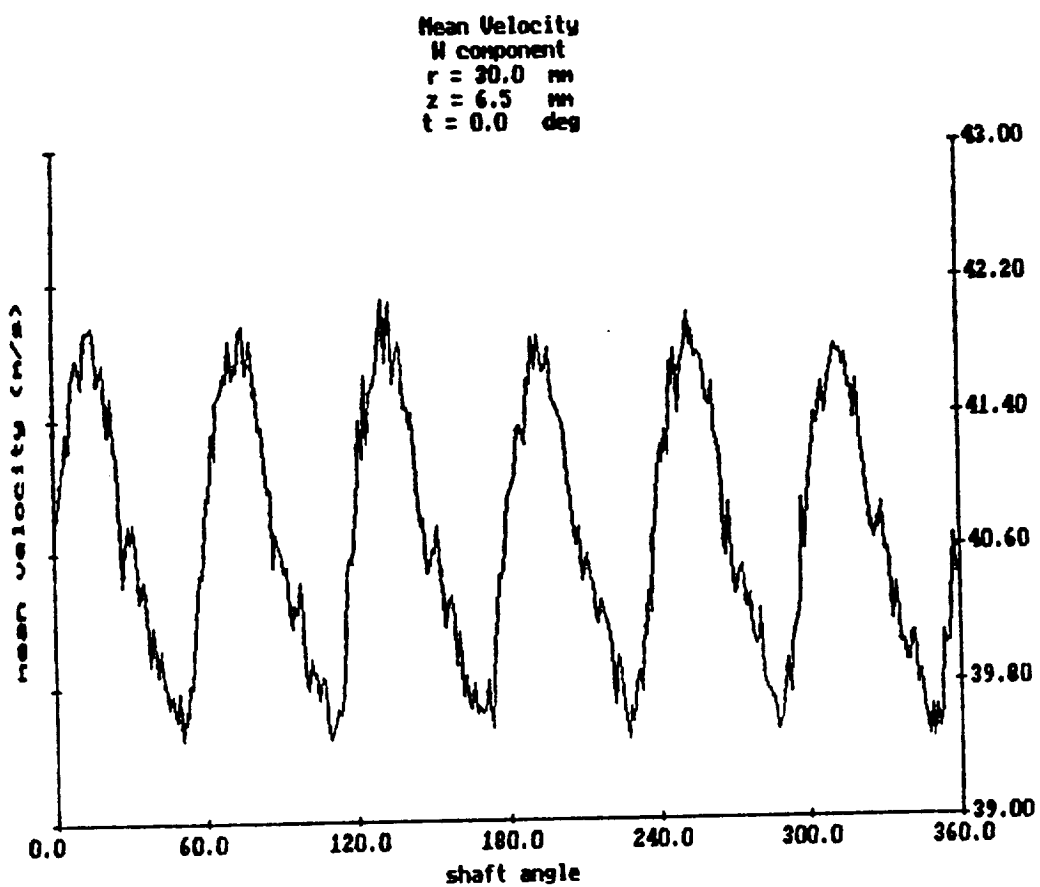


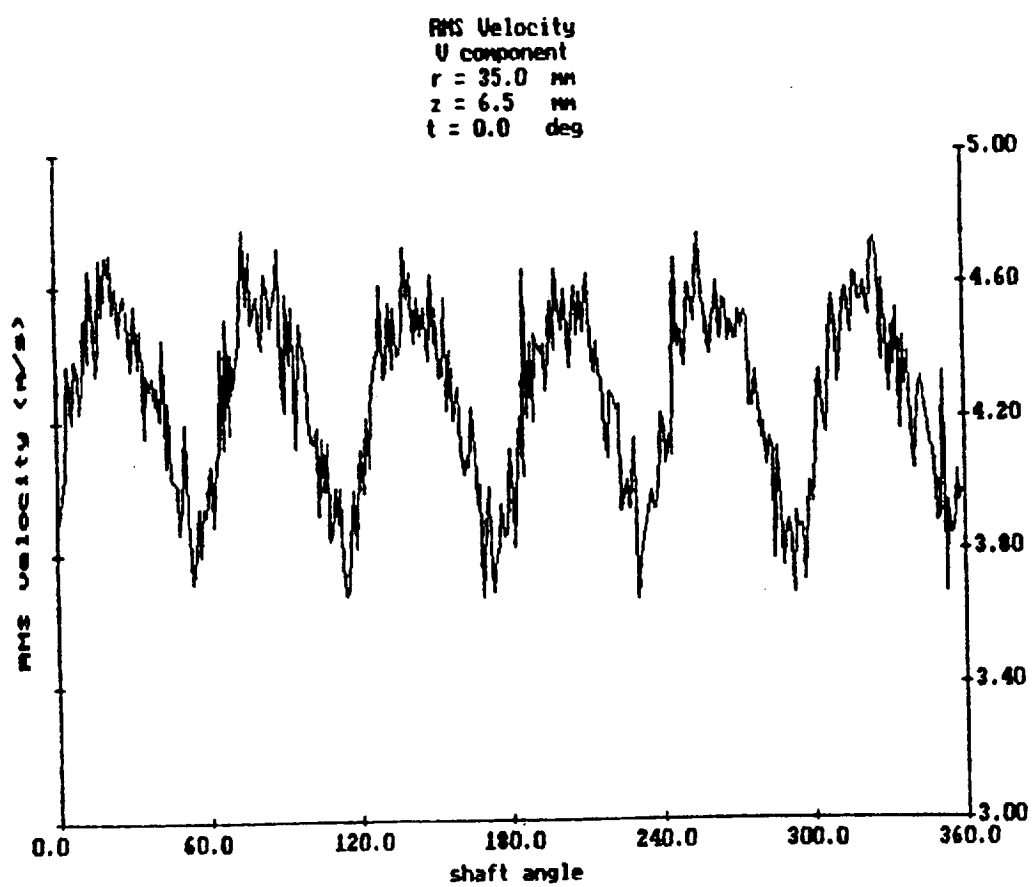
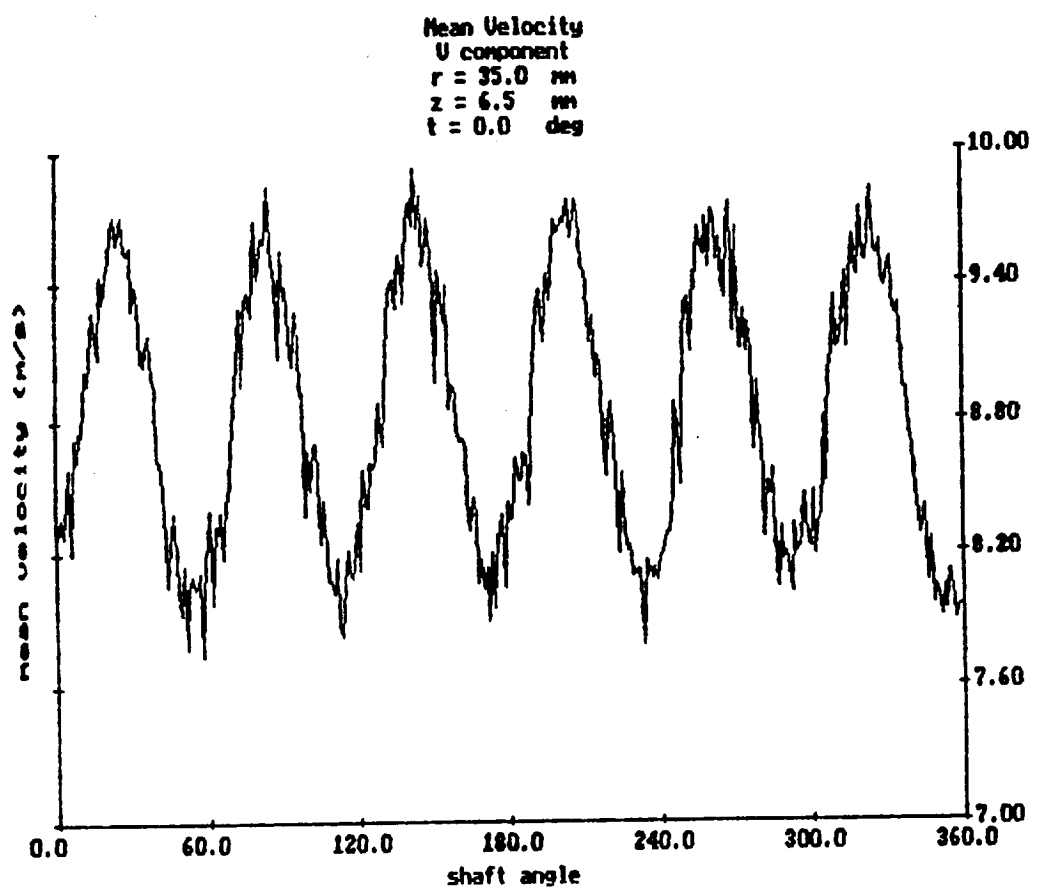
Mean Velocity  
U component  
 $r = 30.0$  mm  
 $z = 6.5$  mm  
 $t = 0.0$  deg



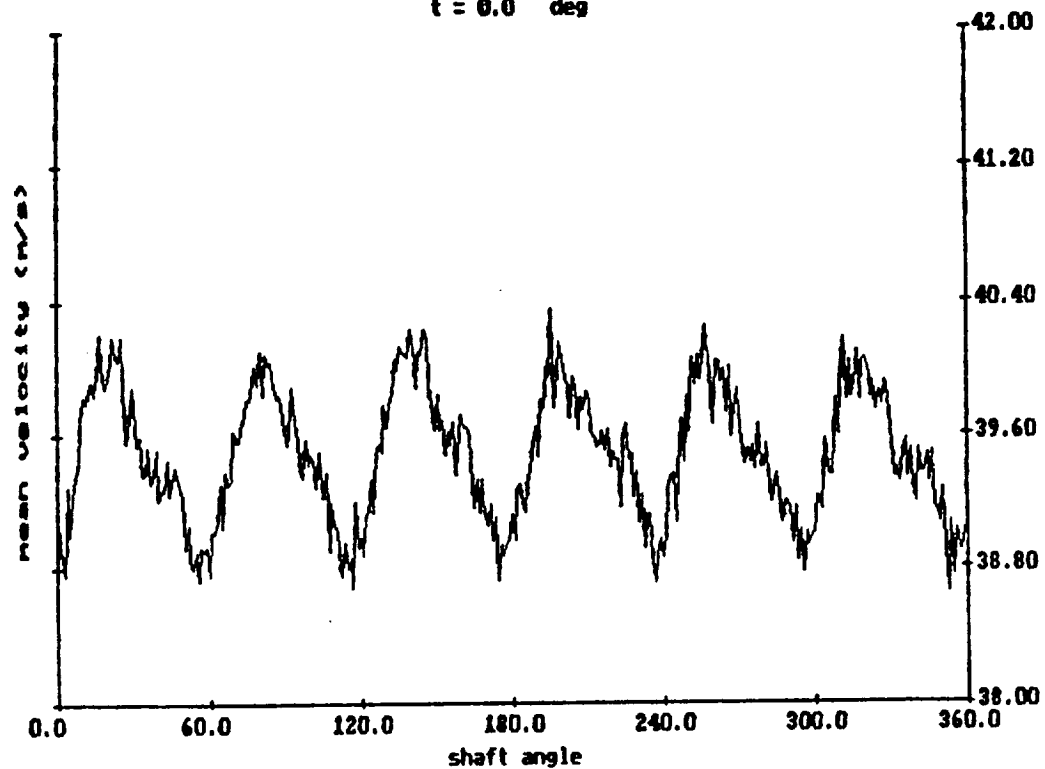
RMS Velocity  
U component  
 $r = 30.0$  mm  
 $z = 6.5$  mm  
 $t = 0.0$  deg



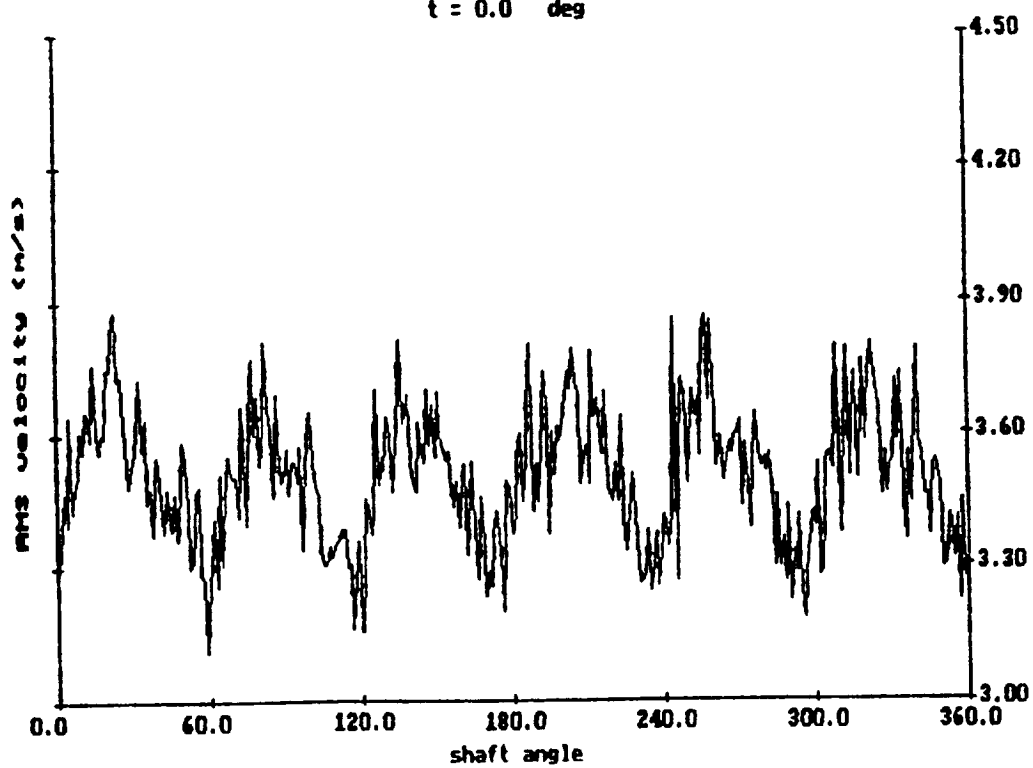


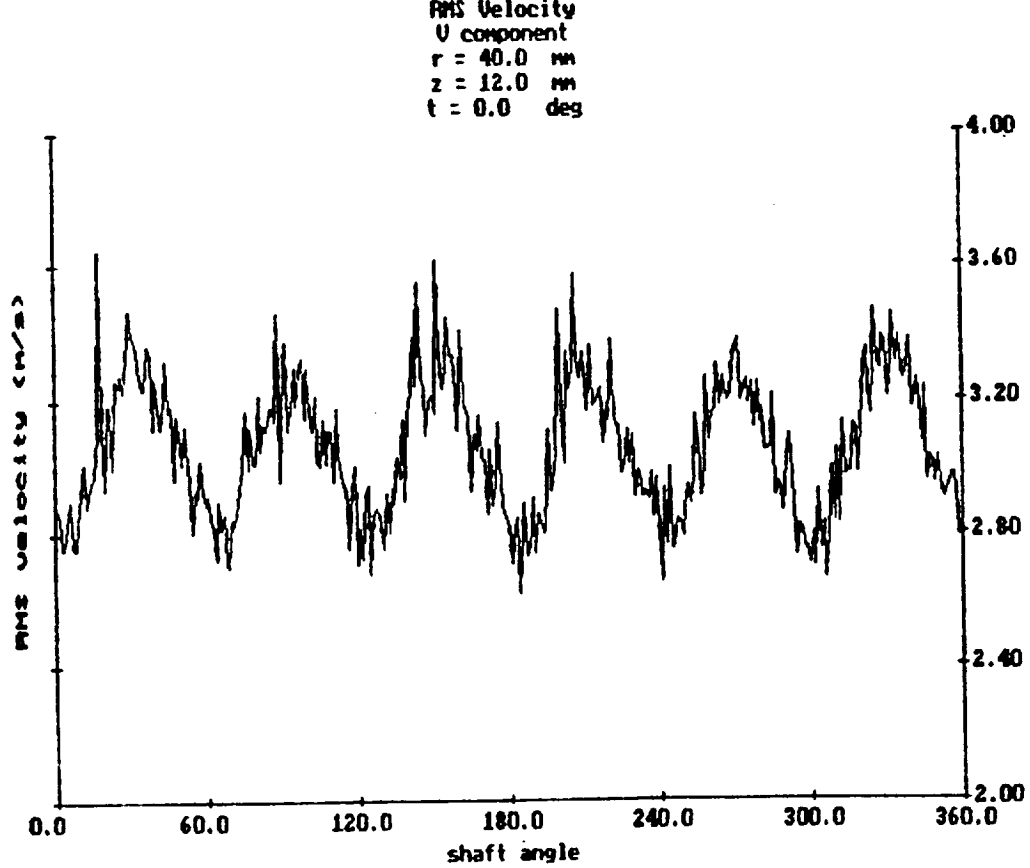
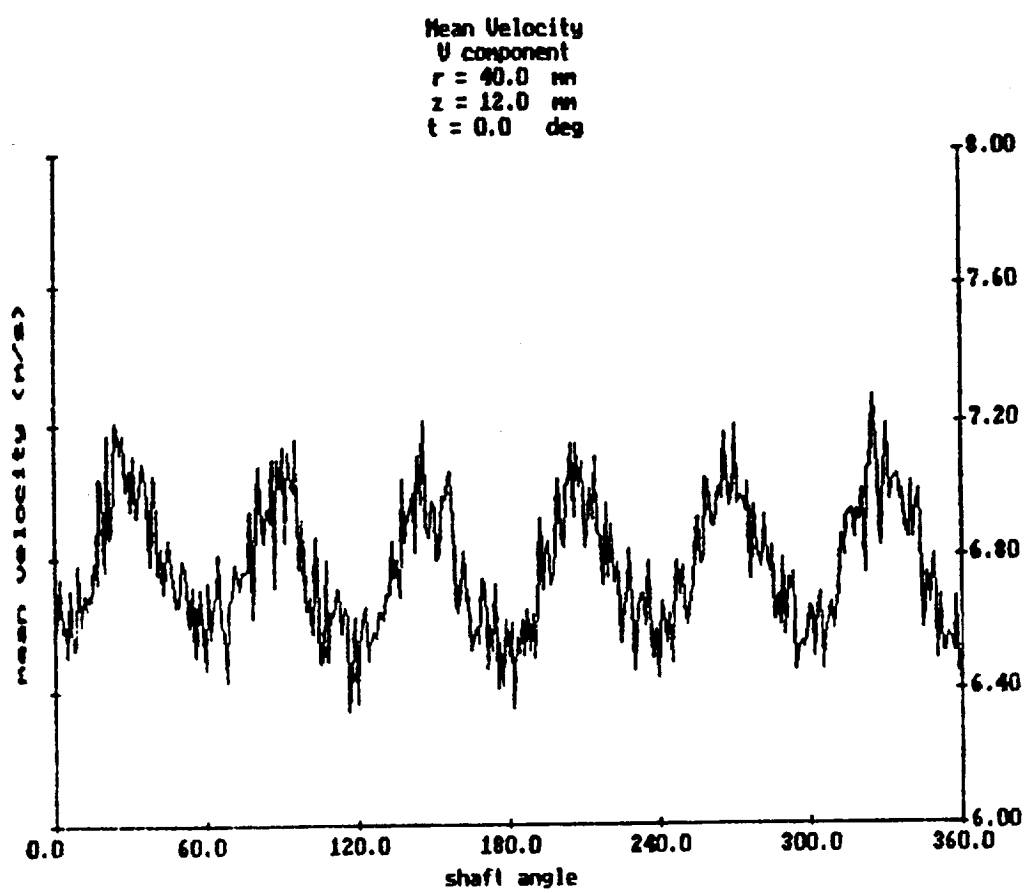


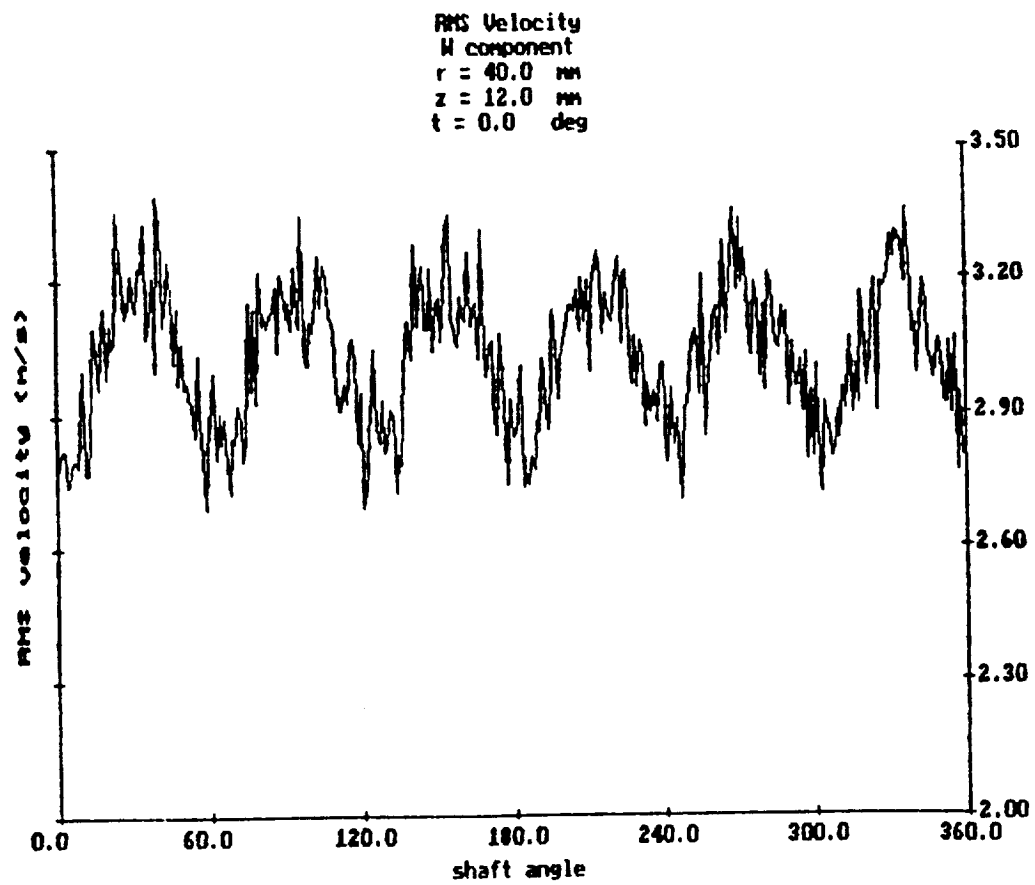
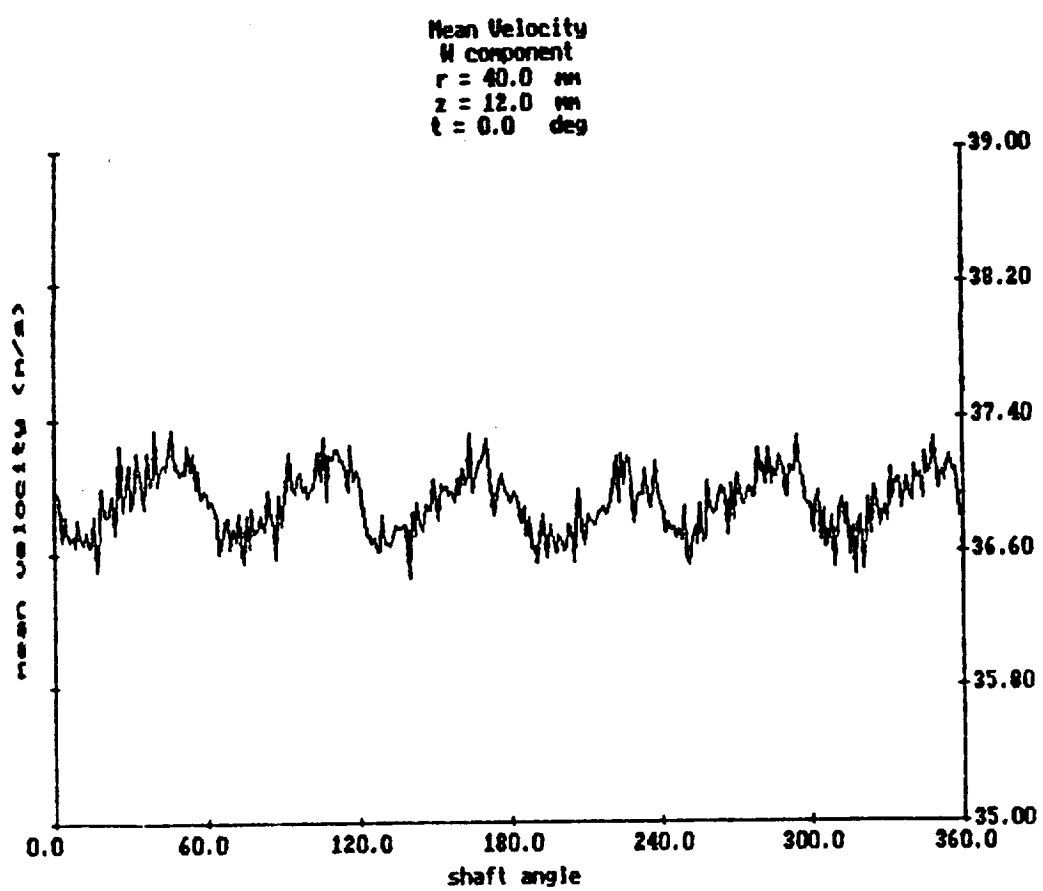
Mean Velocity  
W component  
 $r = 35.0$  mm  
 $z = 6.5$  mm  
 $t = 0.0$  deg

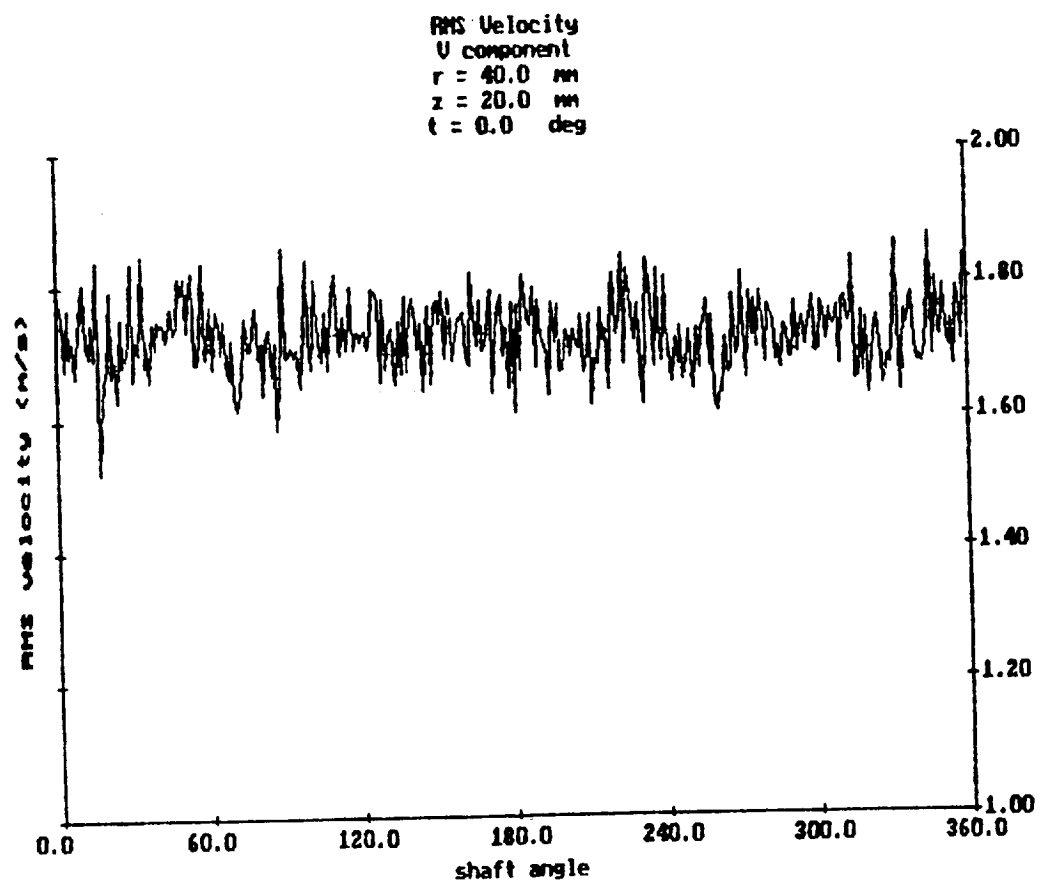
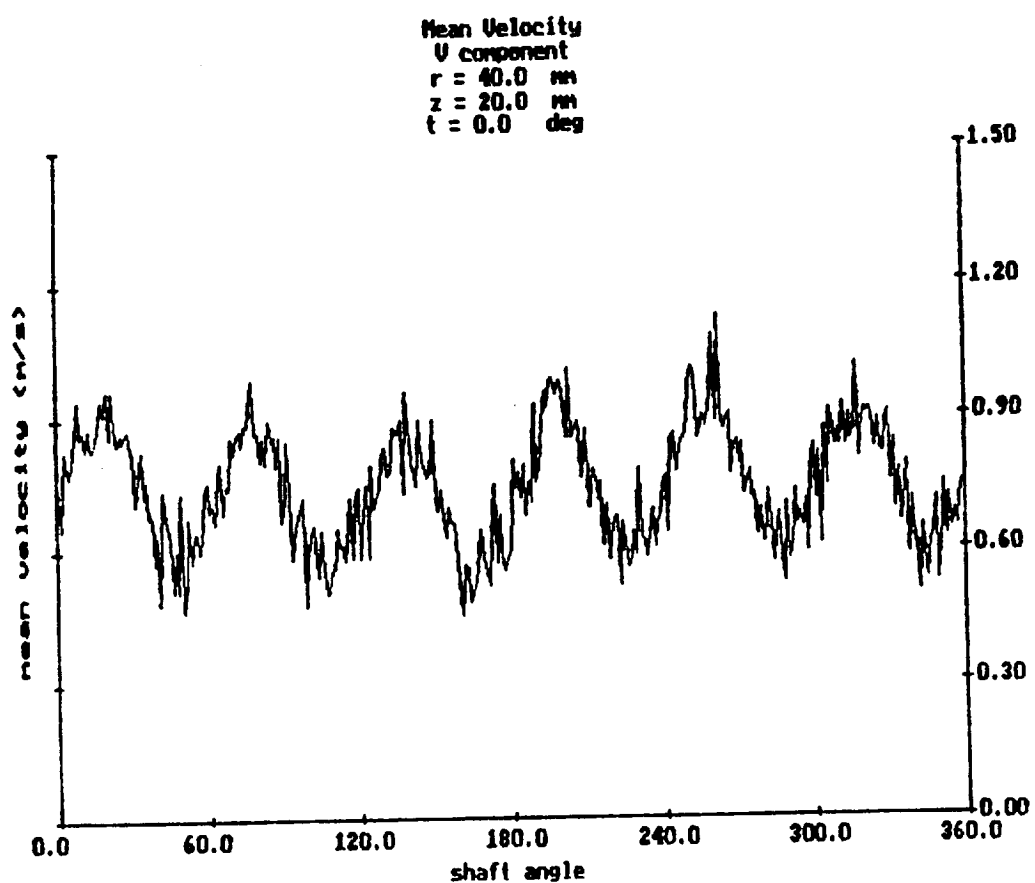


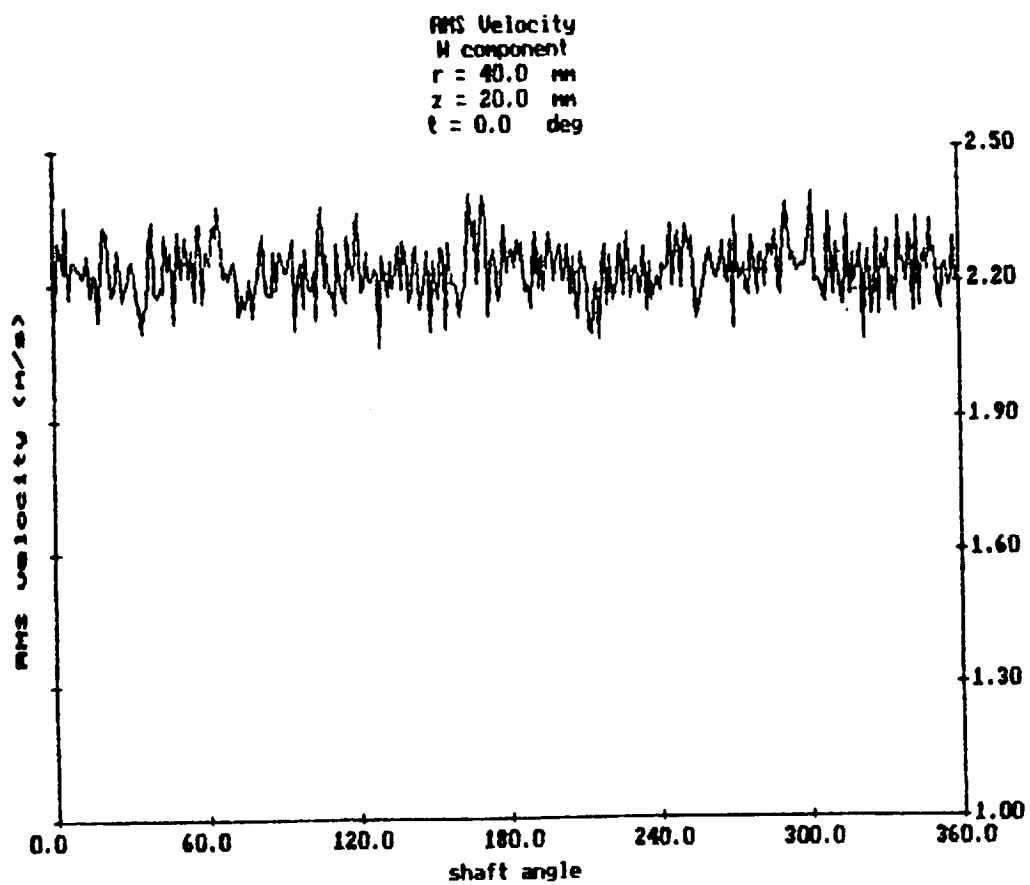
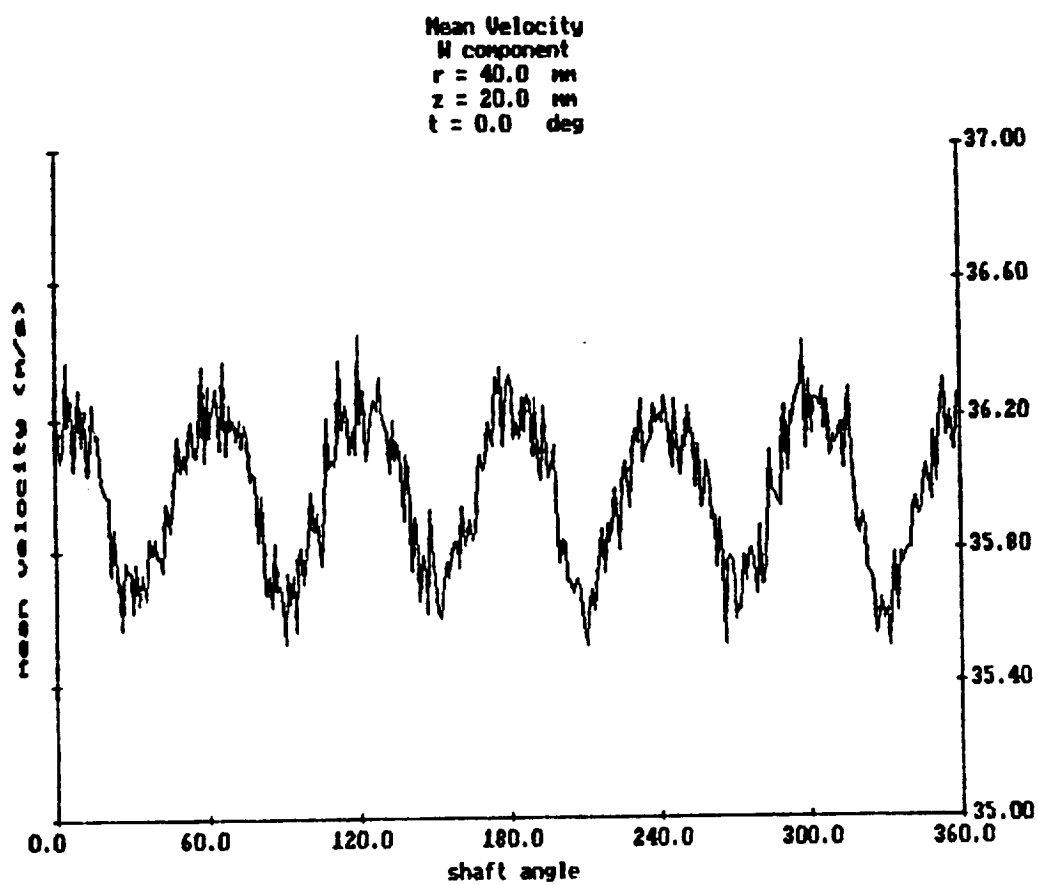
RMS Velocity  
W component  
 $r = 35.0$  mm  
 $z = 6.5$  mm  
 $t = 0.0$  deg



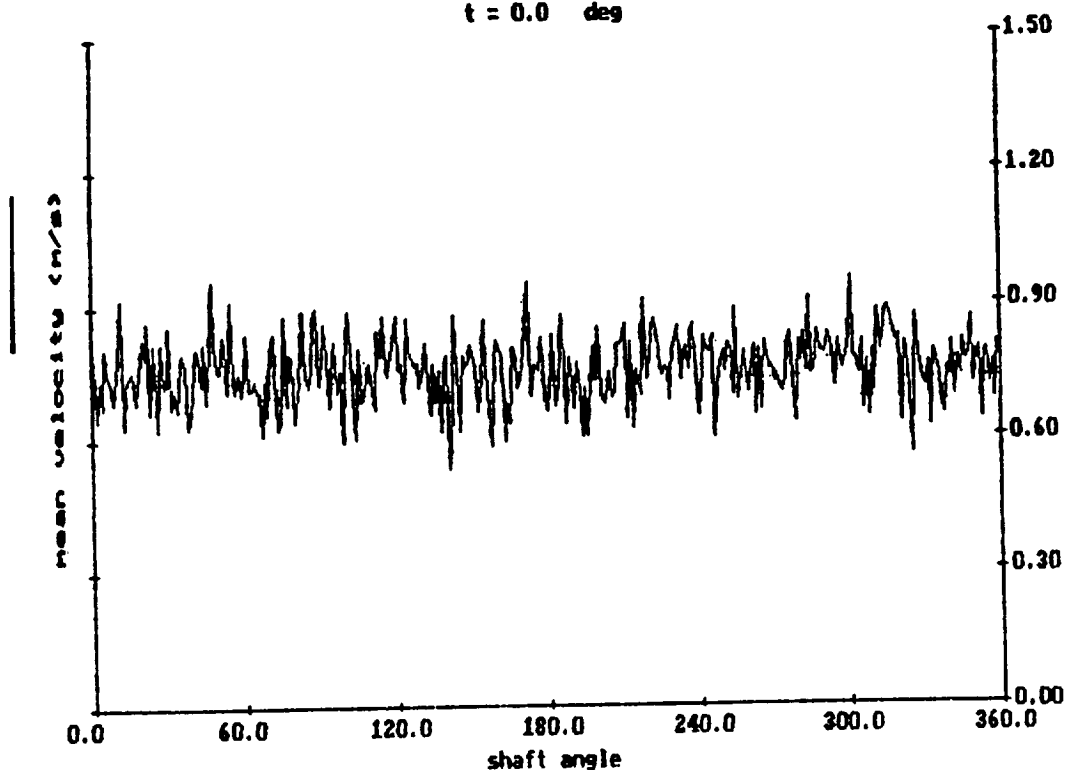




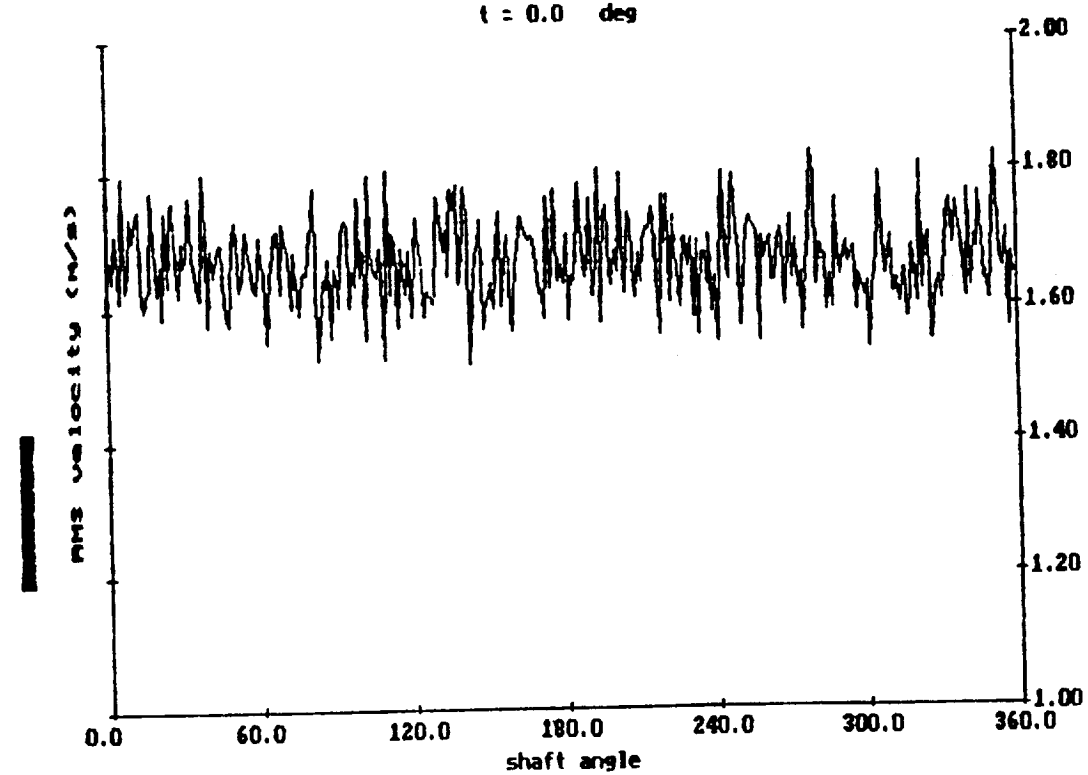


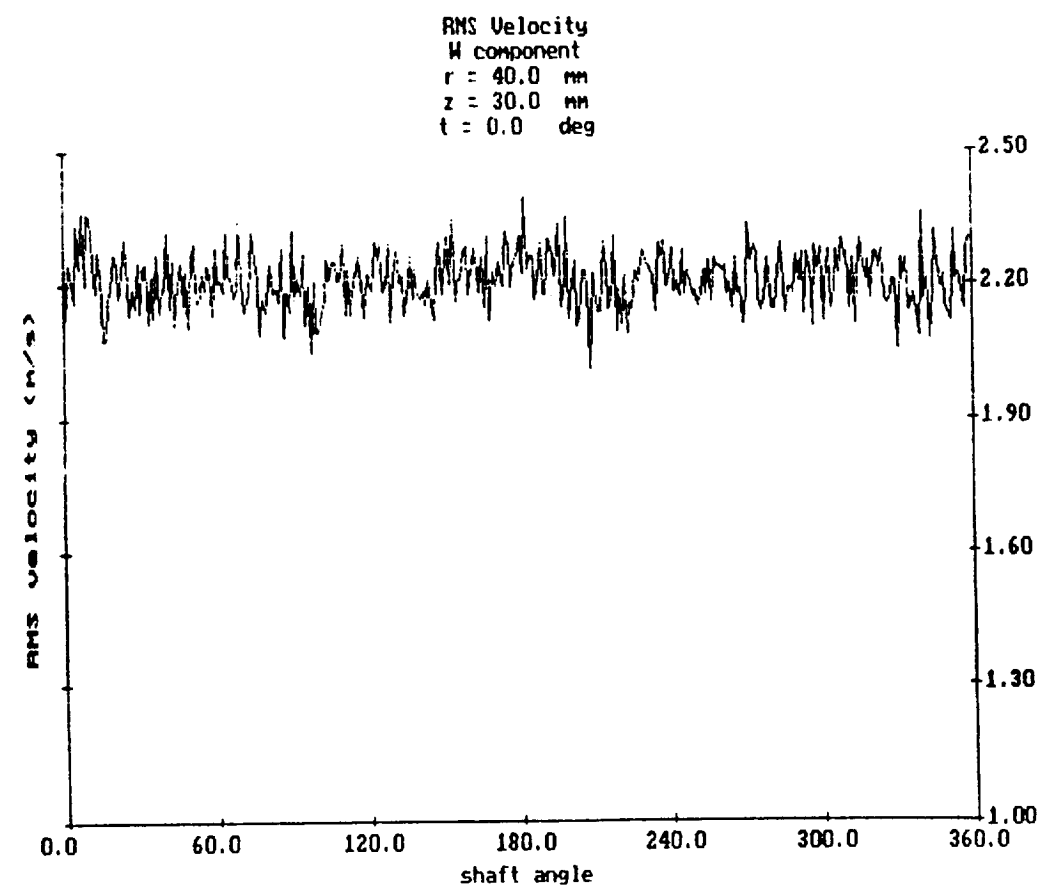
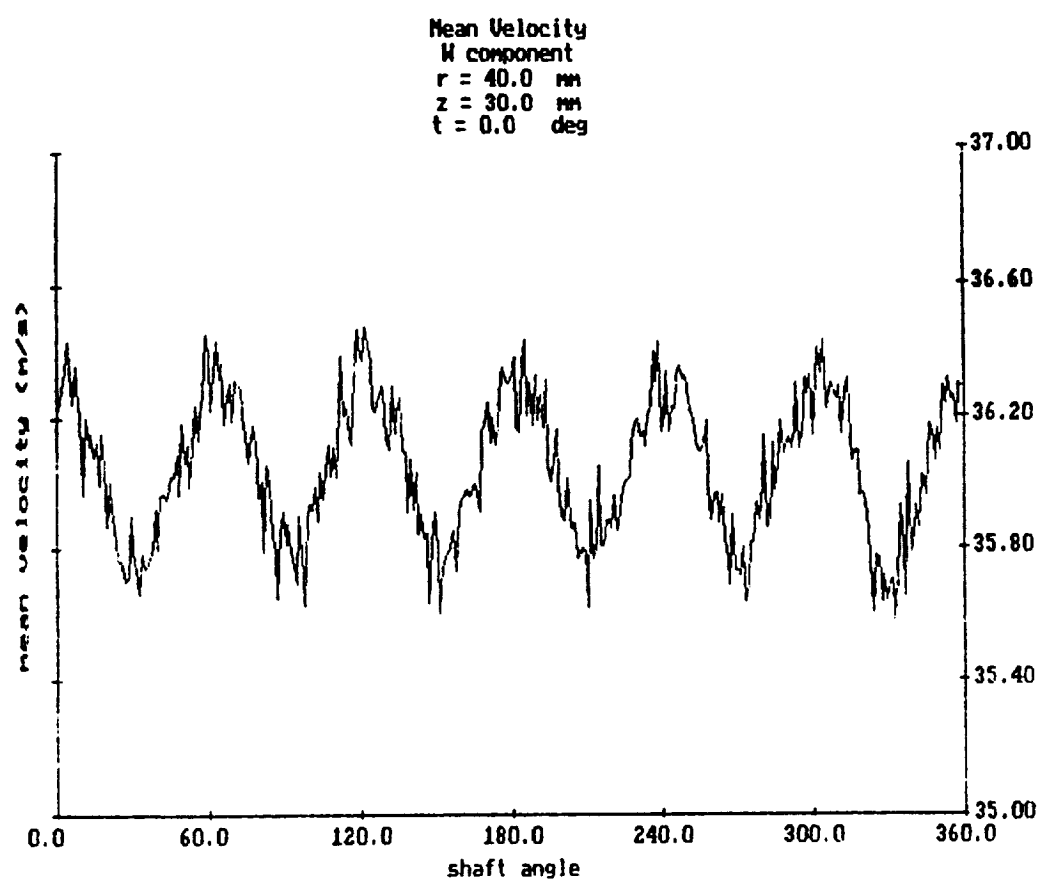


Mean Velocity  
U component  
 $r = 40.0$  mm  
 $z = 30.0$  mm  
 $t = 0.0$  deg

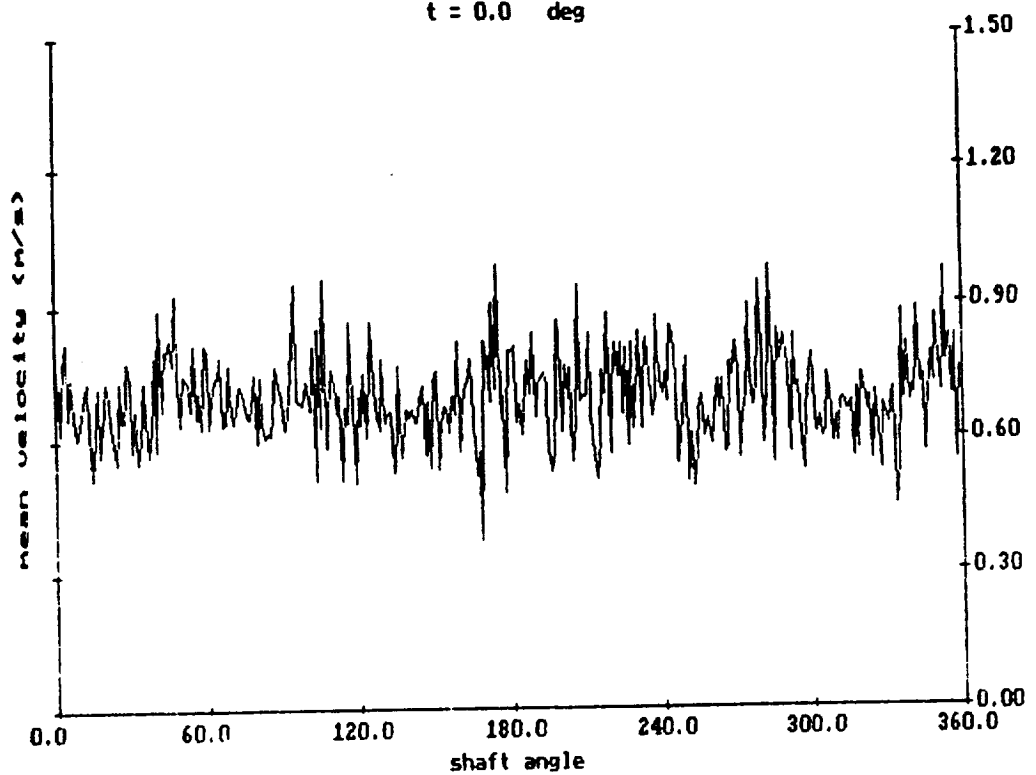


RMS Velocity  
U component  
 $r = 40.0$  mm  
 $z = 30.0$  mm  
 $t = 0.0$  deg

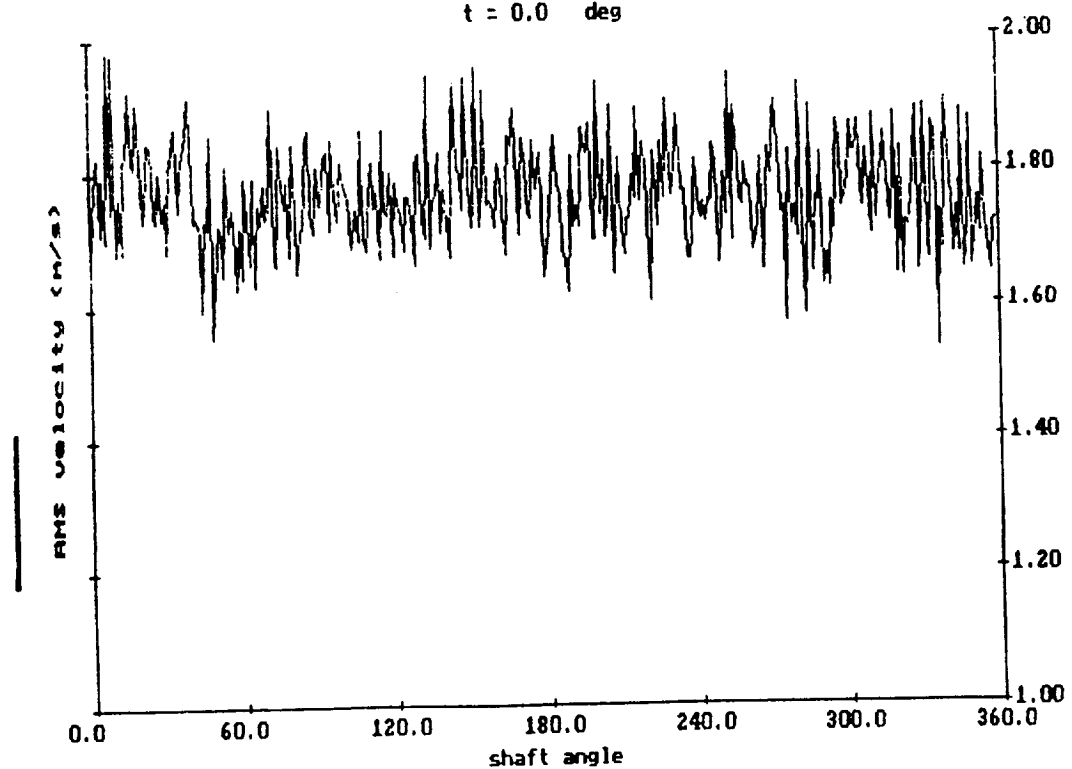




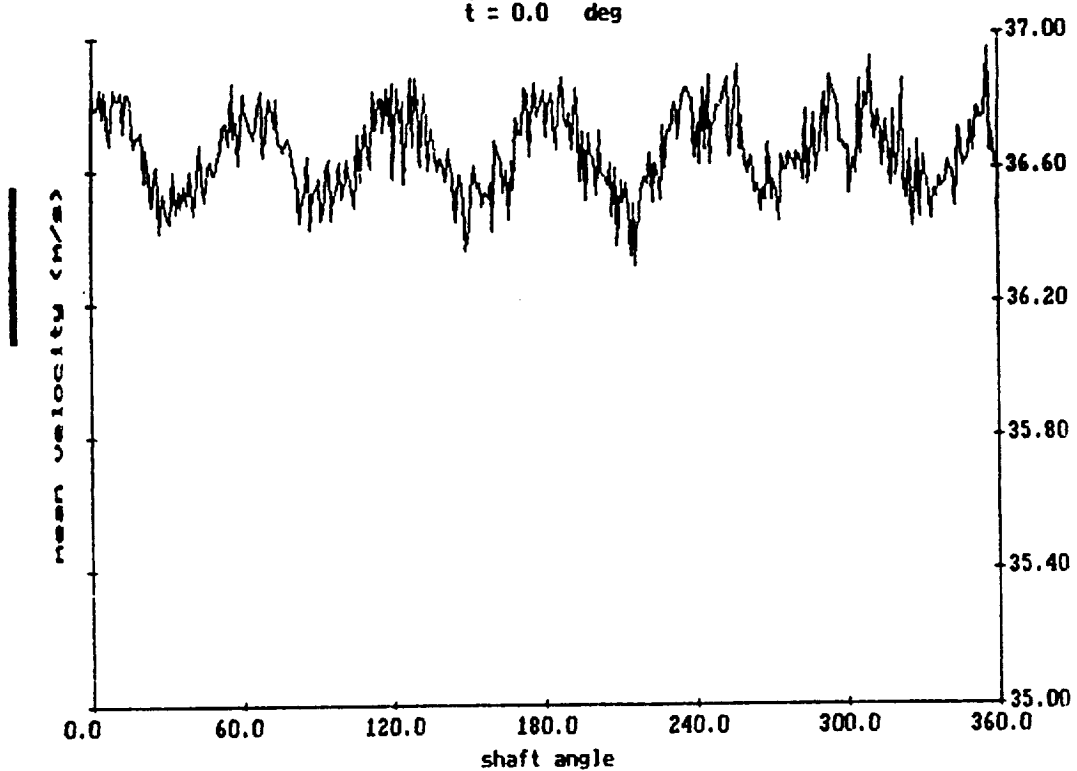
Mean Velocity  
U component  
 $r = 40.0$  mm  
 $z = 40.0$  mm  
 $t = 0.0$  deg



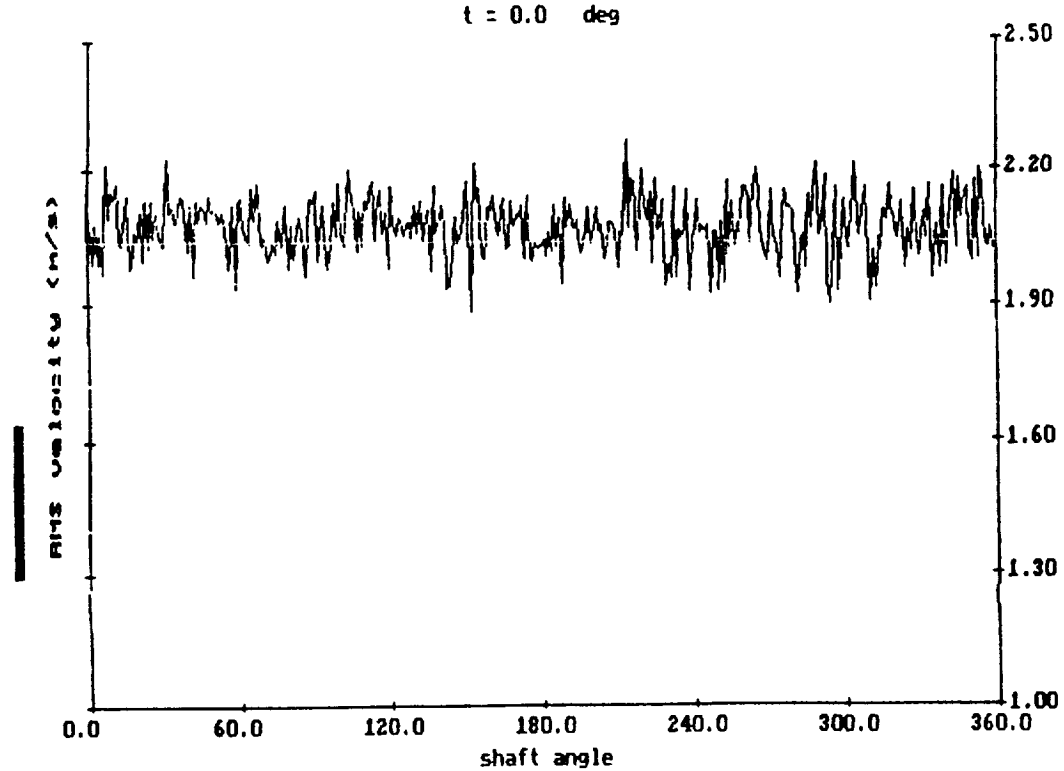
RMS Velocity  
U component  
 $r = 40.0$  mm  
 $z = 40.0$  mm  
 $t = 0.0$  deg



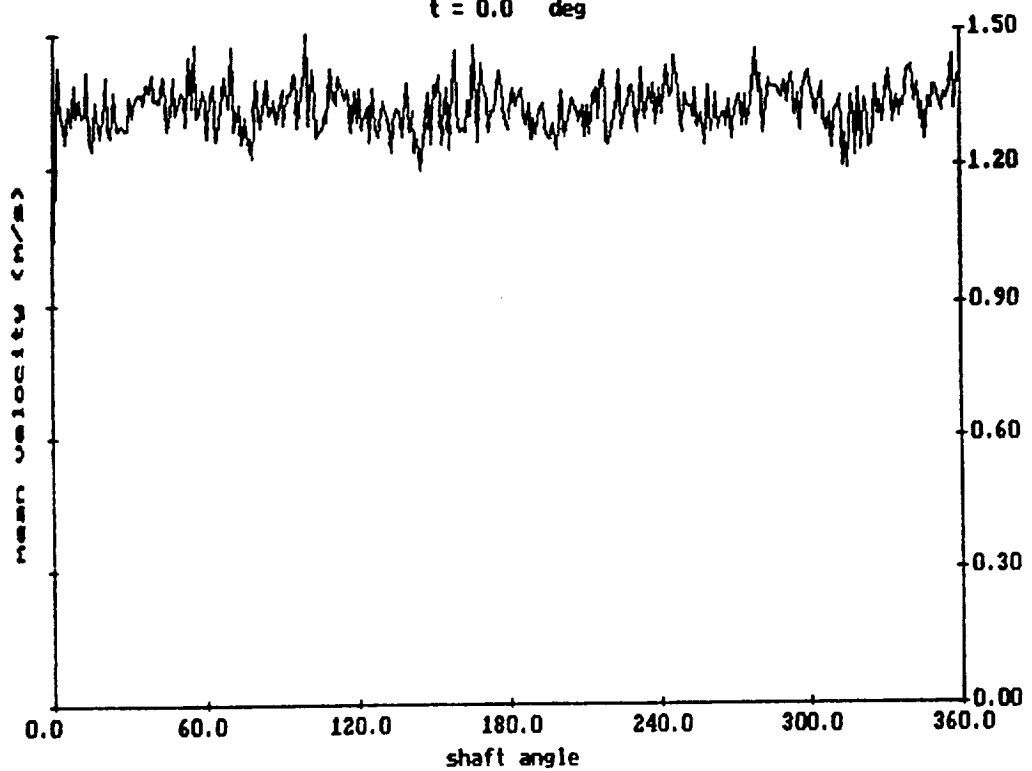
Mean Velocity  
W component  
 $r = 40.0$  mm  
 $z = 40.0$  mm  
 $t = 0.0$  deg



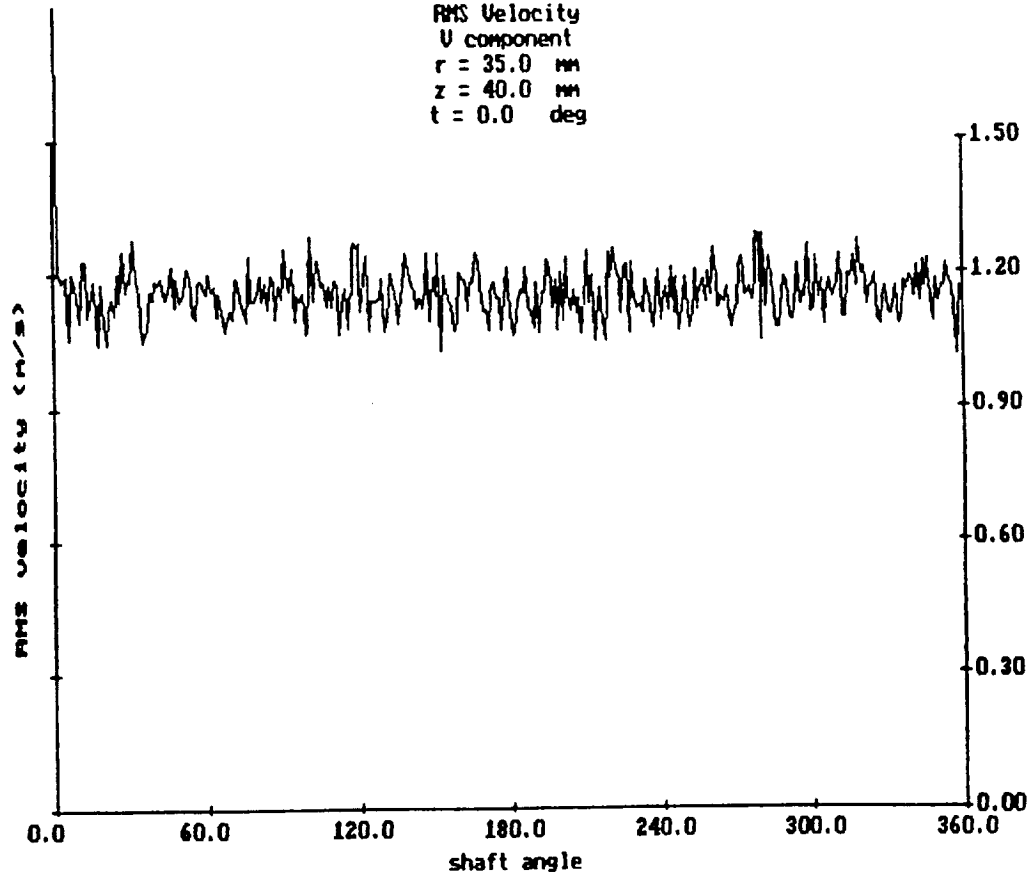
RMS Velocity  
W component  
 $r = 40.0$  mm  
 $z = 40.0$  mm  
 $t = 0.0$  deg



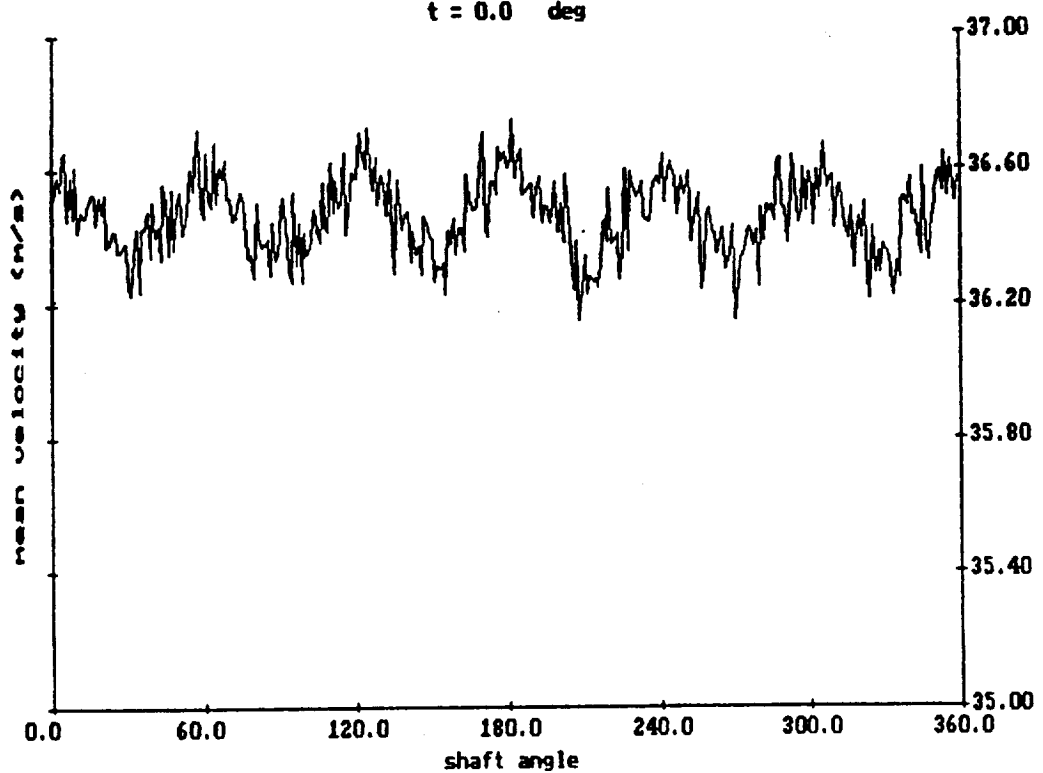
Mean Velocity  
U component  
 $r = 35.0$  mm  
 $z = 40.0$  mm  
 $t = 0.0$  deg



RMS Velocity  
U component  
 $r = 35.0$  mm  
 $z = 40.0$  mm  
 $t = 0.0$  deg



Mean Velocity  
W component  
 $r = 35.0$  mm  
 $z = 40.0$  mm  
 $t = 0.0$  deg



RMS Velocity  
W component  
 $r = 35.0$  mm  
 $z = 40.0$  mm  
 $t = 0.0$  deg

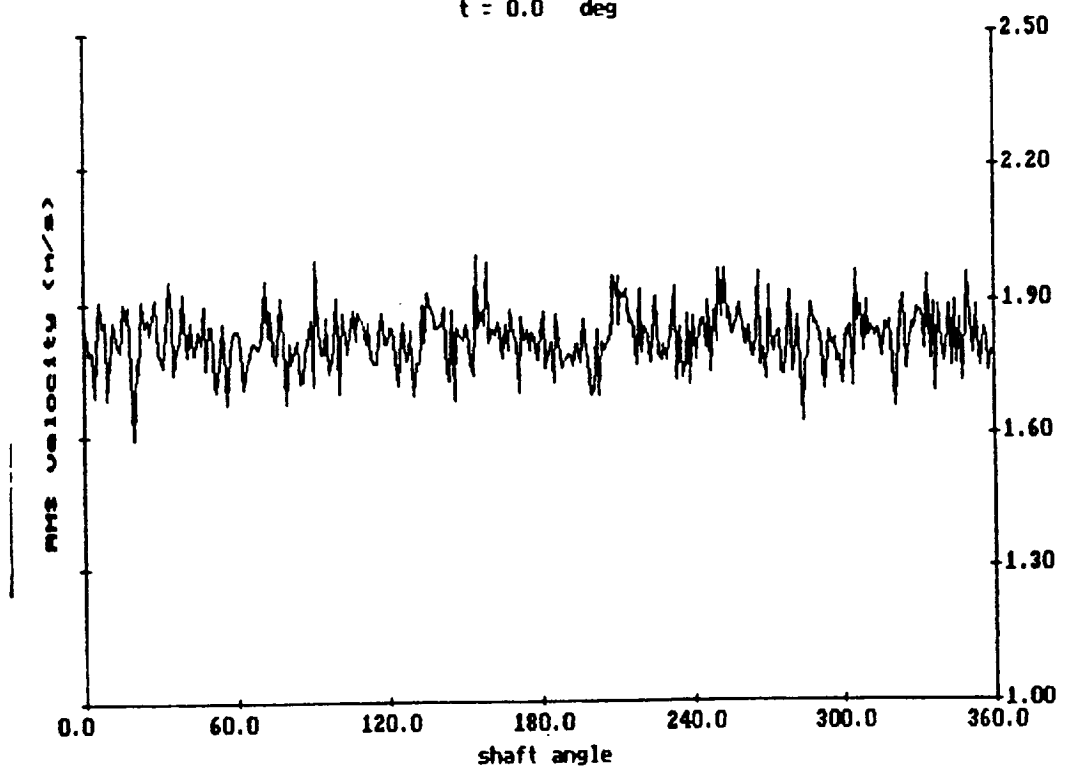
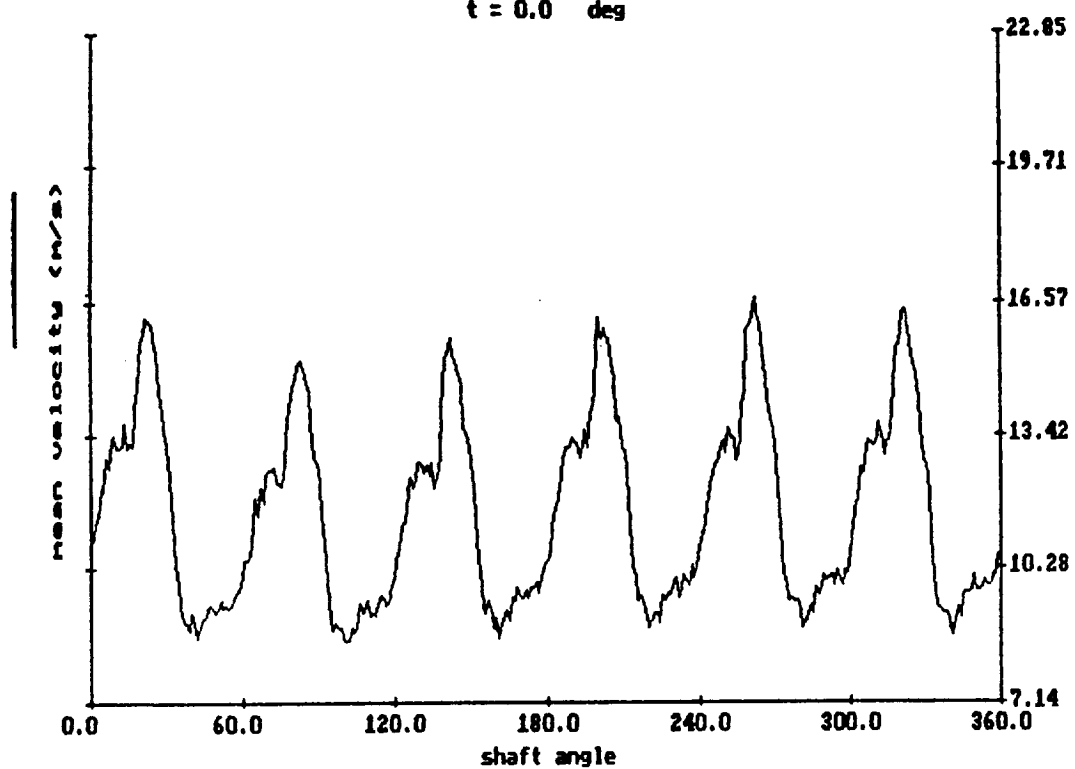


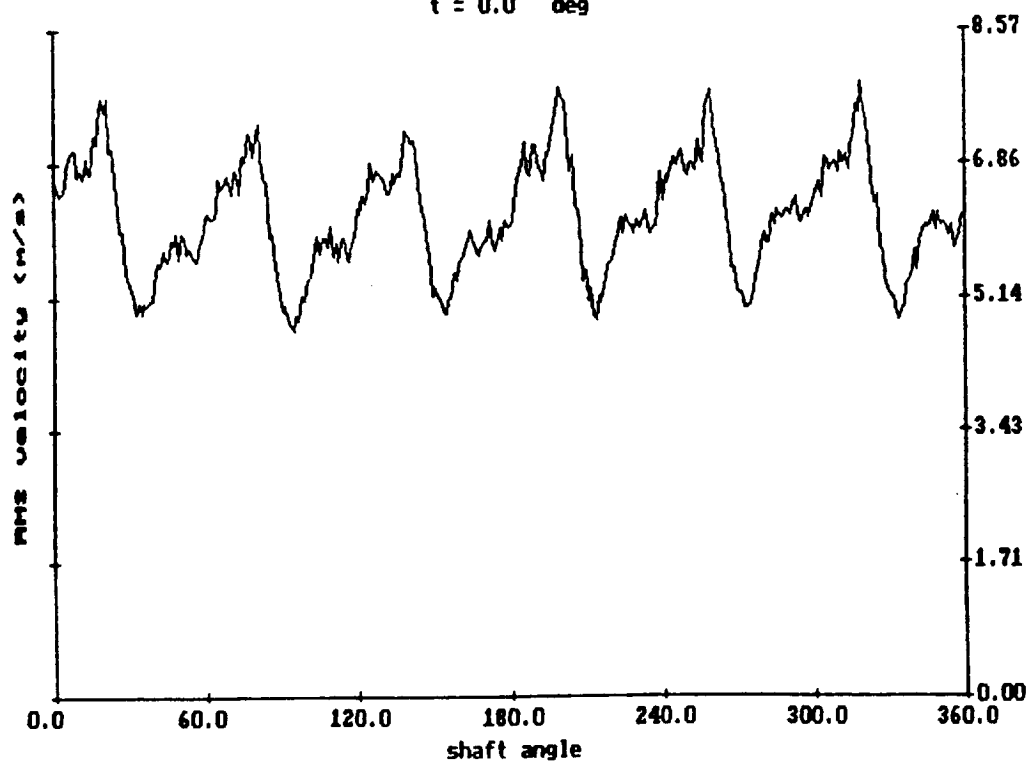
**FIGURE 11**

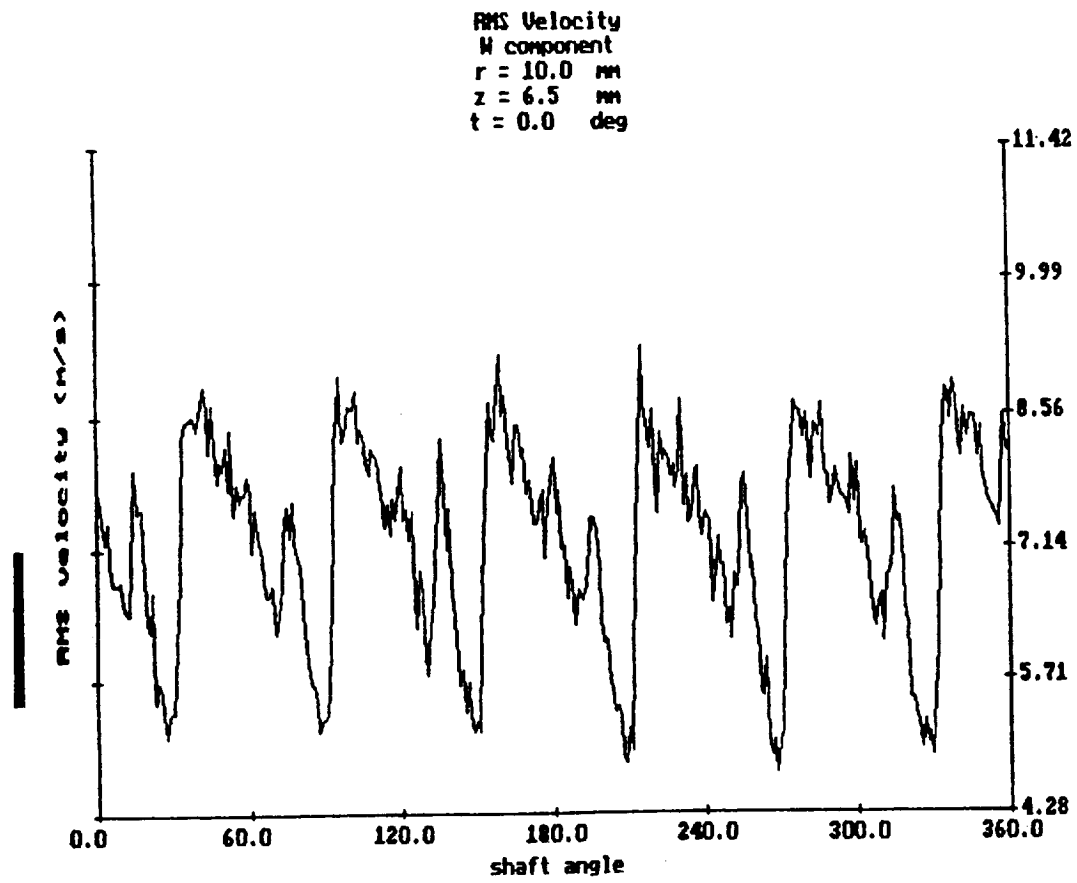
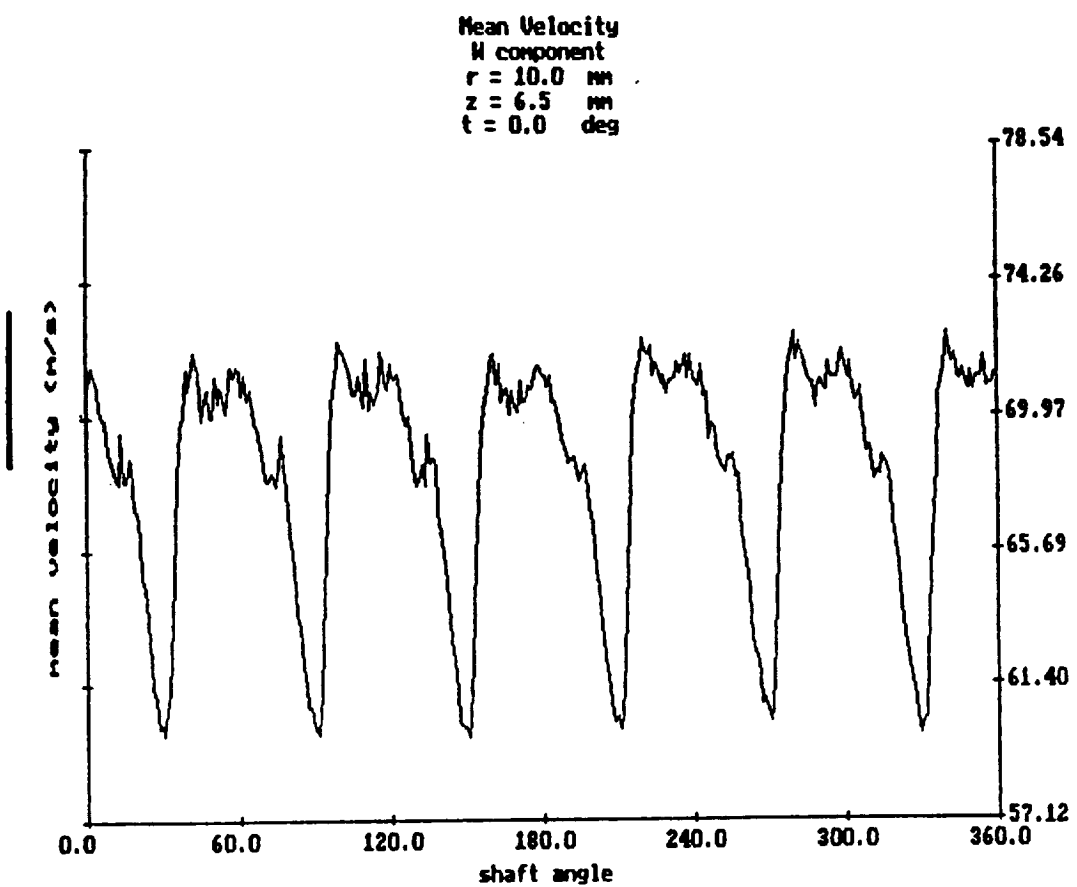
**6084 RPM**

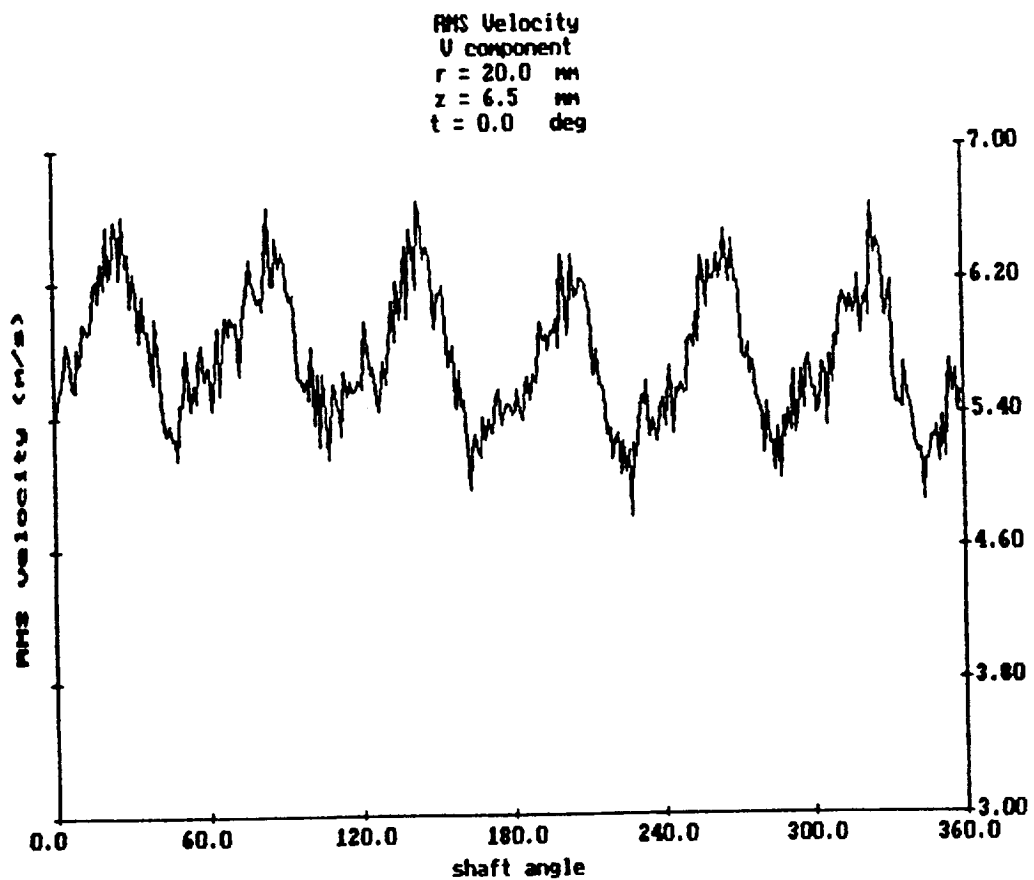
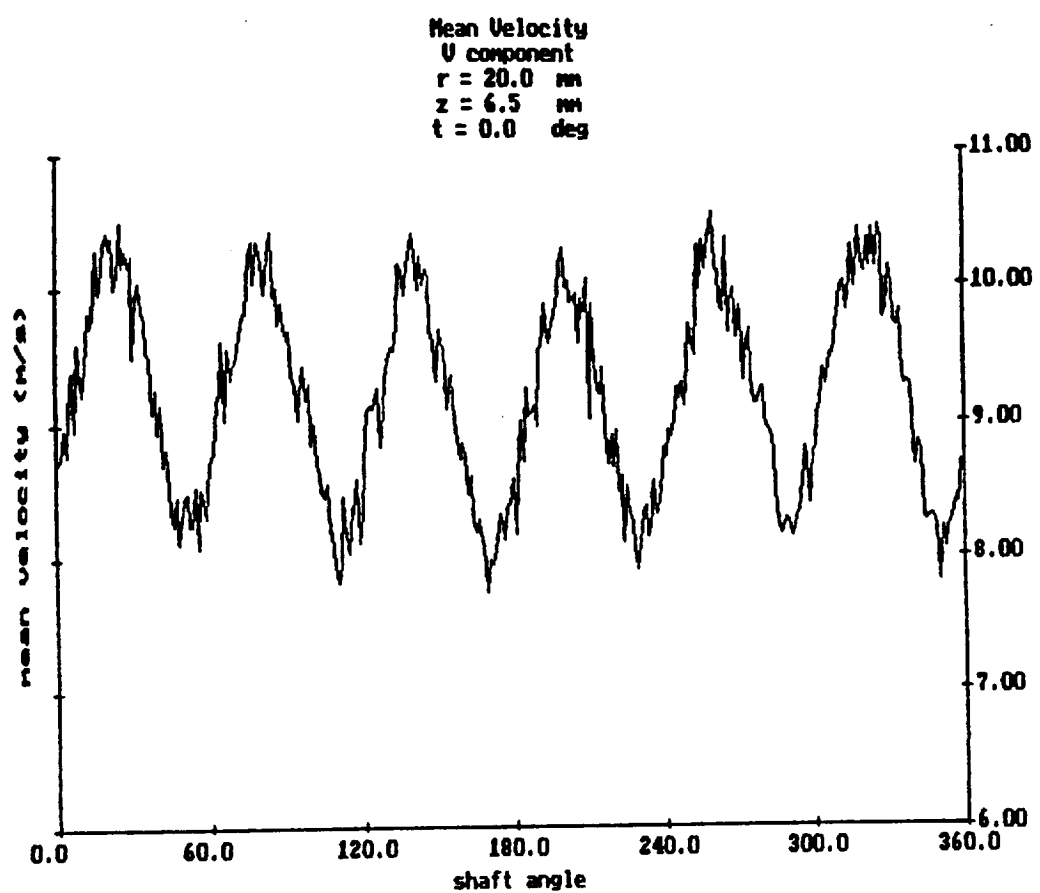
Mean Velocity  
U component  
 $r = 10.0$  mm  
 $z = 6.5$  mm  
 $t = 0.0$  deg



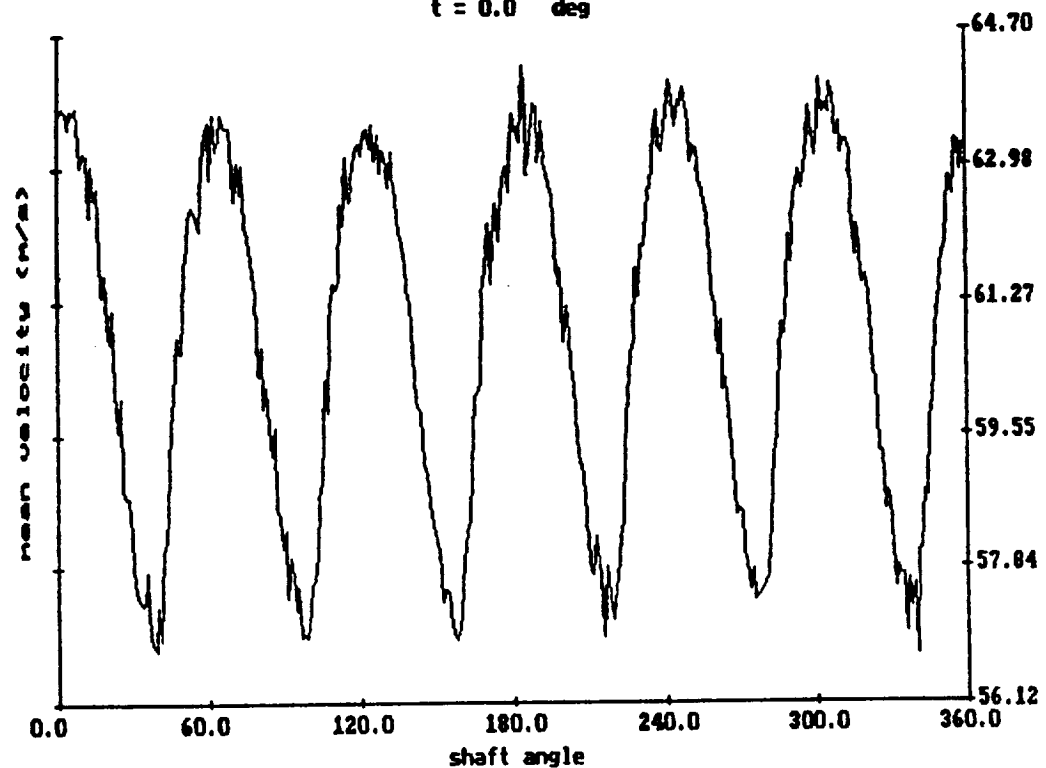
RMS Velocity  
U component  
 $r = 10.0$  mm  
 $z = 6.5$  mm  
 $t = 0.0$  deg



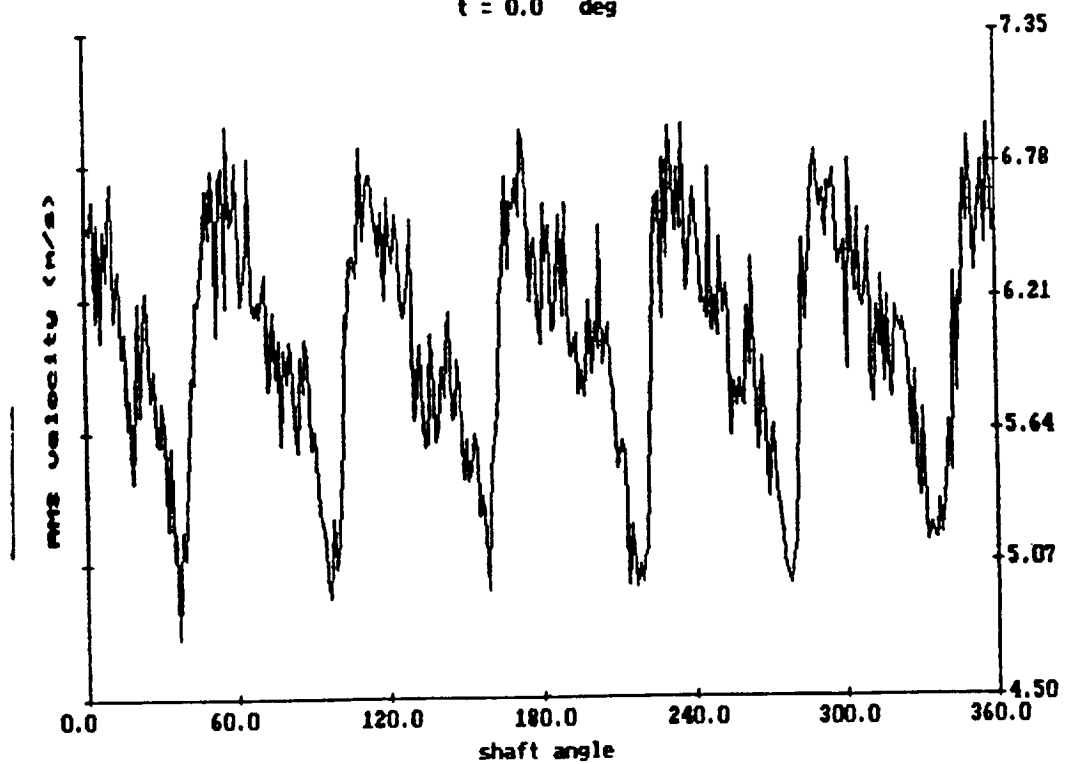


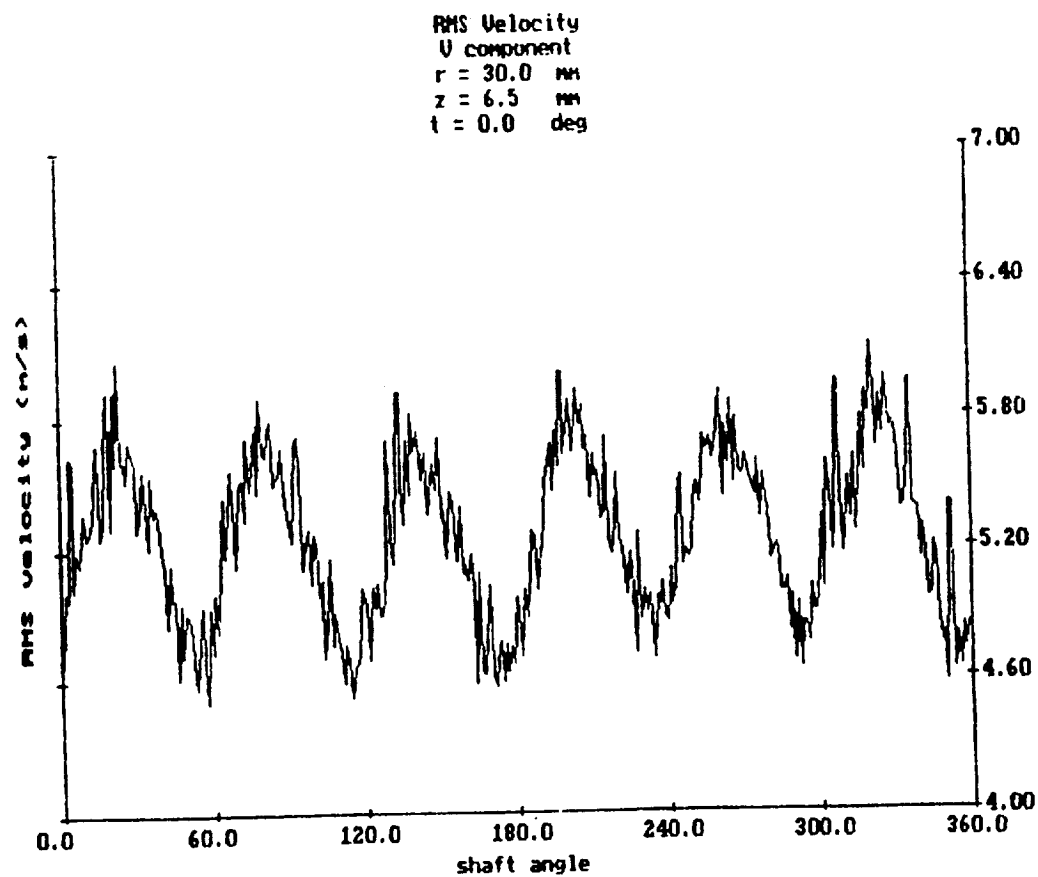
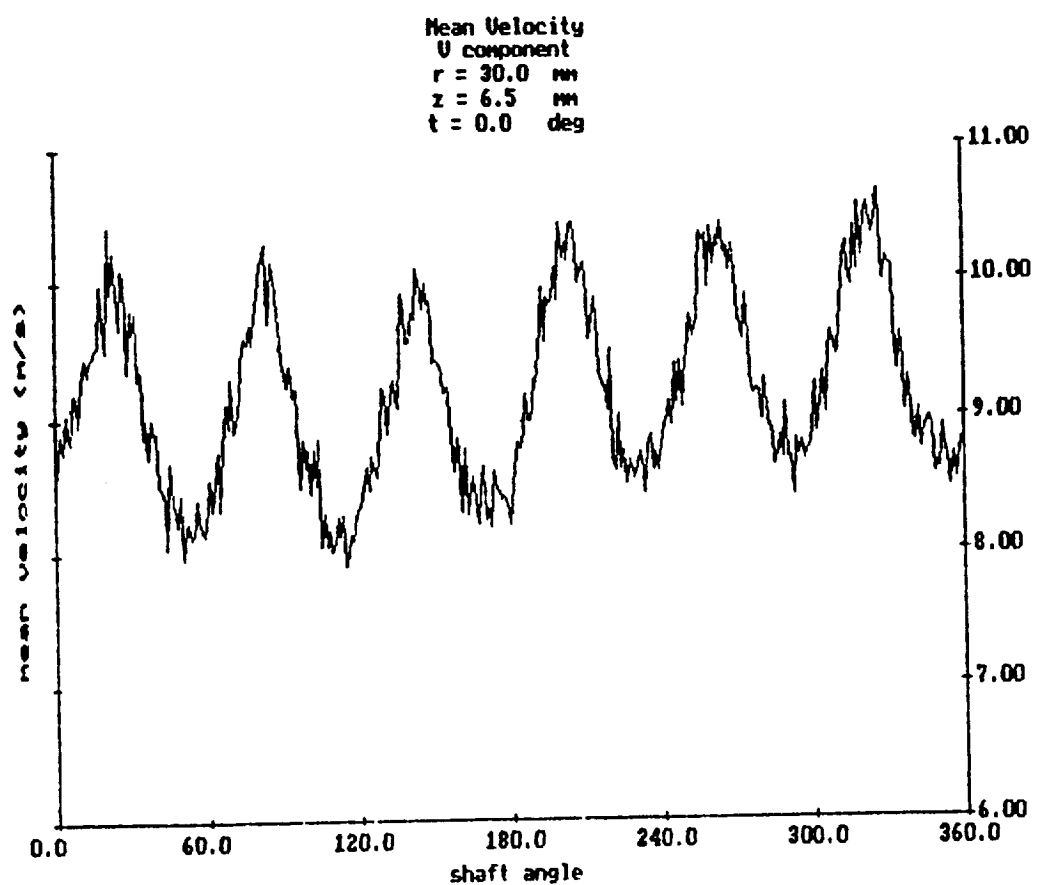


Mean Velocity  
W component  
 $r = 20.0$  mm  
 $z = 6.5$  mm  
 $t = 0.0$  deg



RMS Velocity  
W component  
 $r = 20.0$  mm  
 $z = 6.5$  mm  
 $t = 0.0$  deg





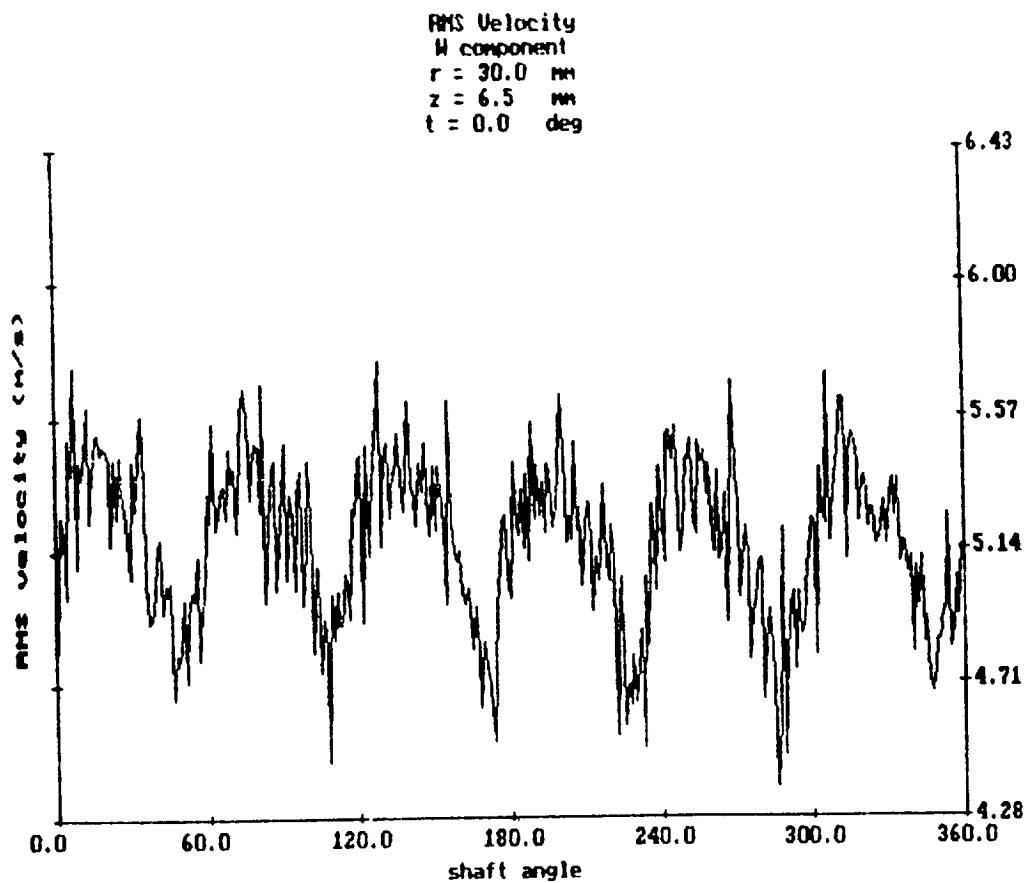
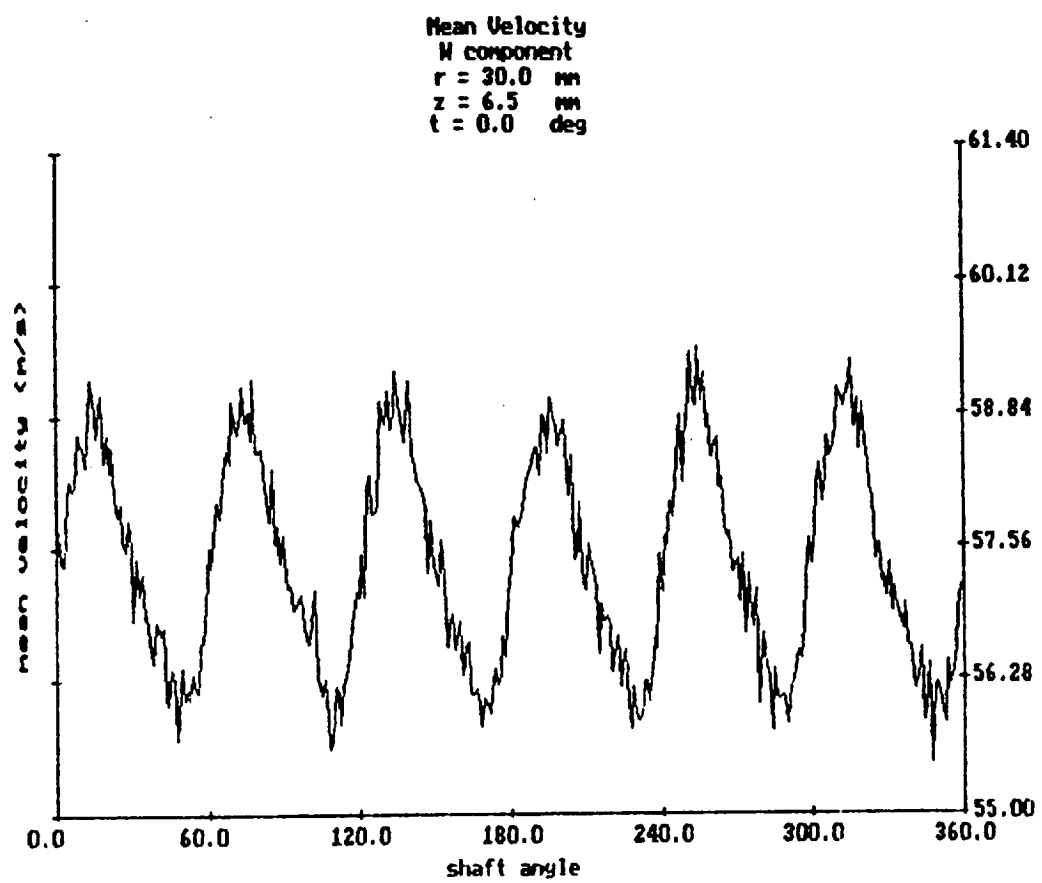
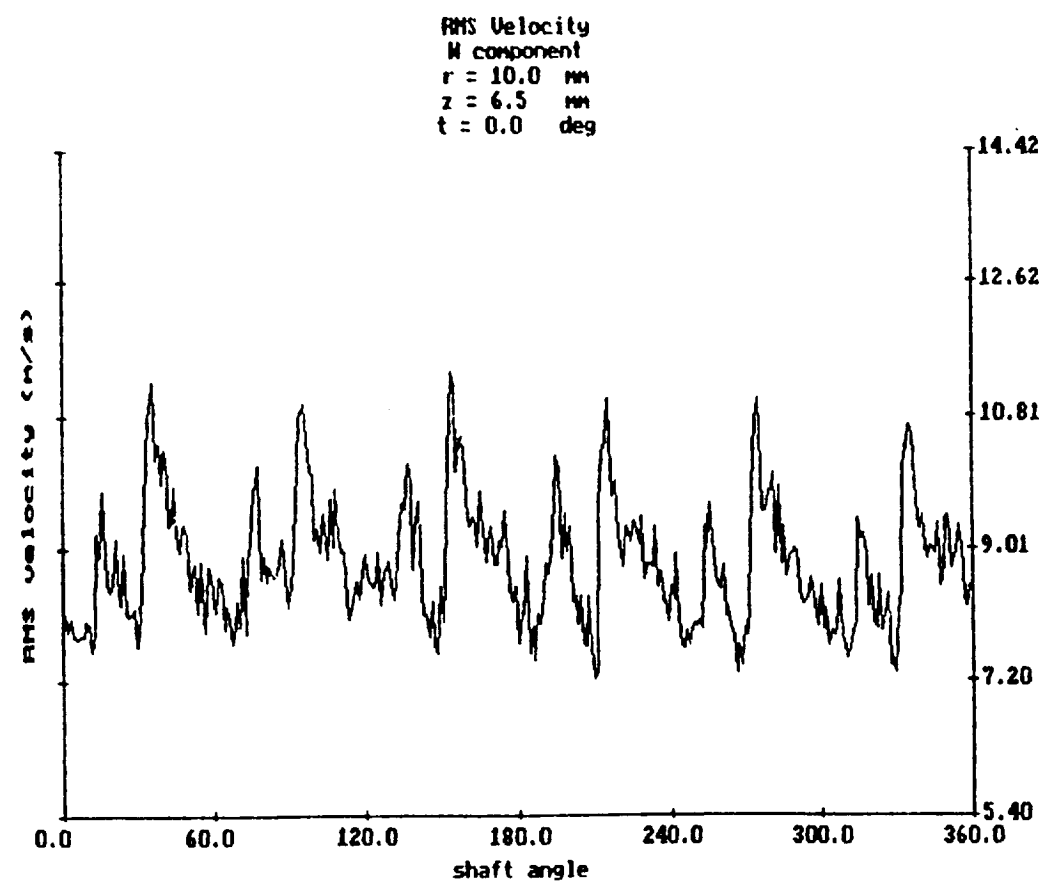
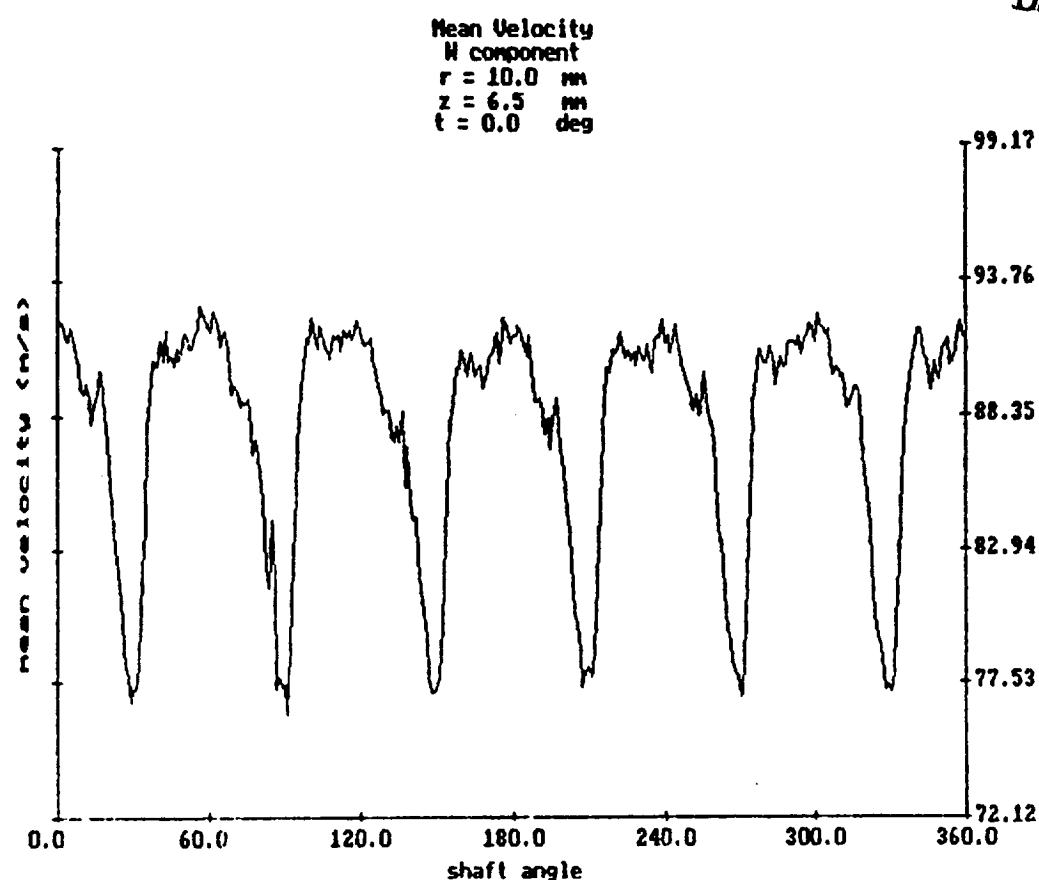


**FIGURE 12**

**7680 RPM**



ORIGINAL PAGE IS  
OF POOR QUALITY

